Advancing Spatiotemporal Individual-Level Modeling of Infectious Disease Transmission Dynamics

by

Amin Abed

A thesis submitted to the Faculty of Graduate and Postdoctoral Studies of
The University of Manitoba
in partial fulfillment of the requirements of the degree of

Doctor of Philosophy

College of Community and Global Health
Rady Faculty of Health Sciences
University of Manitoba
Canada

Abstract

This thesis advances spatiotemporal modeling of infectious disease transmission dynamics by addressing key limitations of the Geographically Dependent Individual-Level Model (GD-ILM) framework. These limitations include reinfection, seasonal transmission, and computational inefficiency for large-scale epidemics. This work is further supported by development of two R packages. In addition, spatiotemporal analyses of Gonorrhea data from Manitoba identify persistent hotspots for targeted interventions.

First, the GD-ILM is extended within a Susceptible–Exposed–Infectious–Recovered–Susceptible framework to capture reinfection dynamics, enabling the model to estimate susceptibility to both primary infection and reinfection while preserving spatially explicit transmission patterns. Application to individual-level Tuberculosis data from Manitoba reveals significant regional and individual-level risk factors and produces fine-scale infection probability maps, providing actionable insights for public health intervention.

Second, the GD-ILM is extended to incorporate seasonally varying transmission, capturing temporal fluctuations in infection risk due to environmental, behavioral, and pathogen-driven factors. Applied to Influenza data from Manitoba, the seasonal GD-ILM identifies high-risk regions and periods, demonstrating the importance of integrating temporal dynamics into spatial models, with simulations confirming the ability to recover spatiotemporal patterns. Parameter estimation in both extensions is performed using a likelihood-based Monte Carlo Expectation Conditional Maximization algorithm.

Third, to overcome computational challenges posed by large-scale epidemics when using the GD-ILM framework, a stratified temporally-weighted Kernel Density Estimation-based Probability Proportional to Size sampling approach, combined with Stochastic Approximation Expectation Conditional Maximization, is developed, enabling efficient parameter estimation and real-time application, and is illustrated through simulations and COVID-19 data from Manitoba.

Fourth, two R packages, `GDILM.SEIRS` and `SeasEpi`, are developed and made publicly available on the Comprehensive R Archive Network (CRAN) to facilitate reproducibility and practical adoption of the proposed frameworks in future spatiotemporal individual-level modeling of infectious disease transmission dynamics.

Finally, spatial, temporal, and spatiotemporal cluster detection analyses of Gonorrhea data from Manitoba identify persistent high-risk areas and time periods, guiding targeted public health interventions.

Acknowledgments

I would like to convey my sincere appreciation to my advisors, Dr. Mahmoud Torabi and Dr. Zeinab Mashreghi, for their invaluable guidance, support, and mentorship during the course of my doctoral studies. Additionally, I am profoundly thankful to my committee members, Dr. Rob Deardon and Dr. Razvan Romanescu, for their insightful critiques, encouragement, and thoughtful recommendations, which have significantly contributed to the successful completion of this thesis.

I am sincerely thankful to the University of Manitoba for awarding me the distinguished **University of Manitoba Graduate Fellowship**. This prestigious recognition provided essential financial support during my doctoral program, enabling me to conduct my research with concentrated effort and commitment.

I express my gratitude to the **Natural Sciences and Engineering Research Council of Canada (NSERC)** for their financial support, which facilitated the progression of my research and academic objectives.

I also wish to thank the Manitoba Centre for Health Policy for recognizing my work with the **Roos Prize for Best Publication in Population Health** and the **Evelyn Shapiro Award for Health Services Research**. The recognition of these awards has been an incredible honor, a significant motivation, and a meaningful affirmation of the relevance and impact of my work in the field of population and health services research.

Dedication

I dedicate this thesis to the loving memory of my late mother, whose love, resilience, and sacrifices formed the foundation of every opportunity I have had. Though she is no longer present, her spirit continues to guide and inspire me each day.

I also dedicate this thesis to my wife, Maryam, whose love, patience, and unwavering support have been a source of strength and inspiration throughout my doctoral journey.

Contributions of Authors

This grouped manuscript thesis comprises four distinct research papers, presented in Chapters Two through Five. Amin Abed led the formulation of the research questions, conducted the investigations, and developed and implemented the methodological frameworks. He performed the analyses, programming, and software development, as well as data curation, validation, and visualization. He systematically incorporated feedback from advisors to ensure conceptual clarity, methodological coherence, and scholarly quality across all research papers included in the thesis.

Dr. Mahmoud Torabi and Dr. Zeinab Mashreghi provided exemplary guidance and strategic supervision throughout this research. Their expertise, guidance, and mentorship were instrumental in shaping the study's framework, achieving its research objectives, strengthening the methodological approach, and ensuring a thorough and accurate interpretation of results across all research papers.

Contents

List of Figures

List of Tables

List of Abbreviations

ARBP: Absolute Relative Bias Percentage

DA: Dissemination Area

ECM: Expectation Conditional Maximization

EM: Expectation-Maximization

Est.: Estimation

GD-ILM: Geographically Dependent Individual Level Model

HAD: Health Authority District

HREB: Health Research Ethics Board

ILM: Individual Level Model

KDE: Kernel Density Estimation

MCEM: Monte Carlo Expectation Maximization

MCECM: Monte Carlo Expectation Conditional Maximization

MCHP: Manitoba Centre for Health Policy

MSE: Mean Squared Error

NSERC: Natural Sciences and Engineering Research Council of Canada

PCCF: Postal Code Conversion File

PCR: Postal Code Region

PHRPC: Provincial Health Research Privacy Committee

PPS: Probability Proportional to Size

RHAD: Regional Health Authority District

SAECM: Stochastic Approximation Expectation Conditional Maximization

S.E.: Standard Error

SEIR: Susceptible-Exposed-Infectious-Recovered

SEIRS: Susceptible-Exposed-Infectious-Recovered-Susceptible

SES: Socio-Economic Status

SIR: Susceptible-Infectious-Recovered

STI: Sexually Transmitted Infections

TB: Tuberculosis

1

Introduction

The dynamics of infectious disease transmission arise from a complex interplay of biological mechanisms, environmental factors, social determinants, and human behaviors, alongside interactions between infectious and susceptible individuals [5]. Compartmental models provide a mathematical framework to systematically describe, analyze, and forecast the dynamics of infectious diseases. They partition a population into distinct groups based on disease status and model transitions among these groups using systems of differential equations [41]. Such models enable researchers to quantify epidemic behavior, predict outbreak trajectories, and evaluate the effectiveness of potential control measures.

While compartmental models can be extended by adding compartments to represent specific aspects of disease dynamics, stochastic models allow for an explicit representation of individual-level variability and random fluctuations in transmission and reinfection events, which deterministic models cannot directly capture. One major benefit is the incorporation of randomness, which allows stochastic models to mirror the natural variability and unpredictability of real-world outbreaks. Stochasticity is particularly important in small populations or during the early stages of an outbreak, where unpredictable events, such as superspreading, can significantly influence epidemic trajectories [85]. Additionally, stochastic models can simulate individual-level interactions and heterogeneity within the population, considering variations in contact patterns, susceptibility, and infectiousness, which lead to more precise and detailed predictions. Although deterministic models are valued for their simplicity and computational efficiency, stochastic models deliver a more comprehensive and realistic representation of infectious disease dynamics, especially in scenarios where randomness and individual differences are significant factors. In contrast, stochastic models incorporate randomness, allowing them to reflect natural variability and unpredictability in real-world outbreaks. Although deterministic models remain valued for their simplicity and computational efficiency, stochastic compartmental models offer a more detailed and realistic representation of infectious disease dynamics, particularly in scenarios where randomness and individual differences play a critical role.

Contemporary advances in infectious disease modeling have increasingly emphasized the integration of spatial and temporal dimensions, a development facilitated by the growing availability of high-resolution geographic data and enhanced computational capacity [87]. Spatiotemporal models have therefore emerged as essential tools, enabling a detailed understanding of outbreak patterns and progression. By jointly capturing spatial and temporal dynamics, these models improve predictive accuracy, inform targeted public health interventions, and optimize the allocation of resources. This integration ultimately enhances the effectiveness of outbreak management strategies [23, 42, 83, 35, 73].

Incorporating spatial components allows these models to capture variations in population density, movement patterns, and local interactions, leading to more accurate predictions of disease transmission and more effective public health interventions. The integration of spatial effects into individual-level stochastic models was further investigated by [23], who proposed a discrete-time framework, referred to as individual-level models (ILMs), for the analysis of infectious disease transmission. ILMs provide a flexible structure to model interactions between susceptible and infectious individuals, where an “individual” can represent entities such as people, schools, farms, or administrative regions. The framework also accommodates shared information, including distances or contact metrics between entities, which supports the identification of key risk factors affecting transmission dynamics. ILMs are constructed based on compartmental models to represent transmission at the individual level.

While the ILM considers the distance between individuals, it does not account for their specific spatial locations. To address this limitation, [57] proposed an extension of the ILM developed by [23], called Geographically Dependent Individual-Level Models (GD-ILMs). The GD-ILM extends the framework by incorporating both spatial separation and location-specific risk factors. The ILMs and GD-ILMs capture heterogeneity across individuals and explicitly account for spatial structure, making them especially relevant for infectious disease transmission in real-world populations.

While general disease mapping techniques are widely applicable and can be used to visualize patterns for both communicable diseases, such as Tuberculosis (TB), and non-communicable diseases, such as cancer, they do not explicitly capture the underlying transmission dynamics. In contrast, GD-ILMs are specifically designed for infectious diseases and provide a mechanistic framework for modeling transmission processes at both the individual and regional levels. By incorporating spatial interactions, heterogeneous susceptibility, and varying infectiousness, GD-ILMs allow for more precise estimation of transmission parameters and offer insights into the disease process that simpler areal or regional models cannot provide.

This chapter begins with an overview of the thesis structure and then presents the preliminaries, including a review of the classical compartmental modeling framework, encompassing widely used formulations such as Susceptible–Infectious–Recovered (SIR), Susceptible–Exposed–Infectious–Recovered (SEIR), and Susceptible–Exposed–Infectious–Recovered–Susceptible (SEIRS) models, along with extensions that incorporate seasonal variability. It then proceeds to provide an overview of ILMs and GD-ILMs.

In addition, this chapter provides an overview of spatial random effects and their role in epidemiological modeling, highlighting their importance in addressing spatial autocorrelation commonly observed in disease data. To ground these concepts in a real-world context, the chapter also outlines the geographical classification system of Manitoba, including its Health Authority Districts (HADs), Regional Health Authority Districts (RHADs), and Postal Code Regions (PCRs), which serve as the spatial units of analysis in this thesis. Finally, the chapter introduces the statistical methodologies for parameter estimation, with a particular focus on likelihood-based approaches and extensions of the Expectation–Maximization (EM) algorithm, including the Monte Carlo Expectation Conditional Maximization (MCECM) and the Stochastic Approximation Expectation Conditional Maximization (SAECM) algorithms.

1.1 Thesis Overview

ILMs and GD-ILMs have been extensively studied in the literature from various perspectives, encompassing a wide range of methodologies and applications. These include, but are not limited to, parameter estimation using Bayesian frameworks [5, 78], likelihood-based methods [58, 8, 7], and machine learning approaches [77, 51, 75]. Additionally, different types of infection kernels [82, 97], and various compartmental frameworks such as SIR [23], SEIR [8, 7], and SEIRS [4] have been explored. Other important areas of exploration include bias correction [40], managing uncertainty from multiple and imperfect diagnostic tests [100], integrating contact network uncertainty [5], continuous-time modeling [6], parameterizing using sampling-based likelihood approximations [58], incorporating infection time uncertainty [58], and linearization of ILMs [46].

Several important features, including reinfection, seasonality, and the capacity to scale to large datasets, are not fully explored within the GD-ILM framework. This thesis seeks to address these limitations through a series of methodological innovations, computational advancements, software developments, and applied analyses. The overarching objective is to strengthen the epidemiological realism, computational efficiency, and practical applicability of GD-ILMs for the study of infectious diseases. The final study applies spatial, temporal, and spatiotemporal analyses to identify high-risk Gonorrhea clusters in Manitoba (2000–2016), using methods outside the GD-ILM framework. Each chapter of this thesis represents an independent study, yet together they form a coherent body of work.

The first methodological contribution of this thesis involves extending GD-ILMs to account for reinfection dynamics, which are particularly important for infectious diseases where recovered individuals may become susceptible again. This aspect is highly relevant for TB, as immunity following infection or treatment is often incomplete. To address this, the GD-ILM is embedded within a Susceptible–Exposed–Infectious–Recovered–Susceptible (SEIRS) framework, allowing the model to estimate susceptibility to both primary infection and reinfection while preserving its spatially explicit structure. Estimation is carried out using the MCECM algorithm, which facilitates likelihood-based inference in the presence of unobserved exposure and infection processes. To test the model's consistency and robustness, extensive simulations are performed across multiple spatial patterns, population scales, and demographic scenarios. When applied to individual-level TB data from Manitoba for the period 2011–2018, the model identifies significant individual and regional risk factors, captures spatial dependence in transmission, and generates fine-scale infection probability maps. These findings provide valuable insights for public health practice, particularly in the areas of targeted prevention, resource allocation, and reinfection management.

The second methodological contribution of this thesis involves extending the GD-ILM framework to account for seasonal variation in transmission. Although reinfection is a key consideration for chronic infectious diseases, many pathogens, particularly respiratory and vector-borne infections, are characterized by pronounced seasonal variation in transmission. Such seasonal forcing may arise from environmental conditions, shifts in human contact behavior, or changes in population susceptibility. It contributes to periodic fluctuations in disease incidence. While the GD-ILM has proven effective in capturing spatial heterogeneity, its standard formulation does not account for these seasonal effects, limiting its ability to reflect temporal trends in transmission.

To address this limitation, the GD-ILM framework is extended to incorporate a seasonally varying spatiotemporal transmission kernel, which allows infection risk to fluctuate periodically over time. This seasonal GD-ILM integrates a seasonally forced infection kernel into the model structure, thereby providing a novel framework capable of simultaneously capturing spatial and temporal variation. Estimation in this high-dimensional setting is carried out using the MCECM algorithm, which enables likelihood-based inference in the presence of unobserved processes. The model is applied to individual-level Influenza data from Manitoba, Canada, where it reveals distinct spatial and seasonal risk patterns and identifies high-risk regions and time periods. These results have important implications for guiding targeted intervention strategies.

The performance of the seasonal GD-ILM is further evaluated through comprehensive simulation studies, which demonstrate that failing to incorporate seasonal effects can lead to biased spatial parameter estimates under a range of prevalence scenarios. By jointly modeling spatial and seasonal variation, this extension enhances the accuracy of risk assessment and strengthens the capacity of public health responses to deliver timely and location-specific interventions.

The third methodological contribution of this thesis involves addressing computational challenges in high-dimensional GD-ILMs. Although these methodological advances substantially improve the epidemiological realism of GD-ILMs, their computational demands limit their applicability to real-time or large-scale analyses. In high-dimensional spatial contexts with many individuals, latent exposure and infection processes, and complex spatial dependencies, full likelihood evaluation becomes computationally infeasible. To address these challenges, an estimation framework is developed that combines a novel stratified temporally-weighted Kernel Density Estimation–based Probability Proportional to Size (KDE–PPS) sampling strategy with a SAECM algorithm. The proposed sampling strategy prioritizes sampling from recently infected individuals and spatial hotspots, focusing computational resources on the most informative observations. The SAECM algorithm facilitates likelihood-based parameter estimation, enhancing scalability and accelerating convergence in high-dimensional settings while accounting for latent spatial dependence. This combined approach enables efficient, statistically rigorous inference for large and complex infectious disease datasets.

Extensive simulation studies are conducted across diverse spatial configurations, population sizes, and demographic scenarios. These studies demonstrate that the framework consistently produces accurate parameter estimates, reduces computational burden, and maintains robustness under varying prevalence and spatial heterogeneity conditions. When applied to high-resolution COVID-19 data from Manitoba, the method identifies substantial spatial variation in transmission rates and uncovers socio-economic disparities associated with higher infection risk. The results provide insights into the geographic and demographic determinants of transmission and highlight the importance of targeting public health interventions to high-risk areas. This framework provides a scalable, computationally efficient, and statistically robust approach to epidemic modeling, allowing rapid estimation of exposure probabilities and supporting informed, data-driven public health decision making at large scales.

Another contribution of this thesis consists of a purely applied analysis involving spatial, temporal, and spatiotemporal analytical methods outside the GD-ILM framework to address a different but equally pressing public health concern: sexually transmitted infections. Using laboratory-confirmed Gonorrhea data from Manitoba (2000–2016), spatial autocorrelation analysis, purely temporal analysis, and space–time scan statistics are employed to detect high-risk clusters. The results indicate that infections are disproportionately concentrated in northern Manitoba and central Winnipeg, with seasonal peaks occurring in late summer and autumn. Persistent, long-duration clusters are identified, highlighting the need for geographically targeted and temporally responsive intervention strategies.

The software development contribution of this thesis focuses on enhancing reproducibility and accessibility in methodological research. Recognizing the importance of these principles, the reinfection-extended GD-ILM and the seasonal GD-ILM are translated into practical and publicly available software tools. This includes the development of the `GDILM.SEIRS` and `SeasEpi` R packages, which are distributed through the Comprehensive R Archive Network (CRAN). These packages provide complete implementations of the proposed modeling and estimation frameworks, support simulation experiments, and enable application to real-world epidemiological data. By making these methods available in open and user-friendly formats, the packages facilitate their use by researchers and public health professionals across a wide range of applications.

The Appendix provides supplementary materials that support the main body of the thesis. Specifically, it includes detailed documentation of the two R packages developed in this research: `GDILM.SEIRS`, which implements the GD-ILM with reinfection framework, and `SeasEpi`, which incorporates seasonal effects into GD-ILMs. For each package, the appendix outlines the package design, core functions, and illustrative examples. These materials serve to enhance reproducibility and facilitate broader use of the proposed methods in future biostatistical and epidemiological studies. These packages are publicly available on CRAN.

Collectively, the research presented in this thesis advances the GD-ILM framework in three principal ways. First, it enhances epidemiological realism by incorporating reinfection dynamics and seasonal variation into spatially explicit transmission models, allowing for a more accurate representation of disease processes. Second, it improves computational feasibility through the development of innovative likelihood approximation and sampling strategies, enabling the application of GD-ILMs to large-scale and high-dimensional epidemic datasets. Third, it demonstrates applied public health relevance by providing high-resolution analyses of TB, Influenza, COVID-19, and Gonorrhea in Manitoba, offering insights that inform targeted interventions and policy decisions. Finally, the work contributes two open-source R packages that implement the proposed GD-ILM frameworks, supporting reproducibility and broader adoption in both research and public health practice.

The research protocol of the present thesis was reviewed and received ethical approvals from both the Health Research Ethics Board (HREB) of the University of Manitoba and the Provincial Health Research Privacy Committee (PHRPC) of Manitoba Health.

1.2 Compartmental Models of Infectious Disease Transmission

A fundamental example of such a model is the SIR model for a closed population, which is deterministic and uses ordinary differential equations to describe the dynamics of three distinct compartments at time t: the numbers of susceptible individuals, $S(t)$, infectious individuals, $I(t)$, and recovered individuals, $R(t)$ [41]. These compartments represent those who can contract the disease, those who can spread the disease, and those who have recovered, been removed, isolated, or died, at time t, respectively.

The SIR model is one of the most widely used compartmental models and forms the foundation for many extensions. It assumes that individuals move directly from the susceptible compartment $S(t)$ to the infectious compartment $I(t)$ upon infection, and then to the recovered compartment $R(t)$ after recovery. The standard deterministic mass-action SIR model is described by the following set of differential equations:

$$\begin{aligned}\frac{\mathrm{d}S(t)}{\mathrm{d}t} &= -\eta S(t)I(t),\\ \frac{\mathrm{d}I(t)}{\mathrm{d}t} &= \eta S(t)I(t) - \nu_I' I(t),\\ \frac{\mathrm{d}R(t)}{\mathrm{d}t} &= \nu_I' I(t),\end{aligned}$$

where η represents the transmission rate of the disease, and ν_I' is the recovery rate. The average infectious period is given by $\nu_I = \nu_I'^{-1}$. In this formulation, mass action refers to the assumption of homogeneous mixing within the population, such that the rate of new infections is proportional to the product of the numbers of susceptible and infectious individuals, reflecting random contacts between them. The model begins with the initial conditions $S(0) > 0$, $I(0) \geqslant 0$, and $R(0) \geqslant 0$, and the total population at time t is expressed as $N(t) = S(t) + I(t) + R(t)$.

1.2.1 SEIR

For many infectious diseases, there is a latent period between infection and the onset of infectiousness. This latent period is captured by the SEIR model, which extends the SIR model by including an additional compartment, $E(t)$, for exposed individuals who are infected but not yet infectious at time t [41]. In this model, when individuals become infected, they move to the $E(t)$ compartment and remain there for an average duration before progressing to the infectious compartment, $I(t)$. The basic mass-action SEIR model is described by the following set of differential equations:

$$\begin{aligned}\frac{\mathrm{d}S(t)}{\mathrm{d}t} &= -\eta S(t)I(t),\\ \frac{\mathrm{d}E(t)}{\mathrm{d}t} &= \eta S(t)I(t) - \nu_E' E(t),\\ \frac{\mathrm{d}I(t)}{\mathrm{d}t} &= \nu_E' E(t) - \nu_I' I(t),\\ \frac{\mathrm{d}R(t)}{\mathrm{d}t} &= \nu_I' I(t),\end{aligned}$$

where the parameter ν'_E represents the rate at which exposed individuals become infectious, with its reciprocal $\nu_E = {\nu'_E}^{-1}$ corresponding to the average latent period. The model begins with the initial conditions $S(0) > 0$, $E(0) \geqslant 0$, $I(0) \geqslant 0$, and $R(0) \geqslant 0$. At any time t, the total population is defined as $N(t) = S(t) + E(t) + I(t) + R(t)$.

1.2.2 SEIRS

The SEIR model operates under the assumption that individuals gain lifelong immunity after recovery. However, for some infectious diseases, immunity wanes over time, necessitating the use of the SEIRS model [41, 88]. This model accounts for the possibility that recovered individuals can return to the susceptible compartment. The basic mass-action SEIRS model is described by the following set of differential equations:

$$\begin{aligned}
\frac{\mathrm{d}S(t)}{\mathrm{d}t} &= -\eta S(t)I(t) + \omega' R(t), \\
\frac{\mathrm{d}E(t)}{\mathrm{d}t} &= \eta S(t)I(t) - \nu'_E E(t), \\
\frac{\mathrm{d}I(t)}{\mathrm{d}t} &= \nu'_E E(t) - \nu'_I I(t), \\
\frac{\mathrm{d}R(t)}{\mathrm{d}t} &= \nu'_I I(t) - \omega' R(t),
\end{aligned}$$

where ω' denotes the rate at which recovered individuals lose immunity and return to the susceptible class, with $\omega = {\omega'}^{-1}$ representing the average duration of immunity. The model is initialized under the conditions $S(0) > 0$, $E(0) \geqslant 0$, $I(0) \geqslant 0$, and $R(0) \geqslant 0$, and the total population at time t is expressed as $N(t) = S(t) + E(t) + I(t) + R(t)$.

1.2.3 Seasonal SEIR

Seasonality can be incorporated into the transmission rate η in the SEIR model by allowing it to vary periodically over time [41]. This time-dependent transmission rate is denoted as $\eta(t)$. With this modification, the seasonal SEIR model is formulated as follows:

$$\begin{aligned}
\frac{\mathrm{d}S(t)}{\mathrm{d}t} &= -\eta(t)S(t)I(t), \\
\frac{\mathrm{d}E(t)}{\mathrm{d}t} &= \eta(t)S(t)I(t) - \nu'_E E(t), \\
\frac{\mathrm{d}I(t)}{\mathrm{d}t} &= \nu'_E E(t) - \nu'_I I(t), \\
\frac{\mathrm{d}R(t)}{\mathrm{d}t} &= \nu'_I I(t).
\end{aligned}$$

A widely adopted technique for characterizing seasonal fluctuations is the sinusoidal function, primarily because of its mathematical simplicity and its effectiveness in modeling periodic structures. Numerous mathematical models have likewise employed sinusoidal formulations to represent seasonal variations in transmission rates. The transmission rate $\eta(t)$ is typically modeled as:

$$\eta(t) = \eta_0 \left(1 + \eta_1 \cos\left(\frac{2\pi t}{T_{\text{cycle}}} + \eta_2\right)\right),$$

where η_0 represents the baseline transmission rate and η_1 determines the amplitude of seasonal fluctuations. The parameter T_{cycle} defines the duration of one complete seasonal cycle, such as a year or a month, depending on the context of the disease. Time t tracks the evolution of the epidemic, while η_2 introduces a phase shift, aligning the peaks and troughs of the transmission curve with observed seasonal patterns. This formulation provides a flexible and interpretable framework for capturing seasonal dynamics in infectious disease models. Although the seasonal SEIR model captures average epidemic trends and seasonal variation, it cannot account for the inherent randomness present in real-world disease transmission. In practice, factors such as individual contact patterns, random environmental changes, and chance events, especially in small or early-stage outbreaks, can significantly influence epidemic dynamics. Stochastic models incorporate this randomness, providing a more realistic representation of disease spread. They enable the study of variability in outcomes, extinction probabilities, and the effectiveness of interventions under uncertainty, making them more suitable for realistic forecasting and policy evaluation in uncertain conditions. ILMs and GD-ILMs are stochastic models, and a brief overview of their structure and properties is provided below.

1.3 Stochastic Models of Infectious Disease Transmission

1.3.1 ILM

The ILM provides a rigorous methodology for modeling the spatiotemporal transmission of infectious diseases. In this framework, the epidemic evolves over T discrete time points. The probability that a susceptible individual i becomes newly infectious during the interval $[t, t+1)$ is denoted by $\mathcal{P}_{(i,t)}(\Theta)$ and is defined as:

$$\mathcal{P}_{(i,t)}(\Theta) = 1 - \exp\left[\left\{-\Upsilon_S(i) \sum_{j \in I(t)} \Upsilon_T(j)\, \kappa(i,j)\right\} + \epsilon(i,t)\right], \quad t = 1, \ldots, T.$$

In this expression, $I(t)$ is the set of infectious individuals at time t.

The function $\Upsilon_S(i)$, called the susceptibility function, represents the susceptibility of individual i and incorporates relevant covariates and risk factors. Individual-level and regional-level characteristics can influence the likelihood that a person becomes exposed. Individual-level covariates may include demographic or behavioral factors such as age, sex, vaccination status, or contact patterns, while regional-level covariates can represent socioeconomic indicators, population density, healthcare accessibility, or environmental risk factors. Incorporating such covariates allows the model to capture heterogeneity in susceptibility across individuals and regions. In the absence of covariate information, a straightforward approach is to assume uniform susceptibility, by setting $\Upsilon_S(i)$ equal to a constant that represents the baseline susceptibility.

The function $\Upsilon_T(j)$, called the transmissibility (or infectivity) function, represents the transmissibility of individual j and incorporates relevant covariates and risk factors. The infectiousness of an individual can vary depending on their characteristics and context. If data are available, individual-level covariates might include factors such as symptom severity, vaccination status, or contact behavior, while regional-level covariates could include local mobility or healthcare accessibility. These covariates could be incorporated into the transmissibility function to account for heterogeneity in transmission potential across individuals and regions, allowing the model to more accurately represent differences in the risk of spreading the disease. In the absence of covariate information, a straightforward approach is to assume uniform infectivity by setting $\Upsilon_T(j)$ equal to a constant representing the baseline level of infectivity.

The infection kernel $\kappa(i, j)$ quantifies the transmission potential between susceptible individual i and infectious individual j, accounting for spatial or behavioral proximity as well as shared risk factors.

The spark function $\epsilon(i, t)$, accounts for random or unexplained infections that may arise due to stochastic processes or external factors not captured by the modeled interactions. Potential covariates for this term could include travel history or other external exposures not included in the main susceptibility and transmissibility functions, such as visits to crowded public places, contact with infectious individuals outside the observed population, exposure to imported cases from other regions, environmental exposures, or participation in mass gatherings.

Finally, Θ denotes the full set of model parameters to be estimated, with its composition determined by specifications of the model components.

1.3.2 GD-ILM

As an extension of ILMs, GD-ILMs are also constructed based on compartmental models. The GD-ILM within an SEIR framework assumes that the study area is partitioned into Z regions, and the epidemic unfolds over T discrete time points. Under the GD-ILM framework, the probability that a susceptible individual i in region z becomes newly infectious during the time interval $[t, t+1)$ is denoted by $\mathcal{P}_{i,t,z}(\Theta)$ and is defined as:

$$\mathcal{P}_{(i,t,z)}(\Theta) = 1 - \exp\left[\left\{-\Upsilon_S(i,z) \sum_{j \in I(t,z,\zeta(z))} \Upsilon_T(j,z)\,\kappa(i,j)\right\} + \epsilon(i,t,z)\right],$$

for $t = 1, \ldots, T$ and $z = 1, \ldots, Z$. In this expression, $\zeta(z)$ denotes the set of neighboring regions adjacent to region z, and $I(t, z, \zeta(z))$ represents the set of infectious individuals at time t within region z and its neighbors. The functions $\Upsilon_S(i, z)$ and $\Upsilon_T(j, z)$ represent the susceptibility and transmissibility (infectivity) functions of risk factors for susceptible individual i and infectious individual j in region z, respectively. The function $\kappa(i, j)$ is a spatial kernel that quantifies the shared risk between susceptible individual i and infectious individual j. The term $\epsilon(i, t, z)$ refers to the spark function related to region z. Furthermore, Θ denotes the full set of model parameters to be estimated, with its composition determined by specifications of the model components.

The model also allows for the representation of unobserved latent covariates with spatial dependence, which can be incorporated using a spatial random effects approach, such as the Conditional Autoregressive (CAR) model [12]. To contextualize this modeling choice, it is important to elaborate on the role of spatial random effects and their relevance in epidemiological applications.

1.4 Spatial Random Effect

A spatial random effect is a statistical term used to model spatial dependence, capturing the tendency of neighboring geographic regions to display similar characteristics in spatial data. This spatial correlation is commonly observed in epidemiological studies, where geographically proximate regions often report similar disease incidence rates due to shared environmental, demographic, or social factors. To accommodate such spatial autocorrelation, random effects are introduced into statistical models, allowing each region's outcome to be partially influenced by those of its neighbors.

These spatial effects are typically modeled as latent Gaussian random fields, assuming a multivariate normal distribution centered at zero. Most regions are expected to follow the underlying spatial trend, while only a few may deviate significantly. This probabilistic structure helps smooth out noisy data and identify spatial clusters more robustly. Several modeling frameworks exist for defining the spatial structure of the random effects, including CAR models, Intrinsic CAR (ICAR) models, and their generalizations.

In this thesis, we adopt the Leroux model [49], a flexible and widely used specification for spatial random effects. Let $\mathbf{\Gamma} = (\gamma_1, \ldots, \gamma_Z)^\top$ represent the spatial random effect vector over Z regions. The Leroux model assumes that:

$$\mathbf{\Gamma} \sim \mathcal{N}_Z(\mathbf{0}, \mathbf{\Sigma}_\Gamma),$$

with the corresponding density function given by:

$$g(\mathbf{\Gamma}) = (2\pi)^{-Z/2}(\tau^2)^{Z/2} \left|(1-\lambda)\mathbf{I}_Z + \lambda\mathcal{R}\right|^{1/2} \exp\left(-\frac{1}{2}\mathbf{\Gamma}^\top \left(\tau^2 \left[(1-\lambda)\mathbf{I}_Z + \lambda\mathcal{R}\right]\right)\mathbf{\Gamma}\right),$$

where $\mathbf{I}_Z$ is the $Z \times Z$ identity matrix, $\mathcal{R}$ is the intrinsic autoregressive matrix encoding the spatial neighborhood structure, τ is the spatial precision, and $\lambda \in [0,1]$ controls the strength of spatial dependence. In the matrix $\mathcal{R}$, the diagonal entry $\mathcal{R}_{zz}$ corresponds to the number of neighbors of region z, while each off-diagonal element $\mathcal{R}_{zz'} = -I\{z \sim z'\}$, where $I\{z \sim z'\}$ is an indicator function equal to 1 if regions z and z' share a border, and 0 otherwise. A value of $\lambda = 0$ implies spatial independence, while values closer to 1 indicate stronger spatial autocorrelation.

To achieve reliable inference within the extended GD-ILM framework, particular attention is devoted to parameter estimation. In this thesis, likelihood-based approaches are employed, with a focus on advanced variants of the Expectation Conditional Maximization (ECM) algorithm. Specifically, the MCECM and the SAECM methods are utilized, both of which are designed to address the computational challenges arising from high-dimensional and incomplete data structures inherent in infectious disease modeling.

1.5 Likelihood-Based Parameter Estimation

The EM algorithm [26] is a widely used iterative method for computing maximum likelihood estimates in statistical models involving latent, hidden variables, or incomplete data [64, 61, 59]. In many real-world applications, direct observation of all relevant variables is either impractical or impossible, resulting in incomplete data. The EM algorithm overcomes this challenge by alternating between two steps: the Expectation (E) step, which estimates the missing data or latent variables based on the current parameter estimates, and the Maximization (M) step, which updates the parameter estimates by maximizing the expected complete-data log-likelihood. This cycle repeats until convergence, enabling efficient parameter estimation even when data are incomplete or partially observed.

In EM-type algorithms, the Q-function is defined as the conditional expectation of the complete-data log-likelihood, given the observed data and the current parameter estimates [64, 61, 59]. At iteration k, the Q-function is expressed as

$$Q(\Theta \mid \Theta^{(k)}) = \mathbb{E}\left[f(\Theta; \mathbf{y}, \mathbf{\Gamma}_l^{(k)}) \mid \mathbf{y},\, \Theta^{(k)}\right],$$

where $\mathbf{y}$ denotes the observed data and $\mathbf{\Gamma}^{(k)}$ is a single sample drawn from the posterior distribution of the latent variable $\mathbf{\Gamma}^{(k)} \sim p(\mathbf{\Gamma} \mid \mathbf{y}; \Theta^{(k)})$. This expectation is taken with respect to the conditional distribution of the complete data given the observed data and the current parameter estimates $\Theta^{(k)}$.

Here, $f(\Theta; \mathbf{y}, \mathbf{\Gamma}_l^{(k)})$ is a general objective function that depends on the model parameters Θ and the complete data $(\mathbf{y}, \mathbf{\Gamma}_l^{(k)})$. It represents the quantity we aim to optimize if the complete data were fully observed, such as a score, a loss, or any function reflecting the fit of the model to the complete information.

The Q-function serves as a surrogate objective function that is iteratively optimized to obtain maximum likelihood estimates when direct maximization of the observed-data likelihood is computationally infeasible.

A well-known extension of the EM algorithm is the ECM algorithm [60], which replaces the single M-step with multiple simpler Conditional Maximization (CM) steps. Each CM step updates a subset of the parameters while keeping the others fixed, often simplifying the optimization and improving numerical stability, especially in high-dimensional or complex models.

The MCECM and SAECM algorithms are two distinct extensions of the EM framework designed to approximate the Q-function in complex scenarios. The key difference between these algorithms lies in the method by which the Q-function is computed and updated at each iteration.

1.5.1 Monte Carlo Expectation Conditional Maximization

The MCECM algorithm is an extension of the ECM algorithm for maximum likelihood estimation that handles cases where the E-step is analytically intractable by approximating it through Monte Carlo integration [102, 7]. This approach is particularly useful in latent variable models with complex or high-dimensional missing data. To initiate the MCECM algorithm, an initial parameter vector $\Theta^{(0)} = (\theta_1^{(0)}, \ldots, \theta_D^{(0)})$ must be provided, where each θ_d represents either a scalar parameter or a block (subset) of the full parameter vector Θ. The MCECM algorithm then proceeds iteratively as follows.

E-step (Monte Carlo Approximation)

At iteration $k+1$, given the current parameter estimate $\Theta^{(k)}$, approximate the Q-function using Monte Carlo simulation:

$$\widetilde{Q}(\Theta \mid \Theta^{(k)}) = \frac{1}{L}\sum_{l=1}^{L} f(\Theta; \mathbf{y}, \mathbf{\Gamma}_l^{(k)}),$$

where the set $\{\mathbf{\Gamma}_1^{(k)}, \ldots, \mathbf{\Gamma}_L^{(k)}\}$ is a Monte Carlo sample drawn from the conditional (posterior) distribution of the latent variable $\mathbf{\Gamma}_l^{(k)} \sim p(\mathbf{\Gamma} \mid \mathbf{y}; \Theta^{(k)}), \quad l = 1, \ldots, L$. This step approximates the expected complete-data log-likelihood by averaging over L independent draws from the posterior distribution of the latent variables $\mathbf{\Gamma}$, given the observed data $\mathbf{y}$ and the current parameter estimate $\Theta^{(k)}$.

CM-step

Instead of maximizing $\widetilde{Q}(\Theta)$ jointly over all components of Θ, the CM-step maximizes conditionally over individual blocks θ_d in coordinate-wise manner. More precisely, for $d = 1, \ldots, D$, the update is given by

$$\theta_d^{(k+1)} = \arg\max_{\theta_d} \widetilde{Q}\left(\Theta \mid \theta_1^{(k+1)}, \ldots, \theta_{d-1}^{(k+1)}, \theta_d, \theta_{d+1}^{(k)}, \ldots, \theta_D^{(k)}\right).$$

This means that at each sub-step d, the component θ_d is updated while conditioning on the most recent updates for the preceding components $\theta_1^{(k+1)}, \ldots, \theta_{d-1}^{(k+1)}$ (i.e., those already updated in the current iteration), as well as the previous values $\theta_{d+1}^{(k)}, \ldots, \theta_D^{(k)}$ for the remaining components that have yet to be updated in this iteration. This block-wise maximization simplifies computation and ensures convergence under standard regularity conditions.

1.5.2 Stochastic Approximation Expectation Conditional Maximization

The SAECM algorithm is an alternative to the MCECM method that incorporates ideas from the SAEM algorithm [25] and Conditional Maximization (CM). The primary computational advantage of SAECM over MCECM lies in its more efficient handling of the E-step. In MCECM, the Q-function is re-estimated from scratch at each iteration using Monte Carlo integration. This typically involves generating a large number of samples from the posterior distribution of the latent variables to obtain an accurate estimate. While this approach yields a relatively low-variance estimate, it becomes computationally intensive, especially as the dimensionality of the latent space increases or when a high number of samples is required to stabilize the variance.

In contrast, SAECM significantly reduces the computational burden by employing a stochastic approximation technique, inspired by [84], wherein the Q-function is updated incrementally using only a single latent sample at each iteration. Rather than discarding past estimates, SAECM retains historical information and recursively updates the Q-function via a weighted average of the previous estimate and the current complete-data log-likelihood evaluated at the new sample. By using a decreasing sequence of weights, the algorithm gradually shifts focus toward more recent iterations, which tend to be more reliable. As demonstrated by [25], this approach maintains convergence while significantly reducing computational demands. Consequently, SAECM drastically lowers both the computational cost and memory requirements per iteration.

Moreover, SAECM is particularly advantageous in high-dimensional latent variable models or situations where sampling is computationally expensive, as it avoids the need for repeated full re-evaluation of the Q-function. By bypassing high-dimensional integration at every iteration and efficiently leveraging information across iterations, SAECM achieves faster convergence in practice compared to MCECM, especially in large-scale or resource-constrained settings.

To initiate the SAECM algorithm, an initial parameter vector $\Theta^{(0)} = (\theta_1^{(0)}, \dots, \theta_D^{(0)})$ must be provided, along with an initial estimate of the Q-function, denoted by $\widetilde{Q}^{(0)}(\Theta)$. Each θ_d may represent a block of parameters, which can be either a vector or a single scalar.

E-step (Stochastic Approximation)

Let $\widetilde{Q}^{(k)}(\Theta)$ denote the approximation of the expected complete-data log-likelihood at iteration k, given the current parameter estimate $\Theta^{(k)}$. The recursive update is given by:

$$\widetilde{Q}^{(k+1)}(\Theta) = \widetilde{Q}^{(k)}(\Theta) + s^{(k)}\left[f(\Theta; \mathbf{y}, \mathbf{\Gamma}^{(k+1)}) - \widetilde{Q}^{(k)}(\Theta)\right],$$

where $s^{(k)} \in (0, 1)$ is a step size function at iteration k, commonly chosen as $s^{(k)} = k^{-\zeta}, \quad \zeta \in (0.5, 1]$, and $\mathbf{\Gamma}^{(k+1)}$ is a single sample drawn from the posterior distribution of the latent variable $\mathbf{\Gamma}^{(k+1)} \sim p(\mathbf{\Gamma} \mid \mathbf{y}; \Theta^{(k)})$. This recursive E-step enables a gradual refinement of the Q-function approximation without requiring large Monte Carlo samples at each iteration.

CM-step

As in the MCECM algorithm, instead of jointly maximizing $\widetilde{Q}^{(k+1)}(\Theta)$ with respect to all components of Θ, the CM-step proceeds by block-wise conditional maximization. Specifically, for each $d = 1, \ldots, D$, the update is given by

$$\theta_d^{(k+1)} = \arg\max_{\theta_d} \widetilde{Q}^{(k+1)}\left(\theta_1^{(k+1)}, \ldots, \theta_{d-1}^{(k+1)}, \theta_d, \theta_{d+1}^{(k)}, \ldots, \theta_D^{(k)}\right).$$

That is, each block θ_d is updated using the most recent values for blocks 1 through $d-1$ and the previous values for the remaining blocks $d+1$ through D.

The trade-off between the MCECM and SAECM methods hinges on balancing computational cost and statistical efficiency. MCECM typically produces more stable and precise parameter updates but incurs higher per-iteration computational complexity, making it well-suited for problems of moderate size or scenarios with ample computational resources. Conversely, SAECM is especially advantageous in high-dimensional settings or large-scale applications where generating numerous posterior samples is computationally prohibitive. Although SAECM may require more iterations to converge due to increased stochastic variability, its lightweight per-iteration updates often lead to faster overall computation and better scalability. Consequently, SAECM offers a practical alternative for fast approximate inference in modern statistical problems with complex latent structures.

Given the central role of spatial context in modeling infectious disease dynamics, it is necessary to establish a clear framework for the geographical units used in this thesis. Standardized spatial classifications not only provide consistency across health research but also allow for meaningful interpretation of results at multiple administrative levels. To this end, the analyses in this thesis adopt the geographical classification of Manitoba developed by the Manitoba Centre for Health Policy (MCHP) and Manitoba Health.

1.6 Geographical Classification of Manitoba

Throughout this thesis and for real data analysis we consider the geographical classification defined by MCHP and Manitoba Health for the allocation of health districts and neighborhood clusters based on municipality and postal codes [3]. Under this classification, Manitoba is organized into 5 HADs: Interlake, Northern, Prairie, Southern, and Winnipeg. These HADs encompass a total of 96 RHADs, distributed as follows: 15 in Interlake, 16 in Northern, 17 in Prairie, 23 in Southern, and 25 in Winnipeg, as illustrated in Figure 1.1. Additionally, Manitoba has 27,897 PCRs in total, with 1,363 located in Interlake, 1,050 in Northern, 3,079 in Prairie, 2,509 in Southern, and 19,896 in Winnipeg. In Canada, postal codes are six-character alphanumeric codes defined and maintained by Canada Post. Each postal code corresponds to a specific geographic area and is structured to provide detailed spatial information. In addition to mail routing, postal codes are widely used in the Canadian census and health research as geographic identifiers, often representing a small group of addresses, city blocks, or even a single building in urban areas.

This geographical classification provides the foundation for the spatial structure incorporated into the extended GD-ILMs developed in this thesis. By aligning data with these standardized health

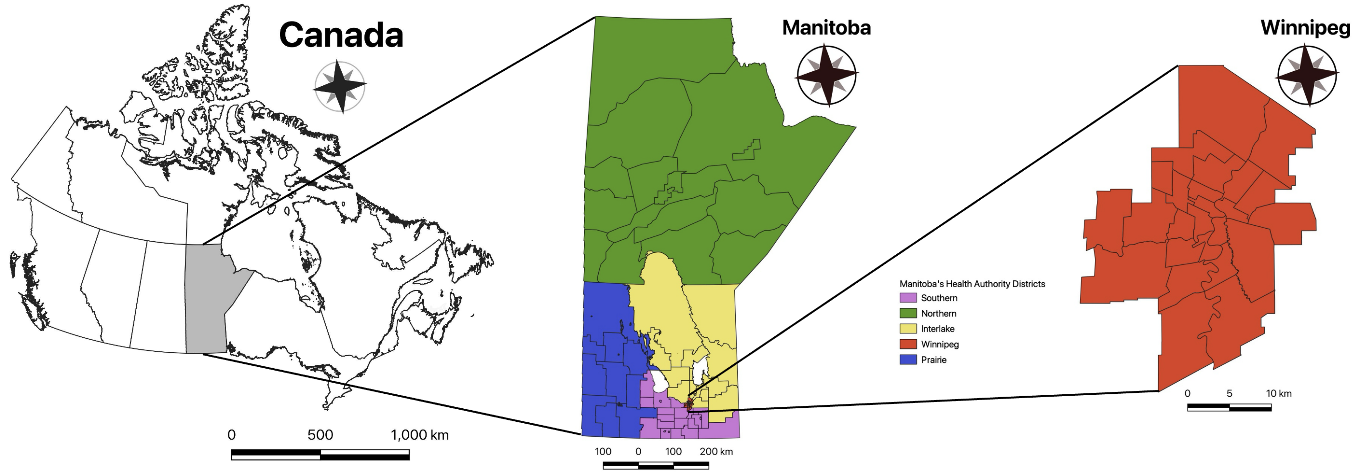

Figure 1.1: Manitoba Province with 5 HADs and 96 RHADs

regions and postal code areas, the models can capture spatial dependencies at multiple scales, thereby improving the accuracy and interpretability of disease transmission analyses across Manitoba.

2

Individual Level Modeling of Infectious Disease Transmission with Reinfection Dynamics

This chapter includes an open access article published in *Spatial and Spatio-temporal Epidemiology* [4]. It is reproduced here in its original form, with only minor formatting adjustments for consistency within the thesis. Reproduction is permitted under the terms of the Creative Commons Attribution-NonCommercial-NoDerivatives 4.0 International License (CC BY-NC-ND 4.0).

2.1 Introduction

Since reinfection is a key factor that significantly impacts disease dynamics, epidemic progression, prevalence, and control strategies for many infectious diseases, accurately integrating it into disease modeling is vital. In this chapter, we aim to extend GD-ILMs within the SEIRS compartmental framework to model infectious diseases with reinfection. TB is particularly relevant in this context because its ability to reinfect individuals complicates both treatment and eradication efforts. This disease is an infection caused by Mycobacterium tuberculosis, primarily affecting the lungs but potentially impacting other parts of the body [30, 107]. TB has two key stages: latent TB infection, where the bacteria remain inactive and symptom-free but can become active later, and active TB disease, where the bacteria multiply and produce symptoms like a persistent cough, chest pain, coughing up blood, fever, night sweats, chills, and weight loss [107]. Active TB can become severe and, if left untreated, spreads through airborne droplets from coughing or sneezing [30]. Reinfection is a serious concern, particularly in high-burden regions where individuals previously treated for TB may become susceptible again, perpetuating transmission [30, 107]. The SEIRS compartmental model effectively captures these complexities by simulating stages of susceptibility, exposure, active infection, recovery, and renewed susceptibility (susceptibility to reinfection), offering a comprehensive framework for understanding and controlling the spread of TB.

In 2021, there were approximately 10.6 million new TB cases globally [109]. Canada reported 1,904 cases, with an incidence rate of 4.8 per 100,000. In Manitoba, the rate was notably higher at 11 per 100,000, reflecting a greater TB burden compared to most other Canadian provinces. TB in Canada primarily affects Canadian-born Indigenous people and immigrants from TB-endemic countries [80]. Factors such as socioeconomic status, population density, and the presence of vulnerable groups, including Indigenous communities and immigrants from TB-endemic areas, contribute to the higher incidence in Manitoba [105].

In this chapter, we extend GD-ILMs within an SEIRS compartmental framework to model infectious diseases with reinfection. We perform simulation studies on both regular and irregular grids to assess the performance and robustness of the proposed model. For real data analysis, we explore TB infection dynamics in Manitoba, focusing on susceptibility to initial infection, reinfection, and infectivity. We utilize individual-level administrative TB data from Manitoba Health, covering the years 2011 to 2018. This approach enables us to evaluate regional differences in susceptibility while accounting for spatial dependencies, considering various geographical classifications and individual-level factors influencing infectivity risk. The findings provide crucial information for public health officials and decision-makers, enhancing their understanding of TB dynamics and guiding targeted interventions.

To enhance reproducibility and facilitate broader adoption in infectious disease research, we developed the `GDILM.SEIRS` R package [1], which is publicly available on CRAN. This package implements the GD-ILM with reinfection framework, providing researchers with a comprehensive suite of tools for conducting spatiotemporal analyses of infectious diseases that include reinfection dynamics. Specifically, it enables likelihood-based parameter estimation using the MCECM algorithm, supports model evaluation and selection through the Akaike Information Criterion (AIC), and allows users to design and execute tailored simulation studies to explore various epidemiological scenarios or assess model performance under different assumptions. By integrating estimation, evaluation, and simulation capabilities within a single framework, `GDILM.SEIRS` offers a flexible and extensible platform for both methodological development and applied research in infectious disease modeling.

The remainder of this chapter is organized as follows. Section 2.2 introduces the GD-ILM with reinfection. Section 2.3 describes its detailed specifications and likelihood function. Section 2.4 outlines the parameter estimation procedure using the MCECM algorithm and associated inference. Section 2.5 presents an inference for the variances of the estimated GD-ILM with reinfection parameters. Section 2.6 assesses the goodness of fit of the model. Section 2.7 illustrates the application of the GD-ILM with reinfection to TB data from Manitoba, Canada. Section 2.8 reports a simulation study evaluating the performance of the proposed method. Finally, Section 2.9 concludes the chapter with a discussion of the findings, including their interpretation, practical significance, and limitations.

2.2 GD-ILM with Reinfection

In the context of the GD-ILM with reinfection (i.e., GD-ILM within the SEIRS compartmental framework), termed GD-ILM SEIRS, the susceptible population is divided into two distinct subpopulations due to the possibility of reinfection: individuals who are susceptible to initial infection, denoted by Ψ, and those who have regained susceptibility after the immunity period, denoted by Φ. Differentiating between initial infection and reinfection is important because these two groups may exhibit distinct characteristics that affect disease transmission. Individuals in Ψ are at risk of becoming infected for the first time, while those in Φ may have altered immune responses due to prior exposure. This distinction allows for a more accurate representation of disease dynamics, as reinfection may occur at a different rate or result in different disease progression compared to the initial infection. Moreover, specific risk factors need to be considered for these sub-populations, treating them as separate groups of susceptible individuals. By treating these groups separately, the model can better capture the complexities of reinfection and improve the precision of disease spread predictions. Assume that the area under study is divided into Z regions, and the epidemic occurs over T time points. In the GD-ILM SEIRS framework, the probability that a susceptible individual i in region z becomes newly exposed within the time interval $[t, t+1)$ is denoted by $\mathcal{P}_{(i,t,z)}(\Theta)$ and is expressed as follows

$$\mathcal{P}_{(i,t,z)}(\Theta) = 1 - \exp\left[\left\{-\Upsilon_{S^{\Psi\cup\Phi}}(i,z) \sum_{j\in I(t,z,\zeta(z))} \Upsilon_T(j,z)\,\kappa(i,j)\right\} + \epsilon(i,t,z)\right] \tag{2.2.1}$$

with

$$\Upsilon_{S^{\Psi\cup\Phi}}(i,z) = \Upsilon_{S^{\Psi}}(i,z) + \Upsilon_{S^{\Phi}}(i,z), \qquad t = 1,\ldots,T \quad \text{and,} \quad z = 1,\ldots,Z.$$

Here, $\Upsilon_{S^{\Psi}}(i,z)$ and $\Upsilon_{S^{\Phi}}(i,z)$ denote the susceptibility functions for individual i in region z. Specifically, $\Upsilon_{S^{\Psi}}(i,z)$ corresponds to individuals who are initially susceptible to infection, while $\Upsilon_{S^{\Phi}}(i,z)$ applies to those who have become susceptible again after the immunity period.

2.3 Specification of GD-ILM SEIRS Components

Susceptibility and Transmissibility Functions

Let the individual-level covariate vectors for susceptible individuals be denoted as $\mathbf{X}_{i^{\Psi}}$ and $\mathbf{X}_{i^{\Phi}}$, respectively, for susceptible units $i^{\Psi} = 1,\ldots,n^{\Psi}$ and $i^{\Phi} = 1,\ldots,n^{\Phi}$. Similarly, let $\mathbf{X}_{zS^{\Psi}}$ and $\mathbf{X}_{zS^{\Phi}}$ represent the regional-level covariate vectors for region z. These covariates can be incorporated into the susceptibility functions $\Upsilon_{S^{\Psi}}(i,z)$ and $\Upsilon_{S^{\Phi}}(i,z)$. Furthermore, let $\mathbf{X}_j$ denote the vector of individual-level covariates for infectious individual j, which can be integrated into the transmissibility function $\Upsilon_T(j,z)$. Specifically, $\Upsilon_{S^{\Psi\cup\Phi}}(i,z)$ and $\Upsilon_T(j,z)$ are defined as follows:

$$\Upsilon_{S^{\Psi\cup\Phi}}(i,z) = (N_{S^{\Psi}}(i,z) + N_{S^{\Phi}}(i,z)) \exp\left(\alpha_{S^{\Psi\cup\Phi}} + \mathbf{X}_{i^{\Psi}}^{\top}\boldsymbol{\beta}_1 + \mathbf{X}_{i^{\Phi}}^{\top}\boldsymbol{\beta}_2 + \mathbf{X}_{zS^{\Psi}}^{\top}\boldsymbol{\beta}_3 + \mathbf{X}_{zS^{\Phi}}^{\top}\boldsymbol{\beta}_4 + \gamma_z\right), \tag{2.3.1}$$

$$\Upsilon_T(j,z) = N_I(j,z)\exp\left(\alpha_T + \mathbf{X}_j^{\top}\boldsymbol{\beta}_5\right), \tag{2.3.2}$$

where $\alpha_{S^{\Psi\cup\Phi}}$ represents the susceptibility intercept. The parameter vectors $\boldsymbol{\beta}_1$, $\boldsymbol{\beta}_2$, $\boldsymbol{\beta}_3$, and $\boldsymbol{\beta}_4$ correspond to $\mathbf{X}_{i^{\Psi}}$, $\mathbf{X}_{i^{\Phi}}$, $\mathbf{X}_{zS^{\Psi}}$, and $\mathbf{X}_{zS^{\Phi}}$, respectively. The term γ_z represents spatial random effects, accounting for latent geographic variation or unmeasured covariate effects, typically through a specified spatial structure between regions. Moreover, $N_{S^{\Psi}}(i,z)$ and $N_{S^{\Phi}}(i,z)$ denote the population size of susceptible individual i, who is vulnerable to initial infection and who has regained susceptibility after the immunity period, respectively, in region z. $N_I(j,z)$ stands for the number of infectious cases for individual unit j in region z, while α_T represents the transmissibility intercept. Lastly, $\boldsymbol{\beta}_5$ is a vector of coefficients associated with $\mathbf{X}_j$.

Spatial Random Effect

We adopt the Leroux model [49] to model the spatial random effect vector $\boldsymbol{\Gamma} = (\gamma_1, \ldots, \gamma_Z)^{\top}$, as described in Section 1.4.

Infection Kernel

We define the infection kernel as a power-law distance function, $\kappa(i,j) = d_{ij}^{-\delta}$, where $\delta > 0$ is the spatial decay parameter, and d_{ij} represents the Euclidean distance between susceptible individual i and infectious individual j. When $d_{ij} = 0$, the kernel tends to infinity, making the probability that susceptible individual i becomes newly exposed during the time interval $[t, t+1)$ to equal 1. For a fixed distance d_{ij}, increasing δ results in a decrease in the probability that a susceptible individual i becomes newly exposed during the time interval $[t, t+1)$.

Likelihood Function

Let $\mathbf{y}$, $\mathbf{z}$, and $\mathbf{\Gamma}$ represent the vectors of responses, the corresponding region of each response, and spatial random effects, respectively. Assuming known infection, exposure, and reinfection times, the probability mass function of all infection and non-infection events during the entire epidemic period observed across all Z regions is given by

$$p(\mathbf{y}|\mathbf{z},\mathbf{\Gamma}) = \prod_{t=1}^{T}\prod_{z=1}^{Z}\left\{\prod_{i\in S^{\Psi\cup\Phi}(t,z)}\left(1-\mathcal{P}_{(i,t,z)}(\Theta)\right)\prod_{i\in E(t+1,z,\zeta(z))\backslash E(t,z,\zeta(z))}\mathcal{P}_{(i,t,z)}(\Theta)\right\},$$

where $S^{\Psi\cup\Phi}(t,z) = S^{\Psi}(t,z)\cup S^{\Phi}(t,z)$ is the set of all susceptible individuals (Ψ and Φ) observed not to be infected at time t in the region z and $E(t+1,z,\zeta(z))\backslash E(t,z,\zeta(z))$ is the set of all newly exposed individuals at time t in the region z. The likelihood function of the complete data $\mathbf{y}_c = (\mathbf{y};\mathbf{z};\mathbf{\Gamma})$ is expressed as

$$\mathcal{L}(\Theta;\mathbf{y}_c) = p(\mathbf{y}|\mathbf{z},\mathbf{\Gamma})g(\mathbf{\Gamma}),$$

where $\Theta = (\alpha_{S^{\Psi\cup\Phi}},\alpha_T,\boldsymbol{\beta}_1,\boldsymbol{\beta}_2,\boldsymbol{\beta}_3,\boldsymbol{\beta}_4,\boldsymbol{\beta}_5,\delta,\tau,\lambda)$, and $g(\mathbf{\Gamma})$ denotes the spatial random effects density.

2.4 Parameter Estimation of GD-ILM SEIRS

To calculate the maximum likelihood estimates of the parameters of our proposed GD-ILM SEIRS, we employ the MCECM algorithm, treating $\mathbf{\Gamma}$ as latent. Algorithm 1 illustrates the MCECM algorithm for estimating the parameters of our GD-ILM SEIRS.

Algorithm 1 : MCECM Parameter Estimation of GD-ILM SEIRS

```
Initialize the set of parameters $\Theta^{(0)} = (\alpha_{S^{\Psi\cup\Phi}}^{(0)}, \alpha_T^{(0)}, \boldsymbol{\beta}_1^{(0)}, \boldsymbol{\beta}_2^{(0)}, \boldsymbol{\beta}_3^{(0)}, \boldsymbol{\beta}_4^{(0)}, \boldsymbol{\beta}_5^{(0)}, \delta^{(0)}, \tau^{(0)}, \lambda^{(0)})$.
Repeat
    E-Step: Approximate $\mathbb{E}\left[\ln \mathcal{L}(\Theta; \mathbf{y}_c)|\mathbf{y}_o, \Theta\right]$ using Metropolis-Hastings algorithm [62, 34]. Let $\mathbf{y}_o = (\mathbf{y}; \mathbf{z})$ denote the observed variables. Consider $g(\boldsymbol{\Gamma})$ as the candidate density and $p(\boldsymbol{\Gamma}|\mathbf{y}_o) \propto p(\mathbf{y}|\mathbf{z}, \boldsymbol{\Gamma}) g(\boldsymbol{\Gamma})$ as the target density. In the $(k+1)$th iteration of the ECM algorithm and with current values $\Theta^{(k)}$:
        For $(l = 1, \ldots, L)$
        In the $l$th iteration with current values of $\boldsymbol{\Gamma}_{k+1,l}$, generate $r \sim \text{Uniform}(0,1)$ and $\tilde{\boldsymbol{\Gamma}} \sim p(\boldsymbol{\Gamma}|\mathbf{y}_o; \Theta^{(k)})$.
            If $r \leqslant \frac{p(\mathbf{y}|\mathbf{z}, \tilde{\boldsymbol{\Gamma}})}{p(\mathbf{y}|\mathbf{z}, \boldsymbol{\Gamma}_{k+1,l})}$, Then
                $\boldsymbol{\Gamma}_{k+1,l+1} = \tilde{\boldsymbol{\Gamma}}$
            Else
                $\boldsymbol{\Gamma}_{k+1,l+1} = \boldsymbol{\Gamma}_{k+1,l}$
            End If
        End For
        Return the random sample $\{\boldsymbol{\Gamma}_{k+1,1}, \boldsymbol{\Gamma}_{k+1,2}, \ldots, \boldsymbol{\Gamma}_{k+1,L}\}$ generated from $p(\boldsymbol{\Gamma}|\mathbf{y}_o; \Theta^{(k)})$ and approximate the expectation by $\mathbb{E}\left[\ln \mathcal{L}(\Theta; \mathbf{y}_c)|\mathbf{y}_o, \Theta\right] = \frac{1}{L}\sum_{l=1}^{L} \ln \mathcal{L}(\Theta; \mathbf{y}; \boldsymbol{\Gamma}_{k+1,l})$ given in (2.4.1).
    M-Step: Maximize $\mathbb{E}\left[\ln \mathcal{L}(\Theta; \mathbf{y}_c)|\mathbf{y}_o, \Theta\right]$, with respect to the following model parameters to obtain $\Theta^{(k+1)}$.
        CM-Step 1: Update $\alpha_{S^{\Psi\cup\Phi}}^{(k+1)}$ using (2.4.2).
        CM-Step 2: Let $\alpha_{S^{\Psi\cup\Phi}} = \alpha_{S^{\Psi\cup\Phi}}^{(k+1)}$. Update $\boldsymbol{\beta}_1^{(k+1)}$ using (2.4.3).
        CM-Step 3: Let $(\alpha_{S^{\Psi\cup\Phi}}, \boldsymbol{\beta}_1) = (\alpha_{S^{\Psi\cup\Phi}}^{(k+1)}, \boldsymbol{\beta}_1^{(k+1)})$. Update $\boldsymbol{\beta}_2^{(k+1)}$ using (2.4.4).
        CM-Step 4: Let $(\alpha_{S^{\Psi\cup\Phi}}, \boldsymbol{\beta}_1, \boldsymbol{\beta}_2) = (\alpha_{S^{\Psi\cup\Phi}}^{(k+1)}, \boldsymbol{\beta}_1^{(k+1)}, \boldsymbol{\beta}_2^{(k+1)})$. Update $\boldsymbol{\beta}_3^{(k+1)}$ using (2.4.5).
        CM-Step 5: Let $(\alpha_{S^{\Psi\cup\Phi}}, \boldsymbol{\beta}_1, \boldsymbol{\beta}_2, \boldsymbol{\beta}_3) = (\alpha_{S^{\Psi\cup\Phi}}^{(k+1)}, \boldsymbol{\beta}_1^{(k+1)}, \boldsymbol{\beta}_2^{(k+1)}, \boldsymbol{\beta}_3^{(k+1)})$. Update $\boldsymbol{\beta}_4^{(k+1)}$ using (2.4.6).
        CM-Step 6: Let $(\alpha_{S^{\Psi\cup\Phi}}, \boldsymbol{\beta}_1, \boldsymbol{\beta}_2, \boldsymbol{\beta}_3, \boldsymbol{\beta}_4) = (\alpha_{S^{\Psi\cup\Phi}}^{(k+1)}, \boldsymbol{\beta}_1^{(k+1)}, \boldsymbol{\beta}_2^{(k+1)}, \boldsymbol{\beta}_3^{(k+1)}, \boldsymbol{\beta}_4^{(k+1)})$. Update $\alpha_T^{(k+1)}$ using (2.4.7).
        CM-Step 7: Let $(\alpha_{S^{\Psi\cup\Phi}}, \alpha_T, \boldsymbol{\beta}_1, \boldsymbol{\beta}_2, \boldsymbol{\beta}_3, \boldsymbol{\beta}_4) = (\alpha_{S^{\Psi\cup\Phi}}^{(k+1)}, \alpha_T^{(k+1)}, \boldsymbol{\beta}_1^{(k+1)}, \boldsymbol{\beta}_2^{(k+1)}, \boldsymbol{\beta}_3^{(k+1)}, \boldsymbol{\beta}_4^{(k+1)})$. Update $\boldsymbol{\beta}_5^{(k+1)}$ using (2.4.8).
        CM-Step 8:
        Let $(\alpha_{S^{\Psi\cup\Phi}}, \alpha_T, \boldsymbol{\beta}_1, \boldsymbol{\beta}_2, \boldsymbol{\beta}_3, \boldsymbol{\beta}_4, \boldsymbol{\beta}_5) = (\alpha_{S^{\Psi\cup\Phi}}^{(k+1)}, \alpha_T^{(k+1)}, \boldsymbol{\beta}_1^{(k+1)}, \boldsymbol{\beta}_2^{(k+1)}, \boldsymbol{\beta}_3^{(k+1)}, \boldsymbol{\beta}_4^{(k+1)}, \boldsymbol{\beta}_5^{(k+1)})$. Update $\delta^{(k+1)}$ using (2.4.9).
        CM-Step 9: Update $\begin{pmatrix}\tau\\ \lambda\end{pmatrix}$ using Newton–Raphson iterative as $\begin{pmatrix}\tau^{(k+1)}\\ \lambda^{(k+1)}\end{pmatrix} = \begin{pmatrix}\tau^{(k)}\\ \lambda^{(k)}\end{pmatrix} - B^{-1}A$, where $A$ and $B$ are in Equations (2.4.10-2.4.14).
Until the set $\Theta^{(k+1)}$ satisfies $\|\Theta^{(k+1)} - \Theta^{(k)}\|_2 < \epsilon_\Theta$, where $\|\cdot\|_2$ denotes the Euclidean norm, and $\epsilon_\Theta$ is a small threshold.
Return the optimal value $\hat{\Theta} = \Theta^{(k+1)}$.
```

2.4.1 CM-Steps in MCECM Algorithm 1

The approximated expectation is given by $\mathbb{E}\left[\ln \mathcal{L}(\Theta; \mathbf{y}_c)|\mathbf{y}_o, \Theta\right] = \frac{1}{L}\sum_{l=1}^{L} \ln \mathcal{L}(\Theta; \mathbf{y}; \boldsymbol{\Gamma}_{k+1,l})$. For simplicity, assume $\boldsymbol{\Gamma}_{k+1,l} = \boldsymbol{\Gamma}_l$ henceforth. Therefore,

$$
\begin{aligned}
\mathbb{E}\left[\ln \mathcal{L}\left(\Theta; \mathbf{y}_c\right)|\mathbf{y}_o, \Theta\right] &= \frac{1}{L}\sum_{t=1}^{T} \sum_{i \in S^{\Psi\cup\Phi}(t,z)} \sum_{z=1}^{Z}\sum_{l=1}^{L}\Bigg[-\left(N_{S^{\Psi}}(i,z) + N_{S^{\Phi}}(i,z)\right)\exp(\alpha_{S^{\Psi\cup\Phi}} + \mathbf{X}_{i^{\Psi}}^{\top}\boldsymbol{\beta}_1 + \mathbf{X}_{i^{\Phi}}^{\top}\boldsymbol{\beta}_2 \\
&+ \mathbf{X}_{zS^{\Psi}}^{\top}\boldsymbol{\beta}_3 + \mathbf{X}_{zS^{\Phi}}^{\top}\boldsymbol{\beta}_4 + \gamma_{zl}) \sum_{j \in I(t,z,\zeta(z))} \Upsilon_T\left(j,z\right) d_{ij}^{-\delta} \Bigg| \mathbf{y}_o \Bigg] \\
&+ \frac{1}{L}\sum_{t=1}^{T} \sum_{i \in E(t+1,z,\zeta(z))\setminus E(t,z,\zeta(z))} \sum_{z=1}^{Z}\sum_{l=1}^{L}\Bigg[\ln\Bigg\{ 1 - \exp(-\left(N_{S^{\Psi}}(i,z) + N_{S^{\Phi}}(i,z)\right)\exp(\alpha_{S^{\Psi\cup\Phi}} + \mathbf{X}_{i^{\Psi}}^{\top}\boldsymbol{\beta}_1 \\
&+ \mathbf{X}_{i^{\Phi}}^{\top}\boldsymbol{\beta}_2 + \mathbf{X}_{zS^{\Psi}}^{\top}\boldsymbol{\beta}_3 + \mathbf{X}_{zS^{\Phi}}^{\top}\boldsymbol{\beta}_4 + \gamma_{zl}) \Bigg\} \sum_{j \in I(t,z,\zeta(z))} \Upsilon_T\left(j,z\right) d_{ij}^{-\delta} \Bigg| \mathbf{y}_o \Bigg] - \frac{Z}{2}\ln(2\pi) + \frac{Z}{2}\ln(\tau^2) \\
&+ \frac{1}{2}\ln\left(|\lambda\mathcal{R} + (1-\lambda)\mathbf{I}|\right) - \frac{\tau^2}{2}\frac{1}{L}\sum_{l=1}^{L}\left[\boldsymbol{\Gamma}_l^{\top}\left(\lambda\mathcal{R} + (1-\lambda)\mathbf{I}\right)\boldsymbol{\Gamma}_l|\mathbf{y}_o\right].
\end{aligned} \tag{2.4.1}
$$

Let $\Upsilon'^{(\cdot,\cdot,\cdot,\cdot,\cdot)}_{S^{\Psi\cup\Phi}}(i,z)$, $\Upsilon''^{(\cdot,\cdot,\cdot,\cdot,\cdot)}_{S^{\Psi\cup\Phi}}(i,z)$, $\Upsilon'^{(\cdot,\cdot,\cdot)}_{T}(j,z)$, and $\Upsilon''^{(\cdot,\cdot,\cdot)}_{T}(j,z)$ be defined in Table 2.1.

CM-Step 1: Update $\alpha_{S^{\Psi\cup\Phi}}$ using the following recursive relationship

$$
\alpha_{S^{\Psi\cup\Phi}}^{(k+1)} = \alpha_{S^{\Psi\cup\Phi}}^{(k)} - \frac{\frac{\partial}{\partial \alpha_{S^{\Psi\cup\Phi}}}\mathbb{E}\left[\ln \mathcal{L}(\Theta; \mathbf{y}_c)|\mathbf{y}_o, \Theta^{(k)}\right]}{\frac{\partial^2}{\partial^2 \alpha_{S^{\Psi\cup\Phi}}}\mathbb{E}\left[\ln \mathcal{L}(\Theta; \mathbf{y}_c)|\mathbf{y}_o, \Theta^{(k)}\right]}, \tag{2.4.2}
$$

where

$$
\begin{aligned}
\frac{\partial \mathbb{E}\left[\ln \mathcal{L}(\Theta; \mathbf{y}_c)|\mathbf{y}_o, \Theta^{(k)}\right]}{\partial \alpha_{S^{\Psi\cup\Phi}}} &= -\sum_{t=1}^{T} \sum_{i \in S^{\Psi\cup\Phi}(t,z)} \sum_{z=1}^{Z} \Upsilon'^{(0,0,0,0,0)}_{S^{\Psi\cup\Phi}}(i,z) \sum_{j \in I(t,z,\zeta(z))} \Upsilon'^{(0,0,0)}_{T}(j,z) \\
&\times \frac{1}{L}\sum_{l=1}^{L}\left[\exp(\gamma_{zl})|\mathbf{y}_o, \Theta^{(k)}\right] + \sum_{t=1}^{T} \sum_{i \in E(t+1,z,\zeta(z))\setminus E(t,z,\zeta(z))} \sum_{z=1}^{Z} \Upsilon'^{(0,0,0,0,0)}_{S^{\Psi\cup\Phi}}(i,z) \\
&\times \sum_{j \in I(t,z,\zeta(z))} \Upsilon'^{(0,0,0)}_{T}(j,z) \frac{1}{L}\sum_{l=1}^{L}\left[\frac{\left(1 - \mathcal{P}_{(i,t,z)}(\Theta)\right)}{\mathcal{P}_{(i,t,z)}(\Theta)} \exp(\gamma_{zl}) \Bigg| \mathbf{y}_o, \Theta^{(k)} \right],
\end{aligned}
$$

Table 2.1: Definitions used in CM-Steps in Algorithm 1

$(\cdot,\cdot,\cdot,\cdot,\cdot)$	$\Upsilon'^{(\cdot,\cdot,\cdot,\cdot,\cdot)}_{S^{\Psi\cup\Phi}}(i,z)$
(0,0,0,0,0)	$(N_{S^\Psi}(i,z)+N_{S^\Phi}(i,z))\exp\left(\alpha_{S^{\Psi\cup\Phi}}^{(k)}+\mathbf{X}_{i^\Psi}^\top\boldsymbol{\beta}_1^{(k)}+\mathbf{X}_{i^\Phi}^\top\boldsymbol{\beta}_2^{(k)}+\mathbf{X}_{zS^\Psi}^\top\boldsymbol{\beta}_3^{(k)}+\mathbf{X}_{zS^\Phi}^\top\boldsymbol{\beta}_4^{(k)}\right)$
(1,0,0,0,0)	$(N_{S^\Psi}(i,z)+N_{S^\Phi}(i,z))\mathbf{X}_{i^\Psi}\exp\left(\alpha_{S^{\Psi\cup\Phi}}^{(k+1)}+\mathbf{X}_{i^\Psi}^\top\boldsymbol{\beta}_1^{(k)}+\mathbf{X}_{i^\Phi}^\top\boldsymbol{\beta}_2^{(k)}+\mathbf{X}_{zS^\Psi}^\top\boldsymbol{\beta}_3^{(k)}+\mathbf{X}_{zS^\Phi}^\top\boldsymbol{\beta}_4^{(k)}\right)$
(1,1,0,0,0)	$(N_{S^\Psi}(i,z)+N_{S^\Phi}(i,z))\mathbf{X}_{i^\Phi}\exp\left(\alpha_{S^{\Psi\cup\Phi}}^{(k+1)}+\mathbf{X}_{i^\Psi}^\top\boldsymbol{\beta}_1^{(k+1)}+\mathbf{X}_{i^\Phi}^\top\boldsymbol{\beta}_2^{(k)}+\mathbf{X}_{zS^\Psi}^\top\boldsymbol{\beta}_3^{(k)}+\mathbf{X}_{zS^\Phi}^\top\boldsymbol{\beta}_4^{(k)}\right)$
(1,1,1,0,0)	$(N_{S^\Psi}(i,z)+N_{S^\Phi}(i,z))\mathbf{X}_{zS^\Psi}\exp\left(\alpha_{S^{\Psi\cup\Phi}}^{(k+1)}+\mathbf{X}_{i^\Psi}^\top\boldsymbol{\beta}_1^{(k+1)}+\mathbf{X}_{i^\Phi}^\top\boldsymbol{\beta}_2^{(k+1)}+\mathbf{X}_{zS^\Psi}^\top\boldsymbol{\beta}_3^{(k)}+\mathbf{X}_{zS^\Phi}^\top\boldsymbol{\beta}_4^{(k)}\right)$
(1,1,1,1,0)	$(N_{S^\Psi}(i,z)+N_{S^\Phi}(i,z))\mathbf{X}_{zS^\Phi}\exp\left(\alpha_{S^{\Psi\cup\Phi}}^{(k+1)}+\mathbf{X}_{i^\Psi}^\top\boldsymbol{\beta}_1^{(k+1)}+\mathbf{X}_{i^\Phi}^\top\boldsymbol{\beta}_2^{(k+1)}+\mathbf{X}_{zS^\Psi}^\top\boldsymbol{\beta}_3^{(k+1)}+\mathbf{X}_{zS^\Phi}^\top\boldsymbol{\beta}_4^{(k)}\right)$
(1,1,1,1,1)	$(N_{S^\Psi}(i,z)+N_{S^\Phi}(i,z))\exp\left(\alpha_{S^{\Psi\cup\Phi}}^{(k+1)}+\mathbf{X}_{i^\Psi}^\top\boldsymbol{\beta}_1^{(k+1)}+\mathbf{X}_{i^\Phi}^\top\boldsymbol{\beta}_2^{(k+1)}+\mathbf{X}_{zS^\Psi}^\top\boldsymbol{\beta}_3^{(k+1)}+\mathbf{X}_{zS^\Phi}^\top\boldsymbol{\beta}_4^{(k+1)}\right)$
$(\cdot,\cdot,\cdot,\cdot,\cdot)$	$\Upsilon''^{(\cdot,\cdot,\cdot,\cdot,\cdot)}_{S^{\Psi\cup\Phi}}(i,z)$
(0,0,0,0,0)	$(N_{S^\Psi}(i,z)+N_{S^\Phi}(i,z))^2\exp\left(2\alpha_{S^{\Psi\cup\Phi}}^{(k)}+2\mathbf{X}_{i^\Psi}^\top\boldsymbol{\beta}_1^{(k)}+2\mathbf{X}_{i^\Phi}^\top\boldsymbol{\beta}_2^{(k)}+2\mathbf{X}_{zS^\Psi}^\top\boldsymbol{\beta}_3^{(k)}+2\mathbf{X}_{zS^\Phi}^\top\boldsymbol{\beta}_4^{(k)}\right)$
(1,0,0,0,0)	$(N_{S^\Psi}(i,z)+N_{S^\Phi}(i,z))^2\mathbf{X}_{i^\Psi}\mathbf{X}_{i^\Psi}^\top\exp\left(2\alpha_{S^{\Psi\cup\Phi}}^{(k+1)}+2\mathbf{X}_{i^\Psi}^\top\boldsymbol{\beta}_1^{(k)}+2\mathbf{X}_{i^\Phi}^\top\boldsymbol{\beta}_2^{(k)}+2\mathbf{X}_{zS^\Psi}^\top\boldsymbol{\beta}_3^{(k)}+2\mathbf{X}_{zS^\Phi}^\top\boldsymbol{\beta}_4^{(k)}\right)$
(1,1,0,0,0)	$(N_{S^\Psi}(i,z)+N_{S^\Phi}(i,z))^2\mathbf{X}_{i^\Phi}\mathbf{X}_{i^\Phi}^\top\exp\left(2\alpha_{S^{\Psi\cup\Phi}}^{(k+1)}+2\mathbf{X}_{i^\Psi}^\top\boldsymbol{\beta}_1^{(k+1)}+2\mathbf{X}_{i^\Phi}^\top\boldsymbol{\beta}_2^{(k)}+2\mathbf{X}_{zS^\Psi}^\top\boldsymbol{\beta}_3^{(k)}+2\mathbf{X}_{zS^\Phi}^\top\boldsymbol{\beta}_4^{(k)}\right)$
(1,1,1,0,0)	$(N_{S^\Psi}(i,z)+N_{S^\Phi}(i,z))^2\mathbf{X}_{zS^\Psi}\mathbf{X}_{zS^\Psi}^\top\exp\left(2\alpha_{S^{\Psi\cup\Phi}}^{(k+1)}+2\mathbf{X}_{i^\Psi}^\top\boldsymbol{\beta}_1^{(k+1)}+2\mathbf{X}_{i^\Phi}^\top\boldsymbol{\beta}_2^{(k+1)}+2\mathbf{X}_{zS^\Psi}^\top\boldsymbol{\beta}_3^{(k)}+2\mathbf{X}_{zS^\Phi}^\top\boldsymbol{\beta}_4^{(k)}\right)$
(1,1,1,1,0)	$(N_{S^\Psi}(i,z)+N_{S^\Phi}(i,z))^2\mathbf{X}_{zS^\Phi}\mathbf{X}_{zS^\Phi}^\top\exp\left(2\alpha_{S^{\Psi\cup\Phi}}^{(k+1)}+2\mathbf{X}_{i^\Psi}^\top\boldsymbol{\beta}_1^{(k+1)}+2\mathbf{X}_{i^\Phi}^\top\boldsymbol{\beta}_2^{(k+1)}+2\mathbf{X}_{zS^\Psi}^\top\boldsymbol{\beta}_3^{(k+1)}+2\mathbf{X}_{zS^\Phi}^\top\boldsymbol{\beta}_4^{(k)}\right)$
(1,1,1,1,1)	$(N_{S^\Psi}(i,z)+N_{S^\Phi}(i,z))^2\exp\left(2\alpha_{S^{\Psi\cup\Phi}}^{(k+1)}+2\mathbf{X}_{i^\Psi}^\top\boldsymbol{\beta}_1^{(k+1)}+2\mathbf{X}_{i^\Phi}^\top\boldsymbol{\beta}_2^{(k+1)}+2\mathbf{X}_{zS^\Psi}^\top\boldsymbol{\beta}_3^{(k+1)}+2\mathbf{X}_{zS^\Phi}^\top\boldsymbol{\beta}_4^{(k+1)}\right)$
$(\cdot,\cdot,\cdot)$	$\Upsilon'^{(\cdot,\cdot,\cdot)}_{T}(j,z)$
(0,0,0)	$N_I(j,z)\exp\left(\alpha_T^{(k)}+\mathbf{X}_j^\top\boldsymbol{\beta}_5^{(k)}\right)d_{ij}^{-\delta^{(k)}}$
(1,0,0)	$N_I(j,z)\mathbf{X}_j\exp\left(\alpha_T^{(k+1)}+\mathbf{X}_j^\top\boldsymbol{\beta}_5^{(k)}\right)d_{ij}^{-\delta^{(k)}}$
(1,1,0)	$N_I(j,z)\exp\left(\alpha_T^{(k+1)}+\mathbf{X}_j^\top\boldsymbol{\beta}_5^{(k+1)}\right)\ln(d_{ij})d_{ij}^{-\delta^{(k)}}$
$(\cdot,\cdot,\cdot)$	$\Upsilon''^{(\cdot,\cdot,\cdot)}_{T}(j,z)$
(1,0,0)	$N_I(j,z)\mathbf{X}_j\mathbf{X}_j^\top\exp\left(\alpha_T^{(k+1)}+\mathbf{X}_j^\top\boldsymbol{\beta}_5^{(k)}\right)d_{ij}^{-\delta^{(k)}}$
(1,1,0)	$N_I(j,z)\exp\left(\alpha_T^{(k+1)}+\mathbf{X}_j^\top\boldsymbol{\beta}_5^{(k+1)}\right)(\ln(d_{ij}))^2d_{ij}^{-\delta^{(k)}}$

and

$$
\begin{aligned}
\frac{\partial^2\mathbb{E}\left[\ln\mathcal{L}(\Theta;\mathbf{y}_c)|\mathbf{y}_o,\Theta^{(k)}\right]}{\partial^2\alpha_{S^{\Psi\cup\Phi}}} &= -\sum_{t=1}^{T}\sum_{i\in S^{\Psi\cup\Phi}(t,z)}\sum_{z=1}^{Z}\Upsilon'^{(0,0,0,0,0)}_{S^{\Psi\cup\Phi}}(i,z)\sum_{j\in I(t,z,\zeta(z))}\Upsilon'^{(0,0,0)}_{T}(j,z)\\
&\times\frac{1}{L}\sum_{l=1}^{L}\left[\exp(\gamma_{zl})\Big|\mathbf{y}_o,\Theta^{(k)}\right]+\sum_{t=1}^{T}\sum_{i\in E(t+1,z,\zeta(z))\setminus E(t,z,\zeta(z))}\sum_{z=1}^{Z}\Upsilon'^{(0,0,0,0,0)}_{S^{\Psi\cup\Phi}}(i,z)\sum_{j\in I(t,z,\zeta(z))}\Upsilon'^{(0,0,0)}_{T}(j,z)\\
&\times\frac{1}{L}\sum_{l=1}^{L}\left[\frac{\left(1-\mathcal{P}_{(i,t,z)}(\Theta)\right)}{\mathcal{P}_{(i,t,z)}(\Theta)}\exp(\gamma_{zl})\Bigg|\mathbf{y}_o,\Theta^{(k)}\right]-\left(\Upsilon''^{(0,0,0,0,0)}_{S^{\Psi\cup\Phi}}(i,z)\right)\left(\sum_{j\in I(t,z,\zeta(z))}\Upsilon'^{(0,0,0)}_{T}(j,z)\right)^2\\
&\times\frac{1}{L}\sum_{l=1}^{L}\left[\frac{\left(1-\mathcal{P}_{(i,t,z)}(\Theta)\right)}{\left(\mathcal{P}_{(i,t,z)}(\Theta)\right)^2}\exp(2\gamma_{zl})\Bigg|\mathbf{y}_o,\Theta^{(k)}\right].
\end{aligned}
$$

CM-Step 2: Update $\boldsymbol{\beta}_1$ using the following recursive relationship

$$\boldsymbol{\beta}_1^{(k+1)} = \boldsymbol{\beta}_1^{(k)} - \frac{\frac{\partial}{\partial \boldsymbol{\beta}_1}\mathbb{E}\left[\ln \mathcal{L}(\Theta;\mathbf{y}_c)|\mathbf{y}_o,\Theta^{(k)}\right]}{\frac{\partial^2}{\partial\boldsymbol{\beta}_1\partial\boldsymbol{\beta}_1^\top}\mathbb{E}\left[\ln \mathcal{L}(\Theta;\mathbf{y}_c)|\mathbf{y}_o,\Theta^{(k)}\right]}, \tag{2.4.3}$$

where

$$\begin{aligned}
\frac{\partial \mathbb{E}\left[\ln \mathcal{L}(\Theta;\mathbf{y}_c)|\mathbf{y}_o,\Theta^{(k)}\right]}{\partial \boldsymbol{\beta}_1} &= -\sum_{t=1}^{T}\sum_{i\in S^{\Psi\cup\Phi}(t,z)}\sum_{z=1}^{Z}\Upsilon'^{(1,0,0,0,0)}_{S^{\Psi\cup\Phi}}(i,z)\sum_{j\in I(t,z,\zeta(z))}\Upsilon'^{(0,0,0)}_{T}(j,z)\\
\times \frac{1}{L}\sum_{l=1}^{L}\left[\exp(\gamma_{zl})\middle|\mathbf{y}_o,\Theta^{(k)}\right] &+ \sum_{t=1}^{T}\sum_{i\in E(t+1,z,\zeta(z))\backslash E(t,z,\zeta(z))}\sum_{z=1}^{Z}\Upsilon'^{(1,0,0,0,0)}_{S^{\Psi\cup\Phi}}(i,z)\\
\times \sum_{j\in I(t,z,\zeta(z))}\Upsilon'^{(0,0,0)}_{T}(j,z)&\frac{1}{L}\sum_{l=1}^{L}\left[\frac{\left(1-\mathcal{P}_{(i,t,z)}(\Theta)\right)}{\mathcal{P}_{(i,t,z)}(\Theta)}\exp(\gamma_{zl})\middle|\mathbf{y}_o,\Theta^{(k)}\right],
\end{aligned}$$

and

$$\begin{aligned}
\frac{\partial^2 \mathbb{E}\left[\ln \mathcal{L}(\Theta;\mathbf{y}_c)|\mathbf{y}_o,\Theta^{(k)}\right]}{\partial \boldsymbol{\beta}_1\partial \boldsymbol{\beta}_1^\top} &= -\sum_{t=1}^{T}\sum_{i\in S^{\Psi\cup\Phi}(t,z)}\sum_{z=1}^{Z}\Upsilon'^{(1,0,0,0,0)}_{S^{\Psi\cup\Phi}}(i,z)\,\mathbf{X}_{i^\Psi}^\top\sum_{j\in I(t,z,\zeta(z))}\Upsilon'^{(0,0,0)}_{T}(j,z)\\
\times \frac{1}{L}\sum_{l=1}^{L}\left[\exp(\gamma_{zl})\middle|\mathbf{y}_o,\Theta^{(k)}\right] &+ \sum_{t=1}^{T}\sum_{i\in E(t+1,z,\zeta(z))\backslash E(t,z,\zeta(z))}\sum_{z=1}^{Z}\Upsilon'^{(1,0,0,0,0)}_{S^{\Psi\cup\Phi}}(i,z)\,\mathbf{X}_{i^\Psi}^\top\sum_{j\in I(t,z,\zeta(z))}\Upsilon'^{(0,0,0)}_{T}(j,z)\\
\times \frac{1}{L}\sum_{l=1}^{L}\left[\frac{\left(1-\mathcal{P}_{(i,t,z)}(\Theta)\right)}{\mathcal{P}_{(i,t,z)}(\Theta)}\exp(\gamma_{zl})\middle|\mathbf{y}_o,\Theta^{(k)}\right] &- \left(\Upsilon''^{(1,0,0,0,0)}_{S^{\Psi\cup\Phi}}(i,z)\right)\left(\sum_{j\in I(t,z,\zeta(z))}\Upsilon'^{(0,0,0)}_{T}(j,z)\right)^2\\
\times \frac{1}{L}\sum_{l=1}^{L}\left[\frac{\left(1-\mathcal{P}_{(i,t,z)}(\Theta)\right)}{\left(\mathcal{P}_{(i,t,z)}(\Theta)\right)^2}\exp(2\gamma_{zl})\middle|\mathbf{y}_o,\Theta^{(k)}\right]&.
\end{aligned}$$

CM-Step 3: Update $\boldsymbol{\beta}_2$ using the following recursive relationship

$$\boldsymbol{\beta}_2^{(k+1)} = \boldsymbol{\beta}_2^{(k)} - \frac{\frac{\partial}{\partial \boldsymbol{\beta}_2}\mathbb{E}\left[\ln \mathcal{L}(\Theta;\mathbf{y}_c)|\mathbf{y}_o,\Theta^{(k)}\right]}{\frac{\partial^2}{\partial\boldsymbol{\beta}_2\partial\boldsymbol{\beta}_2^\top}\mathbb{E}\left[\ln \mathcal{L}(\Theta;\mathbf{y}_c)|\mathbf{y}_o,\Theta^{(k)}\right]}, \tag{2.4.4}$$

where

$$\frac{\partial \mathbb{E}\left[\ln \mathcal{L}(\Theta;\mathbf{y}_c)|\mathbf{y}_o,\Theta^{(k)}\right]}{\partial \boldsymbol{\beta}_2} = -\sum_{t=1}^{T}\sum_{i\in S^{\Psi\cup\Phi}(t,z)}\sum_{z=1}^{Z}\Upsilon'^{(1,1,0,0,0)}_{S^{\Psi\cup\Phi}}(i,z)\sum_{j\in I(t,z,\zeta(z))}\Upsilon'^{(0,0,0)}_{T}(j,z)$$

$$\times\frac{1}{L}\sum_{l=1}^{L}\left[\exp(\gamma_{zl})\middle|\mathbf{y}_o,\Theta^{(k)}\right]+\sum_{t=1}^{T}\sum_{i\in E(t+1,z,\zeta(z))\setminus E(t,z,\zeta(z))}\sum_{z=1}^{Z}\Upsilon'^{(1,1,0,0,0)}_{S^{\Psi\cup\Phi}}(i,z)$$

$$\times\sum_{j\in I(t,z,\zeta(z))}\Upsilon'^{(0,0,0)}_{T}(j,z)\frac{1}{L}\sum_{l=1}^{L}\left[\frac{\left(1-\mathcal{P}_{(i,t,z)}(\Theta)\right)}{\mathcal{P}_{(i,t,z)}(\Theta)}\exp(\gamma_{zl})\middle|\mathbf{y}_o,\Theta^{(k)}\right],$$

and

$$\frac{\partial^2 \mathbb{E}\left[\ln \mathcal{L}(\Theta;\mathbf{y}_c)|\mathbf{y}_o,\Theta^{(k)}\right]}{\partial \boldsymbol{\beta}_2\partial \boldsymbol{\beta}_2^{\top}} = -\sum_{t=1}^{T}\sum_{i\in S^{\Psi\cup\Phi}(t,z)}\sum_{z=1}^{Z}\Upsilon'^{(1,1,0,0,0)}_{S^{\Psi\cup\Phi}}(i,z)\,\mathbf{X}_{i^{\Phi}}^{\top}\sum_{j\in I(t,z,\zeta(z))}\Upsilon'^{(0,0,0)}_{T}(j,z)$$

$$\times\frac{1}{L}\sum_{l=1}^{L}\left[\exp(\gamma_{zl})\middle|\mathbf{y}_o,\Theta^{(k)}\right]+\sum_{t=1}^{T}\sum_{i\in E(t+1,z,\zeta(z))\setminus E(t,z,\zeta(z))}\sum_{z=1}^{Z}\Upsilon'^{(1,1,0,0,0)}_{S^{\Psi\cup\Phi}}(i,z)\,\mathbf{X}_{i^{\Phi}}^{\top}\sum_{j\in I(t,z,\zeta(z))}\Upsilon'^{(0,0,0)}_{T}(j,z)$$

$$\times\frac{1}{L}\sum_{l=1}^{L}\left[\frac{\left(1-\mathcal{P}_{(i,t,z)}(\Theta)\right)}{\mathcal{P}_{(i,t,z)}(\Theta)}\exp(\gamma_{zl})\middle|\mathbf{y}_o,\Theta^{(k)}\right]-\left(\Upsilon''^{(1,1,0,0,0)}_{S^{\Psi\cup\Phi}}(i,z)\right)\left(\sum_{j\in I(t,z,\zeta(z))}\Upsilon'^{(0,0,0)}_{T}(j,z)\right)^2$$

$$\times\frac{1}{L}\sum_{l=1}^{L}\left[\frac{\left(1-\mathcal{P}_{(i,t,z)}(\Theta)\right)}{\left(\mathcal{P}_{(i,t,z)}(\Theta)\right)^2}\exp(2\gamma_{zl})\middle|\mathbf{y}_o,\Theta^{(k)}\right].$$

CM-Step 4: Update $\boldsymbol{\beta}_3$ using the following recursive relationship

$$\boldsymbol{\beta}_3^{(k+1)}=\boldsymbol{\beta}_3^{(k)}-\frac{\frac{\partial}{\partial\boldsymbol{\beta}_3}\mathbb{E}\left[\ln \mathcal{L}(\Theta;\mathbf{y}_c)|\mathbf{y}_o,\Theta^{(k)}\right]}{\frac{\partial^2}{\partial\boldsymbol{\beta}_2\partial\boldsymbol{\beta}_3^{\top}}\mathbb{E}\left[\ln \mathcal{L}(\Theta;\mathbf{y}_c)|\mathbf{y}_o,\Theta^{(k)}\right]}, \tag{2.4.5}$$

where

$$\frac{\partial \mathbb{E}\left[\ln \mathcal{L}(\Theta;\mathbf{y}_c)|\mathbf{y}_o,\Theta^{(k)}\right]}{\partial \boldsymbol{\beta}_3} = -\sum_{t=1}^{T}\sum_{i\in S^{\Psi\cup\Phi}(t,z)}\sum_{z=1}^{Z}\Upsilon'^{(1,1,1,0,0)}_{S^{\Psi\cup\Phi}}(i,z)\sum_{j\in I(t,z,\zeta(z))}\Upsilon'^{(0,0,0)}_{T}(j,z)$$

$$\times\frac{1}{L}\sum_{l=1}^{L}\left[\exp(\gamma_{zl})\middle|\mathbf{y}_o,\Theta^{(k)}\right]+\sum_{t=1}^{T}\sum_{i\in E(t+1,z,\zeta(z))\setminus E(t,z,\zeta(z))}\sum_{z=1}^{Z}\Upsilon'^{(1,1,1,0,0)}_{S^{\Psi\cup\Phi}}(i,z)$$

$$\times\sum_{j\in I(t,z,\zeta(z))}\Upsilon'^{(0,0,0)}_{T}(j,z)\frac{1}{L}\sum_{l=1}^{L}\left[\frac{\left(1-\mathcal{P}_{(i,t,z)}(\Theta)\right)}{\mathcal{P}_{(i,t,z)}(\Theta)}\exp(\gamma_{zl})\middle|\mathbf{y}_o,\Theta^{(k)}\right],$$

and

$$\begin{aligned}\frac{\partial^2 \mathbb{E}\left[\ln \mathcal{L}(\Theta;\mathbf{y}_c)|\mathbf{y}_o,\Theta^{(k)}\right]}{\partial\boldsymbol{\beta}_3\partial\boldsymbol{\beta}_3^\top} &= -\sum_{t=1}^{T}\sum_{i\in S^{\Psi\cup\Phi}(t,z)}\sum_{z=1}^{Z}\Upsilon'^{(1,1,1,0,0)}_{S^{\Psi\cup\Phi}}(i,z)\,\mathbf{X}^\top_{zS^\Psi}\sum_{j\in I(t,z,\zeta(z))}\Upsilon'^{(0,0,0)}_{T}(j,z)\\
&\times\frac{1}{L}\sum_{l=1}^{L}\left[\exp(\gamma_{zl})\Big|\mathbf{y}_o,\Theta^{(k)}\right]+\sum_{t=1}^{T}\sum_{i\in E(t+1,z,\zeta(z))\setminus E(t,z,\zeta(z))}\sum_{z=1}^{Z}\Upsilon'^{(1,1,1,0,0)}_{S^{\Psi\cup\Phi}}(i,z)\,\mathbf{X}^\top_{zS^\Psi}\sum_{j\in I(t,z,\zeta(z))}\Upsilon'^{(0,0,0)}_{T}(j,z)\\
&\times\frac{1}{L}\sum_{l=1}^{L}\left[\frac{\left(1-\mathcal{P}_{(i,t,z)}(\Theta)\right)}{\mathcal{P}_{(i,t,z)}(\Theta)}\exp(\gamma_{zl})\Big|\mathbf{y}_o,\Theta^{(k)}\right]-\left(\Upsilon''^{(1,1,1,0,0)}_{S^{\Psi\cup\Phi}}(i,z)\right)\left(\sum_{j\in I(t,z,\zeta(z))}\Upsilon'^{(0,0,0)}_{T}(j,z)\right)^2\\
&\times\frac{1}{L}\sum_{l=1}^{L}\left[\frac{\left(1-\mathcal{P}_{(i,t,z)}(\Theta)\right)}{\left(\mathcal{P}_{(i,t,z)}(\Theta)\right)^2}\exp(2\gamma_{zl})\Big|\mathbf{y}_o,\Theta^{(k)}\right].\end{aligned}$$

CM-Step 5: Update $\boldsymbol{\beta}_4$ using the following recursive relationship

$$\boldsymbol{\beta}_4^{(k+1)}=\boldsymbol{\beta}_4^{(k)}-\frac{\frac{\partial}{\partial\boldsymbol{\beta}_4}\mathbb{E}\left[\ln \mathcal{L}(\Theta;\mathbf{y}_c)|\mathbf{y}_o,\Theta^{(k)}\right]}{\frac{\partial^2}{\partial\boldsymbol{\beta}_4\partial\boldsymbol{\beta}_4^\top}\mathbb{E}\left[\ln \mathcal{L}(\Theta;\mathbf{y}_c)|\mathbf{y}_o,\Theta^{(k)}\right]}, \tag{2.4.6}$$

where

$$\begin{aligned}\frac{\partial \mathbb{E}\left[\ln \mathcal{L}(\Theta;\mathbf{y}_c)|\mathbf{y}_o,\Theta^{(k)}\right]}{\partial\boldsymbol{\beta}_4} &= -\sum_{t=1}^{T}\sum_{i\in S^{\Psi\cup\Phi}(t,z)}\sum_{z=1}^{Z}\Upsilon'^{(1,1,1,1,0)}_{S^{\Psi\cup\Phi}}(i,z)\sum_{j\in I(t,z,\zeta(z))}\Upsilon'^{(0,0,0)}_{T}(j,z)\\
&\times\frac{1}{L}\sum_{l=1}^{L}\left[\exp(\gamma_{zl})\Big|\mathbf{y}_o,\Theta^{(k)}\right]+\sum_{t=1}^{T}\sum_{i\in E(t+1,z,\zeta(z))\setminus E(t,z,\zeta(z))}\sum_{z=1}^{Z}\Upsilon'^{(1,1,1,1,0)}_{S^{\Psi\cup\Phi}}(i,z)\\
&\times\sum_{j\in I(t,z,\zeta(z))}\Upsilon'^{(0,0,0)}_{T}(j,z)\frac{1}{L}\sum_{l=1}^{L}\left[\frac{\left(1-\mathcal{P}_{(i,t,z)}(\Theta)\right)}{\mathcal{P}_{(i,t,z)}(\Theta)}\exp(\gamma_{zl})\Big|\mathbf{y}_o,\Theta^{(k)}\right],\end{aligned}$$

and

$$\begin{aligned}
\frac{\partial^2\mathbb{E}\left[\ln\mathcal{L}(\Theta;\mathbf{y}_c)|\mathbf{y}_o,\Theta^{(k)}\right]}{\partial\boldsymbol{\beta}_4\partial\boldsymbol{\beta}_4^\top} &= -\sum_{t=1}^{T}\sum_{i\in S^{\Psi\cup\Phi}(t,z)}\sum_{z=1}^{Z}\Upsilon'^{(1,1,1,1,0)}_{S^{\Psi\cup\Phi}}(i,z)\,\mathbf{X}_{zS^{\Phi}}^\top\sum_{j\in I(t,z,\zeta(z))}\Upsilon'^{(0,0,0)}_{T}(j,z)\\
&\times\frac{1}{L}\sum_{l=1}^{L}\left[\exp(\gamma_{zl})\Big|\mathbf{y}_o,\Theta^{(k)}\right]+\sum_{t=1}^{T}\sum_{i\in E(t+1,z,\zeta(z))\setminus E(t,z,\zeta(z))}\sum_{z=1}^{Z}\Upsilon'^{(1,1,1,1,0)}_{S^{\Psi\cup\Phi}}(i,z)\,\mathbf{X}_{zS^{\Phi}}^\top\sum_{j\in I(t,z,\zeta(z))}\Upsilon'^{(0,0,0)}_{T}(j,z)\\
&\times\frac{1}{L}\sum_{l=1}^{L}\left[\frac{\left(1-\mathcal{P}_{(i,t,z)}(\Theta)\right)}{\mathcal{P}_{(i,t,z)}(\Theta)}\exp(\gamma_{zl})\middle|\mathbf{y}_o,\Theta^{(k)}\right]-\left(\Upsilon''^{(1,1,1,1,0)}_{S^{\Psi\cup\Phi}}(i,z)\right)\left(\sum_{j\in I(t,z,\zeta(z))}\Upsilon'^{(0,0,0)}_{T}(j,z)\right)^2\\
&\times\frac{1}{L}\sum_{l=1}^{L}\left[\frac{\left(1-\mathcal{P}_{(i,t,z)}(\Theta)\right)}{\left(\mathcal{P}_{(i,t,z)}(\Theta)\right)^2}\exp(2\gamma_{zl})\middle|\mathbf{y}_o,\Theta^{(k)}\right].
\end{aligned}$$

CM-Step 6: Update α_T using the following recursive relationship

$$\alpha_T^{(k+1)}=\alpha_T^{(k)}-\frac{\frac{\partial}{\partial\alpha_T}\mathbb{E}\left[\ln\mathcal{L}(\Theta;\mathbf{y}_c)|\mathbf{y}_o,\Theta^{(k)}\right]}{\frac{\partial^2}{\partial^2\alpha_T}\mathbb{E}\left[\ln\mathcal{L}(\Theta;\mathbf{y}_c)|\mathbf{y}_o,\Theta^{(k)}\right]},\tag{2.4.7}$$

where

$$\begin{aligned}
\frac{\partial\mathbb{E}\left[\ln\mathcal{L}(\Theta;\mathbf{y}_c)|\mathbf{y}_o,\Theta^{(k)}\right]}{\partial\alpha_T} &= -\sum_{t=1}^{T}\sum_{i\in S^{\Psi\cup\Phi}(t,z)}\sum_{z=1}^{Z}\Upsilon'^{(1,1,1,1,1)}_{S^{\Psi\cup\Phi}}(i,z)\sum_{j\in I(t,z,\zeta(z))}\Upsilon'^{(0,0,0)}_{T}(j,z)\\
&\times\frac{1}{L}\sum_{l=1}^{L}\left[\exp(\gamma_{zl})\Big|\mathbf{y}_o,\Theta^{(k)}\right]+\sum_{t=1}^{T}\sum_{i\in E(t+1,z,\zeta(z))\setminus E(t,z,\zeta(z))}\sum_{z=1}^{Z}\Upsilon'^{(1,1,1,1,1)}_{S^{\Psi\cup\Phi}}(i,z)\\
&\times\sum_{j\in I(t,z,\zeta(z))}\Upsilon'^{(0,0,0)}_{T}(j,z)\frac{1}{L}\sum_{l=1}^{L}\left[\frac{\left(1-\mathcal{P}_{(i,t,z)}(\Theta)\right)}{\mathcal{P}_{(i,t,z)}(\Theta)}\exp(\gamma_{zl})\middle|\mathbf{y}_o,\Theta^{(k)}\right],
\end{aligned}$$

and

$$
\begin{aligned}
\frac{\partial^2 \mathbb{E}\left[\ln \mathcal{L}(\Theta; \mathbf{y}_c)|\mathbf{y}_o, \Theta^{(k)}\right]}{\partial^2 \alpha_T} &= -\sum_{t=1}^{T} \sum_{i \in S^{\Psi\cup\Phi}(t,z)} \sum_{z=1}^{Z} \Upsilon'^{(1,1,1,1,1)}_{S^{\Psi\cup\Phi}}(i,z) \sum_{j \in I(t,z,\zeta(z))} \Upsilon'^{(0,0,0)}_{T}(j,z) \\
&\times \frac{1}{L}\sum_{l=1}^{L}\left[\exp(\gamma_{zl})\Big|\mathbf{y}_o, \Theta^{(k)}\right] + \sum_{t=1}^{T} \sum_{i \in E(t+1,z,\zeta(z))\backslash E(t,z,\zeta(z))} \sum_{z=1}^{Z} \Upsilon'^{(1,1,1,1,1)}_{S^{\Psi\cup\Phi}}(i,z) \sum_{j \in I(t,z,\zeta(z))} \Upsilon'^{(0,0,0)}_{T}(j,z) \\
&\times \frac{1}{L}\sum_{l=1}^{L}\left[\frac{\left(1-\mathcal{P}_{(i,t,z)}(\Theta)\right)}{\mathcal{P}_{(i,t,z)}(\Theta)}\exp(\gamma_{zl})\Bigg|\mathbf{y}_o, \Theta^{(k)}\right] - \left(\Upsilon''^{(1,1,1,1,1)}_{S^{\Psi\cup\Phi}}(i,z)\right)\left(\sum_{j \in I(t,z,\zeta(z))} \Upsilon'^{(0,0,0)}_{T}(j,z)\right)^2 \\
&\times \frac{1}{L}\sum_{l=1}^{L}\left[\frac{\left(1-\mathcal{P}_{(i,t,z)}(\Theta)\right)}{\left(\mathcal{P}_{(i,t,z)}(\Theta)\right)^2}\exp(2\gamma_{zl})\Bigg|\mathbf{y}_o, \Theta^{(k)}\right].
\end{aligned}
$$

CM-Step 7: Update $\boldsymbol{\beta}_5$ using the following recursive relationship

$$
\boldsymbol{\beta}_5^{(k+1)} = \boldsymbol{\beta}_5^{(k)} - \frac{\frac{\partial}{\partial \boldsymbol{\beta}_5}\mathbb{E}\left[\ln \mathcal{L}(\Theta; \mathbf{y}_c)|\mathbf{y}_o, \Theta^{(k)}\right]}{\frac{\partial^2}{\partial \boldsymbol{\beta}_5 \partial \boldsymbol{\beta}_5^{\top}}\mathbb{E}\left[\ln \mathcal{L}(\Theta; \mathbf{y}_c)|\mathbf{y}_o, \Theta^{(k)}\right]}, \tag{2.4.8}
$$

where

$$
\begin{aligned}
\frac{\partial \mathbb{E}\left[\ln \mathcal{L}(\Theta; \mathbf{y}_c)|\mathbf{y}_o, \Theta^{(k)}\right]}{\partial \boldsymbol{\beta}_5} &= -\sum_{t=1}^{T} \sum_{i \in S^{\Psi\cup\Phi}(t,z)} \sum_{z=1}^{Z} \Upsilon'^{(1,1,1,1,1)}_{S^{\Psi\cup\Phi}}(i,z) \sum_{j \in I(t,z,\zeta(z))} \Upsilon'^{(1,0,0)}_{T}(j,z) \\
&\times \frac{1}{L}\sum_{l=1}^{L}\left[\exp(\gamma_{zl})\Big|\mathbf{y}_o, \Theta^{(k)}\right] + \sum_{t=1}^{T} \sum_{i \in E(t+1,z,\zeta(z))\backslash E(t,z,\zeta(z))} \sum_{z=1}^{Z} \Upsilon'^{(1,1,1,1,1)}_{S^{\Psi\cup\Phi}}(i,z) \\
&\times \sum_{j \in I(t,z,\zeta(z))} \Upsilon'^{(1,0,0)}_{T}(j,z) \frac{1}{L}\sum_{l=1}^{L}\left[\frac{\left(1-\mathcal{P}_{(i,t,z)}(\Theta)\right)}{\mathcal{P}_{(i,t,z)}(\Theta)}\exp(\gamma_{zl})\Bigg|\mathbf{y}_o, \Theta^{(k)}\right],
\end{aligned}
$$

and

$$\begin{aligned}
\frac{\partial^2 \mathbb{E}\left[\ln \mathcal{L}(\Theta;\mathbf{y}_c)|\mathbf{y}_o,\Theta^{(k)}\right]}{\partial\boldsymbol{\beta}_5\partial\boldsymbol{\beta}_5^\top} &= -\sum_{t=1}^{T}\sum_{i\in S^{\Psi\cup\Phi}(t,z)}\sum_{z=1}^{Z}\Upsilon'^{(1,1,1,1,1)}_{S^{\Psi\cup\Phi}}(i,z)\sum_{j\in I(t,z,\zeta(z))}\Upsilon''^{(1,0,0)}_{T}(j,z) \\
&\times\frac{1}{L}\sum_{l=1}^{L}\left[\exp(\gamma_{zl})\middle|\mathbf{y}_o,\Theta^{(k)}\right] + \sum_{t=1}^{T}\sum_{i\in E(t+1,z,\zeta(z))\setminus E(t,z,\zeta(z))}\sum_{z=1}^{Z}\Upsilon'^{(1,1,1,1,1)}_{S^{\Psi\cup\Phi}}(i,z)\sum_{j\in I(t,z,\zeta(z))}\Upsilon''^{(1,0,0)}_{T}(j,z) \\
&\times\frac{1}{L}\sum_{l=1}^{L}\left[\frac{\left(1-\mathcal{P}_{(i,t,z)}(\Theta)\right)}{\mathcal{P}_{(i,t,z)}(\Theta)}\exp(\gamma_{zl})\middle|\mathbf{y}_o,\Theta^{(k)}\right] - \left(\Upsilon''^{(1,1,1,1,1)}_{S^{\Psi\cup\Phi}}(i,z)\right)\left(\sum_{j\in I(t,z,\zeta(z))}\Upsilon'^{(1,0,0)}_{T}(j,z)\right) \\
&\times\left(\sum_{j\in I(t,z,\zeta(z))}\Upsilon'^{(1,0,0)}_{T}(j,z)\right)^{\top}\frac{1}{L}\sum_{l=1}^{L}\left[\frac{\left(1-\mathcal{P}_{(i,t,z)}(\Theta)\right)}{\left(\mathcal{P}_{(i,t,z)}(\Theta)\right)^2}\exp(2\gamma_{zl})\middle|\mathbf{y}_o,\Theta^{(k)}\right].
\end{aligned}$$

CM-Step 8: Update δ using the following recursive relationship

$$\delta^{(k+1)} = \delta^{(k)} - \frac{\frac{\partial}{\partial\delta}\mathbb{E}\left[\ln \mathcal{L}(\Theta;\mathbf{y}_c)|\mathbf{y}_o,\Theta^{(k)}\right]}{\frac{\partial^2}{\partial^2\delta}\mathbb{E}\left[\ln \mathcal{L}(\Theta;\mathbf{y}_c)|\mathbf{y}_o,\Theta^{(k)}\right]}, \tag{2.4.9}$$

where

$$\begin{aligned}
\frac{\partial \mathbb{E}\left[\ln \mathcal{L}(\Theta;\mathbf{y}_c)|\mathbf{y}_o,\Theta^{(k)}\right]}{\partial\delta} &= -\sum_{t=1}^{T}\sum_{i\in S^{\Psi\cup\Phi}(t,z)}\sum_{z=1}^{Z}\Upsilon'^{(1,1,1,1,1)}_{S^{\Psi\cup\Phi}}(i,z)\sum_{j\in I(t,z,\zeta(z))}\Upsilon'^{(1,1,0)}_{T}(j,z) \\
&\times\frac{1}{L}\sum_{l=1}^{L}\left[\exp(\gamma_{zl})\middle|\mathbf{y}_o,\Theta^{(k)}\right] + \sum_{t=1}^{T}\sum_{i\in E(t+1,z,\zeta(z))\setminus E(t,z,\zeta(z))}\sum_{z=1}^{Z}\Upsilon'^{(1,1,1,1,1)}_{S^{\Psi\cup\Phi}}(i,z) \\
&\times\sum_{j\in I(t,z,\zeta(z))}\Upsilon'^{(1,1,0)}_{T}(j,z)\frac{1}{L}\sum_{l=1}^{L}\left[\frac{\left(1-\mathcal{P}_{(i,t,z)}(\Theta)\right)}{\mathcal{P}_{(i,t,z)}(\Theta)}\exp(\gamma_{zl})\middle|\mathbf{y}_o,\Theta^{(k)}\right],
\end{aligned}$$

and

$$
\begin{aligned}
\frac{\partial^2 \mathbb{E}\left[\ln \mathcal{L}(\Theta; \mathbf{y}_c) | \mathbf{y}_o, \Theta^{(k)}\right]}{\partial^2 \delta} &= -\sum_{t=1}^{T} \sum_{i \in S^{\Psi \cup \Phi}(t,z)} \sum_{z=1}^{Z} \Upsilon'^{(1,1,1,1,1)}_{S^{\Psi \cup \Phi}}(i,z) \sum_{j \in I(t,z,\zeta(z))} \Upsilon''^{(1,1,0)}_{T}(j,z) \\
&\times \frac{1}{L} \sum_{l=1}^{L} \left[\exp(\gamma_{zl}) \middle| \mathbf{y}_o, \Theta^{(k)}\right] + \sum_{t=1}^{T} \sum_{i \in E(t+1,z,\zeta(z)) \backslash E(t,z,\zeta(z))} \sum_{z=1}^{Z} \Upsilon'^{(1,1,1,1,1)}_{S^{\Psi \cup \Phi}}(i,z) \sum_{j \in I(t,z,\zeta(z))} \Upsilon''^{(1,1,0)}_{T}(j,z) \\
&\times \frac{1}{L} \sum_{l=1}^{L} \left[\frac{\left(1 - \mathcal{P}_{(i,t,z)}(\Theta)\right)}{\mathcal{P}_{(i,t,z)}(\Theta)} \exp(\gamma_{zl}) \middle| \mathbf{y}_o, \Theta^{(k)}\right] - \left(\Upsilon''^{(1,1,1,1,1)}_{S^{\Psi \cup \Phi}}(i,z)\right) \left(\sum_{j \in I(t,z,\zeta(z))} \Upsilon'^{(1,1,0)}_{T}(j,z)\right)^2 \\
&\times \frac{1}{L} \sum_{l=1}^{L} \left[\frac{\left(1 - \mathcal{P}_{(i,t,z)}(\Theta)\right)}{\left(\mathcal{P}_{(i,t,z)}(\Theta)\right)^2} \exp(2\gamma_{zl}) \middle| \mathbf{y}_o, \Theta^{(k)}\right].
\end{aligned}
$$

CM-Step 9: In the $(k+1)$th iteration, A and B are used to estimate τ and λ, where A represents the score vector and B corresponds to the expected information matrix. Given

$$\mathbb{E}\left[\ln p(\mathbf{\Gamma}) | \mathbf{y}_o, \Theta^{(k)}\right] = -\tfrac{Z}{2}\ln(2\pi) + \tfrac{Z}{2}\ln(\tau^2) + \tfrac{1}{2}\ln\left(|\lambda\mathcal{R} + (1-\lambda)\mathbf{I}|\right) - \tfrac{\tau^2}{2}\tfrac{1}{L}\textstyle\sum_{l=1}^{L}\left[\mathbf{\Gamma}_l^\top (\lambda\mathcal{R} + (1-\lambda)\mathbf{I})\, \mathbf{\Gamma}_l | \mathbf{y}_o, \Theta^{(k)}\right],$$

then the elements of these matrices can be defined as follows:

$$A(\tau) = \frac{\partial \mathbb{E}\left[\ln p(\mathbf{\Gamma}) | \mathbf{y}_o, \Theta^{(k)}\right]}{\partial \tau} = \frac{Z}{\tau} - \tau \frac{1}{L} \sum_{l=1}^{L} \left[\mathbf{\Gamma}_l^\top (\lambda\mathcal{R} + (1-\lambda)\mathbf{I})\, \mathbf{\Gamma}_l | \mathbf{y}_o, \Theta^{(k)}\right], \tag{2.4.10}$$

$$A(\lambda) = \tfrac{\partial \mathbb{E}\left[\ln p(\mathbf{\Gamma}) | \mathbf{y}_o, \Theta^{(k)}\right]}{\partial \lambda} = \tfrac{1}{2}\mathrm{tr}\left((\lambda\mathcal{R} + (1-\lambda)\mathbf{I})^{-1}(\mathcal{R} - \mathbf{I})\right) - \tfrac{\tau^2}{2}\tfrac{1}{L}\textstyle\sum_{l=1}^{L}\left[\mathbf{\Gamma}_l^\top (\lambda\mathcal{R} + (1-\lambda)\mathbf{I})\, \mathbf{\Gamma}_l | \mathbf{y}_o, , \Theta^{(k)}\right], \tag{2.4.11}$$

$$B(\tau, \tau) = \frac{\partial^2 \mathbb{E}\left[\ln p(\mathbf{\Gamma}) | \mathbf{y}_o, \Theta^{(k)}\right]}{\partial^2 \tau} = \frac{Z}{\tau^2} + \frac{1}{L} \sum_{l=1}^{L} \left[\mathbf{\Gamma}_l^\top (\lambda\mathcal{R} + (1-\lambda)\mathbf{I})\, \mathbf{\Gamma}_l | \mathbf{y}_o, \Theta^{(k)}\right], \tag{2.4.12}$$

$$B(\tau, \lambda) = \frac{\partial^2 \mathbb{E}\left[\ln p(\mathbf{\Gamma}) | \mathbf{y}_o, \Theta^{(k)}\right]}{\partial \tau \partial \lambda} = \tau \frac{1}{L} \sum_{l=1}^{L} \left[\mathbf{\Gamma}_l^\top (\mathcal{R} - \mathbf{I}) \mathbf{\Gamma}_l | \mathbf{y}_o, \Theta^{(k)}\right], \tag{2.4.13}$$

$$B(\lambda, \lambda) = \frac{\partial^2 \mathbb{E}\left[\ln p(\mathbf{\Gamma}) | \mathbf{y}_o, \Theta^{(k)}\right]}{\partial^2 \lambda} = \frac{1}{2}\mathrm{tr}\left((\mathcal{R} - \mathbf{I})(\lambda\mathcal{R} + (1-\lambda)\mathbf{I})^{-1}(\mathcal{R} - \mathbf{I})(\lambda\mathcal{R} + (1-\lambda)\mathbf{I})^{-1}\right). \tag{2.4.14}$$

2.5 Variances of Estimated GD-ILM SEIRS Parameters

In the MCECM algorithm, variances are calculated using an adapted approach based on the method introduced by [54] and later applied by [8, 7], in which the observed information matrix is defined as

$$\mathcal{I}_{\mathrm{o}}(\hat{\Theta};\mathbf{y}_o) = \mathcal{I}_{\mathrm{c}}(\hat{\Theta};\mathbf{y}_o) - \mathcal{I}_{\mathrm{m}}(\hat{\Theta};\mathbf{y}_o),$$

where $\hat{\Theta}$ denotes the set of parameter estimates obtained using the MCECM algorithm, and $\mathcal{I}_{\mathrm{c}}$ and $\mathcal{I}_{\mathrm{m}}$ are the complete data and missing data information matrices, respectively. These matrices are approximated as follows:

$$\mathcal{I}_{\mathrm{c}}(\Theta;\mathbf{y}_o) = -\mathbb{E}\left[\frac{\partial^2}{\partial\Theta\partial\Theta^\top}\ln\mathcal{L}(\Theta;\mathbf{y}_c)\bigg|\mathbf{y}_o,\Theta\right] = -\frac{1}{L}\sum_{l=1}^{L}\frac{\partial^2}{\partial\Theta\partial\Theta^\top}\ln\mathcal{L}(\Theta;\mathbf{y}_c^{(l)}),$$

and

$$\begin{aligned}\mathcal{I}_{\mathrm{m}}(\Theta;\mathbf{y}_o) &= \mathbb{E}\left[\left(\frac{\partial}{\partial\Theta}\ln\mathcal{L}(\Theta;\mathbf{y}_c)\right)\left(\frac{\partial}{\partial\Theta^\top}\ln\mathcal{L}(\Theta;\mathbf{y}_c)\right)\bigg|\mathbf{y}_o,\Theta\right]\\ &\quad - \mathbb{E}\left[\frac{\partial}{\partial\Theta}\ln\mathcal{L}(\Theta;\mathbf{y}_c)\bigg|\mathbf{y}_o,\Theta\right]\mathbb{E}\left[\frac{\partial}{\partial\Theta^\top}\ln\mathcal{L}(\Theta;\mathbf{y}_c)\bigg|\mathbf{y}_o,\Theta\right]\\ &= \frac{1}{L}\sum_{l=1}^{L}\frac{\partial}{\partial\Theta}\ln\mathcal{L}(\Theta;\mathbf{y}_c^{(l)})\frac{\partial}{\partial\Theta^\top}\ln\mathcal{L}(\Theta;\mathbf{y}_c^{(l)})\\ &\quad - \left(\frac{1}{L}\sum_{l=1}^{L}\frac{\partial}{\partial\Theta}\ln\mathcal{L}(\Theta;\mathbf{y}_c^{(l)})\right)\left(\frac{1}{L}\sum_{l=1}^{L}\frac{\partial}{\partial\Theta^\top}\ln\mathcal{L}(\Theta;\mathbf{y}_c^{(l)})\right),\end{aligned}$$

where each $\mathbf{y}_c^{(l)} = (\mathbf{y};\mathbf{z};\mathbf{\Gamma}_l)$, with $\mathbf{\Gamma}_l$ representing draws from the conditional distribution of the spatial random effect (missing data) given the observed data and the parameter $\hat{\Theta}$ estimated via MCECM. At the MCECM estimate $\hat{\Theta}$, the average score function across the Monte Carlo samples satisfies:

$$\frac{1}{L}\sum_{l=1}^{L}\frac{\partial}{\partial\Theta}\ln\mathcal{L}(\Theta;\mathbf{y}_c^{(l)})\bigg|_{\Theta=\hat{\Theta}} = 0,$$

which simplifies the observed information matrix to:

$$\mathcal{I}_{\mathrm{o}}(\hat{\Theta};\mathbf{y}_o) = -\frac{1}{L}\sum_{l=1}^{L}\frac{\partial^2}{\partial\Theta\partial\Theta^\top}\ln\mathcal{L}(\hat{\Theta};\mathbf{y}_c^{(l)}) - \frac{1}{L}\sum_{l=1}^{L}\left(\frac{\partial}{\partial\Theta}\ln\mathcal{L}(\hat{\Theta};\mathbf{y}_c^{(l)})\right)\left(\frac{\partial}{\partial\Theta^\top}\ln\mathcal{L}(\hat{\Theta};\mathbf{y}_c^{(l)})\right).$$

The variance-covariance matrix of $\hat{\Theta}$ is obtained by inverting the observed information matrix, with the diagonal elements corresponding to the variances of the parameter estimates.

2.6 Goodness of Fit

Goodness of fit measures how well a statistical model matches observed data, summarizing the difference between actual and predicted values [21]. Let $\tilde{E}(t,z)$ represent the number of exposed individuals at time t in region z. Assuming that $S(t,z)$ is independent for all $t = 1,\dots,T$ and $z = 1,\dots,Z$, hence

$$\tilde{E}(t,z) \sim \text{Binomial}\left(S(t,z), \mathcal{P}_{(t,z)}(\Theta)\right), \qquad t = 1,\dots,T \quad \text{and,} \quad z = 1,\dots,Z,$$

where

$$\mathcal{P}_{(t,z)}(\Theta) = \frac{1}{N_z}\sum_{i=1}^{N_z} \mathcal{P}_{(i,t,z)}(\Theta), \tag{2.6.1}$$

represents the average infectivity rate, $S(t,z)$ is the number of susceptible individual units at time t in region z, and N_z is the population size of region z. Additionally, let $E(t,z)$ denote the actual number of exposed individuals at time t in region z and $\mathbb{E}\{\tilde{E}(t,z)\} = S(t,z)\mathcal{P}_{(t,z)}(\Theta)$ represents the expected value of the $\tilde{E}(t,z)$. This value can be determined as the number of infectious individuals at time $(t-\nu_E)$ in region z. Assuming the null hypothesis that the number of exposed individuals at time t in region z follows the specified binomial distribution, we use Pearson's chi-square test [74] with $T-1$ degrees of freedom for each region z with the following test statistic;

$$\chi_z^2 = \sum_{t=1}^{T} \frac{[E(t,z) - \mathbb{E}\{\tilde{E}(t,z)\}]^2}{\mathbb{E}\{\tilde{E}(t,z)\}}.$$

It is important to note that this framework may not provide a comprehensive assessment of model adequacy. Alternative goodness of fit measures and model evaluation strategies could be further explored to more thoroughly assess the performance of GD-ILMs, particularly given their complexity and stochastic structure. Nevertheless, the primary intention here is not to conduct an exhaustive model validation, but rather to provide a rough diagnostic evaluation of whether the proposed model captures the observed exposure patterns reasonably well.

2.7 Application: TB in Manitoba

This study utilized administrative daily health records of TB in Manitoba, Canada, from 2011 to 2018, provided by Manitoba Health. The individual level dataset includes information such as birth date, recorded biological sex, date of diagnosis, and 6-digit residential postal codes, with scrambled personal health identification numbers for confirmed TB cases.

We consider the geographical classification of Manitoba defined by MCHP and Manitoba Health for the allocation of health districts and neighborhood clusters based on municipality and postal codes [3]. Figures 2.1a and 2.1b present the incidence rate of TB in Manitoba and Winnipeg.

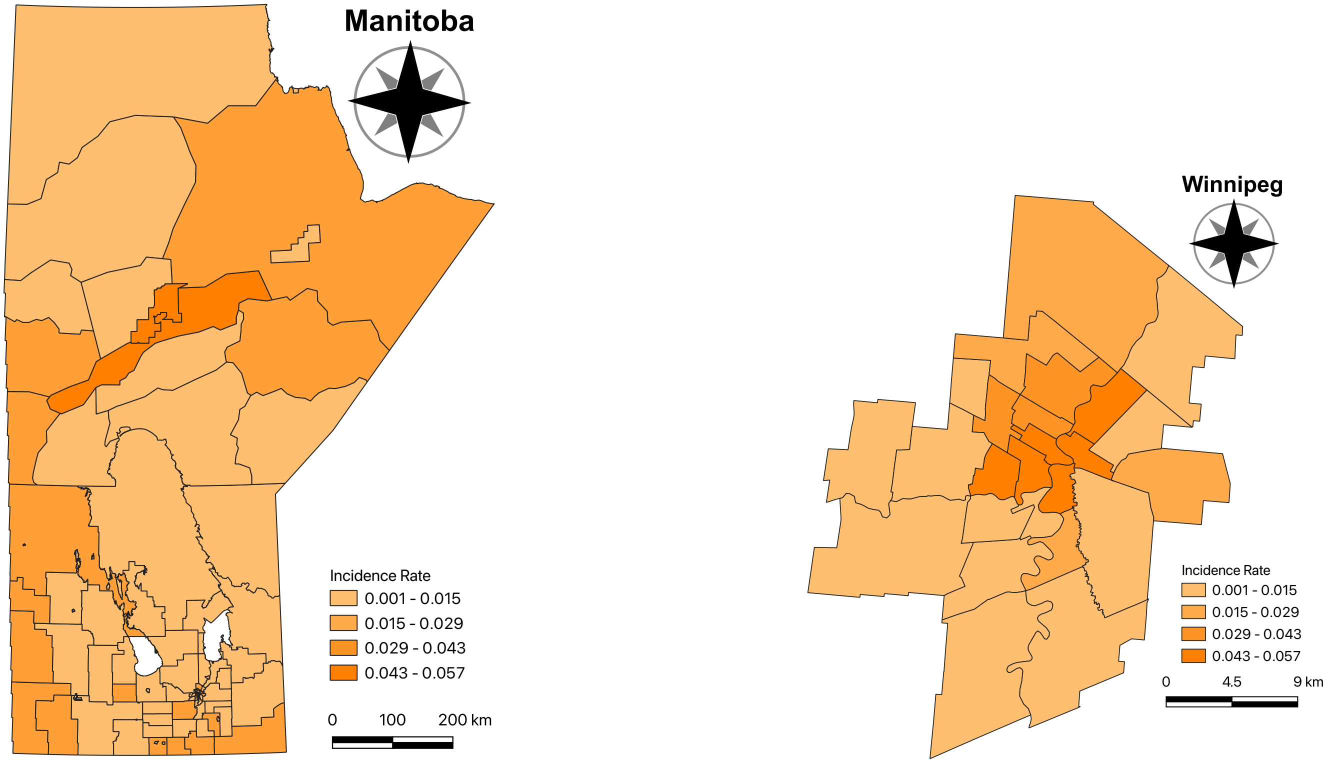

(a) Manitoba

(b) Winnipeg

Figure 2.1: Incidence rate of TB in Manitoba and Winnipeg from 2011 to 2018

The SEIRS model described in the Methods section was used to analyze TB disease patterns within HADs and across Manitoba. Model parameters were estimated using the Nelder-Mead algorithm [68]. The Nelder-Mead algorithm is a widely used optimization technique for maximum likelihood estimation, particularly when the objective function is non-differentiable or challenging to differentiate. It works by iteratively modifying a set of points, known as a simplex, to find the optimal parameter values that minimize (or maximize) the objective function, which in the case of maximum likelihood estimation, is the negative log-likelihood. The algorithm refines the simplex through processes such as reflection, expansion, and contraction, moving closer to the solution with each iteration. In Table 2.2, results from the fitted SEIRS model highlighted variations in transmission rates, and latent, infectious, and immunity periods across different HADs, indicating diverse disease dynamics. Reinfection rates (loss of immunity) in Manitoba and its five HADs show notable regional differences and variations in susceptibility to reinfections. The overall reinfection rate for Manitoba is 6.26%, with rates differing across its five HADs: the Interlake HAD has a rate of 5.26%, Northern 7.64%, Prairie 14%, Southern 6.25%, and Winnipeg 5.11%. These discrepancies highlight the regional variations in reinfection rates throughout Manitoba. The variation in the parameters presented in Table 2.2 across different HADs reflects the diverse epidemiological and demographic characteristics of these regions. Differences in the contact rate η may indicate varying levels of interaction and exposure among individuals within each district, influenced by factors such as population density, social behavior, and healthcare access. The latent period ν_E and infectious period ν_I vary likely due to regional differences in healthcare infrastructure, disease surveillance, and early detection practices, which may affect the duration of latent and active TB phases. Additionally, the immunity period ω differs across regions, likely due to varying rates of reinfection, vaccination coverage, and overall immunity within the populations. These regional disparities suggest that the dynamics of TB transmission are not uniform across Manitoba, making it inappropriate to apply a single GD-ILM

Table 2.2: Results of fitted SEIRS model for Manitoba and its five HADs

District	**Interlake**	**Northern**	**Prairie**	**Southern**	**Winnipeg**	**Manitoba**
Contact Rate η	0.040	0.051	0.048	0.083	0.019	0.025
Latent Period ν_E (days)	26	21	20	17	45	34
Infectious Period ν_I (days)	57	36	66	21	62	44
Immunity Period ω (days)	456	569	729	457	618	595

SEIRS to the entire province.

Given the unique characteristics of TB, which follows the SEIRS framework, we utilize our proposed GD-ILM SEIRS to analyze the TB data. Moreover, due to variations between each HAD in factors such as the duration of latent, infectious, and immunity periods, reinfection rates, and the availability of both individual and regional data, we apply the GD-ILM SEIRS separately to each HAD. We estimate the parameters using the MCECM method presented in Algorithm 1, with a convergence threshold of $\epsilon_{\Theta} = 10^{-3}$. This value ensures that parameter estimates reach a stable solution while preventing unnecessary computational expenses. In this study, we treated RHADs as regional units and PCRs as individual units, allowing for a model with a high-resolution analysis. For each TB case within a PCR, we utilized two individual level covariates related to infectivity to incorporate in (2.3.2): the proportion of males and the proportion of individuals aged over 60 years, as both are considered risk factors for TB. Each TB case was assigned to one of Manitoba's RHADs based on the 6-digit residential postal code, using the Postal Code Conversion File (PCCF) provided by Manitoba Health. We estimated the average population size of each PCR by taking the population size of the Dissemination Area (DA) from the 2016 Canadian Census dataset and dividing it by the number of PCRs within each DA, as provided in the PCCF. The two individual level covariates related to infectivity within a PCR were obtained by utilizing data on the proportion of males and the proportion of individuals aged over 60 years for each DA from the 2016 Canadian Census dataset, along with the count of PCRs within each DA as documented in the PCCF. By merging the Census and PCCF datasets, we could estimate the proportion of males and individuals aged over 60 years in each PCR. We aimed to investigate the geographical variation in susceptibility risk factors for TB and examine their association with regional indicators, including Socio-Economic Status (SES) and the prevalence of Sexually Transmitted Infections (STIs), for inclusion in (2.3.1). We utilized a SES factor score developed by [7], which is based on four census variables (income, unemployment, education, and single-parent households) at the RHAD level. The SES factor scores were standardized through principal component analysis conducted on these specific variables, where a higher SES factor score corresponds to lower income, higher unemployment rates, lower educational attainment, and a higher proportion of single-parent households. The SES factor scores of RHADs within each HAD are depicted in Figures 2.2, 2.3a, 2.3b, 2.4a, and 2.4b. Administrative daily health records of STIs at the individual level for the province of Manitoba from 2011 to 2016 were obtained from Manitoba Health. STI cases were categorized into one of Manitoba's RHADs based on their 6-digit residential postal code using Manitoba Health's PCCF. This allowed us to determine the STI rate within each RHAD. The distance d_{ij} between PCRs i and j was determined using the Euclidean distance metric.

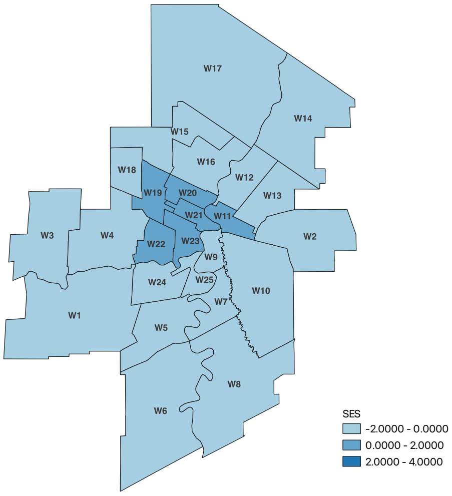

Figure 2.2: SES factor score across RHADs in Winnipeg HAD

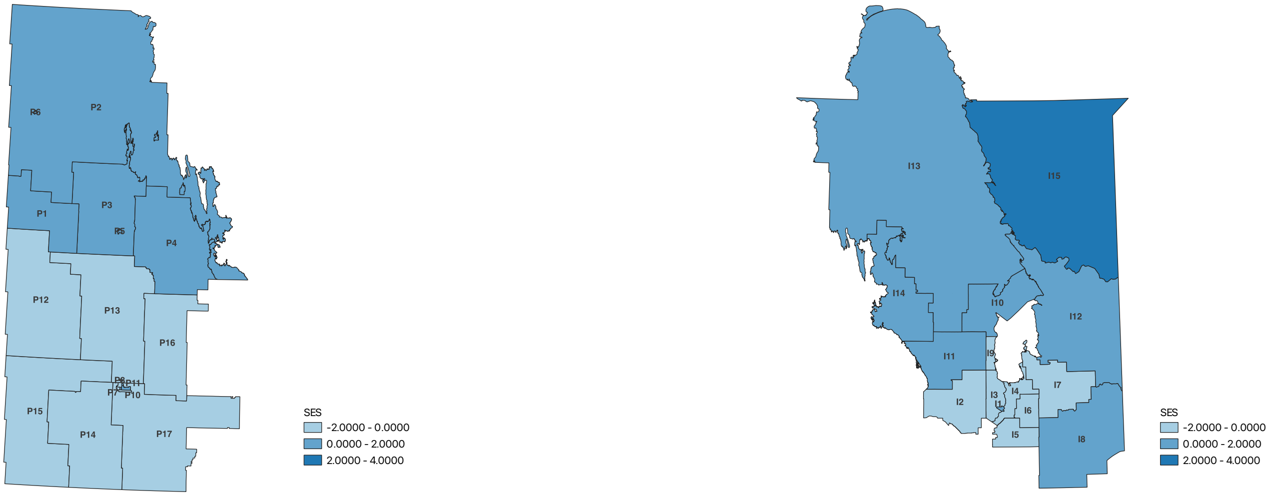

(a) Prairie

(b) Interlake

Figure 2.3: SES factor score across RHADs in Prairie and Interlake HADs

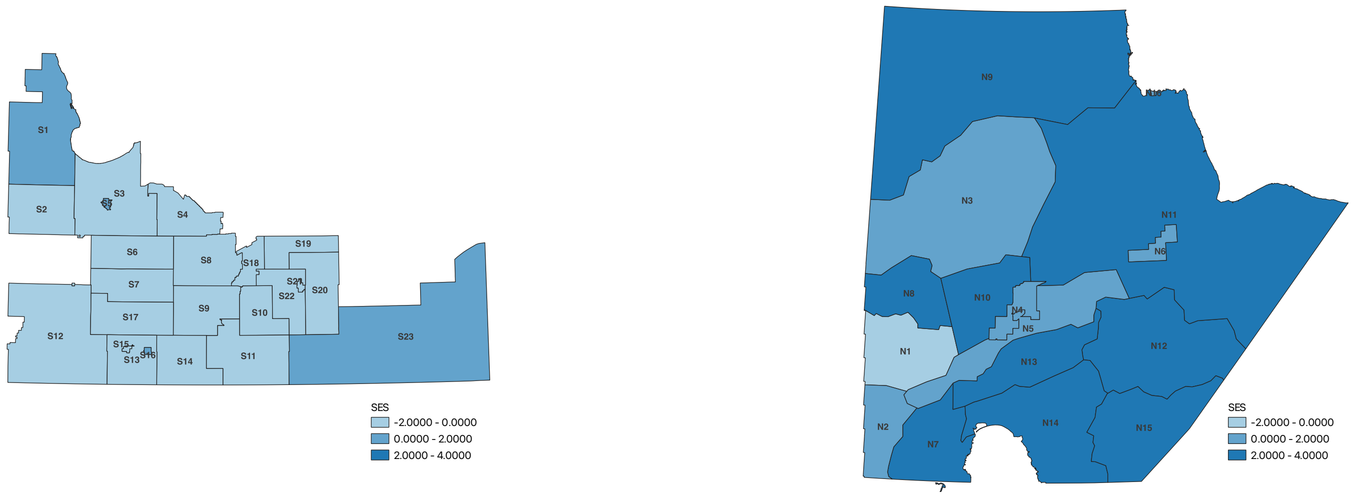

(a) Southern

(b) Northern

Figure 2.4: SES factor score across RHADs in Southern and Northern HADs

Table 2.3: Parameter estimates (Est.) and their standard errors (S.E.) for the GD-ILM SEIRS fitted to Manitoba's five HADs

	Interlake		**Northern**		**Prairie**		**Southern**		**Winnipeg**	
Parameter	Est.	S.E.	Est.	S.E.	Est.	S.E.	Est.	S.E.	Est.	S.E.
Susceptibility										
$\alpha_{S^{\Psi\cup\Phi}}$	-2	$4.21e^{-5}$	-2	$4.51e^{-5}$	-1	$3.15e^{-5}$	-2	$4.01e^{-5}$	-2	$7.24e^{-6}$
Initial Infection										
SES	1.783	$6.85e^{-5}$	2.082	$7.86e^{-6}$	2.345	$5.68e^{-6}$	3.288	$1.82e^{-5}$	1.863	$7.55e^{-5}$
STI Rate	1.872	$2.54e^{-5}$	2.073	$4.85e^{-5}$	2.152	$6.76e^{-6}$	1.383	$5.86e^{-5}$	2.267	$3.45e^{-5}$
Reinfection										
SES	1.825	$5.58e^{-5}$	2.125	$6.75e^{-6}$	2.278	$4.75e^{-5}$	2.042	$2.70e^{-5}$	2.425	$7.53e^{-6}$
STI Rate	2.465	$3.85e^{-6}$	2.543	$3.74e^{-5}$	2.763	$6.78e^{-6}$	2.453	$7.15e^{-5}$	2.533	$5.42e^{-5}$
Infectivity										
α_T	-1	$4.52e^{-6}$	-2	$2.78e^{-6}$	-2	$4.42e^{-6}$	-1	$7.27e^{-5}$	-2	$5.23e^{-5}$
Male Rate	0.523	$3.42e^{-5}$	0.657	$4.31e^{-5}$	0.732	$5.45e^{-5}$	0.563	$3.35e^{-6}$	0.852	$5.53e^{-5}$
Age 60+	0.852	$5.23e^{-6}$	0.883	$3.52e^{-6}$	0.785	$3.53e^{-5}$	0.812	$1.21e^{-6}$	0.772	$5.36e^{-5}$
Spatial										
δ	2.564	$4.42e^{-5}$	2.253	$6.45e^{-5}$	2.756	$7.86e^{-6}$	2.357	$1.41e^{-6}$	2.138	$2.52e^{-6}$
τ	0.778	$5.45e^{-6}$	0.723	$2.39e^{-5}$	0.704	$3.45e^{-6}$	0.642	$7.02e^{-6}$	0.778	$7.01e^{-6}$
λ	0.712	$2.23e^{-6}$	0.745	$5.78e^{-5}$	0.812	$5.45e^{-6}$	0.674	$2.75e^{-5}$	0.864	$6.42e^{-5}$

Results

The findings presented in Table 2.3 indicate that individuals residing in HADs, characterized by higher SES (lower income, higher unemployment rates, lower education levels, and a higher prevalence of single-parent households) and increased STI rates, were more prone to both initial TB infections and reinfection.

In terms of initial TB infection risk, HADs with higher SES were associated with an increased risk of initial TB infection, with the most significant effect observed in the Southern HAD (Est.=3.288, S.E.=1.82×10^{-5}). Elevated STI rates were consistently linked to a greater likelihood of initial TB infection, with the strongest impact in the Winnipeg HAD (Est.=2.267, S.E.=3.45×10^{-5}).

Regarding TB reinfection, higher SES was associated with a greater likelihood of reinfection, with the most pronounced effect in the Winnipeg HAD (Est.=2.425, S.E.=7.53×10^{-6}). Likewise, elevated STI rates remained a significant risk factor for TB reinfection, with the strongest association found in Prairie (Est.=2.763, S.E.=6.78×10^{-5}).

In terms of infectivity, both the male population rate and the population aged over 60 showed a positive association with TB infection risk. The impact of the male population rate varied from 0.523 (S.E.=$3.42e^{-5}$) in Interlake to 0.852 (S.E.=$5.53e^{-5}$) in Winnipeg. Additionally, individuals aged over 60 were linked to an increased risk of TB infection, with the highest association observed in the Northern HAD (Est.=0.883, S.E.=$3.52e^{-6}$).

The results indicate strong spatial clustering of TB infection risk, with stable spatial effects across RHADs. The spatial dependence parameter λ, which measures how strongly TB infection risk in one RHAD is correlated with its neighboring RHADs, was significantly high and positive. This suggests that the risk of TB infection tends to cluster geographically, meaning that RHADs with a high-risk of TB infection are surrounded by other high-risk RHADs. The spatial decay parameter δ, which determines how quickly spatial correlation in TB infection risk weakens with distance, was positive, confirming that the influence of one PCR on another decreases as the distance between them increases.

Table 2.3 also shows the estimated parameters of the GD-ILM SEIRS for each of the five HADs within Manitoba. The estimated parameters allow for the computation of TB infection probabilities for every PCR across all time points t and within any RHAD in Manitoba. This capability proves highly advantageous for Manitoba Health and public health authorities, facilitating the formulation of targeted and localized prevention strategies and the implementation of TB infection control measures at an exceptionally detailed geographical level. Applying the goodness of fit test, introduced in Section 2.6, confirmed that the model fits well. This indicates that the model accurately captures the key factors and patterns in TB transmission within each HAD. In the visual representations illustrated in Figures 2.5a and 2.5b, we integrated the average infectivity rate for RHADs in equation 2.6.1. Figure 2.5a demonstrates that central RHADs located within the northern HAD exhibit the highest average rates of infectivity, identifying them as key TB clusters and hotspots. Similarly, Figure 2.5b reveals that both central and northern RHADs in the Winnipeg HAD exhibit elevated average infectivity rates, identifying them as significant TB clusters and high-risk transmission areas.

It is important to acknowledge that unobserved or unmeasured covariates may contribute to variability in the model estimates and outcomes. While the presented results reflect patterns captured from the available data, some inherent uncertainty remains due to potential influences not incorporated in the analysis, such as contextual, behavioral, or environmental factors. Consequently, the findings should be interpreted with caution, recognizing that additional data or covariates could further refine or modify the model's conclusions.

2.8 Simulation Study

2.8.1 Regular Grid

In this study, we conducted simulations to evaluate the effectiveness of our proposed model. We considered PCRs as individual level units distributed across a 10×10 grid, where each grid cell represents a distinct geographic area. The number of PCRs in each grid cell was randomly generated from a $\text{Uniform}(10, 20)$ distribution. The geographic coordinates for the PCRs were systematically assigned as (Latitude, Longitude) pairs ranging from 10 to 100 in steps of 10. Figure 2.6 shows the randomly generated PCRs within grid areas. To simulate the population within each PCR, we randomly assigned the population size using a $\text{Uniform}(10, 100)$ distribution. For PCRs, we considered

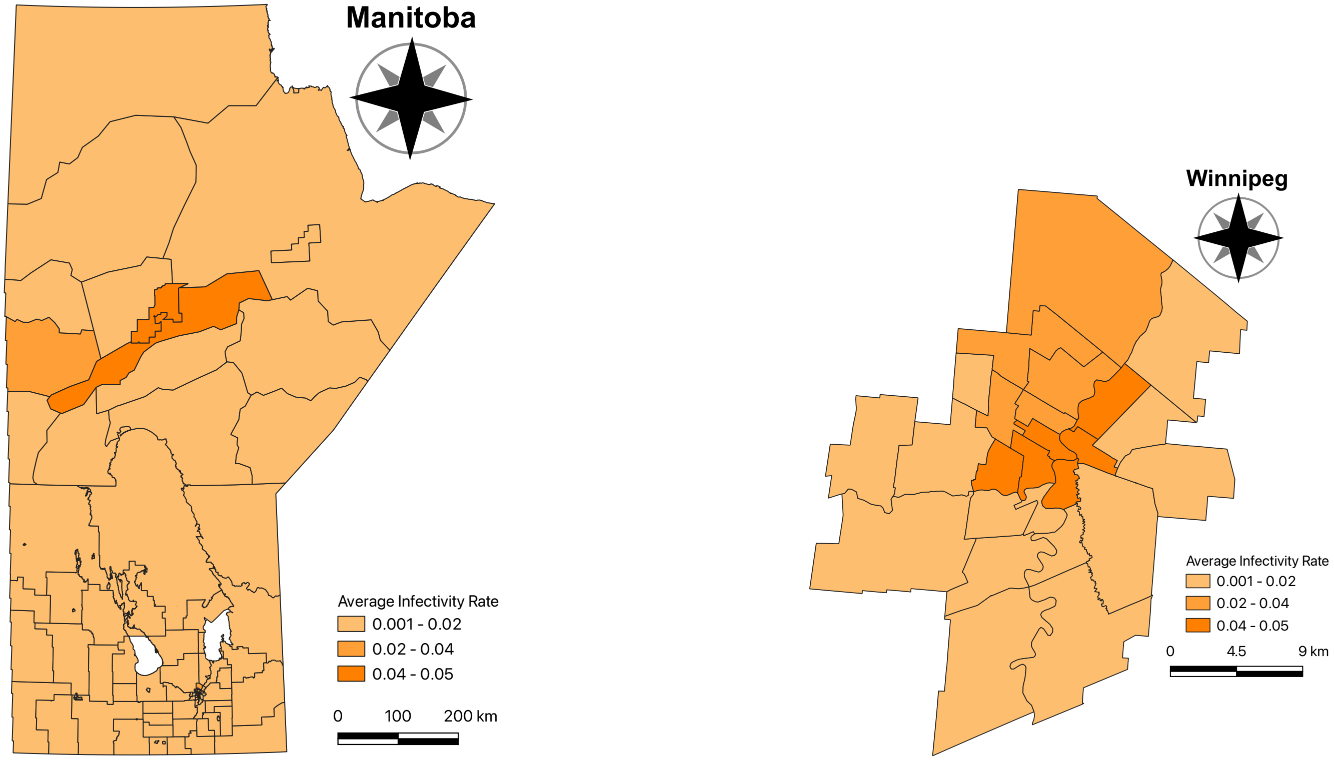

(a) Manitoba

(b) Winnipeg

Figure 2.5: Average infectivity rate of TB in Manitoba and Winnipeg from 2011 to 2018

the number of infected individuals using two different infection rates P_I: 10% and 20% of residents, along with the number of reinfected individuals based on reinfection rates P_R of 5% and 10% of residents. Regional-level covariates X_1 and X_2, sampled from Logistic$(0, 1)$ and Laplace$(0, 1)$ distributions, respectively, were integrated into our model to evaluate susceptibility during the initial infection phase. These covariates continued to be assessed during subsequent reinfections, denoted as X_3 and X_4. Additionally, individual level covariates X_5 and X_6, drawn from $\mathcal{N}(0, 1)$ and Uniform$(0, 1)$ distributions respectively, were included to evaluate their impact on infection transmissibility. The distance d_{ij} between PCRs i and j was determined using the Euclidean distance metric. We generated spatial random effects using a $\mathcal{N}_Z(0, \mathbf{\Sigma_\Gamma})$ distribution, where $\mathbf{\Sigma_\Gamma} = \tau^{-2}\left[(1-\lambda)\,\mathbf{I}_Z + \lambda\mathcal{R}\right]^{-1}$. To incorporate spatial variability, we set the precision parameters $\tau = 0.50$ and spatial dependence $\lambda = 0.80$ to assess the strength of spatial correlation. We conducted simulations with 500 datasets using the GD-ILM SEIRS on a 10×10 grid. Each simulation on the 10×10 grid began with a single PCR randomly exposed in each grid cell at $t = 1$, with latent, infectious, and immunity periods of 6, 8, and 19, respectively, to model the epidemics over $T = 30$ time units.

We then divided the grid into four sub-grids 4×4, 6×4, 4×6, and 6×6. To determine the latent, infectious, and immunity periods, we applied the homogeneous SEIRS model to data generated by our discrete-time GD-ILM SEIRS. We estimated the latent, infectious, and immunity periods separately across the entire 10×10 grid and for each sub-grid. Table 2.4 illustrates that the latent, infectious, and immunity periods vary significantly between sub-grids, differing from those of the entire 10×10 grid. Specifically, the 6×4 sub-grid demonstrated the longest latent period ($\nu_E = 7$), while the 4×6 sub-grid exhibited the shortest latent period ($\nu_E = 4$), both of which differed from the values found in the entire 10×10 grid ($\nu_E = 6$). Likewise, the 6×4 sub-grid displayed the longest infectious period ($\nu_I = 7$), whereas the 4×6 sub-grid showed the shortest infectious period ($\nu_I = 5$), differing from the values observed in the entire 10×10 grid ($\nu_I = 8$). Additionally, the 4×6 sub-grid had the shortest immunity period ($\omega = 15$), in contrast to the 4×4 sub-grid, which exhibited the longest immunity period ($\omega = 21$), differing from the 10×10 grid value ($\omega = 19$). These results indicate that spatial heterogeneity plays a crucial role in disease dynamics. We used the MCECM method presented in Algorithm 1 for estimating the parameters of the GD-ILM SEIRS with a convergence threshold of

$\epsilon_\Theta = 10^{-3}$. Subsequently, we present simulation results based on 500 runs for each sub-grid.

Table 2.4: Rounded latent, infectious, and immunity periods of the grids (days)

Grid	4×4	6×4	4×6	6×6	10×10
Latent Period ν_E	5	7	4	5	6
Infectious Period ν_I	7	9	5	6	8
Immunity Period ω	21	17	15	20	19

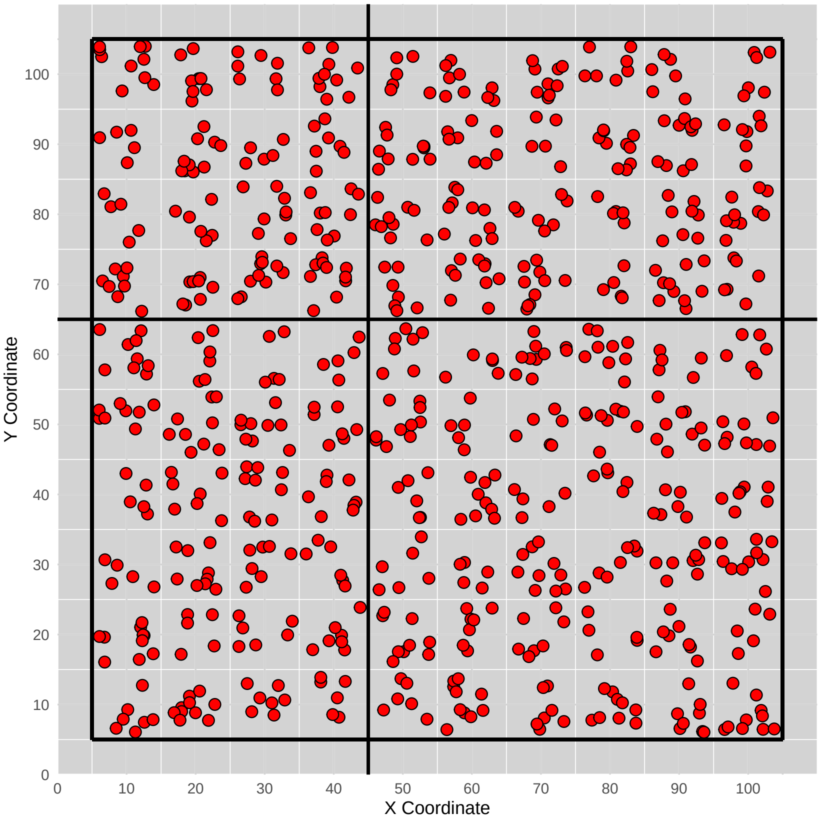

Figure 2.6: Regular grid simulation and generated PCRs within grid areas

Results

The results of our simulation study presented in Tables 2.5 and 2.6 are promising, demonstrating the effectiveness and robustness of our proposed model across various grid configurations and infection scenarios. The average of the parameter estimations was close to the true values, with slight variations depending on the grid size, P_I, and P_R rates. For instance, β_1 was estimated at 1.975, with a Standard Error (S.E.) equal to 0.092 for $P_I = 10\%$ and $P_R = 5\%$ on the 4×4 grid, closely aligning with the

Table 2.5: The results of the epidemic simulation study based on 10 × 10, 4 × 4, and 4 × 6 regular grids

		10 × 10 Grid							
		$P_I = 10\%$, $P_R = 5\%$		$P_I = 10\%$, $P_R = 10\%$		$P_I = 20\%$, $P_R = 5\%$		$P_I = 20\%$, $P_R = 10\%$	
Parameter	True	Est.	S.E.	Est.	S.E.	Est.	S.E.	Est.	S.E.
Susceptibility									
$\alpha_{S^{\Psi\cup\Phi}}$	1	0.976	0.173	1.045	0.0290	0.983	0.161	1.067	0.030
Initial Infection									
β_1	2	2.038	0.092	1.946	0.189	1.975	0.084	2.054	0.183
β_3	2	1.983	0.064	2.042	0.192	2.112	0.069	1.954	0.191
Reinfection									
β_2	2	1.941	0.129	2.058	0.096	1.995	0.125	2.061	0.103
β_4	2	2.073	0.145	2.006	0.142	2.138	0.150	1.985	0.138
Infectivity									
α_T	1	1.054	0.180	0.984	0.054	1.021	0.183	0.947	0.059
β_5	2	1.973	0.046	2.031	0.101	2.084	0.048	1.952	0.098
Spatial									
δ	2.8	2.728	0.067	2.811	0.241	2.765	0.064	2.789	0.244
τ	0.5	0.526	0.004	0.494	0.159	0.508	0.003	0.478	0.162
λ	0.8	0.773	0.085	0.836	0.184	0.811	0.081	0.788	0.181
		4 × 4 Grid							
		$P_I = 10\%$, $P_R = 5\%$		$P_I = 10\%$, $P_R = 10\%$		$P_I = 20\%$, $P_R = 5\%$		$P_I = 20\%$, $P_R = 10\%$	
Parameter	True	Est.	S.E.	Est.	S.E.	Est.	S.E.	Est.	S.E.
Susceptibility									
$\alpha_{S^{\Psi\cup\Phi}}$	1	1.105	0.171	1.089	0.0276	1.092	0.163	1.081	0.029
Initial Infection									
β_1	2	1.975	0.092	2.028	0.187	1.982	0.087	2.037	0.179
β_3	2	2.132	0.064	2.085	0.194	2.141	0.067	2.077	0.189
Reinfection									
β_2	2	2.146	0.129	1.903	0.098	2.153	0.126	1.912	0.104
β_4	2	2.122	0.143	2.107	0.144	2.128	0.147	2.098	0.141
Infectivity									
α_T	1	1.121	0.176	0.980	0.053	1.127	0.181	0.974	0.057
β_5	2	2.119	0.044	2.093	0.099	2.128	0.047	2.102	0.102
Spatial									
δ	2.8	2.740	0.064	2.794	0.236	2.748	0.068	2.787	0.241
τ	0.5	0.469	0.003	0.560	0.158	0.474	0.004	0.555	0.162
λ	0.8	0.899	0.086	0.782	0.183	0.893	0.082	0.789	0.178
		4 × 6 Grid							
		$P_I = 10\%$, $P_R = 5\%$		$P_I = 10\%$, $P_R = 10\%$		$P_I = 20\%$, $P_R = 5\%$		$P_I = 20\%$, $P_R = 10\%$	
Parameter	True	Est.	S.E.	Est.	S.E.	Est.	S.E.	Est.	S.E.
Susceptibility									
$\alpha_{S^{\Psi\cup\Phi}}$	1	1.060	0.140	1.20	0.032	1.090	0.150	1.110	0.037
Initial Infection									
β_1	2	1.890	0.100	2.110	0.150	2.070	0.110	2.090	0.160
β_3	2	2.220	0.090	1.990	0.180	2.190	0.080	1.980	0.175
Reinfection									
β_2	2	2.060	0.130	1.970	0.100	1.960	0.140	2.050	0.090
β_4	2	1.930	0.150	2.240	0.160	1.910	0.60	2.250	0.165
Infectivity									
α_T	1	1.080	0.170	1.050	0.057	1.100	0.180	1.040	0.052
β_5	2	2.010	0.060	2.110	0.120	2.020	0.065	2.120	0.125
Spatial									
δ	2.8	2.720	0.130	2.810	0.220	2.710	0.135	2.820	0.210
τ	0.5	0.510	0.012	0.470	0.150	0.500	0.015	0.460	0.145
λ	0.8	0.870	0.070	0.750	0.170	0.860	0.065	0.760	0.160

Table 2.6: The results of the epidemic simulation study based on 6 × 4 and 6 × 6 regular grids

6 × 4 Grid

		$P_I = 10\%$, $P_R = 5\%$		$P_I = 10\%$, $P_R = 10\%$		$P_I = 20\%$, $P_R = 5\%$		$P_I = 20\%$, $P_R = 10\%$	
Parameter	True	Est.	S.E.	Est.	S.E.	Est.	S.E.	Est.	S.E.
Susceptibility									
$\alpha_{S^{\Psi\cup\Phi}}$	1	1.250	0.125	1.180	0.055	0.980	0.180	1.070	0.045
Initial Infection									
β_1	2	2.180	0.110	1.970	0.210	2.150	0.120	1.950	0.180
β_3	2	2.270	0.140	1.950	0.170	2.190	0.130	2.030	0.160
Reinfection									
β_2	2	1.890	0.115	2.130	0.120	1.950	0.125	2.120	0.110
β_4	2	2.020	0.165	2.230	0.190	2.080	0.155	2.180	0.200
Infectivity									
α_T	1	1.030	0.190	1.150	0.060	1.020	0.200	1.130	0.065
β_5	2	1.910	0.050	2.080	0.130	1.920	0.055	2.060	0.140
Spatial									
δ	2.8	2.600	0.150	2.910	0.250	2.630	0.145	2.870	0.255
τ	0.5	0.540	0.020	0.460	0.130	0.550	0.025	0.470	0.140
λ	0.8	0.720	0.070	0.850	0.160	0.730	0.075	0.860	0.165

6 × 6 Grid

		$P_I = 10\%$, $P_R = 5\%$		$P_I = 10\%$, $P_R = 10\%$		$P_I = 20\%$, $P_R = 5\%$		$P_I = 20\%$, $P_R = 10\%$	
Parameter	True	Est.	S.E.	Est.	S.E.	Est.	S.E.	Est.	S.E.
Susceptibility									
$\alpha_{S^{\Psi\cup\Phi}}$	1	1.130	0.160	1.150	0.034	1.100	0.130	1.140	0.037
Initial Infection									
β_1	2	2.010	0.100	2.040	0.130	2.050	0.090	2.080	0.140
β_3	2	2.240	0.070	2.060	0.150	2.210	0.100	2.070	0.155
Reinfection									
β_2	2	2.030	0.120	1.950	0.105	1.980	0.125	2.030	0.095
β_4	2	2.110	0.140	2.160	0.170	1.920	0.150	2.220	0.160
Infectivity									
α_T	1	1.090	0.160	1.060	0.058	1.120	0.170	1.050	0.055
β_5	2	2.030	0.050	2.090	0.110	2.040	0.055	2.100	0.115
Spatial									
δ	2.8	2.650	0.140	2.870	0.220	2.600	0.135	2.850	0.200
τ	0.5	0.530	0.010	0.480	0.135	0.520	0.012	0.490	0.140
λ	0.8	0.850	0.065	0.770	0.150	0.830	0.070	0.780	0.155

true value of 2. Similarly, the parameters for infectivity, α_T and β_5, and spatial dependence, τ and λ, also showed accurate estimations, indicating the model's ability to capture the underlying dynamics effectively. Particularly, λ was estimated at 0.899 (S.E. = 0.086) for $P_I = 10\%$ and $P_R = 5\%$, indicating a strong spatial correlation. The precision parameter τ was also accurately estimated at 0.469 (S.E. = 0.003) under the same scenario. These findings were consistent across different scenarios. Moreover, the simulation results consistently demonstrated that the latent and infectious periods estimated for the sub-grids differ significantly from the entire 10×10 grid, highlighting the importance of considering spatial heterogeneity in epidemic modeling. The consistent and accurate parameter estimations across multiple configurations and conditions demonstrate the robustness of our proposed model, establishing it as a valuable tool for understanding and managing infectious diseases, especially those characterized by reinfection spread in spatially structured populations.

2.8.2 Irregular Grid

For the irregular grid study, we analyzed epidemic simulation within Winnipeg's 25 RHADs. For this simulation study, we treated RHADs as regional units and PCRs as the individual units. Each simulation involved generating PCRs, where the number of PCRs for each of the 25 RHADs was uniformly sampled from a $\text{Uniform}(10, 30)$ distribution. The latitude and longitude coordinates for each PCR within each RHAD were randomly selected using stratified spatial sampling. Figure 2.7 shows the sampled PCRs within Winnipeg's 25 RHADs. We assumed that each individual has a constant latent period of 5 time units and remains infectious for 7 time units before moving to the removed stage. We generated 1000 epidemic datasets, and for each simulated epidemic, one individual was randomly chosen to be infectious at time $t = 1$, and epidemics lasted over $T = 30$ time units within each Winnipeg's 25 RHADs. The remaining steps were aligned with those of the regular grid simulation study.

Results

The simulation study using irregular grids, detailed in Table 2.7, demonstrates the efficacy of our proposed model in modeling Winnipeg's 25 RHADs. The average of the parameter α_S was estimated

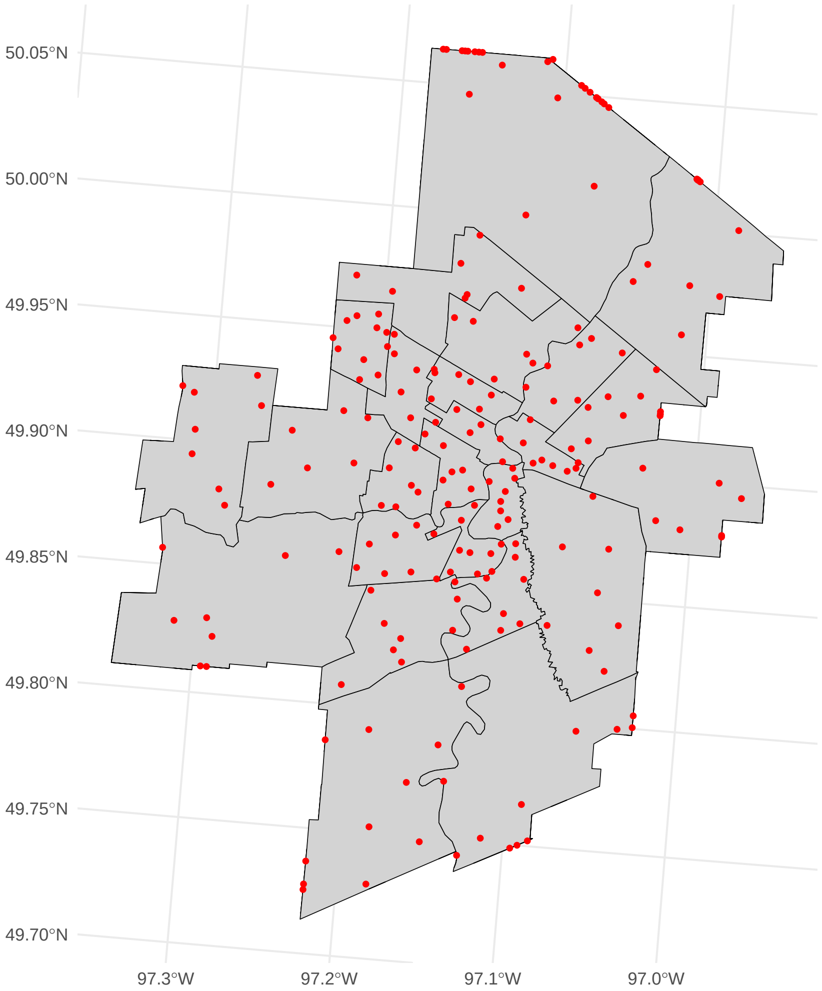

Figure 2.7: Irregular grid epidemic simulation and generated PCRs within Winnipeg's 25 RHADs.

Table 2.7: The results of the epidemic simulation study based on the Winnipeg's 25 irregular RHADs.

		$P_I = 10\%$, $P_R = 5\%$		$P_I = 10\%$, $P_R = 10\%$		$P_I = 20\%$, $P_R = 5\%$		$P_I = 20\%$, $P_R = 10\%$	
Parameter	True	Est.	S.E.	Est.	S.E.	Est.	S.E.	Est.	S.E.
Susceptibility									
$\alpha_{S^{\Psi \cup \Phi}}$	1	1.080	0.150	1.090	0.029	1.090	0.140	1.120	0.035
Initial Infection									
β_1	2	1.970	0.110	2.030	0.160	2.060	0.100	2.070	0.130
β_3	2	2.120	0.080	2.050	0.160	2.230	0.090	2.040	0.170
Reinfection									
β_2	2	2.050	0.140	1.980	0.110	1.950	0.120	2.020	0.100
β_4	2	2.000	0.160	2.140	0.150	1.900	0.130	2.180	0.140
Infectivity									
α_T	1	1.110	0.180	1.040	0.050	1.100	0.160	1.020	0.052
β_5	2	2.030	0.070	2.100	0.100	2.050	0.060	2.090	0.105
Spatial									
δ	2.8	2.700	0.140	2.850	0.240	2.690	0.150	2.860	0.230
τ	0.5	0.510	0.015	0.470	0.140	0.490	0.010	0.460	0.135
λ	0.8	0.880	0.050	0.770	0.160	0.840	0.060	0.780	0.145

with high precision, yielding values of 1.080 (S.E. = 0.150) for $P_I = 10\%$ and 1.090 (S.E. = 0.029) for $P_R = 5\%$ and $P_R = 10\%$. The averages of the estimations for susceptibility parameters during the initial infection phase, β_1 and β_3, and the reinfection phase, β_2 and β_4, were also close to their true values. Specifically, β_1 was estimated at 1.970 (S.E. = 0.110) and 2.030 (S.E. = 0.160) under varying infection and reinfection rates, while β_3 ranged from 2.120 (S.E. = 0.080) to 2.050 (S.E. = 0.160). Similarly, the average of the estimates for β_2 and β_4 was within acceptable ranges, with the values of 2.050 (S.E. = 0.140) and 2.000 (S.E. = 0.160), respectively.

The parameters related to infectivity, α_T and β_5, as well as the spatial dependence parameters, τ and λ, were accurately estimated across different infection and reinfection scenarios. These results affirm the robustness and applicability of our method, showing consistent and reliable performance across various configurations, infections, and reinfection scenarios. The results highlight the proposed model's effectiveness for real-world epidemic modeling in spatially heterogeneous environments, especially in scenarios involving reinfection.

2.9 Discussion

The study introduces a novel approach, the GD-ILM SEIRS, which uniquely addresses the complexities of infectious disease dynamics, particularly focusing on reinfection scenarios within spatially structured populations. This model categorizes the susceptible population into distinct groups based on infection history, distinguishing between susceptibility to initial infection for those who have never contracted the infection and susceptibility to reinfection for those who have regained susceptibility after a period of immunity. This distinction is crucial in understanding the varying susceptibility and transmission dynamics observed across different spatial configurations, as demonstrated in both regular and irregular grid simulations.

The analysis of TB infection patterns within Manitoba's HADs reveals distinct risk factors associated with both initial infection and reinfection. The study reveals that RHADs characterized by lower socioeconomic status and elevated STI rates exhibit increased vulnerability to TB. Additionally, demographic factors such as age over 60 and being born male are significantly associated with increased infectivity within PCRs across RHADs. The spatial dependency observed between RHADs within each HAD underscores the critical role of localized transmission dynamics, reinforcing the need for geographically targeted prevention and control strategies.

By introducing the GD-ILM SEIRS, this research advances the understanding of TB transmission and reinfection in spatially structured populations. The model distinguishes between individuals susceptible to initial infection and those vulnerable to reinfection, offering a refined perspective on immunity waning and reinfection risks. Capturing spatial heterogeneity at a fine geographic scale enhances the model's utility for public health authorities, facilitating precise resource allocation and intervention planning. The ability to compute infection probabilities across RHADs enables health officials to optimize screening, diagnostic, and treatment services, particularly in high-risk areas. These findings provide policymakers with a data-driven foundation for addressing health disparities, improving healthcare accessibility in underserved regions, and advocating for more equitable public health policies.

The study underscores the importance of integrating spatial modeling tools in public health planning, illustrating how the GD-ILM SEIRS can contribute to real-time adjustments in TB control strategies based on geographic transmission patterns. Validation of the model across both regular and irregular spatial grids confirms its robustness and adaptability to real-world epidemiological settings. In addition to its methodological contributions, this research highlights the importance of public health campaigns focused on high-risk groups, particularly individuals over 60 years old, males, and communities with a historically high prevalence of TB, as demonstrated by the TB application in this study. Moreover, healthcare providers can use these insights to enhance patient education on reinfection risks, adherence to treatment, and the importance of regular follow-ups.

This study provides a comprehensive framework for understanding and mitigating TB transmission in Manitoba. By identifying high-risk regions and vulnerable populations, while introducing a novel modeling approach to analyze reinfection dynamics, this research contributes to the development of more effective, spatially informed TB control strategies. The findings have direct implications for public health authorities, policymakers, healthcare providers, and the general public, offering a foundation for targeted interventions that aim to reduce transmission rates and improve health outcomes across the province.

An important limitation of the present study relates to the distinction between true reinfection and cases resulting from treatment failure. Our analysis classifies recurrent TB cases as reinfections based on available data; however, some of these cases may, in fact, reflect incomplete or unsuccessful treatment. This limitation should be considered when interpreting the results, as it introduces potential uncertainty in the estimates of susceptibility to reinfection and may affect the inferred transmission dynamics. Future studies with access to detailed treatment outcomes could help disentangle reinfection from treatment failure, providing a more precise understanding of TB dynamics in spatially structured populations.

Simulations across various grid sizes revealed significant spatial heterogeneity in the latent and infectious periods, highlighting how spatial granularity affects disease spread dynamics. For instance, sub-grid configurations exhibited prolonged infectious periods compared to the overall grid averages, illustrating spatial variations in disease transmission dynamics. Parameter estimations for susceptibility, infectivity, and spatial dependence consistently aligned closely with the true values across different scenarios, emphasizing the model's robustness in capturing real-world epidemic dynamics.

In the context of Winnipeg's RHADs, our irregular grid simulations further validated the model's effectiveness in heterogeneous spatial settings. The study identified varying levels of susceptibility and transmission dynamics across different RHADs, reflecting the real-world complexities of spatially structured populations. Parameters for susceptibility and for infection and reinfection phases exhibited consistent estimates, indicating the model's ability to adapt to diverse geographic and demographic conditions.

Evaluation of the model revealed no identifiability issues, a common concern in complex infectious disease frameworks. This was supported by simulation studies, where the GD-ILM SEIRS parameters were consistently and accurately estimated, with low standard errors across replications. These results demonstrate that the model is both identifiable and stable, highlighting its reliability for examining TB transmission and reinfection dynamics. Because the theoretical distribution of the parameter estimates is not available in this framework, traditional confidence intervals cannot be constructed, and standard inferential approaches for quantifying uncertainty are not applicable.

To promote accessibility and reproducibility, we have developed the `GDILM.SEIRS` R package [1], which is publicly available on CRAN. This package implements the GD-ILM with reinfection framework (GD-ILM SEIRS) and offers a comprehensive suite of tools for likelihood-based parameter estimation via the MCECM algorithm, model assessment using AIC, and flexible simulation studies that can be adapted to diverse research objectives.

Overall, this study demonstrates the effectiveness of the GD-ILM SEIRS in capturing the complexities of infectious disease transmission, particularly by incorporating reinfection dynamics within spatially structured populations. By accounting for spatial heterogeneity, demographic risk factors, and localized transmission patterns, the model provides a comprehensive framework for understanding disease spread and immunity waning. Its validation across various spatial configurations reinforces its adaptability to real-world epidemiological settings, making it a valuable tool for epidemic management, control strategies, and public health decision-making.

3

Spatial Individual-Level Models for Transmission Dynamics of Seasonal Infectious Diseases

This chapter includes the manuscript that has been accepted for publication in *Statistics in Medicine*. It is reproduced here largely in its original form, with only slight formatting modifications to ensure consistency within the thesis. Reproduction is made with permission from the publisher.

3.1 Introduction

Infectious diseases often exhibit patterns that repeat annually, with changes in case frequency or disease intensity occurring at regular intervals throughout the year [67, 27, 32]. These recurring patterns may arise from a combination of ecological, biological, and social factors [67, 27, 32]. Pathogens may circulate more actively during certain times of the year, particularly in regions where climatic shifts between seasons are pronounced. These temporal fluctuations are frequently aligned with environmental conditions, such as temperature, humidity, and precipitation levels. Seasonal light exposure can also modulate physiological processes in humans, potentially altering immune responses and vulnerability to infection [67, 27, 32]. Importantly, each acute infectious disease tends to follow its own seasonal window of occurrence; a window that may vary substantially across geographic regions and even differ among co-circulating diseases within the same location. This variation reflects how local environmental conditions, population behaviors, and pathogen-specific factors interact to shape seasonal transmission dynamics [67, 27, 32]. Human activity, shaped both by climate and cultural norms, further contributes to these temporal trends. Periods of increased indoor contact during colder months, large-scale population movements linked to holidays or school terms, and the seasonal use of heating or cooling systems can all create opportunities for disease transmission. Notably, some behaviors are linked to specific times of the year for cultural or social reasons, independent of weather or climate [67, 27, 32].

Given the complexity and multifactorial nature of seasonal influences, modeling seasonality is essential for understanding and predicting disease dynamics. Accurate models that incorporate seasonal variation enable researchers and public health officials to anticipate the timing and magnitude of outbreaks, assess the potential impact of interventions, and optimize the allocation of preventive resources. Without accounting for these cyclical patterns, models may misrepresent transmission processes, leading to under- or overestimation of risk during key periods of the year. As such, integrating seasonality into infectious disease models enhances both scientific insight and the effectiveness of time-sensitive public health strategies.

Seasonality is well studied in the compartmental framework of infectious disease modeling, where it is commonly incorporated through time-varying transmission rates, often modeled using periodic functions such as sine or cosine terms [79, 9, 66, 63, 16, 71]. These approaches have been effective in capturing the recurrent nature of outbreaks and in explaining temporal fluctuations in incidence across a wide range of diseases. Incorporating seasonality in compartmental models has also enhanced the evaluation of intervention strategies, such as vaccination timing and resource allocation, by aligning them with periods of heightened transmission. However, such seasonal considerations are less commonly integrated into individual-level or spatially explicit models, leaving a gap in capturing fine-scale spatiotemporal patterns of transmission.

The GD-ILM has been effective in modeling infectious diseases but does not incorporate seasonal effects, limiting its ability to capture seasonal trends. Since many infectious diseases exhibit strong seasonal patterns , omitting these effects can result in biased parameter estimates, inaccurate forecasts, and suboptimal intervention planning. Therefore, extending the GD-ILM framework to incorporate seasonality is crucial for enhancing its realism and predictive accuracy. This extension allows for a more comprehensive understanding of temporal dynamics and improves its utility in public health decision-making.

This chapter presents a novel method to introduce and incorporate seasonality within the GD-ILM framework, specifically constructed based on a SEIR model. In this study, we extend the GD-ILM by introducing a seasonally varying transmission component, allowing the model to account for periodic fluctuations in infection risk. Our approach integrates a seasonally forced infection kernel to model periodic changes in transmission rates. For parameter estimation of our specified model and to address computational challenges, we employ the MCECM algorithm, which ensures reliable and robust estimation in complex settings. By accounting for seasonality, this study improves the robustness, accuracy, and practical usefulness of GD-ILMs, thereby increasing their effectiveness for large-scale epidemic analysis and informed public health decision-making. To illustrate the applicability and robustness of our model, we perform Influenza data analysis at a high geographical resolution using administrative individual-level data, along with simulation studies. These analyses emphasize the model's potential for practical and effective disease control and prevention. To enhance reproducibility and enable broader applicability, we developed the `SeasEpi` R package [2] that is publicly available on CRAN, which implements the seasonal GD-ILM framework. The package facilitates likelihood-based parameter estimation via the MCECM algorithm, supports model selection through the Akaike Information Criterion (AIC), and allows for the design and execution of customized simulation studies. These features make `SeasEpi` a practical and extensible tool for conducting spatiotemporal analyses of seasonal infectious disease transmission.

The rest of this chapter is structured as follows. Section 3.2 introduces the seasonal GD-ILM. Section 3.3 describes its specifications and the corresponding likelihood function. Section 3.4 outlines the parameter estimation procedure using the MCECM algorithm and discusses inference. Section 3.5 focuses on the inference for the variances of the estimated seasonal GD-ILM parameters. Section 3.6 presents a simulation study to assess the proposed method, while Section 3.7 illustrates its application to Influenza data. Finally, Section 3.8 concludes with a summary of the main findings and final remarks.

3.2 Seasonal GD-ILM

We aim to incorporate seasonal patterns and their influence on disease transmission into the discrete-time GD-ILM framework within the SEIR model. Specifically, we propose enhancing the model's infection probability components by integrating a seasonal adjustment. By embedding this adjustment, the infection probability can be dynamically modified over time in interaction with other factors already present in the GD-ILM.

The susceptibility and infectivity functions, $\Upsilon_S(i,z)$ and $\Upsilon_T(j,z)$, primarily capture relatively stable or slowly changing intrinsic characteristics, such as age, sex, and other demographic factors. While some of these may exhibit minor seasonal variations, they are not well suited to capturing rapidly changing periodic trends. Their main role is to reflect static or long-term individual or regional vulnerability and infectivity.

The spatial kernel function $\kappa(i,j)$, a core component of both the ILM and GD-ILM, quantifies how spatial proximity between an infectious individual j and a susceptible individual i affects the probability of disease transmission. It is typically modeled as $\kappa(i,j) = f(d_{ij})$, where d_{ij} denotes the spatial distance between the two individuals. Common functional forms include exponential decay or inverse distance functions, which reflect the well-established epidemiological principle that transmission likelihood decreases as the spatial distance between individuals increases. This captures local interactions and spatial heterogeneity in transmission risk, allowing the model to represent how the disease spreads through geographical space. However, while spatial kernels implicitly account for the geography of transmission and interaction, they lack an explicit temporal component and do not model time-dependent factors that influence the intensity and likelihood of transmission between individuals, even if their spatial configuration remains constant. Among the most critical of these factors is seasonality, which influences both susceptibility and infectivity. These effects include environmental conditions, social behaviors, and pathogen characteristics that fluctuate throughout the year. For example, winter conditions may increase transmission due to more indoor interactions, whereas summer conditions might reduce the risk, even with similar spatial proximities, because of increased outdoor activity and better ventilation. As such, two individuals at the same spatial distance may have vastly different transmission risks depending on the time of year, emphasizing the inadequacy of a purely spatial kernel in dynamic, real-world settings. Incorporating seasonality into the infection kernel thus allows the model to represent more accurately the complex interaction between space and time in infectious disease transmission.

To address this limitation, we propose enhancing the infection kernel in the GD-ILM by incorporating both temporal (seasonal) variations and spatial interactions. Specifically, we define a spatiotemporal infection kernel $\kappa(i,j,t)$ as the product of separate spatial and temporal kernels:

$$\kappa(i,j,t) = \kappa(i,j) \times \kappa(t),$$

where $\kappa(t)$ is a temporal kernel that captures temporal dynamics, such as seasonal fluctuations. The temporal kernel may take the form of a periodic function (e.g., sinusoidal or Fourier-based) or use season-specific coefficients to modulate existing terms. This approach enables the GD-ILM to model spatiotemporal transmission dynamics more flexibly and realistically. Therefore, in the seasonal GD-ILM framework, the probability that a susceptible individual i in region z becomes newly exposed during the time interval $[t, t+1)$ is denoted by $\mathcal{P}_{(i,t,z)}(\Theta)$, and is given by:

$$\mathcal{P}_{(i,t,z)}(\Theta) = 1 - \exp\left[\left\{-\Upsilon_S\left(i,z\right) \sum_{j \in I(t,z,\zeta(z))} \Upsilon_T\left(j,z\right)\kappa\left(i,j,t\right)\right\} + \epsilon\left(i,t,z\right)\right],$$

for $t = 1,\ldots,T$ and $z = 1,\ldots,Z$. To effectively represent the estimated probabilities $\mathcal{P}_{(i,t,z)}(\Theta)$, it is essential to aggregate these probabilities across all individuals i for each region. We define the average infectivity rate for region z at time t as

$$\mathcal{P}_{t,z}(\Theta) = \frac{1}{N_z}\sum_{i=1}^{N_z} P_{(i,t,z)}(\Theta),$$

where N_z denotes the population size of region z.

3.3 Specification of Seasonal GD-ILM Components

Susceptibility

We define the susceptibility and transmissibility functions, $\Upsilon_S(i,z)$ and $\Upsilon_T(j,z)$, by incorporating both individual-level and regional-level covariates. Let $\mathbf{X}_i$ $(i = 1, \ldots, n)$ denote the covariate vector for the susceptible individual i, and let $\mathbf{X}_{zS}$ $(z = 1, \ldots, Z)$ denote the covariate vector for the region z. These covariates are integrated into the susceptibility function $\Upsilon_S(i,z)$, which captures the likelihood that individual i in region z becomes exposed to the disease. Specifically, the susceptibility function is defined as:

$$\Upsilon_S(i,z) = \exp\left(\alpha_S + \mathbf{X}_i^\top \boldsymbol{\beta}_1 + \mathbf{X}_{zS}^\top \boldsymbol{\beta}_2 + \gamma_z\right), \tag{3.3.1}$$

where α_S is the intercept term representing baseline susceptibility, and $\boldsymbol{\beta}_1$ and $\boldsymbol{\beta}_2$ are vectors of regression coefficients corresponding to the individual- and region-level covariates, respectively. The term γ_z captures unobserved spatial heterogeneity through a random effect associated with region z, accounting for latent geographic variation or unmeasured region-specific factors. This spatial component is typically modeled using a structured random effects approach, such as a CAR models or Gaussian processes, to reflect potential spatial correlation between neighboring regions.

Transmissibility

Due to the absence of detailed individual-level and regional-level information related to infectious individuals in our Influenza dataset, we do not incorporate covariates into the transmissibility function. As a result, the transmissibility function is assumed to be constant across all individuals, time points, and regions and is specified as

$$\Upsilon_T(j,z) = 1.$$

This assumption implies homogeneous infectiousness among all infected individuals, meaning that each contributes equally to the risk of transmission, regardless of their characteristics or location.

Spatiotemporal Kernel

To capture both spatial proximity and temporal variation in transmission dynamics, we define a spatiotemporal kernel that combines distance-based attenuation with a seasonally fluctuating component. The spatial component of the kernel is modeled as an exponential decay function given by

$$\kappa(i, j) = \exp(-\delta d_{ij}),$$

where d_{ij} represents the geographic distance between individuals i and j, and $\delta > 0$ is a decay parameter that controls how rapidly the transmission likelihood decreases with distance. This formulation reflects the intuitive notion that individuals who are geographically closer are more likely to transmit infections to each other.

To account for temporal variation, particularly the seasonal effects commonly observed in infectious diseases such as Influenza, we define a temporal kernel to model periodic fluctuations. This temporal kernel takes the following form

$$\kappa(t) = \exp\left(\zeta_1 \sin\left(\frac{2\pi t}{T_{\text{cycle}}}\right) + \zeta_2 \cos\left(\frac{2\pi t}{T_{\text{cycle}}}\right)\right),$$

where T_{cycle} denotes the length of one full seasonal cycle (e.g., 12 months), and the parameters ζ_1 and ζ_2 regulate the magnitude and phase of seasonal oscillations, respectively. The sine function controls the timing and shape of seasonal fluctuations, while the cosine function adjusts the phase or shift of the seasonal pattern.

By combining these spatial and temporal elements, we define the spatiotemporal kernel as

$$\kappa(i, j, t) = \exp\left(-\delta d_{ij} + \zeta_1 \sin\left(\frac{2\pi t}{T_{\text{cycle}}}\right) + \zeta_2 \cos\left(\frac{2\pi t}{T_{\text{cycle}}}\right)\right). \tag{3.3.2}$$

This formulation adds a periodic adjustment to the kernel and enables it to capture seasonal variations in transmission intensity while maintaining its spatial structure.

Spark Function

For the sake of simplicity in our formulation, we assume that

$$\epsilon(i, t, z) = 0.$$

This assumption implies that there are no additional unobserved stochastic effects contributing to the infection process beyond what is already captured by the model's structured components. In other words, we consider the infection dynamics for individual i at time t in region z to be entirely determined by the specified susceptibility and transmissibility functions, the spatiotemporal kernel, and the observed covariates. By excluding $\epsilon(i, t, z)$, we effectively remove random noise or unexplained variability from the model, consequently focusing on the deterministic interaction of covariates, spatial proximity, and seasonal effects in shaping transmission probability. This assumption is common in early-stage model development or when assessing the explanatory power of key structured terms, though it may later be relaxed to capture residual heterogeneity or to improve model fit in more complex or noisy datasets.

Spatial Random Effect

We adopt the Leroux model [49], a flexible and widely used specification for spatial random effects $\mathbf{\Gamma} = (\gamma_1, \ldots, \gamma_Z)^\top$, as described in Section 1.4.

Specified Model

Building on the model components described earlier, we formally define Model 1 and Model 2 as follows.

Model 1 is defined as the standard GD-ILM without incorporating seasonal effects, and its formulation is given by

$$\textbf{Model 1:} \quad \mathcal{P}_{(i,t,z)}(\Theta) = 1 - \exp\left[-\exp\left(\alpha_S + \mathbf{X}_i^\top \boldsymbol{\beta}_1 + \mathbf{X}_{zS}^\top \boldsymbol{\beta}_2 + \gamma_z\right) \sum_{j \in I(t,z,\zeta(z))} \exp\left(-\delta d_{ij}\right) \right],$$

for $t = 1, \ldots, T$ and $z = 1, \ldots, Z$.

Model 2 represents the seasonal GD-ILM, which specifies the probability that a susceptible individual i in region z becomes newly exposed within the time interval $[t, t+1)$. This probability, denoted by $\mathcal{P}_{(i,t,z)}(\Theta)$, is expressed as:

$$\textbf{Model 2:}\quad \mathcal{P}_{(i,t,z)}(\Theta) = 1 - \exp\left[-\exp\left(\alpha_S + \mathbf{X}_i^\top \boldsymbol{\beta}_1 + \mathbf{X}_{zS}^\top \boldsymbol{\beta}_2 + \gamma_z\right) \textstyle\sum_{j \in I(t,z,\zeta(z))} \exp\left(-\delta d_{ij} + \zeta_1 \sin\left(\frac{2\pi t}{T_{\text{cycle}}}\right) + \zeta_2 \cos\left(\frac{2\pi t}{T_{\text{cycle}}}\right)\right)\right], \tag{3.3.3}$$

for $t = 1, \ldots, T$ and $z = 1, \ldots, Z$.

Likelihood Function

Let $\mathbf{y}_o$ denote the observed response vector and $\mathbf{y}_c = (\mathbf{y}_o; \boldsymbol{\Gamma})$ the complete data. We model the spatial random effect vector $\boldsymbol{\Gamma}$ using the Leroux model [49] and treat $\boldsymbol{\Gamma}$ as latent variables within the MCECM algorithm to estimate the parameters of our proposed model in (3.3.3). Assuming known infection, exposure, and reinfection times, the complete-data likelihood for all infection and non-infection events over the epidemic period across Z regions is given by

$$\begin{aligned}
\mathcal{L}(\Theta; \mathbf{y}_c) =& p(\mathbf{y}|\boldsymbol{\Gamma}) g(\boldsymbol{\Gamma}) \\
=& \prod_{t=1}^{T} \prod_{z=1}^{Z} \left\{ \prod_{i \in S(t,z)} \left(1 - \mathcal{P}_{(i,t,z)}(\Theta)\right) \prod_{i \in E(t+1,z,\zeta(z)) \backslash E(t,z,\zeta(z))} \mathcal{P}_{(i,t,z)}(\Theta) \right\} \\
& \times \left\{ (2\pi)^{-Z/2} (\tau^2)^{Z/2} |(1-\lambda)\mathbf{I}_Z + \lambda \mathcal{R}|^{1/2} \exp\left(-\frac{1}{2} \boldsymbol{\Gamma}^\top \left(\tau^2 \left[(1-\lambda)\mathbf{I}_Z + \lambda \mathcal{R}\right]\right) \boldsymbol{\Gamma} \right) \right\}.
\end{aligned}$$

Here, $S(t, z)$ denotes the set of susceptible individuals not infected at time t in region z, and $E(t + 1, z, \zeta(z)) \backslash E(t, z, \zeta(z))$ represents the set of newly exposed individuals at time t in region z and its neighbors.

3.4 Parameter Estimation of Seasonal GD-ILM

The parameter vector to be estimated is given by $\Theta = (\alpha_S, \boldsymbol{\beta}_1, \boldsymbol{\beta}_2, \delta, \zeta_1, \zeta_2, \tau, \lambda)$, and its estimation is carried out using the MCECM procedure described in Algorithm 2. Model performance can be evaluated based on the AIC, defined as

$$\mathrm{AIC} = -2 \log \mathcal{L}(\hat{\Theta}; \mathbf{y}_o) + 2n_p,$$

where $\log \mathcal{L}(\hat{\Theta}; \mathbf{y}_o)$ is the maximum log-likelihood of the fitted model, and n_p is the number of parameters in the model.

Algorithm 2 : MCECM Parameter Estimation of Seasonal GD-ILM

```
Initialize the initial value $\Theta^{(0)} = (\alpha_S^{(0)}, \boldsymbol{\beta}_1^{(0)}, \boldsymbol{\beta}_2^{(0)}, \delta^{(0)}, \zeta_1^{(0)}, \zeta_2^{(0)}, \tau^{(0)}, \lambda^{(0)})$.
Repeat
    E-Step: Approximate $\mathbb{E}\left[\ln \mathcal{L}(\Theta; \mathbf{y}_c)|\mathbf{y}_o, \Theta\right]$ using Metropolis–Hastings algorithm [62, 34]. Let $\mathbf{y}_o = (\mathbf{y}; \mathbf{z})$ denotes the observed variables. Consider $g(\boldsymbol{\Gamma})$ as the candidate density and $p(\boldsymbol{\Gamma}|\mathbf{y}_o) \propto p(\mathbf{y}|\mathbf{z}, \boldsymbol{\Gamma})g(\boldsymbol{\Gamma})$ as the target density. In the $(k+1)$th iteration of the ECM algorithm and with current values $\Theta^{(k)}$:
        For $(l = 1, \ldots, L)$
        In the $l$th iteration with current values of $\boldsymbol{\Gamma}_{k+1,l}$, generate $r \sim \text{Uniform}(0,1)$ and $\tilde{\boldsymbol{\Gamma}} \sim p(\boldsymbol{\Gamma}|\mathbf{y}_o; \Theta^{(k)})$.
            If $r \leqslant \frac{p(\mathbf{y}|\mathbf{z}, \tilde{\boldsymbol{\Gamma}})}{p(\mathbf{y}|\mathbf{z}, \boldsymbol{\Gamma}_{k+1,l})}$, Then
                $\boldsymbol{\Gamma}_{k+1,l+1} = \tilde{\boldsymbol{\Gamma}}$
            Else
                $\boldsymbol{\Gamma}_{k+1,l+1} = \boldsymbol{\Gamma}_{k+1,l}$
            End If
        End For
        Return the random sample $\{\boldsymbol{\Gamma}_{k+1,1}, \boldsymbol{\Gamma}_{k+1,2}, \ldots, \boldsymbol{\Gamma}_{k+1,L}\}$ generated from $p(\boldsymbol{\Gamma}|\mathbf{y}_o; \Theta^{(k)})$ and approximate the expectation by $\mathbb{E}\left[\ln \mathcal{L}(\Theta; \mathbf{y}_c)|\mathbf{y}_o, \Theta\right] = \frac{1}{L}\sum_{l=1}^{L} \ln \mathcal{L}(\Theta; \mathbf{y}; \boldsymbol{\Gamma}_{k+1,l})$ given in (3.4.1).
    M-Step: Maximize $\mathbb{E}\left[\ln \mathcal{L}(\Theta; \mathbf{y}_c)|\mathbf{y}_o, \Theta\right]$, with respect to the following model parameters to obtain $\Theta^{(k+1)}$.
        CM-Step 1: Update $\alpha_S^{(k+1)}$ using (3.4.2).
        CM-Step 2: Let $\alpha_S = \alpha_S^{(k+1)}$. Update $\boldsymbol{\beta}_1^{(k+1)}$ using (3.4.3).
        CM-Step 3: Let $(\alpha_S, \boldsymbol{\beta}_1) = (\alpha_S^{(k+1)}, \boldsymbol{\beta}_1^{(k+1)})$. Update $\boldsymbol{\beta}_2^{(k+1)}$ using (3.4.4).
        CM-Step 4: Let $(\alpha_S, \boldsymbol{\beta}_1, \boldsymbol{\beta}_2) = (\alpha_S^{(k+1)}, \boldsymbol{\beta}_1^{(k+1)}, \boldsymbol{\beta}_2^{(k+1)})$. Update $\delta^{(k+1)}$ using (3.4.5).
        CM-Step 5: Let $(\alpha_S, \boldsymbol{\beta}_1, \boldsymbol{\beta}_2, \delta) = (\alpha_S^{(k+1)}, \boldsymbol{\beta}_1^{(k+1)}, \boldsymbol{\beta}_2^{(k+1)}, \delta^{(k+1)})$. Update $\zeta_1^{(k+1)}$ using (3.4.6).
        CM-Step 6: Let $(\alpha_S, \boldsymbol{\beta}_1, \boldsymbol{\beta}_2, \delta, \zeta_1) = (\alpha_S^{(k+1)}, \boldsymbol{\beta}_1^{(k+1)}, \boldsymbol{\beta}_2^{(k+1)}, \delta^{(k+1)}, \zeta_1^{(k+1)})$. Update $\zeta_2^{(k+1)}$ using (3.4.7).
        CM-Step 7: Update $\begin{pmatrix}\tau\\ \lambda\end{pmatrix}$ using Newton–Raphson iterative as $\begin{pmatrix}\tau^{(k+1)}\\ \lambda^{(k+1)}\end{pmatrix} = \begin{pmatrix}\tau^{(k)}\\ \lambda^{(k)}\end{pmatrix} - B^{-1}A$, where $A$ and $B$ are in Equations (3.4.8-3.4.12).
Until the set $\Theta^{(k+1)}$ satisfies $\|\Theta^{(k+1)} - \Theta^{(k)}\|_2 < \epsilon_\Theta$, where $\|\cdot\|_2$ denotes the Euclidean norm, and $\epsilon_\Theta$ is a small threshold.
Return the estimated parameter set $\hat{\Theta} = \Theta^{(k+1)}$, corresponding to the last updated set of parameters estimates.
```

CM-Steps in MCECM Algorithm 2

Let $\Upsilon'^{(\cdot,\cdot,\cdot)}_S(i,z)$ and $\Upsilon''^{(\cdot,\cdot,\cdot)}_S(i,z)$ be as defined in Table 3.1. Additionally, define the following quantities:

$$\bar{G}^{(k)}_z = \frac{1}{L}\sum_{l=1}^{L}\left[\exp(\gamma_{z,k+1,l}) \mid \mathbf{y}_o, \Theta^{(k)}\right],$$

$$\bar{H}^{(k)}_{(i,t,z)} = \frac{1}{L}\sum_{l=1}^{L}\left[\frac{1-\mathcal{P}_{(i,t,z)}(\Theta)}{\mathcal{P}_{(i,t,z)}(\Theta)}\exp(\gamma_{z,k+1,l}) \mid \mathbf{y}_o, \Theta^{(k)}\right],$$

$$\bar{Q}^{(k)}_{(i,t,z)} = \frac{1}{L}\sum_{l=1}^{L}\left[\frac{1-\mathcal{P}_{(i,t,z)}(\Theta)}{(\mathcal{P}_{(i,t,z)}(\Theta))^2}\exp(2\gamma_{z,k+1,l}) \mid \mathbf{y}_o, \Theta^{(k)}\right].$$

Table 3.1: Definitions used in CM-Steps in Algorithm 2

$(\cdot,\cdot,\cdot)$	$\Upsilon'^{(\cdot,\cdot,\cdot)}_S(i,z)$
(0,0,0)	$\exp\left(\alpha_S^{(k)} + \mathbf{X}_i^\top\boldsymbol{\beta}_1^{(k)} + \mathbf{X}_{zS}^\top\boldsymbol{\beta}_2^{(k)}\right)$
(1,0,0)	$\mathbf{X}_i\exp\left(\alpha_S^{(k+1)} + \mathbf{X}_i^\top\boldsymbol{\beta}_1^{(k)} + \mathbf{X}_{zS}^\top\boldsymbol{\beta}_2^{(k)}\right)$
(1,1,0)	$\mathbf{X}_{zS}\exp\left(\alpha_S^{(k+1)} + \mathbf{X}_i^\top\boldsymbol{\beta}_1^{(k+1)} + \mathbf{X}_{zS}^\top\boldsymbol{\beta}_2^{(k)}\right)$
(1,1,1)	$\exp\left(\alpha_S^{(k+1)} + \mathbf{X}_i^\top\boldsymbol{\beta}_1^{(k+1)} + \mathbf{X}_{zS}^\top\boldsymbol{\beta}_2^{(k+1)}\right)$
$(\cdot,\cdot,\cdot)$	$\Upsilon''^{(\cdot,\cdot,\cdot)}_S(i,z)$
(0,0,0)	$\exp\left(2\alpha_S^{(k)} + 2\mathbf{X}_i^\top\boldsymbol{\beta}_1^{(k)} + 2\mathbf{X}_{zS}^\top\boldsymbol{\beta}_2^{(k)}\right)$
(1,0,0)	$\mathbf{X}_i\mathbf{X}_i^\top\exp\left(2\alpha_S^{(k+1)} + 2\mathbf{X}_i^\top\boldsymbol{\beta}_1^{(k)} + 2\mathbf{X}_{zS}^\top\boldsymbol{\beta}_2^{(k)}\right)$
(1,1,0)	$\mathbf{X}_{zS}\mathbf{X}_{zS}^\top\exp\left(2\alpha_S^{(k+1)} + 2\mathbf{X}_i^\top\boldsymbol{\beta}_1^{(k+1)} + 2\mathbf{X}_{zS}^\top\boldsymbol{\beta}_2^{(k)}\right)$
(1,1,1)	$\exp\left(2\alpha_S^{(k+1)} + 2\mathbf{X}_i^\top\boldsymbol{\beta}_1^{(k+1)} + 2\mathbf{X}_{zS}^\top\boldsymbol{\beta}_2^{(k+1)}\right)$
$(\cdot,\cdot,\cdot)$	$\kappa'^{(\cdot,\cdot,\cdot)}(i,j,t)$
(0,0,0)	$-d_{ij}\exp\left(-\delta^{(k)}d_{ij} + \zeta_1^{(k)}\sin\left(\frac{2\pi t}{T_{\text{cycle}}}\right) + \zeta_2^{(k)}\cos\left(\frac{2\pi t}{T_{\text{cycle}}}\right)\right)$
(1,0,0)	$\sin\left(\frac{2\pi t}{T_{\text{cycle}}}\right)\exp\left(-\delta^{(k+1)}d_{ij} + \zeta_1^{(k)}\sin\left(\frac{2\pi t}{T_{\text{cycle}}}\right) + \zeta_2^{(k)}\cos\left(\frac{2\pi t}{T_{\text{cycle}}}\right)\right)$
(1,1,0)	$\cos\left(\frac{2\pi t}{T_{\text{cycle}}}\right)\exp\left(-\delta^{(k+1)}d_{ij} + \zeta_1^{(k+1)}\sin\left(\frac{2\pi t}{T_{\text{cycle}}}\right) + \zeta_2^{(k)}\cos\left(\frac{2\pi t}{T_{\text{cycle}}}\right)\right)$
$(\cdot,\cdot,\cdot)$	$\kappa''^{(\cdot,\cdot,\cdot)}(i,j,t)$
(0,0,0)	$d_{ij}^2\exp\left(-\delta^{(k)}d_{ij} + \zeta_1^{(k)}\sin\left(\frac{2\pi t}{T_{\text{cycle}}}\right) + \zeta_2^{(k)}\cos\left(\frac{2\pi t}{T_{\text{cycle}}}\right)\right)$
(1,0,0)	$\sin^2\left(\frac{2\pi t}{T_{\text{cycle}}}\right)\exp\left(-\delta^{(k+1)}d_{ij} + \zeta_1^{(k)}\sin\left(\frac{2\pi t}{T_{\text{cycle}}}\right) + \zeta_2^{(k)}\cos\left(\frac{2\pi t}{T_{\text{cycle}}}\right)\right)$
(1,1,0)	$\cos^2\left(\frac{2\pi t}{T_{\text{cycle}}}\right)\exp\left(-\delta^{(k+1)}d_{ij} + \zeta_1^{(k+1)}\sin\left(\frac{2\pi t}{T_{\text{cycle}}}\right) + \zeta_2^{(k)}\cos\left(\frac{2\pi t}{T_{\text{cycle}}}\right)\right)$

The approximated expectation is given by $\mathbb{E}\left[\ln \mathcal{L}(\Theta;\mathbf{y}_c)|\mathbf{y}_o,\Theta\right] = \frac{1}{L}\sum_{l=1}^{L} \ln \mathcal{L}(\Theta;\mathbf{y};\mathbf{\Gamma}_{k+1,l})$. Therefore,

$$\begin{aligned}
\mathbb{E}\left[\ln \mathcal{L}\left(\Theta;\mathbf{y}_c\right)|\mathbf{y}_o,\Theta\right] &= \frac{1}{L}\sum_{t=1}^{T}\sum_{i\in S(t,z)}\sum_{z=1}^{Z}\sum_{l=1}^{L}\left[-\exp(\alpha_S+\mathbf{X}_i^\top\boldsymbol{\beta}_1+\mathbf{X}_{zS}^\top\boldsymbol{\beta}_2+\gamma_{z,k+1,l})\sum_{j\in I(t,z,\zeta(z))}\kappa(i,j,t)\middle|\mathbf{y}_o\right] \\
&+\frac{1}{L}\sum_{t=1}^{T}\sum_{i\in E(t+1,z,\zeta(z))\backslash E(t,z,\zeta(z))}\sum_{z=1}^{Z}\sum_{l=1}^{L}\left[\ln\left\{1-\exp(\exp(\alpha_S+\mathbf{X}_i^\top\boldsymbol{\beta}_1+\mathbf{X}_{zS}^\top\boldsymbol{\beta}_2+\gamma_{z,k+1,l})\right\}\sum_{j\in I(t,z,\zeta(z))}\kappa(i,j,t)\middle|\mathbf{y}_o\right] \\
&-\frac{Z}{2}\ln(2\pi)+\frac{Z}{2}\ln(\tau^2)+\frac{1}{2}\ln\left(|\lambda\mathcal{R}+(1-\lambda)\mathbf{I}|\right)-\frac{\tau^2}{2}\frac{1}{L}\sum_{l=1}^{L}\left[\mathbf{\Gamma}_{k+1,l}^\top(\lambda\mathcal{R}+(1-\lambda)\mathbf{I})\,\mathbf{\Gamma}_{k+1,l}|\mathbf{y}_o\right],
\end{aligned} \tag{3.4.1}$$

where $\kappa(i,j,t)$ is defined in (3.3.2).

CM-Step 1: Update α_S using the following recursive relationship

$$\alpha_S^{(k+1)} = \alpha_S^{(k)} - \frac{\frac{\partial}{\partial\alpha_S}\mathbb{E}\left[\ln\mathcal{L}(\Theta;\mathbf{y}_c)|\mathbf{y}_o,\Theta^{(k)}\right]}{\frac{\partial^2}{\partial\alpha_S^2}\mathbb{E}\left[\ln\mathcal{L}(\Theta;\mathbf{y}_c)|\mathbf{y}_o,\Theta^{(k)}\right]}, \tag{3.4.2}$$

where

$$\begin{aligned}
\frac{\partial\mathbb{E}\left[\ln\mathcal{L}(\Theta;\mathbf{y}_c)|\mathbf{y}_o,\Theta^{(k)}\right]}{\partial\alpha_S} &= -\sum_{t=1}^{T}\sum_{i\in S}\sum_{z=1}^{Z}\Upsilon_S'^{(0,0,0)}\left(i,z\right)\sum_{j\in I(t,z,\zeta(z))}\kappa'^{(0,0,0)}(i,j,t)\bar{G}_z^{(k)} \\
&+\sum_{t=1}^{T}\sum_{i\in E(t+1,z,\zeta(z))\backslash E(t,z,\zeta(z))}\sum_{z=1}^{Z}\Upsilon_S'^{(0,0,0)}\left(i,z\right)\sum_{j\in I(t,z,\zeta(z))}\kappa'^{(0,0,0)}(i,j,t)\bar{H}_{(i,t,z)}^{(k)},
\end{aligned}$$

and

$$\begin{aligned}
\frac{\partial^2\mathbb{E}\left[\ln\mathcal{L}(\Theta;\mathbf{y}_c)|\mathbf{y}_o,\Theta^{(k)}\right]}{\partial^2\alpha_S} &= -\sum_{t=1}^{T}\sum_{i\in S}\sum_{z=1}^{Z}\Upsilon_S'^{(0,0,0)}\left(i,z\right)\sum_{j\in I(t,z,\zeta(z))}\kappa'^{(0,0,0)}(i,j,t) \\
&\times\bar{G}_z^{(k)}+\sum_{t=1}^{T}\sum_{i\in E(t+1,z,\zeta(z))\backslash E(t,z,\zeta(z))}\sum_{z=1}^{Z}\Upsilon_S'^{(0,0,0)}\left(i,z\right)\sum_{j\in I(t,z,\zeta(z))}\kappa'^{(0,0,0)}(i,j,t)\bar{H}_{(i,t,z)}^{(k)} \\
&-\left(\Upsilon_S''^{(0,0,0)}\left(i,z\right)\right)\left(\sum_{j\in I(t,z,\zeta(z))}\kappa'^{(0,0,0)}(i,j,t)\right)^2\bar{Q}_{(i,t,z)}^{(k)}.
\end{aligned}$$

CM-Step 2: Update $\boldsymbol{\beta}_1$ using the following recursive relationship

$$\boldsymbol{\beta}_1^{(k+1)} = \boldsymbol{\beta}_1^{(k)} - \frac{\frac{\partial}{\partial\boldsymbol{\beta}_1}\mathbb{E}\left[\ln\mathcal{L}(\Theta;\mathbf{y}_c)|\mathbf{y}_o,\Theta^{(k)}\right]}{\frac{\partial^2}{\partial\boldsymbol{\beta}_1\partial\boldsymbol{\beta}_1^\top}\mathbb{E}\left[\ln\mathcal{L}(\Theta;\mathbf{y}_c)|\mathbf{y}_o,\Theta^{(k)}\right]}, \tag{3.4.3}$$

where

$$\frac{\partial \mathbb{E}\left[\ln \mathcal{L}(\Theta; \mathbf{y}_c)|\mathbf{y}_o, \Theta^{(k)}\right]}{\partial \boldsymbol{\beta}_1} = -\sum_{t=1}^{T}\sum_{i\in S}\sum_{z=1}^{Z} \Upsilon_S'^{(1,0,0)}\left(i,z\right) \sum_{j\in I(t,z,\zeta(z))} \kappa'^{(0,0,0)}(i,j,t)\bar{G}_z^{(k)}$$

$$+\sum_{t=1}^{T} \sum_{i\in E(t+1,z,\zeta(z))\backslash E(t,z,\zeta(z))} \sum_{z=1}^{Z} \Upsilon_S'^{(1,0,0)}\left(i,z\right) \sum_{j\in I(t,z,\zeta(z))} \kappa'^{(0,0,0)}(i,j,t)\bar{H}_{(i,t,z)}^{(k)},$$

and

$$\frac{\partial^2 \mathbb{E}\left[\ln \mathcal{L}(\Theta; \mathbf{y}_c)|\mathbf{y}_o, \Theta^{(k)}\right]}{\partial \boldsymbol{\beta}_1 \partial \boldsymbol{\beta}_1^\top} = -\sum_{t=1}^{T}\sum_{i\in S}\sum_{z=1}^{Z} \Upsilon_S'^{(1,0,0)}\left(i,z\right)\mathbf{X}_i^\top \sum_{j\in I(t,z,\zeta(z))} \kappa'^{(0,0,0)}(i,j,t)$$

$$\times \bar{G}_z^{(k)} + \sum_{t=1}^{T} \sum_{i\in E(t+1,z,\zeta(z))\backslash E(t,z,\zeta(z))} \sum_{z=1}^{Z} \Upsilon_S'^{(1,0,0)}\left(i,z\right)\mathbf{X}_i^\top \sum_{j\in I(t,z,\zeta(z))} \kappa'^{(0,0,0)}(i,j,t)\bar{H}_{(i,t,z)}^{(k)}$$

$$-\left(\Upsilon_S''^{(1,0,0)}\left(i,z\right)\right)\left(\sum_{j\in I(t,z,\zeta(z))} \kappa'^{(0,0,0)}(i,j,t)\right)^2 \bar{Q}_{(i,t,z)}^{(k)}.$$

CM-Step 3: Update $\boldsymbol{\beta}_2$ using the following recursive relationship

$$\boldsymbol{\beta}_2^{(k+1)} = \boldsymbol{\beta}_2^{(k)} - \frac{\frac{\partial}{\partial \boldsymbol{\beta}_2}\mathbb{E}\left[\ln \mathcal{L}(\Theta; \mathbf{y}_c)|\mathbf{y}_o, \Theta^{(k)}\right]}{\frac{\partial^2}{\partial \boldsymbol{\beta}_2 \partial \boldsymbol{\beta}_2^\top}\mathbb{E}\left[\ln \mathcal{L}(\Theta; \mathbf{y}_c)|\mathbf{y}_o, \Theta^{(k)}\right]}, \tag{3.4.4}$$

where

$$\frac{\partial \mathbb{E}\left[\ln \mathcal{L}(\Theta; \mathbf{y}_c)|\mathbf{y}_o, \Theta^{(k)}\right]}{\partial \boldsymbol{\beta}_2} = -\sum_{t=1}^{T}\sum_{i\in S}\sum_{z=1}^{Z} \Upsilon_S'^{(1,1,0)}\left(i,z\right) \sum_{j\in I(t,z,\zeta(z))} \kappa'^{(0,0,0)}(i,j,t)\bar{G}_z^{(k)}$$

$$+\sum_{t=1}^{T} \sum_{i\in E(t+1,z,\zeta(z))\backslash E(t,z,\zeta(z))} \sum_{z=1}^{Z} \Upsilon_S'^{(1,1,0)}\left(i,z\right) \sum_{j\in I(t,z,\zeta(z))} \kappa'^{(0,0,0)}(i,j,t)\bar{H}_{(i,t,z)}^{(k)},$$

and

$$\frac{\partial^2 \mathbb{E}\left[\ln \mathcal{L}(\Theta; \mathbf{y}_c)|\mathbf{y}_o, \Theta^{(k)}\right]}{\partial \boldsymbol{\beta}_2 \partial \boldsymbol{\beta}_2^\top} = -\sum_{t=1}^{T}\sum_{i\in S}\sum_{z=1}^{Z} \Upsilon_S'^{(1,1,0)}\left(i,z\right)\mathbf{X}_{zS}^\top \sum_{j\in I(t,z,\zeta(z))} \kappa'^{(0,0,0)}(i,j,t)\bar{G}_z^{(k)}$$

$$+\sum_{t=1}^{T} \sum_{i\in E(t+1,z,\zeta(z))\backslash E(t,z,\zeta(z))} \sum_{z=1}^{Z} \Upsilon_S'^{(1,1,0,0,0)}\left(i,z\right)\mathbf{X}_{zS}^\top \sum_{j\in I(t,z,\zeta(z))} \kappa'^{(0,0,0)}(i,j,t)\bar{H}_{(i,t,z)}^{(k)}$$

$$-\left(\Upsilon_S''^{(1,1,0}\left(i,z\right)\right)\left(\sum_{j\in I(t,z,\zeta(z))} \kappa'^{(0,0,0)}(i,j,t)\right)^2 \bar{Q}_{(i,t,z)}^{(k)}.$$

CM-Step 4: Update δ using the following recursive relationship

$$\delta^{(k+1)} = \delta^{(k)} - \frac{\frac{\partial}{\partial \delta}\mathbb{E}\left[\ln \mathcal{L}(\Theta; \mathbf{y}_c)|\mathbf{y}_o, \Theta^{(k)}\right]}{\frac{\partial^2}{\partial^2 \delta}\mathbb{E}\left[\ln \mathcal{L}(\Theta; \mathbf{y}_c)|\mathbf{y}_o, \Theta^{(k)}\right]}, \tag{3.4.5}$$

where

$$\begin{aligned}\frac{\partial \mathbb{E}\left[\ln \mathcal{L}(\Theta; \mathbf{y}_c)|\mathbf{y}_o, \Theta^{(k)}\right]}{\partial \delta} &= -\sum_{t=1}^{T}\sum_{i\in S}\sum_{z=1}^{Z} \Upsilon_S'^{(1,1,1)}(i,z) \sum_{j\in I(t,z,\zeta(z))} \kappa'^{(0,0,0)}(i,j,t)\bar{G}_z^{(k)} \\ &+ \sum_{t=1}^{T} \sum_{i\in E(t+1,z,\zeta(z))\backslash E(t,z,\zeta(z))} \sum_{z=1}^{Z} \Upsilon_S'^{(1,1,1)}(i,z) \sum_{j\in I(t,z,\zeta(z))} \kappa'^{(0,0,0)}(i,j,t)\bar{H}_{(i,t,z)}^{(k)},\end{aligned}$$

and

$$\begin{aligned}\frac{\partial^2 \mathbb{E}\left[\ln \mathcal{L}(\Theta; \mathbf{y}_c)|\mathbf{y}_o, \Theta^{(k)}\right]}{\partial^2 \delta} &= -\sum_{t=1}^{T}\sum_{i\in S}\sum_{z=1}^{Z} \Upsilon_S'^{(1,1,1)}(i,z) \sum_{j\in I(t,z,\zeta(z))} \kappa_T''^{(0,0,0)}(i,j,t)\bar{G}_z^{(k)} \\ &+ \sum_{t=1}^{T} \sum_{i\in E(t+1,z,\zeta(z))\backslash E(t,z,\zeta(z))} \sum_{z=1}^{Z} \Upsilon_S'^{(1,1,1)}(i,z) \sum_{j\in I(t,z,\zeta(z))} \kappa''^{(0,0,0)}(i,j,t)\bar{H}_{(i,t,z)}^{(k)} \\ &- \left(\Upsilon_S''^{(1,1,1)}(i,z)\right)\left(\sum_{j\in I(t,z,\zeta(z))} \kappa''^{(0,0,0)}(i,j,t)\right)^2 \bar{Q}_{(i,t,z)}^{(k)}.\end{aligned}$$

CM-Step 5: Update ζ_1 using the following recursive relationship

$$\zeta_1^{(k+1)} = \zeta_1^{(k)} - \frac{\frac{\partial}{\partial \zeta_1}\mathbb{E}\left[\ln \mathcal{L}(\Theta; \mathbf{y}_c)|\mathbf{y}_o, \Theta^{(k)}\right]}{\frac{\partial^2}{\partial^2 \zeta_1}\mathbb{E}\left[\ln \mathcal{L}(\Theta; \mathbf{y}_c)|\mathbf{y}_o, \Theta^{(k)}\right]}, \tag{3.4.6}$$

where

$$\begin{aligned}\frac{\partial \mathbb{E}\left[\ln \mathcal{L}(\Theta; \mathbf{y}_c)|\mathbf{y}_o, \Theta^{(k)}\right]}{\partial \zeta_1} &= -\sum_{t=1}^{T}\sum_{i\in S}\sum_{z=1}^{Z} \Upsilon_S'^{(1,1,1)}(i,z) \sum_{j\in I(t,z,\zeta(z))} \kappa'^{(1,0,0)}(i,j,t)\bar{G}_z^{(k)} \\ &+ \sum_{t=1}^{T} \sum_{i\in E(t+1,z,\zeta(z))\backslash E(t,z,\zeta(z))} \sum_{z=1}^{Z} \Upsilon_S'^{(1,1,1)}(i,z) \sum_{j\in I(t,z,\zeta(z))} \kappa'^{(1,0,0)}(i,j,t)\bar{H}_{(i,t,z)}^{(k)},\end{aligned}$$

and

$$\begin{aligned}\frac{\partial^2 \mathbb{E}\left[\ln \mathcal{L}(\Theta; \mathbf{y}_c)|\mathbf{y}_o, \Theta^{(k)}\right]}{\partial^2 \zeta_1} &= -\sum_{t=1}^{T}\sum_{i\in S}\sum_{z=1}^{Z} \Upsilon_S'^{(1,1,1)}(i,z) \sum_{j\in I(t,z,\zeta(z))} \kappa''^{(1,0,0)}(i,j,t)\bar{G}_z^{(k)} \\ &+ \sum_{t=1}^{T} \sum_{i\in E(t+1,z,\zeta(z))\backslash E(t,z,\zeta(z))} \sum_{z=1}^{Z} \Upsilon_S'^{(1,1,1)}(i,z) \sum_{j\in I(t,z,\zeta(z))} \kappa''^{(1,0,0)}(i,j,t)\bar{H}_{(i,t,z)}^{(k)} \\ &- \left(\Upsilon_S''^{(1,1,1)}(i,z)\right)\left(\sum_{j\in I(t,z,\zeta(z))} \kappa''^{(1,0,0)}(i,j,t)\right)^2 \bar{Q}_{(i,t,z)}^{(k)}.\end{aligned}$$

CM-Step 6: Update ζ_2 using the following recursive relationship

$$\zeta_2^{(k+1)} = \zeta_2^{(k)} - \frac{\frac{\partial}{\partial \zeta_2}\mathbb{E}\left[\ln \mathcal{L}(\Theta; \mathbf{y}_c)|\mathbf{y}_o, \Theta^{(k)}\right]}{\frac{\partial^2}{\partial \zeta_2^2}\mathbb{E}\left[\ln \mathcal{L}(\Theta; \mathbf{y}_c)|\mathbf{y}_o, \Theta^{(k)}\right]}, \tag{3.4.7}$$

where

$$\frac{\partial \mathbb{E}\left[\ln \mathcal{L}(\Theta; \mathbf{y}_c)|\mathbf{y}_o, \Theta^{(k)}\right]}{\partial \zeta_2} = -\sum_{t=1}^{T}\sum_{i\in S}\sum_{z=1}^{Z} \Upsilon_S'^{(1,1,1)}(i,z) \sum_{j\in I(t,z,\zeta(z))} \kappa'^{(1,1,0)}(i,j,t)\bar{G}_z^{(k)}$$
$$+\sum_{t=1}^{T}\sum_{i\in E(t+1,z,\zeta(z))\setminus E(t,z,\zeta(z))}\sum_{z=1}^{Z} \Upsilon_S'^{(1,1,1)}(i,z) \sum_{j\in I(t,z,\zeta(z))} \kappa'^{(1,1,0)}(i,j,t)\bar{H}_{(i,t,z)}^{(k)},$$

and

$$\frac{\partial^2 \mathbb{E}\left[\ln \mathcal{L}(\Theta; \mathbf{y}_c)|\mathbf{y}_o, \Theta^{(k)}\right]}{\partial^2 \zeta_2} = -\sum_{t=1}^{T}\sum_{i\in S}\sum_{z=1}^{Z} \Upsilon_S'^{(1,1,1,1,1)}(i,z) \sum_{j\in I(t,z,\zeta(z))} \kappa''^{(1,1,0)}(i,j,t)\bar{G}_z^{(k)}$$
$$+\sum_{t=1}^{T}\sum_{i\in E(t+1,z,\zeta(z))\setminus E(t,z,\zeta(z))}\sum_{z=1}^{Z} \Upsilon_S'^{(1,1,1)}(i,z) \sum_{j\in I(t,z,\zeta(z))} \kappa''^{(1,1,0)}(i,j,t)\bar{H}_{(i,t,z)}^{(k)}$$
$$-\left(\Upsilon_S''^{(1,1,1)}(i,z)\right)\left(\sum_{j\in I(t,z,\zeta(z))} \kappa''^{(1,1,0)}(i,j,t)\right)^2 \bar{Q}_{(i,t,z)}^{(k)}.$$

CM-Step 7: A and B are used to estimate τ and λ in the $(k+1)$th iteration and are represented by the score vector and the expected information matrix, respectively. Given

$$\mathbb{E}\left[\ln p(\boldsymbol{\Gamma})|\mathbf{y}_o, \Theta^{(k)}\right] = -\frac{Z}{2}\ln(2\pi) + \frac{Z}{2}\ln(\tau^2) + \frac{1}{2}\ln\left(|\lambda\mathcal{R} + (1-\lambda)\mathbf{I}|\right)$$
$$-\frac{\tau^2}{2}\frac{1}{L}\sum_{l=1}^{L}\left[\boldsymbol{\Gamma}_{k+1,l}^{\top}(\lambda\mathcal{R} + (1-\lambda)\mathbf{I})\,\boldsymbol{\Gamma}_{k+1,l}|\mathbf{y}_o, \Theta^{(k)}\right],$$

then the elements of these matrices can be defined as follows:

$$A(\tau) = \frac{\partial \mathbb{E}\left[\ln p(\boldsymbol{\Gamma})|\mathbf{y}_o, \Theta^{(k)}\right]}{\partial \tau} = \frac{Z}{\tau} - \tau\frac{1}{L}\sum_{l=1}^{L}\left[\boldsymbol{\Gamma}_{k+1,l}^{\top}(\lambda\mathcal{R} + (1-\lambda)\mathbf{I})\,\boldsymbol{\Gamma}_{k+1,l}|\mathbf{y}_o, \Theta^{(k)}\right], \tag{3.4.8}$$

$$A(\lambda) = \frac{\partial \mathbb{E}\left[\ln p(\boldsymbol{\Gamma})|\mathbf{y}_o, \Theta^{(k)}\right]}{\partial \lambda} = \frac{1}{2}\mathrm{tr}\left((\lambda\mathcal{R} + (1-\lambda)\mathbf{I})^{-1}(\mathcal{R} - \mathbf{I})\right) - \frac{\tau^2}{2}\frac{1}{L}\sum_{l=1}^{L}\left[\boldsymbol{\Gamma}_{k+1,l}^{\top}(\lambda\mathcal{R} + (1-\lambda)\mathbf{I})\,\boldsymbol{\Gamma}_{k+1,l}|\mathbf{y}_o, , \Theta^{(k)}\right], \tag{3.4.9}$$

$$B(\tau,\tau) = \frac{\partial^2 \mathbb{E}\left[\ln p(\boldsymbol{\Gamma})|\mathbf{y}_o, \Theta^{(k)}\right]}{(\partial \tau)^2} = \frac{Z}{\tau^2} + \frac{1}{L}\sum_{l=1}^{L}\left[\boldsymbol{\Gamma}_{k+1,l}^{\top}(\lambda\mathcal{R} + (1-\lambda)\mathbf{I})\,\boldsymbol{\Gamma}_{k+1,l}|\mathbf{y}_o, \Theta^{(k)}\right], \tag{3.4.10}$$

$$B(\tau, \lambda) = \frac{\partial^2 \mathbb{E}\left[\ln p(\boldsymbol{\Gamma})|\mathbf{y}_o, \Theta^{(k)}\right]}{\partial \tau \partial \lambda} = \tau \frac{1}{L}\sum_{l=1}^{L}\left[\boldsymbol{\Gamma}_{k+1,l}^{\top}(\mathcal{R} - \mathbf{I})\boldsymbol{\Gamma}_{k+1,l}|\mathbf{y}_o, \Theta^{(k)}\right], \tag{3.4.11}$$

$$B(\lambda, \lambda) = \frac{\partial^2 \mathbb{E}\left[\ln p(\boldsymbol{\Gamma})|\mathbf{y}_o, \Theta^{(k)}\right]}{(\partial \lambda)^2} = \frac{1}{2}\mathrm{tr}\left((\mathcal{R} - \mathbf{I})\left(\lambda\mathcal{R} + (1-\lambda)\mathbf{I}\right)^{-1}(\mathcal{R} - \mathbf{I})\left(\lambda\mathcal{R} + (1-\lambda)\mathbf{I}\right)^{-1}\right). \tag{3.4.12}$$

3.5 Variances of Estimated Seasonal GD-ILM Parameters

The estimation of variances within the MCECM algorithm follows a modified version of the approach originally proposed by [54] and subsequently applied by [8, 7]. In this framework, the observed information matrix is defined as

$$\mathcal{I}_{\mathrm{o}}(\hat{\Theta}; \mathbf{y}_o) = \mathcal{I}_{\mathrm{c}}(\hat{\Theta}; \mathbf{y}_o) - \mathcal{I}_{\mathrm{m}}(\hat{\Theta}; \mathbf{y}_o),$$

where $\mathcal{I}_{\mathrm{c}}$ and $\mathcal{I}_{\mathrm{m}}$ denote the complete data and missing data information matrices, respectively, and $\hat{\Theta}$ represents the parameter estimates obtained through the MCECM procedure. Approximations for these matrices are derived as follows:

$$\mathcal{I}_{\mathrm{c}}(\Theta; \mathbf{y}_o) = -\mathbb{E}\left[\frac{\partial^2}{\partial\Theta\partial\Theta^{\top}}\ln\mathcal{L}(\Theta; \mathbf{y}_c)\bigg|\mathbf{y}_o, \Theta\right] = -\frac{1}{L}\sum_{l=1}^{L}\frac{\partial^2}{\partial\Theta\partial\Theta^{\top}}\ln\mathcal{L}(\Theta; \mathbf{y}_c^{(l)}),$$

and

$$\begin{aligned}\mathcal{I}_{\mathrm{m}}(\Theta; \mathbf{y}_o) &= \mathbb{E}\left[\left(\frac{\partial}{\partial\Theta}\ln\mathcal{L}(\Theta; \mathbf{y}_c)\right)\left(\frac{\partial}{\partial\Theta^{\top}}\ln\mathcal{L}(\Theta; \mathbf{y}_c)\right)\bigg|\mathbf{y}_o, \Theta\right] \\ &\quad - \mathbb{E}\left[\frac{\partial}{\partial\Theta}\ln\mathcal{L}(\Theta; \mathbf{y}_c)\bigg|\mathbf{y}_o, \Theta\right]\mathbb{E}\left[\frac{\partial}{\partial\Theta^{\top}}\ln\mathcal{L}(\Theta; \mathbf{y}_c)\bigg|\mathbf{y}_o, \Theta\right] \\ &= \frac{1}{L}\sum_{l=1}^{L}\frac{\partial}{\partial\Theta}\ln\mathcal{L}(\Theta; \mathbf{y}_c^{(l)})\frac{\partial}{\partial\Theta^{\top}}\ln\mathcal{L}(\Theta; \mathbf{y}_c^{(l)}) \\ &\quad - \left(\frac{1}{L}\sum_{l=1}^{L}\frac{\partial}{\partial\Theta}\ln\mathcal{L}(\Theta; \mathbf{y}_c^{(l)})\right)\left(\frac{1}{L}\sum_{l=1}^{L}\frac{\partial}{\partial\Theta^{\top}}\ln\mathcal{L}(\Theta; \mathbf{y}_c^{(l)})\right),\end{aligned}$$

where each $\mathbf{y}_c^{(l)} = (\mathbf{y}_o, \boldsymbol{\Psi}_l)$, with $\boldsymbol{\Psi}_l$ denoting samples drawn from the conditional distribution of the spatial random effect (missing data) given the observed data and the parameter $\hat{\Theta}$ estimated via the MCECM algorithm. At the MCECM estimate $\hat{\Theta}$, the mean score function computed across all

Monte Carlo samples satisfies the following condition:

$$\frac{1}{L}\sum_{l=1}^{L}\frac{\partial}{\partial\Theta}\ln\mathcal{L}(\Theta;\mathbf{y}_c^{(l)})\bigg|_{\Theta=\hat{\Theta}}=0,$$

which leads to the following simplified form of the observed information matrix:

$$\mathcal{I}_{\mathrm{o}}(\hat{\Theta};\mathbf{y}_o)=-\frac{1}{L}\sum_{l=1}^{L}\frac{\partial^2}{\partial\Theta\partial\Theta^\top}\ln\mathcal{L}(\hat{\Theta};\mathbf{y}_c^{(l)})-\frac{1}{L}\sum_{l=1}^{L}\left(\frac{\partial}{\partial\Theta}\ln\mathcal{L}(\hat{\Theta};\mathbf{y}_c^{(l)})\right)\left(\frac{\partial}{\partial\Theta^\top}\ln\mathcal{L}(\hat{\Theta};\mathbf{y}_c^{(l)})\right).$$

The variance-covariance matrix of $\hat{\Theta}$ is derived by inverting the observed information matrix. The resulting diagonal entries represent the variances associated with each parameter estimate.

3.6 Simulation Study

To evaluate the performance of our proposed seasonal GD-ILM, we conducted a comprehensive simulation study. Simulated PCRs were distributed across a hexagonal grid, with each cell representing a distinct geographic area. The number of PCRs per cell was randomly drawn from a uniform distribution, and population sizes were independently assigned to each PCR from a separate uniform distribution. The number of infectious individuals was then determined based on predefined infection rates (Figure 3.1).

We incorporated both regional and individual-level covariates to assess susceptibility and transmissibility. Spatial proximity between PCRs was calculated using the Euclidean distance metric, given by

$$d_{ij}=\sqrt{(x_j-x_i)^2+(y_j-y_i)^2},$$

where x_i and x_j are the coordinates of PCRs i and j. Spatial random effects were introduced using precision and dependence parameters, and spatial and temporal decay effects were applied to account for seasonal transmission dynamics. The incubation and infectious periods were kept constant across the grid. Each simulation began with a single, randomly exposed PCR per grid cell at $t=1$ and proceeded for $T=156$ weeks.

To assess the consequences of fitting a misspecified model, we generated data from Model 2. We then estimated the parameters of each simulated dataset using both Model 1 and Model 2. This approach allowed us to evaluate the impact of omitting seasonal effects and to examine the ability of each model to recover the true underlying parameters. Parameter estimation for Model 2 was performed using the MCECM method (Algorithm 2). To estimate the parameters of Model 1 using the MCECM method, one can modify Algorithm 2 by removing steps 5 and 6, setting $\zeta_1 = \zeta_2 = 0$, and applying the resulting inference procedure to Model 1. A convergence criterion of $\epsilon_\Theta = 10^{-3}$ was applied to achieve an optimal trade-off between computational efficiency and the accuracy of the parameter estimates. A detailed summary of the epidemic simulation setup is presented in Table 3.2.

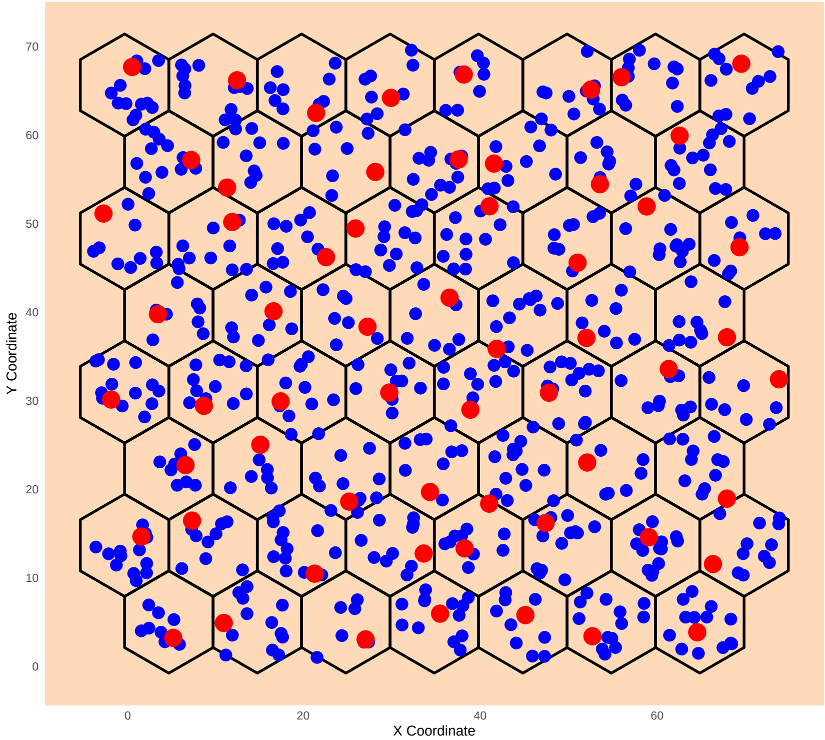

Figure 3.1: Grid epidemic simulation at time $t = 1$ and generated PCRs within grid areas. Blue dots are the susceptible PCRs and red dots are the infected PCRs.

Table 3.2: Summary of the epidemic simulation setup

Simulation Aspect	Setup
Grid and Population Settings	
Grid	Hexagonal grid with 60 cells
PCR distribution per cell	Uniform$(10, 20)$
Population per PCR	Uniform$(10, 100)$
Epidemiological Parameters	
Infection rates	$P_I = \{5\%, 10\%, 20\%, 30\%\}$
Incubation period	5 days
Infectious period	10 days
Susceptibility Covariates	
Individual-level covariate	Laplace$(0, 1)$
Regional-level covariate	Logistic$(0, 1)$
Spatial and Temporal Effects	
Distance metric	Euclidean distance
Spatial random effects	Leroux model [49] with $\tau = 0.40$ and $\lambda = 0.60$
Spatial decay parameter	$\delta = 2$
Seasonality parameters	ζ_1=1, ζ_2=1.5
Simulation and Estimation	
Time span	$T = 156$ weeks
Cycle duration	T_{cycle}=52 (weekly)
Simulation runs	500
Estimation method	MCECM (Algorithm 2)
Threshold	$\epsilon_\Theta = 10^{-3}$

Results

Tables 3.3 and 3.4 present the results of the simulation study, displaying the average parameter estimates and their corresponding standard errors based on 500 replications across four distinct infection prevalence scenarios. Table 3.3 corresponds to Model 1, which omits the seasonal component and thus represents a misspecified model. In contrast, Table 3.4 reports results for Model 2, which correctly incorporates the seasonal component and serves as the well-specified reference model.

In Table 3.3, the estimates for the susceptibility intercept (α_S) and covariate effects (β_1 and β_2) remain robust and relatively unbiased across all prevalence levels. For instance, α_S is estimated at 1.023 for 5% prevalence and 0.988 for 30% prevalence, both approximating the true value of 1.0. Similarly, the estimates for β_1 and β_2 converge toward their respective true values, indicating that the estimation of covariate effects remains reliable even under model misspecification.

Table 3.3: Parameter estimates (Est.) and their standard errors (S.E.) for Model 1 in the epidemic simulation study

		$\boldsymbol{P_I}$ = 5%		$\boldsymbol{P_I}$ = 10%		$\boldsymbol{P_I}$ = 20%		$\boldsymbol{P_I}$ = 30%	
Parameter	True	Est.	S.E.	Est.	S.E.	Est.	S.E.	Est.	S.E.
Susceptibility									
α_S	1	1.023	0.146	1.115	0.101	0.968	0.054	0.988	0.117
β_1	1	0.942	0.126	1.118	0.047	1.124	0.104	1.005	0.014
β_2	2	1.920	0.150	2.171	0.125	1.897	0.045	1.907	0.119
Spatial Kernel									
δ	2	0.730	0.126	0.787	0.117	0.823	0.097	0.957	0.102
Spatial Random Effect									
τ	0.4	0.342	0.024	0.304	0.019	0.330	0.051	0.325	0.029
λ	0.6	0.783	0.056	0.821	0.023	0.835	0.052	0.853	0.048

Table 3.4: Parameter estimates (Est.) and their standard errors (S.E.) for Model 2 in the epidemic simulation study

		$\boldsymbol{P_I}$ = 5%		$\boldsymbol{P_I}$ = 10%		$\boldsymbol{P_I}$ = 20%		$\boldsymbol{P_I}$ = 30%	
Parameter	True	Est.	S.E.	Est.	S.E.	Est.	S.E.	Est.	S.E.
Susceptibility									
α_S	1	1.103	0.093	1.008	0.056	0.972	0.167	1.092	0.038
β_1	1	1.093	0.046	0.918	0.141	1.034	0.056	1.089	0.139
β_2	2	1.926	0.052	2.021	0.034	2.078	0.145	2.014	0.129
Spatiotemporal Kernel									
δ	2	2.118	0.153	2.086	0.067	1.991	0.148	2.103	0.063
ζ_1	1	1.076	0.082	1.082	0.113	1.075	0.013	1.043	0.105
ζ_2	1.5	1.477	0.065	1.532	0.109	1.489	0.054	1.515	0.034
Spatial Random Effect									
τ	0.4	0.394	0.025	0.410	0.051	0.390	0.012	0.391	0.045
λ	0.6	0.585	0.026	0.603	0.058	0.590	0.018	0.589	0.021

However, substantial bias is observed in the spatial parameters, particularly the spatial decay parameter (δ) and the spatial dependence parameter (λ). The true value of δ is 2.0; yet, it is consistently underestimated, with values falling below 1 across all prevalence levels. Since spatial decay is modeled as $d_{ij}^{-\delta}$, a lower estimated δ implies slower attenuation of spatial dependence with distance, which can overestimate long-range spatial interactions.

Concurrently, the spatial dependence parameter λ, which has a true value of 0.6, is systematically overestimated across all scenarios. This overestimation, in conjunction with the underestimated δ, reflects a compensatory behavior within the misspecified model. Specifically, in the absence of the seasonal component, the model misattributes unexplained temporal variation to the spatial structure, leading to artificial inflation of spatial correlation.

The underestimation of δ results in an inferred spatial correlation structure that decays more gradually with geographic distance than it should. Consequently, the model overstates the degree of influence that distant RHADs exert on one another, effectively flattening the spatial gradient of infection risk. This distortion arises because the omitted seasonal component fails to account for cyclical fluctuations in transmission, causing the model to reallocate temporal variability to the spatial component. As a result, the decay parameter δ is underestimated, capturing the temporal autocorrelation that should be attributed to seasonal effects.

Similarly, the overestimation of λ indicates that the model attributes excessive strength to the spatially structured component of the infection process. This parameter captures the magnitude of spatial autocorrelation after adjusting for covariates and other components. Its inflation suggests that the model interprets the residual temporal clustering as intensified spatial dependence.

The systematic underestimation of δ and overestimation of λ generate a misleading representation of the underlying spatial transmission dynamics. The model implies both stronger spatial autocorrelation and a broader geographic extent of influence than actually exist. Such distortions can have serious implications for public health policy, potentially leading to ineffective or misdirected spatial interventions based on erroneous transmission pathways.

By contrast, Table 3.4 demonstrates that Model 2, which includes the seasonal component, produces accurate and unbiased parameter estimates across all levels of infection prevalence. The estimates of the susceptibility intercept and covariate effects demonstrate high precision. The spatial dependence parameter λ is accurately recovered with low variability, while the precision parameter τ remains stably estimated across all scenarios. Additionally, the spatiotemporal kernel parameters ζ_1 and ζ_2, unique to Model 2, are consistently estimated near their true values, demonstrating the efficacy of the MCECM algorithm in capturing seasonally modulated transmission dynamics.

These findings emphasize the critical importance of incorporating an appropriate temporal structure, such as seasonal components, in GD-ILMs, particularly when applied to infectious disease data exhibiting periodic trends. The omission of key temporal covariates leads to significant biases in the estimation of spatial parameters δ and λ, which can severely compromise inference on spatial transmission patterns. In contrast, the correctly specified Model 2 enables valid statistical inference across all parameters and prevalence conditions, highlighting the necessity of proper model specification in spatiotemporal epidemiological modeling.

3.7 Real Data Analysis

This study utilized administrative weekly health records of Influenza type A in Manitoba, Canada, from December 2018 to December 2021, provided by Manitoba Health. The individual-level dataset includes information such as date of diagnosis and 6-digit residential postal codes, with scrambled personal health identification numbers for confirmed Influenza cases. We consider the geographical classification of Manitoba defined by MCHP and Manitoba Health for the allocation of health districts and neighborhood clusters based on municipality and postal codes [3].

Table 3.5: Seasonal SEIR model parameter estimations

HAD	**Interlake**	**Northern**	**Prairie**	**Southern**	**Winnipeg**
Number of PCRs	1,363	1,050	3,079	2,509	19,896
Contact Rate	0.294	0.305	0.210	0.241	0.327
Incubation Period (days)	3	8	5	4	7
Infectious Period (days)	7	10	9	8	12

The incidence rates of the disease are visualized in Figures 3.2, 3.3a, 3.3b, 3.4a, and 3.4b, with the numbers on the maps corresponding to the RHAD names. The incidence rate figures indicate that higher rates of the disease are concentrated in the central and southern areas of Winnipeg, the southern parts of Prairie, the central and southern parts of Southern, and the central areas of Northern. Disease patterns within these HAD. were analyzed using the seasonal SEIR model, which was applied separately to each HAD. Model parameters were estimated via maximum likelihood using the Nelder-Mead algorithm. Table 3.5 summarizes the underlying epidemiological parameters derived from a seasonal SEIR model fitted separately for each HAD. The parameter estimates in Table 3.5 demonstrate considerable regional variation, reflecting underlying differences in demographic and epidemiological conditions across HADs. Winnipeg recorded the highest contact rate at 0.327, suggesting a higher frequency of interactions conducive to Influenza A transmission in this urban environment. In contrast, the Prairie HAD exhibited the lowest contact rate at 0.210. Differences were also evident in the estimated incubation and infectious periods, with Winnipeg showing a longer infectious duration of 12 days compared to 7 days in Interlake, further emphasizing the heterogeneity in Influenza A dynamics across the province.

Differences in the estimated contact rates may reflect varying levels of interpersonal interaction and exposure, shaped by factors such as population density, social mixing patterns, and access to healthcare services. These regional disparities highlight the fact that the transmission dynamics of Influenza A are not uniform across Manitoba. Consequently, applying a single seasonal GD-ILM to the entire province may overlook important local variations and lead to oversimplified conclusions.

In this study, we treated RHADs as regional units and PCRs as individual units, allowing for a model with high-resolution analysis. Each Influenza case was assigned to one of Manitoba's RHADs based on the 6-digit residential postal code, using the PCCF provided by Manitoba Health. Regarding susceptibility risk factors for Influenza, we were interested in exploring their geographical variation and how they relate to regional indicators such as SES to include in (3.3.1). The Euclidean distance metric was used to calculate spatial proximity between PCRs.

The seasonal cycle (T_{cycle}) was set to 52 weeks, representing one full year composed of two main periods: fall and winter, when Influenza activity is highest, and spring and summer, when activity is lower. This specification captures both peak and low transmission phases within each annual cycle, allowing the model to accurately reflect the seasonal dynamics of Influenza throughout the year.

We conducted a comparative analysis of Model 1 and Model 2 by fitting both models to the Influenza data. Parameter estimation for Model 2 was carried out using the MCECM algorithm described in Algorithm 2. To ensure consistency in the comparison, Model 1 was estimated using a modified version of the same algorithm: Steps 5 and 6 were removed, and the parameters $\zeta_1 = \zeta_2 = 0$ were fixed to reflect the structure of Model 1. For both models, the MCECM procedure was implemented with a convergence threshold of $\epsilon_\Theta = 10^{-3}$, balancing computational efficiency with the stability of the parameter estimates. This unified estimation framework allows for a robust comparison of the models in terms of fit, complexity, and parameter behavior.

Results

Table 3.6: Estimated parameters (Est.) and standard errors (S.E.) for Model 2 using Influenza data from Manitoba

	Interlake		**Northern**		**Prairie**		**Southern**		**Winnipeg**	
Parameter	Est.	S.E.	Est.	S.E.	Est.	S.E.	Est.	S.E.	Est.	S.E.
Susceptibility										
α_S	-1	0.075	-1	0.059	-3	0.083	-1	0.067	-2	0.041
SES	1.534	0.0093	1.433	0.0057	1.824	0.0182	1.278	0.0069	2.111	0.0041
Spatiotemporal Kernel										
δ	2.336	0.0048	2.586	0.0091	2.479	0.0033	2.438	0.0062	2.196	0.0076
ζ_1	0.894	0.0065	0.842	0.0151	0.758	0.0049	0.838	0.0093	0.767	0.0271
ζ_2	0.802	0.0056	0.861	0.0127	0.735	0.0072	0.819	0.0088	0.781	0.0259
Spatial Random Effect										
τ	0.593	0.0097	0.621	0.0104	0.589	0.0213	0.631	0.0069	0.698	0.0042
λ	0.394	0.0085	0.552	0.0023	0.605	0.0071	0.673	0.0048	0.729	0.0325
Model										
AIC	42472		31782		28245		31434		34534	

The results from Model 2 (Table 3.6), which incorporates both spatial structure and seasonal components, reveal substantial heterogeneity in susceptibility and transmission dynamics across Manitoba's HADs. The susceptibility intercept (α_S) was negative across all districts, with the most pronounced effect observed in Prairie (-3), indicating low baseline susceptibility after adjusting for covariates. These negative intercepts reflect an overall reduced infection risk in the absence of additional risk factors.

The covariate for the SES factor score exhibited a positive association with susceptibility in all HADs, with the strongest effects estimated in Winnipeg (2.111) and Prairie (1.824). These results

Table 3.7: Estimated parameters (Est.) and standard errors (S.E.) for Model 1 using Influenza data from Manitoba

	Interlake		**Northern**		**Prairie**		**Southern**		**Winnipeg**	
Parameter	Est.	S.E.	Est.	S.E.	Est.	S.E.	Est.	S.E.	Est.	S.E.
Susceptibility										
α_S	-1	0.0029	-1	0.0048	-2	0.0397	-1	0.0037	-2	0.0072
SES	1.925	0.0046	1.153	0.0018	1.502	0.0213	1.711	0.0024	1.982	0.0081
Spatial Kernel										
δ	2.803	0.0066	2.765	0.0054	2.695	0.0015	2.847	0.0189	2.856	0.0043
Spatial Random Effect										
τ	0.481	0.0291	0.523	0.0026	0.503	0.0072	0.593	0.0193	0.578	0.0374
λ	0.536	0.0092	0.605	0.0665	0.694	0.0237	0.767	0.0451	0.851	0.0067
Model										
AIC	49128		35769		33434		37453		40786	

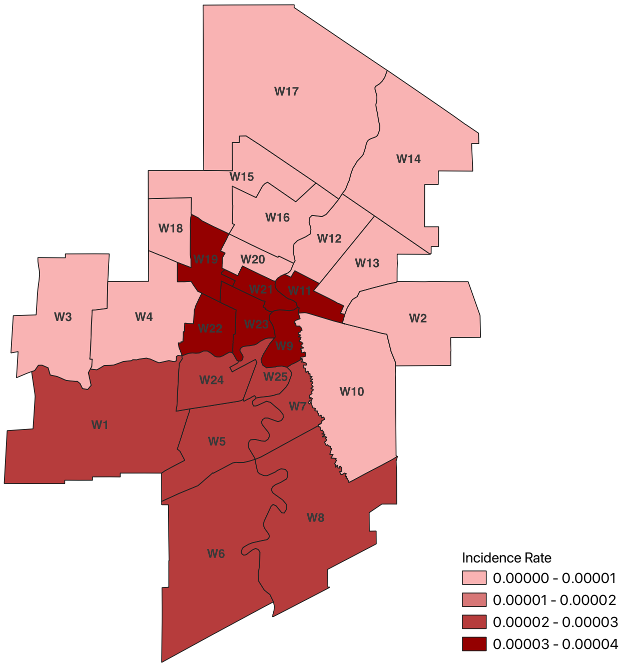

Figure 3.2: Influenza incidence rates across RHADs in Winnipeg HAD

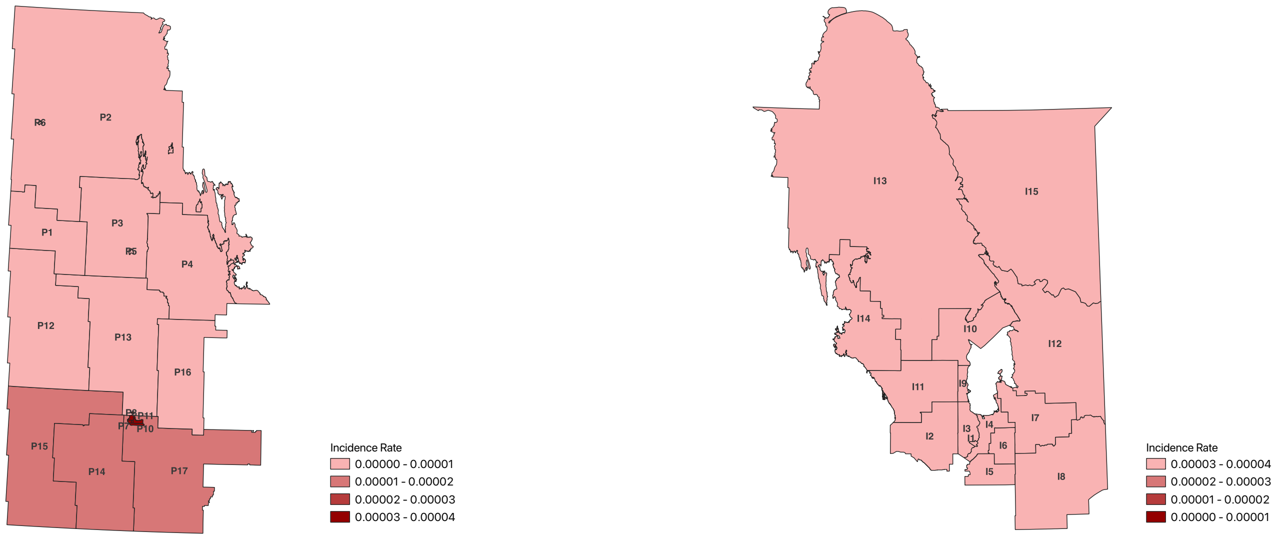

(a) Prairie

(b) Interlake

Figure 3.3: Influenza incidence rates across RHADs in Prairie and Interlake HADs

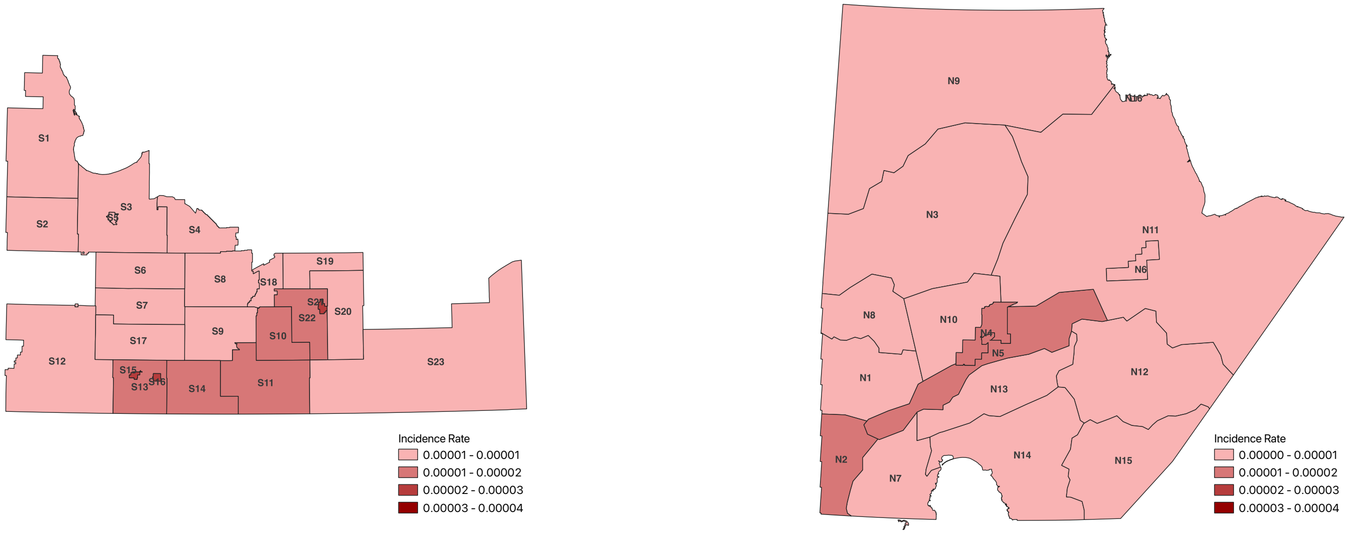

(a) Southern

(b) Northern

Figure 3.4: Influenza incidence rates across RHADs in Southern and Northern HADs

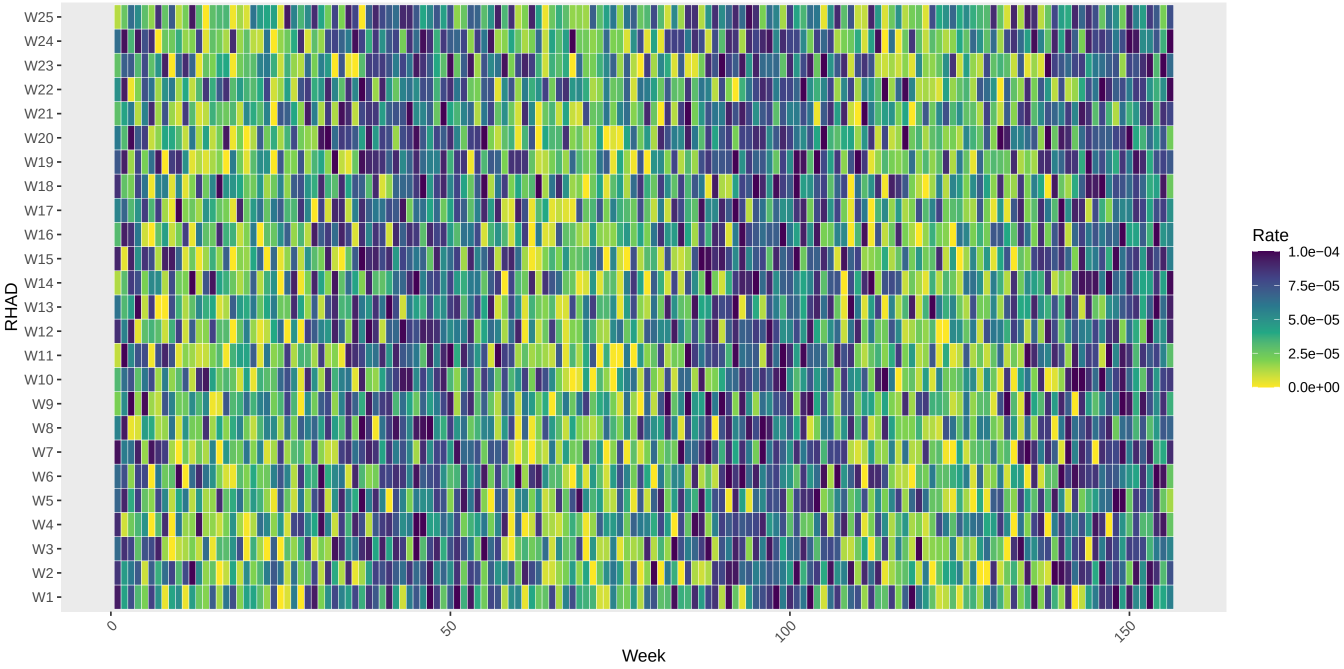

Figure 3.5: Average infectivity rates across RHADs in Winnipeg HAD

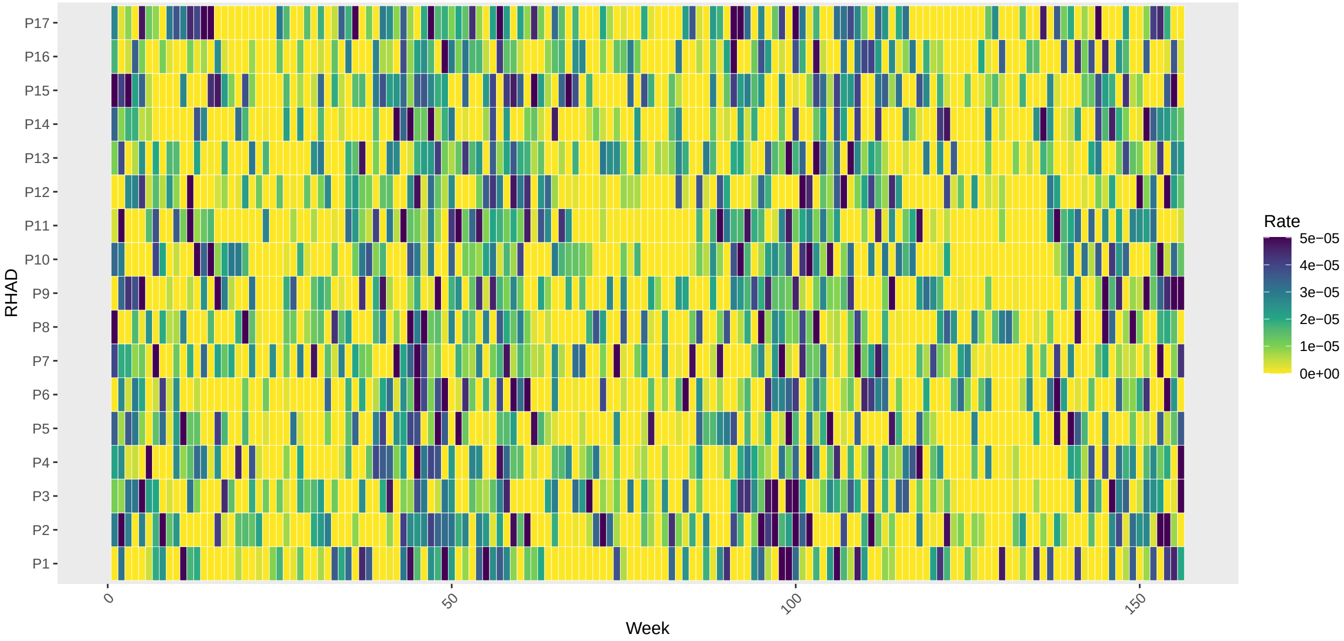

Figure 3.6: Average infectivity rates across RHADs in Prairie HAD

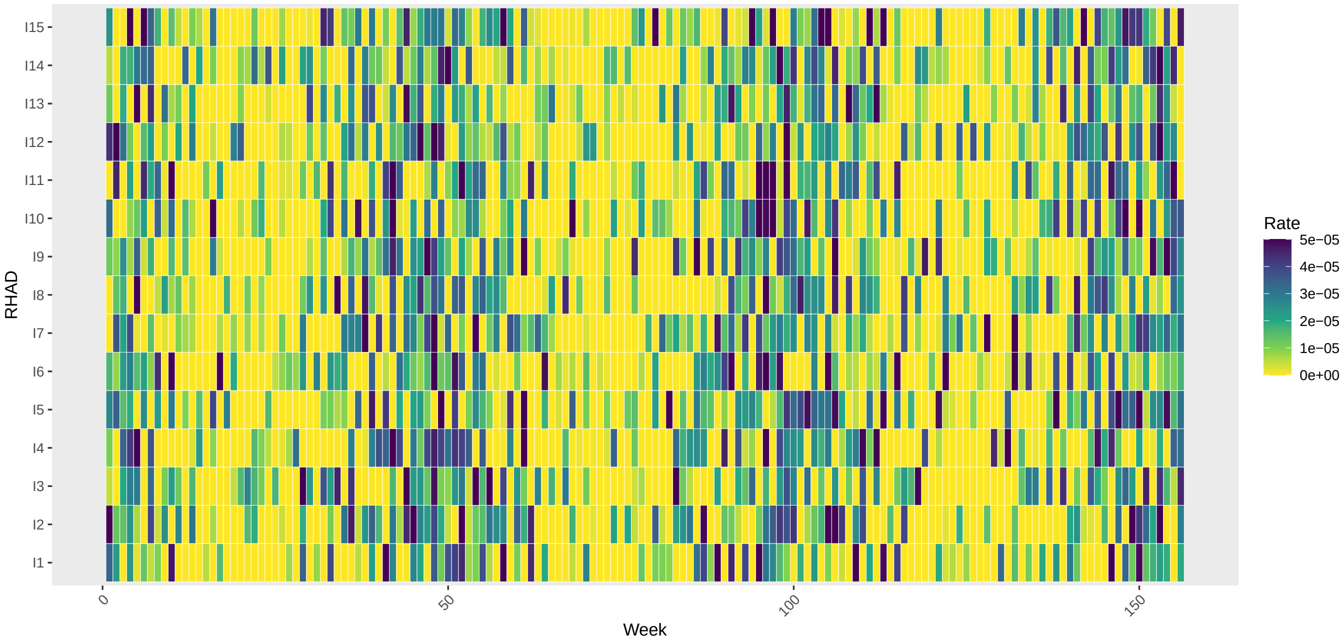

Figure 3.7: Average infectivity rates across RHADs in Interlake HAD

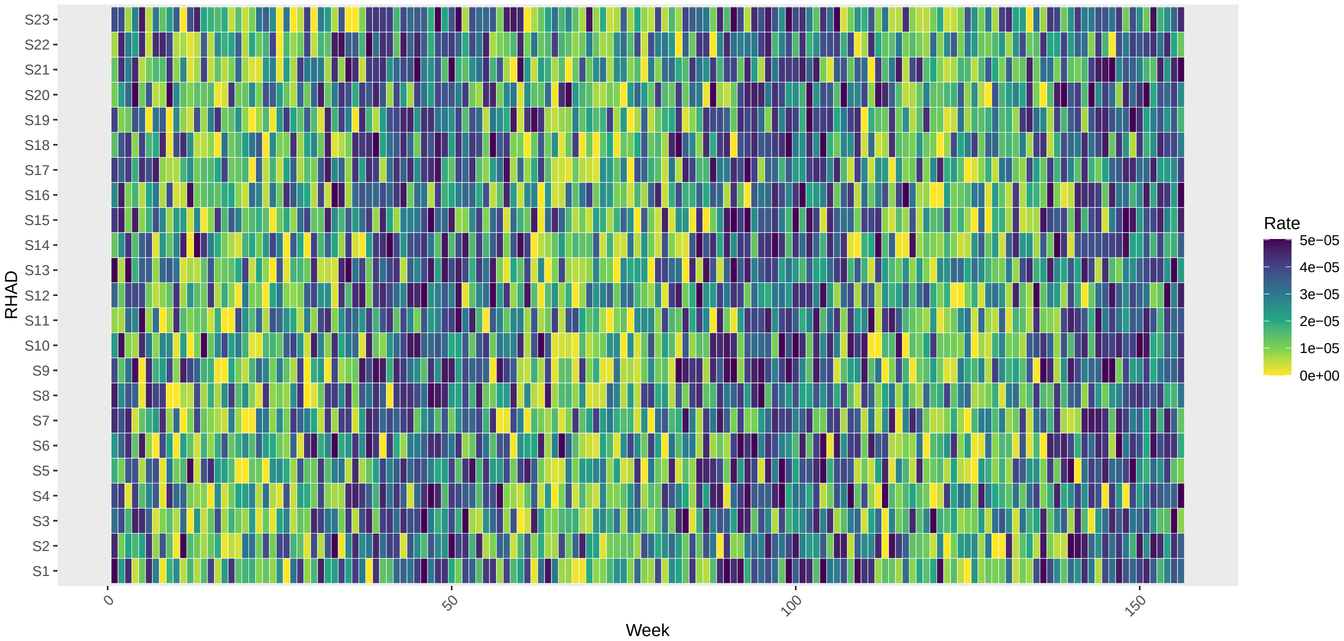

Figure 3.8: Average infectivity rates across RHADs in Southern HAD

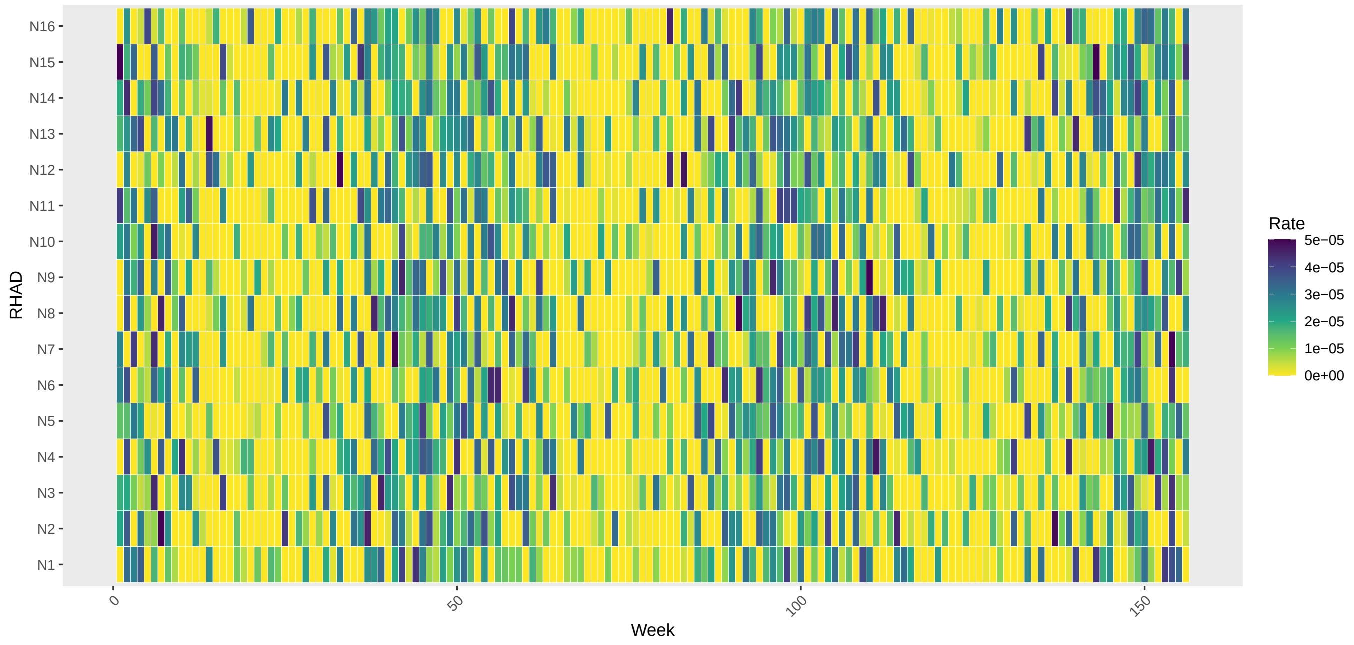

Figure 3.9: Average infectivity rates across RHADs in Northern HAD

suggest that individuals residing in RHADs with higher SES factor score exhibit increased susceptibility to infection, likely attributable to underlying social determinants such as lower income levels, higher unemployment rates, lower educational attainment, and a greater prevalence of single-parent households. The particularly strong SES factor score effect in Winnipeg highlights the compounding influence of urban disadvantage on infectious disease vulnerability.

The spatial decay parameter (δ) was consistently estimated to be between 2.2 and 2.6 across all HADs, confirming that transmission probability decreases as spatial distance increases. This finding supports the presence of highly localized transmission patterns, with most infections likely occurring among proximate PCRs. The magnitude of δ reflects strong spatial structuring in transmission risk, emphasizing the importance of accounting for geographic proximity when modeling infection dynamics.

Seasonal variation in transmission was captured by the periodic parameters ζ_1 and ζ_2, both estimated near 0.8 in all districts. These values indicate a consistent, cyclical seasonal trend in transmission over the study period, with peaks likely aligning with the colder months. The inclusion of these parameters enables the model to adjust for the known periodicity of Influenza activity, improving the accuracy and interpretability of temporal risk predictions.

The spatial random effects were governed by the spatial dependence parameter (λ) and the precision parameter (τ). Among all HADs, Winnipeg exhibited the strongest spatial dependence ($\lambda = 0.729$) and the lowest precision ($\tau = 0.698$), indicating substantial residual spatial heterogeneity and localized clustering of unexplained risk. In contrast, the Northern and Interlake HADs demonstrated weaker spatial dependence and higher precision, suggesting more homogeneous spatial distributions of transmission risk and fewer localized hotspots of unexplained variability.

Model 1, which excluded seasonal effects and modeled spatial interactions alone, produced similar estimates for susceptibility and SES covariates (Table 3.7). However, the model demonstrated inferior performance in capturing the spatial structure of transmission. Specifically, precision parameters were uniformly lower, while spatial dependence parameters were inflated, suggesting that the absence of a seasonal component led to an artificial concentration of residual variability within the spatial component. Additionally, the spatial decay parameter (δ) was consistently overestimated in Model 1, reflecting an exaggerated interpretation of spatial influence in the absence of temporal adjustment.

Model fit was evaluated using the AIC. Across all HADs, Model 2 exhibited substantially lower AIC values, indicating a superior fit. For example, in Winnipeg, the AIC decreased from 40,786 under Model 1 to 34,534 under Model 2. Similarly, in Prairie, the AIC decreased from 33,434 under Model 1 to 28,245 under Model 2. The percentage improvement in AIC was calculated using the formula:

$$\text{AIC Improvement (\%)} = \frac{\text{AIC}_{\text{Model 1}} - \text{AIC}_{\text{Model 2}}}{\text{AIC}_{\text{Model 1}}} \times 100.$$

A summary of AIC values and the corresponding improvements across all HADs is presented in Table 3.8.

HAD	$\textbf{AIC}_{\textbf{Model 1}}$	$\textbf{AIC}_{\textbf{Model 2}}$	**AIC Improvement (%)**
Interlake	49,128	42,472	13.54%
Prairie	33,434	28,245	15.52%
Southern	35,769	31,782	11.16%
Northern	37,453	31,434	16.06%
Winnipeg	40,786	34,534	15.33%

Table 3.8: AIC improvements across HADs

The percentage improvements in AIC emphasize the critical importance of including seasonality to adequately model Influenza transmission. Failure to account for temporal periodicity results in diminished explanatory power and may obscure important cyclical risk patterns.

Heat maps for each HAD and their corresponding RHADs under Model 2, shown in Figures 3.5, 3.6, 3.7, 3.8, and 3.9, visually illustrate the spatiotemporal dynamics of estimated Influenza transmission rates across Manitoba on a weekly basis. Each map captures temporal slices of the study period, with time represented in weeks, enabling clear observation of both seasonal patterns and localized fluctuations in transmission intensity. The seasonal trend is readily apparent: darker shading, which indicates higher estimated transmission risk, consistently aligns with the winter months, which correspond to known peaks in Influenza activity.

The heat maps clearly illustrate significant spatial heterogeneity across HADs. Winnipeg and Southern HADs exhibit a higher concentration of high-risk RHADs, with infection rates escalating during peak transmission weeks. In contrast, Interlake, Northern, and Prairie HADs consistently show lower infection rates, suggesting reduced transmission dynamics. This contrast highlights the importance of HAD-specific public health strategies and targeted resource allocation to address localized outbreaks more effectively.

This observed disparity may be driven by several interrelated factors. First, Winnipeg and parts of Southern Manitoba are more urbanized and densely populated, creating conditions that facilitate faster disease spread through increased person-to-person contact. These areas also experience higher levels of human mobility due to commuting, social interactions, and economic activities, all of which contribute to elevated transmission. Additionally, SES diversity within RHADs may contribute to the presence of vulnerable subpopulations, such as individuals residing in overcrowded housing or lacking sufficient access to healthcare, thereby increasing their susceptibility to infection.

In contrast, HADs such as Northern, Interlake, and Prairie tend to be more rural, characterized by lower population densities and limited mobility, which naturally reduce opportunities for widespread transmission. Moreover, occupational and environmental factors may contribute to regional differences; for example, the presence of large agricultural or industrial workplaces in the Southern HAD could elevate risk, whereas more remote areas lack such high-risk settings. Variations in public health infrastructure, reporting practices, and access to care may also play a role, with urban areas potentially demonstrating higher case detection due to stronger surveillance systems. Finally, behavioral and cultural factors, including differences in compliance with public health guidelines, may further influence the spatial distribution of risk across Manitoba.

In summary, the joint modeling of spatial interaction and seasonality in Model 2 provides a more comprehensive and biologically plausible representation of Influenza transmission dynamics in Manitoba. The findings highlight the necessity of geographically and temporally resolved public health strategies. In particular, the observed spatial clustering and seasonal variation in risk support the implementation of targeted interventions, such as HAD-specific vaccination campaigns initiated in advance of expected seasonal peaks.

3.8 Conclusion

We propose a novel extension to the GD-ILM framework originally constructed upon a SEIR model by integrating seasonality into the transmission dynamics. This is achieved by introducing a seasonally varying transmission component, enabling the model to capture periodic fluctuations in infection risk more effectively. Central to our approach is the incorporation of a seasonally forced infection kernel, which models cyclical changes in transmission rates. To estimate the parameters of this enhanced model and to manage the associated computational complexity, we utilize the MCECM algorithm, which ensures robust and reliable inference in intricate settings. Incorporating seasonality significantly enhances the GD-ILM's robustness, precision, and practical applicability, particularly for large-scale epidemic modeling and data-driven public health decision-making. We demonstrate the model's performance and real-world relevance through high-resolution spatial analysis using administrative individual-level data of Influenza in Manitoba, complemented by simulation studies to validate its effectiveness.

The Influenza data analysis demonstrates significant improvements in model fit and interpretability when incorporating seasonal variation alongside spatial structure. The seasonal parameters capture well-known cyclical trends in transmission, while the spatial parameters identify localized clusters of high infection risk. The heterogeneous effects of SES on susceptibility highlight the importance of social determinants in infectious disease dynamics. These spatial and temporal insights provide a granular understanding of transmission patterns across Manitoba's HADs, revealing critical urban-rural disparities that should inform tailored public health interventions.

The simulation study confirms the importance of correctly specifying temporal components to avoid bias in spatial parameter estimation. The misspecified model that omits seasonality results in distorted spatial dynamics, while the full model accurately recovers key parameters under diverse prevalence scenarios. This highlights the methodological necessity of integrating seasonality for reliable inference in spatiotemporal infectious disease modeling.

From a health policy perspective, the findings of this study have direct implications for the design and implementation of targeted disease control strategies. The identification of seasonally driven transmission peaks enables the timely deployment of preventive measures such as vaccination campaigns, public awareness initiatives, and resource mobilization ahead of anticipated surges. The clear spatial heterogeneity and clustering patterns support geographically focused interventions, allowing health authorities to prioritize high-risk districts and allocate resources efficiently.

Moreover, the demonstrated role of SES in shaping susceptibility emphasizes the need for policies that address social inequities exacerbating infectious disease vulnerability. Tailored outreach and support for communities with lower income, higher unemployment rates, lower educational attainment, and a higher proportion of single-parent households could reduce disparities in infection risk and improve overall population health outcomes.

In summary, by integrating seasonal dynamics with spatial heterogeneity, this enhanced GD-ILM framework provides public health officials and policymakers with a more precise and timely understanding of the spread of infectious diseases. This improved modeling capability supports data-driven decisions that can optimize the timing and location of interventions, ultimately reducing transmission and health disparities. The model's ability to identify high-risk periods, HADs, and vulnerable communities equips health systems to better allocate resources, design targeted prevention strategies, and implement equitable policies that address both biological and social determinants of disease. To enhance accessibility and reproducibility, we have developed and released the `SeasEpi` R package [2] publicly available on CRAN. This package implements the seasonal GD-ILM framework and provides comprehensive tools for likelihood-based parameter estimation via the MCECM algorithm, supports model evaluation using AIC, and enables flexible simulation studies tailored to specific research needs. Thus, this work advances epidemiological modeling and contributes directly to public health responses that are more equitable, timely, and just.

One limitation of this study stems from the real data, which relied on the covariates available in the dataset and did not account for other potentially influential factors. Consequently, the model's results may be sensitive to the inclusion of additional covariates, and the potential effects of omitted covariates should be carefully considered when interpreting the findings.

Building on the findings of this study, several avenues for further research are promising. Future work can explore alternative mathematical forms for the spatial kernel, such as Gaussian or exponential, to more accurately reflect diverse spatial transmission patterns across different diseases and regions. Similarly, more flexible representations of seasonality, including piecewise models, spline-based approaches, or multi-frequency harmonic functions, could better capture complex temporal and seasonal variations. Depending on the nature of the disease and the data, seasonal effects might also be incorporated directly into the spark function to model sudden outbreaks more precisely. Moreover, extending the proposed framework to an SEIRS compartmental model, which explicitly accounts for reinfection dynamics, would broaden its applicability to diseases characterized by waning immunity or repeated infections.

4

Accelerating Parameter Estimation of Geographically-Dependent Individual-Level Models of Infectious Diseases in Large-Scale Epidemics

This chapter includes a preprint manuscript intended for submission to *Spatial Statistics*. It is reproduced here largely in its original form, with only slight formatting modifications to ensure consistency within the thesis.

4.1 Introduction

Parameter estimation for GD-ILMs is particularly challenging due to the complex model structure, which incorporates spatial dependencies and individual-level heterogeneity, making the full likelihood function intractable. As a result, direct maximization of the likelihood is often computationally prohibitive, especially for large datasets with high spatial resolution. ECM algorithms and their variants, including the MCECM algorithm, have been developed for parameter estimation in GD-ILMs [8, 7]. Nonetheless, these methods remain computationally intensive for large-scale applications.

Bayesian approaches employing MCMC methods are widely used for parameter estimation in spatial epidemic models [58, 78] and GD-ILMs [57]. Despite their popularity, MCMC methods frequently face limitations in scalability and are computationally intensive, particularly for large and complex datasets [87, 5, 101].

To address these computational limitations, [58] developed a set of sampling-based likelihood approximations for ILMs within the SIR compartmental framework, including the Spatial ILM and the Foot-and-Mouth Disease ILM, which account for uncertainty in infection times. Their approach incorporates both simple random sampling and spatially stratified sampling schemes, substantially reducing the computational burden while preserving acceptable levels of estimation accuracy. The results demonstrate that such approximations are particularly valuable in large-scale epidemic contexts.

However, likelihood approximation techniques have not yet been extended to GD-ILMs, which are inherently more complex due to spatially varying risk factors and spatial dependence. Consequently, to the best of our knowledge, the computational challenges associated with parameter estimation in GD-ILMs remain unresolved.

Our work presents a new, scalable framework for parameter estimation in GD-ILMs within a SEIR compartmental structure. Our approach integrates the SAECM algorithm with a novel stratified temporally-weighted KDE-based PPS sampling method for selecting cases from the dataset. The stratified temporally-weighted KDE-based PPS sampling method prioritizes infectious disease cases by incorporating spatial intensity and a time-sensitive infectiousness profile, assigning higher weight to recently infected individuals with greater transmission potential. This targeted sampling method reduces the data volume needed for likelihood approximation, substantially decreasing computational costs while maintaining estimation accuracy. Incorporating this sampling method within the SAECM framework enables efficient and robust parameter estimation while enhancing both convergence speed and scalability, particularly for large, high-resolution spatial epidemic datasets where traditional maximum likelihood or Bayesian MCMC methods are computationally intensive.

By prioritizing sampling in regions and time periods with elevated transmission risk, our approach effectively captures the spatiotemporal heterogeneity of infectious disease spread. This improves model fidelity and enables rapid inference, which is crucial for timely public health decision-makings. Overall, this work accelerates parameter estimation for GD-ILMs by providing a computationally efficient, accurate, and scalable framework for large-scale epidemic modeling and real-time surveillance.

To evaluate the computational efficiency and accuracy of our SAECM algorithm combined with a stratified temporally-weighted KDE-based PPS sampling method for likelihood approximation, we conducted a comprehensive simulation study across grids of increasing spatial resolution (10×10, 20×20, and 30×30) and within-cell heterogeneity.

This setup enables the evaluation of the robustness and scalability of the proposed model under diverse demographic scenarios. Through these simulations, we examined the effects of sampling fraction, spatial complexity, and demographic heterogeneity on parameter estimation. Additionally, both regional and individual-level covariates were incorporated to capture realistic transmission dynamics.

We compared the performance of the MCECM and SAECM algorithms under both full and partial sampling scenarios, quantifying estimation accuracy using the Absolute Relative Bias Percentage (ARBP). Furthermore, we applied our methodology to individual-level administrative COVID-19 data from Manitoba, Canada, covering the period from September 2020 to March 2021. Using a high-resolution spatial framework comprising 96 RHADs and 27,897 PCRs, we examined regional SES disparities in disease transmission patterns. Additionally, the fitted model provided estimates of the probability of exposure for each PCR at every time step.

The remainder of this chapter is organized as follows. Section 4.2 provides an introduction to the study along with two-dimensional KDE. Section 4.3 presents the stratified temporally-weighted KDE-based PPS sampling method for infectious disease cases. Section 4.4 details the specifications of the GD-ILM components and the full and approximated likelihood formulations. Section 4.5 describes the parameter estimation procedures, including both the MCECM and SAECM algorithms. Section 4.6 reports simulation studies assessing estimation performance and computational efficiency. Section 4.7 illustrates the application of the proposed methods to COVID-19 data from Manitoba. Finally, Section 4.8 concludes with a discussion of potential directions for future research.

4.2 Background

4.2.1 Total Infectious Load

In the GD-ILM, formulated within the SEIR compartmental framework, the following term

$$\Psi(i,t,z,\zeta(z)) = \sum_{j \in I(t,z,\zeta(z))} \Upsilon_T(j,z)\,\kappa(i,j). \tag{4.2.1}$$

represents the total infectious load on a susceptible individual, which is computed by aggregating the influence of all infectious individuals in the region and its neighboring regions. A key computational challenge in this framework arises from evaluating the total infectious load. During large-scale outbreaks, the set $I(t,z,\zeta(z))$ can grow considerably, leading to intensive computational demands due to repeated summations over large infectious populations. This creates a significant bottleneck for likelihood-based inference and simulation, particularly in large populations and over extended time periods.

In Section 4.3, we propose alleviating this burden by approximating $\Psi(i,t,z,\zeta(z))$ by $\widetilde{\Psi}(i,t,z,\zeta(z))$, using a representative sample drawn from the set $I(t,z,\zeta(z))$.

4.2.2 Two-dimensional KDE

Two-dimensional KDE is a widely used non-parametric technique for estimating the probability density function of a spatially distributed random variable from observed data [10, 89, 39]. Beyond its foundational role in statistics, KDE has emerged as a key tool for hotspot detection in fields such as epidemiology, criminology, and environmental science [91, 50, 43, 81, 28, 24].

KDE evaluates event concentration at a given location by centering a smooth kernel function over a defined neighborhood, weighting events by the inverse distance from the target location, and aggregating the weighted contributions of all events within the kernel window [39].

This approach enables detailed visualization of spatial patterns and facilitates the identification of areas with high event intensity, commonly referred to as hotspots. Formally, for a set of n spatial observations $\{(x_1, y_1), (x_2, y_2), \ldots, (x_n, y_n)\}$, the KDE at a point (x, y) is defined as:

$$f(x,y) = \frac{1}{nh_s^2} \sum_{i=1}^{n} K_s\left(\frac{x-x_i}{h_s}, \frac{y-y_i}{h_s}\right),$$

where $K_s(\cdot)$ is the spatial kernel function, which is typically a smooth, symmetric probability density function, such as the Gaussian kernel, and h_s is the bandwidth parameter that controls the degree of smoothing. The choice of bandwidth is critical, as it determines the trade-off between sensitivity to local variation and noise suppression.

By transforming discrete spatial events into a continuous surface without relying on rigid parametric assumptions, KDE provides a flexible and intuitive framework for spatial data analysis. Its ability to reveal underlying spatial structures and highlight high-intensity regions has made it indispensable in a wide range of applied research fields that require robust spatial pattern recognition [10, 89].

4.3 Stratified Temporally-Weighted KDE-Based PPS Sampling Method

Efficient sampling of infectious individuals is crucial for scalable and accurate inference in spatiotemporal infectious disease models. Conventional approaches, such as simple random sampling and stratified sampling, though straightforward to implement, often fail to capture the complex and heterogeneous dynamics of epidemic spread. Simple random sampling selects individuals uniformly at random, disregarding spatial and temporal context, which can result in the underrepresentation of key transmission areas and increased variability in parameter estimates. Stratified sampling introduces some structure by dividing the population into predefined strata, but it lacks the flexibility to adapt to dynamically evolving hotspots and spatial clustering inherent in infectious disease outbreaks.

To address these limitations, we develop a KDE–based PPS sampling method, guided by spatial and temporal information. This approach utilizes the spatial locations and infection times of observed cases to generate a continuous, data-driven estimate of infection intensity across space and time. KDE naturally highlights clusters of infectious individuals by assigning higher density values to areas with concentrated cases currently within their infectious periods. Consequently, sampling is directed toward active hotspots rather than isolated cases, reflecting the biological and social mechanisms of disease transmission induced by proximity to infectious individuals. This targeted strategy enables more efficient sampling and improves the accuracy of epidemiological surveillance and inference.

To ensure radial symmetry in the KDE, such that the resulting density contours are circular rather than axis-aligned, the spatial kernel is defined using the Euclidean distance between the evaluation point (x, y) and each observed point (x_i, y_i), given by $\sqrt{(x - x_i)^2 + (y - y_i)^2}$. We adopt a Gaussian spatial kernel for this purpose, defined as:

$$K_s\left(\frac{x - x_i}{h_s}, \frac{y - y_i}{h_s}\right) = \frac{1}{2\pi} \exp\left[-\frac{(x - x_i)^2 + (y - y_i)^2}{2h_s^2}\right],$$

which leads to the following form of the KDE:

$$f(x, y) = \frac{1}{2\pi n h_s^2} \sum_{i=1}^{n} \exp\left[-\frac{(x - x_i)^2 + (y - y_i)^2}{2h_s^2}\right].$$

This formulation ensures smooth, symmetric density surfaces that accurately reflect spatial clustering.

The Gaussian spatial kernel is infinitely supported, ensuring that the density estimate is both smooth and rotation-invariant. This makes it particularly well-suited for modeling isotropic spatial data, where no directional bias is assumed in the spread of infection.

The bandwidth parameter h_s was selected using Silverman's Rule of Thumb [89] given by:

$$h_s = 1.06 \min\left(\sigma_s, \frac{\text{IQR}}{1.34}\right) n^{-1/5},$$

where σ_s denotes the standard deviation and IQR is the interquartile range. Here, σ_s and IQR are computed from the empirical distribution of pairwise Euclidean distances between observed case locations and summarize the overall spatial dispersion used to define a single isotropic bandwidth. This selection method minimizes the asymptotic mean integrated squared error under the assumption of an approximately normal underlying distribution and is widely adopted as a robust, data-driven approach for bandwidth determination in KDE. This bandwidth selection was applied consistently throughout the remainder of the paper, including both the simulation study and the real data analysis.

Figure 4.1 (left) depicts an example of spatial distribution of infectious individuals across a grid, with each black dot representing an infected person. Figure 4.1 (right) presents the corresponding heat map generated using Gaussian KDE. The spatial bandwidth parameter, h_s, determines the degree of smoothing: smaller values of h_s capture fine-scale transmission patterns, such as within-household or neighborhood-level spread, whereas larger values smooth over broader spatial scales, suitable for slower-spreading diseases or settings with delayed reporting. As demonstrated, regions exhibiting stronger spatial clustering and higher concentrations of cases generate elevated density values on the KDE surface, which consequently assigns them greater selection probabilities. This visualization demonstrates how KDE effectively identifies transmission hotspots by detecting local aggregations of cases.

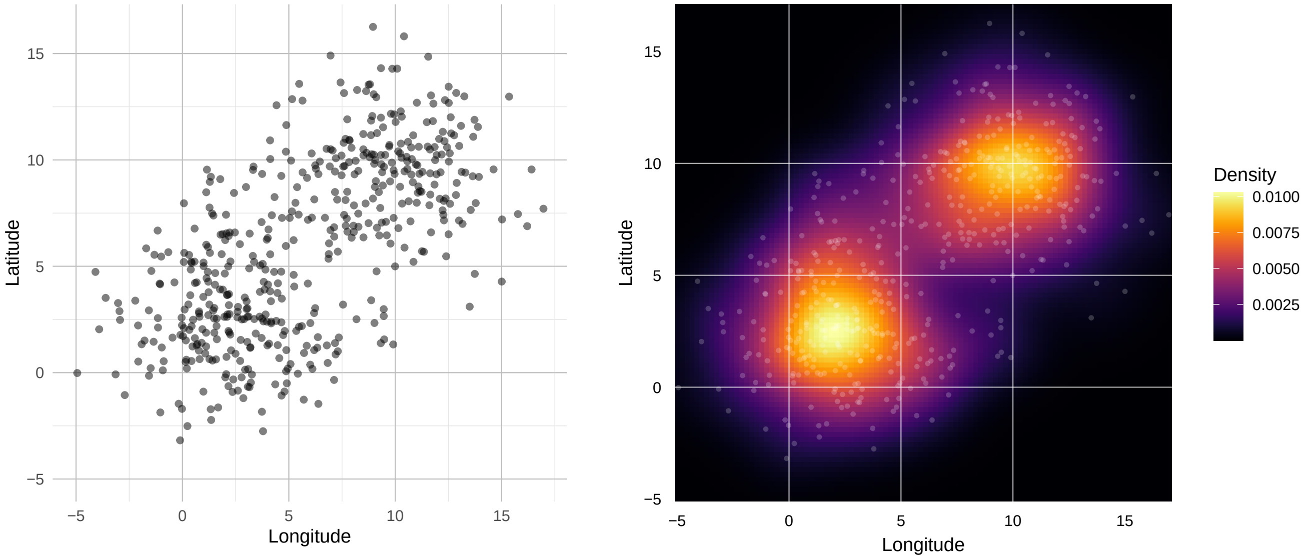

Figure 4.1: Example of KDE-based hotspot identification: (Left) Spatial distribution of infectious individuals (black dots); (Right) Gaussian KDE heatmap, where higher density regions correspond to probable transmission hotspots.

Within our framework, selection probabilities are further refined by incorporating the infectiousness profile of each individual, which reflects the temporal progression of infectiousness after infection. Individuals who were infected recently or are at the peak of their infectious period are assigned higher selection probabilities, given their greater potential to drive ongoing transmission [33]. Conversely, individuals approaching the end of their infectious period contribute less to the density surface [33].

To model this temporal dynamic, we adopt a truncated exponential decay function. Let t_j denote the infectious onset time of individual j, and $t - t_j$ represent the time since infection, constrained to $0 \leqslant t - t_j \leqslant \rho$, where ρ is the infectious period. The infectiousness function is defined as:

$$\eta(t - t_j) = \exp\left[\frac{\ln(\varepsilon)}{\rho}(t - t_j)\right]\mathbf{1}_{\{0 \leqslant t - t_j \leqslant \rho\}}. \tag{4.3.1}$$

This function ensures that infectiousness decays from 1 at $t = t_j$ to a minimum threshold ε (e.g., $\varepsilon = 0.01$) at $t = t_j + \rho$. This truncated exponential form provides a biologically plausible representation of the infectious period, reflecting the empirical observation that individuals are most infectious shortly after infectious onset, with infectious potential declining rapidly due to the immune response, behavioral adaptations, or treatment. The exponential decay function captures this pattern efficiently and supports a more realistic estimation of transmission risk in KDE-based sampling.

Figure 4.2 illustrates the infectiousness profile of an individual over time following the infectious onset, assuming an infectious period of 8 days, modeled with an exponential decay function. The vertical axis represents relative infectiousness, while the horizontal axis denotes time since infection. The curve demonstrates a steep initial decline, with peak transmissibility occurring immediately after infectious onset, consistent with biological evidence of early-stage infectiousness.

To evaluate the spatial distribution of infectious individuals over time, we introduce a temporally-weighted KDE approach. This method estimates the spatial intensity of infectiousness at a specific time point t, where each individual's contribution to the spatial density is scaled by their current level of infectiousness. Let each infectious individual be located at (x_j, y_j) with infection time t_j. The KDE is then evaluated at any spatial location (x, y) and time t, incorporating both spatial proximity and temporal infectiousness.

We employ a Gaussian kernel for spatial smoothing and an exponential decay function to model

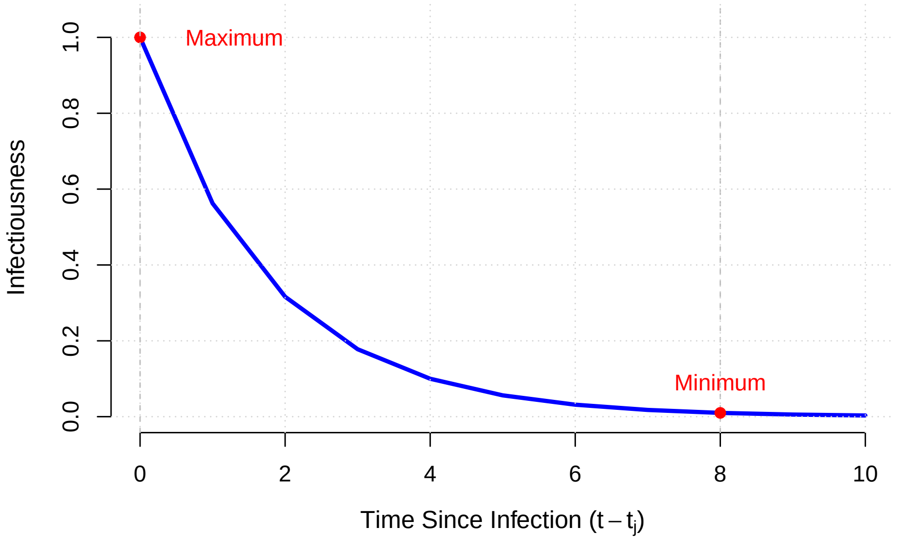

Figure 4.2: Infectiousness profile over time, modeled with a truncated exponential decay function, assuming an 8-day infectious period and $\varepsilon = 0.01$.

infectiousness. The resulting temporally-weighted KDE is defined as:

$$f_t(x, y) = \frac{1}{2\pi h_s^2} \frac{\sum_{j \in I(t,z,\zeta(z))} \eta(t - t_j) \exp\left[-\frac{(x-x_j)^2 + (y-y_j)^2}{2h_s^2}\right]}{\sum_{j \in I(t,z,\zeta(z))} \eta(t - t_j)}, \tag{4.3.2}$$

where $\eta(t - t_j)$ is defined in (4.3.1). This formulation enables the KDE to reflect time-varying transmission potential: areas with recently infected, spatially clustered individuals yield higher density estimates and are flagged as likely hotspots. In contrast, infections that are temporally distant or spatially isolated are down-weighted due to their lower epidemiological relevance. As a result, this approach produces a dynamic, data-driven representation of spatial transmission risk that closely mirrors the naturally occurring clustering patterns of infectious disease spread.

It is important to distinguish this method from full spatiotemporal KDE [39], which applies kernel smoothing jointly across space and time:

$$f_{st}(x, y) = \frac{1}{n h_s^2 h_t} \sum_{i=1}^{n} K_s\left(\frac{x - x_i}{h_s}, \frac{y - y_i}{h_s}\right) K_t\left(\frac{t - t_i}{h_t}\right),$$

where $K_t(\cdot)$ is the temporal kernel function and h_t is the temporal bandwidth. While the spatiotemporal KDE smooths events across both dimensions, our temporally-weighted KDE maintains spatial resolution at each time point and incorporates temporal variation through time-dependent weights $\eta(t - t_j)$.

To operationalize the proposed sampling method based on the temporally-weighted KDE, we developed a probabilistic algorithm that balances epidemiological fidelity with computational efficiency. The algorithm is designed to preserve spatial clustering by focusing on geographic areas with high infection intensity and to ensure temporal continuity by tracking individuals throughout their infectious periods. These features are essential for accurately representing transmission dynamics and capturing the full contribution of each infectious individual. The algorithm proceeds sequentially for time points $t = 1$ to T, following the steps outlined below.

Step 1: Identification of Infectious Individuals

To accurately model transmission dynamics, it is crucial to identify all individuals currently infectious within the focal region and its neighboring regions at each time point. This ensures that both local infections and spatial spillover infections are properly accounted for. Formally, at discrete time t for region z, the infectious set is defined as:

$$I(t, z, \zeta(z)) = \{ j \mid t - \rho + 1 \leqslant t_j \leqslant t, \quad j \in z \cup \zeta(z) \} .$$

This definition ensures that all individuals whose infectious onset occurred within the last ρ discrete time units are considered actively infectious at time t.

Step 2: Sampling Threshold

Given potentially large variations in the number of infectious individuals, computational tractability requires limiting the number of individuals included in the analysis. To achieve this, we define a sampling threshold $n_{\max}$, which places an upper limit on the size of the infectious set. Let $| \cdot |$ represent the cardinality of a set. If $|I(t, z, \phi(z))| < n_{\max}$, then no sampling is performed, and the full infectious set is retained, i.e., $I_s(t, z, \zeta(z)) = I(t, z, \zeta(z))$, where $I_s(t, z, \phi(z))$ denotes the final infectious sample. The total infectious load experienced by a susceptible individual i is $\Psi(i, t, z, \zeta(z))$

given in (4.2.1). However, if $|I(t, z, \zeta(z))| \geqslant n_{\max}$, a representative sample of size n_s is drawn via the stratified temporally-weighted KDE-based PPS sampling method (described in Step 3).

The sampling threshold $n_{\max}$ is selected based on the distribution of infectious individuals observed in the data. It is set at a level that captures the majority of infection events while preventing excessively large sets that would make computations infeasible. In other words, it reflects a balance between adequately representing high-incidence periods and maintaining manageable computational cost.

Step 3: Stratification

To avoid bias arising from truncated infectious trajectories, sampling must preserve the temporal continuity of infectious individuals. Stratification separates persistently infectious individuals, who became infectious in previous time steps and are therefore retained without sampling, from newly infectious cases, which are sampled using a stratified temporally-weighted KDE-based PPS sampling method. This approach maintains both epidemiological fidelity and statistical robustness.

- **Stratum 1 (Persistently Infectious):**

  This stratum ensures the temporal continuity in infectious trajectories, a critical feature of the KDE-based approach. Unlike naive sampling at every time point, which risks excluding individuals still within their infectious period, our method retains any individual included in the sample at time $t-1$ until their infectious period ends. This guaranties that each individual's full transmission potential is modeled accurately. Without this persistence, truncated infectious trajectories would distort transmission dynamics and bias parameter estimates related to secondary infections and contact structures. Formally, individuals sampled at $t-1$ and still infectious at time t form the set:

  $$I_{\text{persist}}(t, z, \zeta(z)) = \{ j \in I(t-1, z, \zeta(z)) \mid t_j \geqslant t - \rho + 1 \}.$$

- **Stratum 2 (Newly Infectious):**

  This stratum contains individuals whose infectious onset occurs at the current time t. These are identified by removing persistently infectious individuals (Stratum 1) from the full infectious set:

$$I_{\text{new}}(t,z,\zeta(z)) = I(t,z,\zeta(z)) \backslash I_{\text{persist}}(t,z,\zeta(z)) = \{j \mid t_j = t,\ j \in z \cup \zeta(z)\}.$$

Let ξ represent the sampling fraction, and $\lceil \cdot \rceil$ maps a real number to the smallest integer greater than or equal to it. From the subset $I_{\text{new}}(t,z,\zeta(z))$, a PPS sample $I_{\text{pps}}(t,z,\zeta(z))$ of size $n_s = \lceil \xi \times |I_{\text{new}}(t,z,\zeta(z))| \rceil$ is drawn with inclusion probabilities:

$$\pi(j,t,z) = n_s \frac{f_t(x_j,y_j)}{\sum_{j' \in I_{\text{new}}(t,z,\zeta(z))} f_t(x_{j'},y_{j'})},$$

where $f_t(x_j,y_j)$ is defined in (4.3.2).

Step 4: Final Sample Assembly and Approximation of Total Infectious Load

The final infectious sample combines individuals from both strata: persistently infectious individuals (fully retained) and the PPS-sampled newly infectious cases. The combined sample is:

$$I_s(t,z,\zeta(z)) = I_{\text{persist}}(t,z,\zeta(z)) \cup I_{\text{pps}}(t,z,\zeta(z)).$$

To ensure unbiased estimation, sampling weights are applied to correct for unequal inclusion probabilities. Accordingly, the total infectious load $\Psi(i,t,z,\zeta(z))$ is approximated by

$$\widetilde{\Psi}(i,t,z,\zeta(z)) = \sum_{j \in I_s(t,z,\zeta(z))} \omega(j,t,z)\widetilde{\Upsilon}_T(j,z)\widetilde{\kappa}(i,j), \tag{4.3.3}$$

where $\widetilde{\kappa}(i,j)$ and $\widetilde{\Upsilon}_T(j,z)$ are approximations of $\kappa(i,j)$ and $\Upsilon_T(j,z)$, respectively, and the weights are

$$\omega(j,t,z) = \begin{cases} \pi^{-1}(j,t,z), & j \in I_{\text{pps}}(t,z,\zeta(z)), \\ 1, & j \in I_{\text{persist}}(t,z,\zeta(z)). \end{cases}$$

The stratified temporally-weighted KDE-based PPS sampling method for the infectious set $I(t,z,\zeta(z))$ is summarized in Algorithm 3.

Algorithm 3 Stratified Temporally-Weighted KDE-Based PPS Sampling of $I(t, z, \zeta(z))$

```
For $t = 1$ to $T$:
    1. Construct $I(t, z, \zeta(z))$: Define $I(t, z, \zeta(z))$ based on the selected sample from the previous time point $I_s(t-1, z, \zeta(z))$.
    2. If $|I(t, z, \zeta(z))| \leqslant n_{\max}$:
        • Return the final sample: Set $I_s(t, z, \zeta(z)) = I(t, z, \zeta(z))$.
        • Return the total infectious load:
            $\Psi(i, t, z, \zeta(z)) = \sum_{j \in I_s(t,z,\zeta(z))} \Upsilon_T(j, z)\kappa(i, j)$
    3. If $|I(t, z, \zeta(z))| > n_{\max}$:
        • Define strata: $I_{\text{persist}}(t, z, \zeta(z))$ (persistently infectious), $I_{\text{new}}(t, z, \zeta(z))$ (newly infectious).
        • Estimate kernel density for each $j \in I(t, z, \zeta(z))$:
            $f_t(x_j, y_j) = \frac{1}{2\pi h_s^2} \frac{\sum_{j' \in I(t,z,\zeta(z))} \eta(t - t_{j'}) \exp\left[-\frac{(x_j - x_{j'})^2 + (y_j - y_{j'})^2}{2h_s^2}\right]}{\sum_{j' \in I(t,z,\zeta(z))} \eta(t - t_{j'})}.$
        • Compute inclusion probabilities for sampling:
            $\pi(j, t, z) = n_s \frac{f_t(x_j, y_j)}{\sum_{j' \in I_{\text{new}}(t,z,\zeta(z))} f_t(x_{j'}, y_{j'})}, \quad \forall j \in I_{\text{new}}(t, z, \zeta(z))$
        • Draw sample: Take the PPS sample $I_{\text{pps}}(t, z, \zeta(z))$ of size $n_s$ from $I_{\text{new}}(t, z, \zeta(z))$ with inclusion probabilities $\pi(j, t, z)$.
        • Return the final sample:
            $I_s(t, z, \zeta(z)) = I_{\text{persist}}(t, z, \zeta(z)) \cup I_{\text{pps}}(t, z, \zeta(z))$
        • Return the approximated total infectious load:
            $\widetilde{\Psi}(i, t, z, \zeta(z)) = \sum_{j \in I_s(t,z,\zeta(z))} \omega(j, t, z)\widetilde{\Upsilon}_T(j, z)\widetilde{\kappa}(i, j),$
          where
            $\omega(j, t, z) = \begin{cases} \pi^{-1}(j, t, z), & \text{if } j \in I_{\text{pps}}(t, z, \zeta(z)), \\ 1, & \text{if } j \in I_{\text{persist}}(t, z, \zeta(z)). \end{cases}$
```

4.4 Specification of GD-ILM Components

Susceptibility and Transmissibility Functions

We define the susceptibility function $\Upsilon_S(i, z)$ and the transmissibility function $\Upsilon_T(j, z)$ as follows. Let $\mathbf{X}_i$ denote the individual-level covariate vector for susceptible individual $i = 1, \ldots, n$, and $\mathbf{X}_{zS}$ denote the regional-level susceptibility covariate vector for region z. These covariates are incorporated into the susceptibility function $\Upsilon_S(i, z)$. Similarly, let $\mathbf{X}_j$ denote the individual-level covariate vector for infectious unit j, which is included in the transmissibility function $\Upsilon_T(j, z)$. Specifically, the functions are defined as:

$$\Upsilon_S(i, z) = \exp\left(\alpha_S + \mathbf{X}_i^\top \boldsymbol{\beta}_1 + \mathbf{X}_{zS}^\top \boldsymbol{\beta}_2 + \gamma_z\right) \tag{4.4.1}$$

and

$$\Upsilon_T(j, z) = \exp\left(\alpha_T + \mathbf{X}_j^\top \boldsymbol{\beta}_3\right), \tag{4.4.2}$$

where α_S is the susceptibility intercept, and $\boldsymbol{\beta}_1$ and $\boldsymbol{\beta}_2$ are the coefficient vectors corresponding to $\mathbf{X}_i$ and $\mathbf{X}_{zS}$, respectively. Likewise, α_T is the transmissibility intercept, and $\boldsymbol{\beta}_3$ is the coefficient vector associated with $\mathbf{X}_j$. The term γ_z denotes spatial random effects, capturing latent geographic variation or unmeasured covariate effects, typically modeled via a specified spatial structure among regions.

Spatial Random Effect

In this work, we adopt the Leroux model [49] to model the spatial random effects vector $\boldsymbol{\Gamma} = (\gamma_1, \ldots, \gamma_Z)^\top$, as described in Section 1.4.

Infection Kernel

We define the infection kernel as an exponential decay function: $\kappa(i, j) = \exp(-\delta d_{ij})$, where $\delta > 0$ is the spatial decay parameter and d_{ij} represents the distance between susceptible individual i and infectious individual j. We also set $\epsilon(i,t,z) = 0$ for model simplicity. Therefore, our GD-ILM is expressed as:

$$\mathcal{P}_{(i,t,z)}(\Theta) = 1 - \exp\left[-\exp\left(\alpha_S + \mathbf{X}_i^\top \boldsymbol{\beta}_1 + \mathbf{X}_{zS}^\top \boldsymbol{\beta}_2 + \gamma_z\right) \Psi(i,t,z,\zeta(z))\right], \tag{4.4.3}$$

where

$$\Psi(i,t,z,\zeta(z)) = \sum_{j \in I(t,z,\zeta(z))} \exp\left(\alpha_T + \mathbf{X}_j^\top \boldsymbol{\beta}_3 - \delta d_{ij}\right),$$

for $t = 1, \ldots, T$ and $z = 1, \ldots, Z$, if sampling is not needed.

Likelihood and Approximation

Let $\mathbf{y}_c = (\mathbf{y}, \mathbf{z}, \boldsymbol{\Gamma})$ denote the complete data, which includes regional information and spatial random effects, and let $\mathbf{y}$ denote the observed data. Also, let $g(\boldsymbol{\Gamma})$ be the density function proposed by [49], as explained earlier in this paper. Assuming that infection and exposure times are known, the likelihood function of the complete data, including all infection and non-infection events observed throughout the entire epidemic period across all Z regions, is given by

$$\begin{aligned}
\mathcal{L}(\Theta; \mathbf{y}_c) =& p(\mathbf{y}|\mathbf{z}, \boldsymbol{\Gamma}) g(\boldsymbol{\Gamma}) \\
=& \prod_{t=1}^{T} \prod_{z=1}^{Z} \left\{ \prod_{i \in S(t,z)} \left(1 - \mathcal{P}_{(i,t,z)}(\Theta)\right) \prod_{i \in E(t+1,z,\zeta(z)) \backslash E(t,z,\zeta(z))} \mathcal{P}_{(i,t,z)}(\Theta) \right\} \\
& \times \left\{ (2\pi)^{-Z/2} (\tau^2)^{Z/2} |(1-\lambda)\mathbf{I}_Z + \lambda \mathcal{R}|^{1/2} \exp\left(-\frac{1}{2} \boldsymbol{\Gamma}^\top \left\{ \tau^2 \left[(1-\lambda)\mathbf{I}_Z + \lambda \mathcal{R} \right] \right\} \boldsymbol{\Gamma} \right) \right\},
\end{aligned}$$

where $S(t,z)$ is the set of susceptible individuals who are uninfected at time t in region z, and $E(t+1,z,\zeta(z)) \backslash E(t,z,\zeta(z))$ is the set of newly exposed individuals at time t in region z.

By taking a sample $I_s(t,z,\zeta(z))$ from the infectious set $I(t,z,\zeta(z))$ using the sampling method described previously, we then approximate the $\mathcal{P}_{(i,t,z)}(\Theta)$ by $\widetilde{\mathcal{P}}_{(i,t,z)}(\Theta)$, given as follows:

$$\mathcal{P}_{(i,t,z)}(\Theta) \approx \widetilde{\mathcal{P}}_{(i,t,z)}(\Theta) = 1 - \exp\left[-\exp\left(\alpha_S + \mathbf{X}_i^\top \boldsymbol{\beta}_1 + \mathbf{X}_{zS}^\top \boldsymbol{\beta}_2 + \gamma_z\right) \widetilde{\Psi}(i,t,z,\zeta(z))\right], \tag{4.4.4}$$

where $\widetilde{\Psi}(i,t,z,\zeta(z))$ is defined in (4.3.3), with

$$\widetilde{\kappa}(i,j) = \exp\left(-\widetilde{\delta} d_{ij}\right),$$

and

$$\widetilde{\Upsilon}_T(j,z) = \exp\left(\widetilde{\alpha}_T + \mathbf{X}_j^\top \widetilde{\boldsymbol{\beta}}_3\right).$$

Here, $\widetilde{\delta}$, $\widetilde{\alpha}_T$, and $\widetilde{\boldsymbol{\beta}}_3$ are approximations of δ, α_T, and $\boldsymbol{\beta}_3$, respectively. This approximation leads to an approximate likelihood function $\mathcal{L}(\Theta;\mathbf{y}_c)$, denoted by $\widetilde{\mathcal{L}}(\Theta;\mathbf{y}_c)$, which is given by

$$\begin{aligned}\widetilde{\mathcal{L}}(\Theta;\mathbf{y}_c) =& \widetilde{p}(\mathbf{y}|\mathbf{z},\mathbf{\Gamma})g(\mathbf{\Gamma}) \qquad (4.4.5)\\ =& \prod_{t=1}^{T}\prod_{z=1}^{Z}\left\{\prod_{i\in S(t,z)}\left(1-\widetilde{\mathcal{P}}_{(i,t,z)}(\Theta)\right)\prod_{i\in E_s(t+1,z,\zeta(z))\setminus E_s(t,z,\zeta(z))}\widetilde{\mathcal{P}}_{(i,t,z)}(\Theta)\right\}\\ &\times\left\{(2\pi)^{-Z/2}(\tau^2)^{Z/2}|(1-\lambda)\mathbf{I}_Z+\lambda\mathcal{R}|^{1/2}\exp\left(-\frac{1}{2}\mathbf{\Gamma}^\top\left\{\tau^2\left[(1-\lambda)\mathbf{I}_Z+\lambda\mathcal{R}\right]\right\}\mathbf{\Gamma}\right)\right\}.\end{aligned}$$

This approach leads to the calculation of the total infectious load based on a significantly smaller subset $I_s(t,z,\zeta(z))$ in $\widetilde{\mathcal{P}}_{(i,t,z)}(\Theta)$, rather than the full set $I(t,z,\zeta(z))$ used in $\mathcal{P}_{(i,t,z)}(\Theta)$. Likewise, the likelihood $\mathcal{L}(\Theta;\mathbf{y}_c)$ is evaluated over the reduced set of exposed individuals $E_s(t,z,\zeta(z))$ in $\widetilde{\mathcal{L}}(\Theta;\mathbf{y}_c)$ instead of the full set $E(t,z,\zeta(z))$. These reductions lead to more efficient computations in each iteration of the MCECM algorithm. Therefore, we intend to estimate the parameter vector $\Theta = (\alpha_S, \widetilde{\alpha}_T, \boldsymbol{\beta}_1, \boldsymbol{\beta}_2, \widetilde{\boldsymbol{\beta}}_3, \widetilde{\delta}, \tau, \lambda)$.

4.5 Parameter Estimation of GD-ILM

We estimate the GD-ILM parameters specified in (4.4.4) using the MCECM algorithm, based on the stratified temporally-weighted KDE-based PPS sampling method and the approximated maximum likelihood in (4.4.5), with $\mathbf{\Gamma}$ treated as latent. The complete MCECM procedure is summarized in Algorithm 4.

Algorithm 4 MCECM

```
Initialize the set of parameters $\Theta^{(0)} = (\alpha_S^{(0)}, \widetilde{\alpha}_T^{(0)}, \boldsymbol{\beta}_1^{(0)}, \boldsymbol{\beta}_2^{(0)}, \widetilde{\boldsymbol{\beta}}_3^{(0)}, \widetilde{\delta}^{(0)}, \tau^{(0)}, \lambda^{(0)})$.
Repeat
    E-Step: Consider $g(\boldsymbol{\Gamma})$ as the candidate density and $p(\boldsymbol{\Gamma}|\mathbf{y}) \propto p(\mathbf{y}|\mathbf{z}, \boldsymbol{\Gamma}) g(\boldsymbol{\Gamma})$ as the target density. At iteration $(k+1)$ of the MCECM algorithm, with current values $\Theta^{(k)}$:
        For $(l = 1, \ldots, L)$
        Given the current value of $\boldsymbol{\Gamma}_l^{(k+1)}$, generate $r \sim \text{Uniform}(0,1)$ and take a sample $\widetilde{\boldsymbol{\Gamma}} \sim p(\boldsymbol{\Gamma}|\mathbf{y}; \Theta^{(k)})$ using the Metropolis-Hastings method.
            If $r \leqslant \frac{p(\mathbf{y}|\mathbf{z}, \widetilde{\boldsymbol{\Gamma}})}{p(\mathbf{y}|\mathbf{z}, \boldsymbol{\Gamma}_l^{(k+1)})}$, Then
                $\boldsymbol{\Gamma}_{l+1}^{(k+1)} = \widetilde{\boldsymbol{\Gamma}}$
            Else
                $\boldsymbol{\Gamma}_{l+1}^{(k+1)} = \boldsymbol{\Gamma}_l^{(k+1)}$
            End If
        End For
    Return the approximated expectation $\widetilde{Q}(\Theta \mid \Theta^{(k+1)})$ given in (4.5.1), using the random sample $\{\boldsymbol{\Gamma}_1^{(k+1)}, \boldsymbol{\Gamma}_2^{(k+1)}, \ldots, \boldsymbol{\Gamma}_L^{(k+1)}\}$ generated from $p(\boldsymbol{\Gamma}|\mathbf{y}; \Theta^{(k)})$.

    M-Step: Maximize $\widetilde{Q}(\Theta \mid \Theta^{(k)})$, with respect to the following model parameters to obtain $\Theta^{(k+1)}$.

        CM-Step 1: Update $\alpha_S^{(k+1)}$ using (4.5.2).
        CM-Step 2: Let $\alpha_S = \alpha_S^{(k+1)}$. Update $\boldsymbol{\beta}_1^{(k+1)}$ using (4.5.3).
        CM-Step 3: Let $(\alpha_S, \boldsymbol{\beta}_1) = (\alpha_S^{(k+1)}, \boldsymbol{\beta}_1^{(k+1)})$. Update $\boldsymbol{\beta}_2^{(k+1)}$ using (4.5.4).
        CM-Step 4: Let $(\alpha_S, \boldsymbol{\beta}_1, \boldsymbol{\beta}_2) = (\alpha_S^{(k+1)}, \boldsymbol{\beta}_1^{(k+1)}, \boldsymbol{\beta}_2^{(k+1)})$. Update $\widetilde{\alpha}_T^{(k+1)}$ using (4.5.5).
        CM-Step 5: Let $(\alpha_S, \alpha_T, \boldsymbol{\beta}_1, \boldsymbol{\beta}_2) = (\alpha_S^{(k+1)}, \widetilde{\alpha}_T^{(k+1)}, \boldsymbol{\beta}_1^{(k+1)}, \boldsymbol{\beta}_2^{(k+1)})$. Update $\widetilde{\boldsymbol{\beta}}_3^{(k+1)}$ using (4.5.6).
        CM-Step 6: Let $(\alpha_S, \alpha_T, \boldsymbol{\beta}_1, \boldsymbol{\beta}_2, \boldsymbol{\beta}_3) = (\alpha_S^{(k+1)}, \widetilde{\alpha}_T^{(k+1)}, \boldsymbol{\beta}_1^{(k+1)}, \boldsymbol{\beta}_2^{(k+1)}, \widetilde{\boldsymbol{\beta}}_3^{(k+1)})$. Update $\widetilde{\delta}^{(k+1)}$ using (4.5.7).
        CM-Step 7: Let $(\tau, \lambda) = (\tau^{(k)}, \lambda^{(k)})$. Update $(\tau^{(k+1)}, \lambda^{(k+1)})$ using (4.5.8-4.5.12)
Until the set $\Theta^{(k+1)}$ satisfies $\|\Theta^{(k+1)} - \Theta^{(k)}\|_2 < \epsilon_\Theta$, where $\| \cdot \|_2$ denotes the Euclidean norm, and $\epsilon_\Theta$ is a small convergence threshold.
Return the optimal value $\hat{\Theta} = \Theta^{(k+1)}$.
```

We also apply the SAECM algorithm to estimate the GD-ILM parameters specified in (4.4.4), using the stratified temporally-weighted KDE-based PPS sampling method and the approximated maximum likelihood in (4.4.5), while treating $\mathbf{\Gamma}$ as latent. The SAECM procedure is summarized in Algorithm 5.

Algorithm 5 SAECM

```
Initialize the set of parameters $\Theta^{(0)} = (\alpha_S^{(0)}, \widetilde{\alpha}_T^{(0)}, \boldsymbol{\beta}_1^{(0)}, \boldsymbol{\beta}_2^{(0)}, \widetilde{\boldsymbol{\beta}}_3^{(0)}, \widetilde{\delta}^{(0)}, \tau^{(0)}, \lambda^{(0)})$ and $\widetilde{Q}^{(0)}(\Theta) = 0$.
Repeat
    E-Step: At iteration $(k+1)$ of the SAECM algorithm, with current values $\Theta^{(k)}$:
            Generate $\mathbf{\Gamma}^{(k+1)} \sim p(\mathbf{\Gamma}|\mathbf{y};\Theta^{(k)})$ and update the step size $s^{(k+1)} = (k+1)^{-\zeta_{\mathrm{SA}}}, \quad \zeta_{\mathrm{SA}} \in (0.5, 1]$.
    Return the approximated expectation $\widetilde{Q}^{(k+1)}(\Theta)$ given in (4.5.13).
    M-Step: Maximize $\widetilde{Q}^{(k+1)}(\Theta)$, with respect to the following model parameters to obtain $\Theta^{(k+1)}$.
        CM-Step 1: Update $\alpha_S^{(k+1)}$ using (4.5.2).
        CM-Step 2: Let $\alpha_S = \alpha_S^{(k+1)}$. Update $\boldsymbol{\beta}_1^{(k+1)}$ using (4.5.3).
        CM-Step 3: Let $(\alpha_S, \boldsymbol{\beta}_1) = (\alpha_S^{(k+1)}, \boldsymbol{\beta}_1^{(k+1)})$. Update $\boldsymbol{\beta}_2^{(k+1)}$ using (4.5.4).
        CM-Step 4: Let $(\alpha_S, \boldsymbol{\beta}_1, \boldsymbol{\beta}_2) = (\alpha_S^{(k+1)}, \boldsymbol{\beta}_1^{(k+1)}, \boldsymbol{\beta}_2^{(k+1)})$. Update $\widetilde{\alpha}_T^{(k+1)}$ using (4.5.5).
        CM-Step 5: Let $(\alpha_S, \alpha_T, \boldsymbol{\beta}_1, \boldsymbol{\beta}_2) = (\alpha_S^{(k+1)}, \widetilde{\alpha}_T^{(k+1)}, \boldsymbol{\beta}_1^{(k+1)}, \boldsymbol{\beta}_2^{(k+1)})$. Update $\widetilde{\boldsymbol{\beta}}_3^{(k+1)}$ using (4.5.6).
        CM-Step 6: Let $(\alpha_S, \alpha_T, \boldsymbol{\beta}_1, \boldsymbol{\beta}_2, \boldsymbol{\beta}_3) = (\alpha_S^{(k+1)}, \widetilde{\alpha}_T^{(k+1)}, \boldsymbol{\beta}_1^{(k+1)}, \boldsymbol{\beta}_2^{(k+1)}, \widetilde{\boldsymbol{\beta}}_3^{(k+1)})$. Update $\widetilde{\delta}^{(k+1)}$ using (4.5.7).
        CM-Step 7: Let $(\tau, \lambda) = (\tau^{(k)}, \lambda^{(k)})$. Update $(\tau^{(k+1)}, \lambda^{(k+1)})$ using (4.5.14-4.5.18)
Until the set $\Theta^{(k+1)}$ satisfies $\|\Theta^{(k+1)} - \Theta^{(k)}\|_2 < \epsilon_\Theta$, where $\|\cdot\|_2$ denotes the Euclidean norm, and $\epsilon_\Theta$ is a small convergence threshold.
Return the optimal value $\hat{\Theta} = \Theta^{(k+1)}$.
```

4.5.1 CM-Steps in MCECM Algorithm 4

Let $\Upsilon_S'^{(\cdot,\cdot,\cdot)}(i,z)$, $\Upsilon_S''^{(\cdot,\cdot,\cdot)}(i,z)$, $\widetilde{\Psi}'^{(\cdot,\cdot,\cdot)}(i,t,z,\zeta(z))$, and $\widetilde{\Psi}''^{(\cdot,\cdot,\cdot)}(i,t,z,\zeta(z))$ be defined in Table 4.1.

Table 4.1: Definitions used in CM-Steps in MCECM Algorithm

$(\cdot,\cdot,\cdot)$	$\Upsilon_S'^{(\cdot,\cdot,\cdot)}(i,z)$
(0,0,0)	$\exp\left(\alpha_S^{(k)} + \mathbf{X}_i^\top \boldsymbol{\beta}_1^{(k)} + \mathbf{X}_{zS}^\top \boldsymbol{\beta}_2^{(k)}\right)$
(1,0,0)	$\mathbf{X}_i \exp\left(\alpha_S^{(k+1)} + \mathbf{X}_i^\top \boldsymbol{\beta}_1^{(k)} + \mathbf{X}_{zS}^\top \boldsymbol{\beta}_2^{(k)}\right)$
(1,1,0)	$\mathbf{X}_{zS} \exp\left(\alpha_S^{(k+1)} + \mathbf{X}_i^\top \boldsymbol{\beta}_1^{(k+1)} + \mathbf{X}_{zS}^\top \boldsymbol{\beta}_2^{(k)}\right)$
(1,1,1)	$\exp\left(\alpha_S^{(k+1)} + \mathbf{X}_i^\top \boldsymbol{\beta}_1^{(k+1)} + \mathbf{X}_{zS}^\top \boldsymbol{\beta}_2^{(k+1)}\right)$
$(\cdot,\cdot,\cdot)$	$\Upsilon_S''^{(\cdot,\cdot,\cdot)}(i,z)$
(0,0,0)	$\exp\left(2\alpha_S^{(k)} + 2\mathbf{X}_i^\top \boldsymbol{\beta}_1^{(k)} + 2\mathbf{X}_{zS}^\top \boldsymbol{\beta}_2^{(k)}\right)$
(1,0,0)	$\mathbf{X}_i \mathbf{X}_i^\top \exp\left(2\alpha_S^{(k+1)} + 2\mathbf{X}_i^\top \boldsymbol{\beta}_1^{(k)} + 2\mathbf{X}_{zS}^\top \boldsymbol{\beta}_2^{(k)}\right)$
(1,1,0)	$\mathbf{X}_{zS} \mathbf{X}_{zS}^\top \exp\left(2\alpha_S^{(k+1)} + 2\mathbf{X}_i^\top \boldsymbol{\beta}_1^{(k+1)} + 2\mathbf{X}_{zS}^\top \boldsymbol{\beta}_2^{(k)}\right)$
(1,1,1)	$\exp\left(2\alpha_S^{(k+1)} + 2\mathbf{X}_i^\top \boldsymbol{\beta}_1^{(k+1)} + 2\mathbf{X}_{zS}^\top \boldsymbol{\beta}_2^{(k+1)}\right)$
$(\cdot,\cdot,\cdot)$	$\widetilde{\Psi}'^{(\cdot,\cdot,\cdot)}(i,t,z,\zeta(z))$
(0,0,0)	$\sum_{j \in I_s(t,z,\zeta(z))} \omega(j,t,z) \exp\left(\widetilde{\alpha}_T^{(k)} + \mathbf{X}_j^\top \widetilde{\boldsymbol{\beta}}_3^{(k)} - \widetilde{\delta}^{(k)} d_{ij}\right)$
(1,0,0)	$\sum_{j \in I_s(t,z,\zeta(z))} \omega(j,t,z) \mathbf{X}_j \exp\left(\widetilde{\alpha}_T^{(k+1)} + \mathbf{X}_j^\top \widetilde{\boldsymbol{\beta}}_3^{(k)} - \widetilde{\delta}^{(k)} d_{ij}\right)$
(1,1,0)	$-\sum_{j \in I_s(t,z,\zeta(z))} \omega(j,t,z) d_{ij} \exp\left(\widetilde{\alpha}_T^{(k+1)} + \mathbf{X}_j^\top \widetilde{\boldsymbol{\beta}}_3^{(k+1)} - \widetilde{\delta}^{(k)} d_{ij}\right)$
$(\cdot,\cdot,\cdot)$	$\widetilde{\Psi}''^{(\cdot,\cdot,\cdot)}(i,t,z,\zeta(z))$
(1,0,0)	$\sum_{j \in I_s(t,z,\zeta(z))} \omega(j,t,z) \mathbf{X}_j \mathbf{X}_j^\top \exp\left(\widetilde{\alpha}_T^{(k+1)} + \mathbf{X}_j^\top \widetilde{\boldsymbol{\beta}}_3^{(k)} - \widetilde{\delta}^{(k)} d_{ij}\right)$
(1,1,0)	$\sum_{j \in I_s(t,z,\zeta(z))} \omega(j,t,z) d_{ij} \exp\left(\widetilde{\alpha}_T^{(k+1)} + \mathbf{X}_j^\top \widetilde{\boldsymbol{\beta}}_3^{(k+1)} - \widetilde{\delta}^{(k)} d_{ij}\right)$

The approximated expectation is given by $\widetilde{Q}(\Theta \mid \Theta^{(k)}) = \frac{1}{L}\sum_{l=1}^{L} \ln \widetilde{\mathcal{L}}(\Theta; \mathbf{y}, \boldsymbol{\Gamma}_l^{(k)})$. Therefore,

$$\begin{aligned}
\widetilde{Q}(\Theta \mid \Theta^{(k)}) &= \frac{1}{L}\sum_{t=1}^{T} \sum_{i \in S(t,z)} \sum_{z=1}^{Z} \sum_{l=1}^{L} \left[-\exp(\alpha_S + \mathbf{X}_i^\top \boldsymbol{\beta}_2 + \mathbf{X}_{zS}^\top \boldsymbol{\beta}_2 + \gamma_{zl}) \widetilde{\Psi}(i,t,z,\zeta(z)) \Big| \mathbf{y} \right] \\
&+ \frac{1}{L}\sum_{t=1}^{T} \sum_{i \in E_s(t+1,z,\zeta(z)) \setminus E_s(t,z,\zeta(z))} \sum_{z=1}^{Z} \sum_{l=1}^{L} \left(\ln \left\{ 1 - \exp[\exp(\alpha_S + \mathbf{X}_i^\top \boldsymbol{\beta}_1 + \mathbf{X}_{zS}^\top \boldsymbol{\beta}_2 + \gamma_{zl}) \widetilde{\Psi}(i,t,z,\zeta(z))] \right\} \Bigg| \mathbf{y} \right) \\
&- \frac{Z}{2}\ln(2\pi) + \frac{Z}{2}\ln(\tau^2) + \frac{1}{2}\ln\left(|\lambda \mathcal{R} + (1-\lambda)\mathbf{I}|\right) - \frac{\tau^2}{2}\frac{1}{L}\sum_{l=1}^{L} \left[(\boldsymbol{\Gamma}_l^{(k)})^\top (\lambda \mathcal{R} + (1-\lambda)\mathbf{I}) \, (\boldsymbol{\Gamma}_l^{(k)}) | \mathbf{y} \right].
\end{aligned} \tag{4.5.1}$$

CM-Step 1: Update α_S using the following recursive relationship

$$\alpha_S^{(k+1)} = \alpha_S^{(k)} - \frac{\frac{\partial}{\partial \alpha_S}\widetilde{Q}(\Theta \mid \Theta^{(k)})}{\frac{\partial^2}{\partial \alpha_S^2}\widetilde{Q}(\Theta \mid \Theta^{(k)})}, \tag{4.5.2}$$

where

$$\begin{aligned}
\frac{\partial \widetilde{Q}(\Theta \mid \Theta^{(k)})}{\partial \alpha_S} &= -\sum_{t=1}^{T}\sum_{i\in S(t,z)}\sum_{z=1}^{Z}\Upsilon_S'^{(0,0,0)}\,(i,z)\,\widetilde{\Psi}'^{(0,0,0)}(i,t,z,\zeta(z)) \\
&\times \frac{1}{L}\sum_{l=1}^{L}\left[\exp(\gamma_{zl})|\mathbf{y},\Theta^{(k)}\right] + \sum_{t=1}^{T}\sum_{i\in E_s(t+1,z,\zeta(z))\setminus E_s(t,z,\zeta(z))}\sum_{z=1}^{Z}\Upsilon_S'^{(0,0,0)}\,(i,z) \\
&\times \widetilde{\Psi}'^{(0,0,0)}(i,t,z,\zeta(z))\frac{1}{L}\sum_{l=1}^{L}\left[\frac{\left(1-\widetilde{\mathcal{P}}_{(i,t,z)}(\Theta)\right)}{\widetilde{\mathcal{P}}_{(i,t,z)}(\Theta)}\exp(\gamma_{zl})\Big|\mathbf{y},\Theta^{(k)}\right],
\end{aligned}$$

and

$$\begin{aligned}
\frac{\partial^2 \widetilde{Q}(\Theta \mid \Theta^{(k)})}{\partial^2 \alpha_S} &= -\sum_{t=1}^{T}\sum_{i\in S(t,z)}\sum_{z=1}^{Z}\Upsilon_S'^{(0,0,0)}\,(i,z)\,\widetilde{\Psi}'^{(0,0,0)}(i,t,z,\zeta(z)) \\
&\times \frac{1}{L}\sum_{l=1}^{L}\left[\exp(\gamma_{zl})\Big|\mathbf{y},\Theta^{(k)}\right] + \sum_{t=1}^{T}\sum_{i\in E_s(t+1,z,\zeta(z))\setminus E_s(t,z,\zeta(z))}\sum_{z=1}^{Z}\Upsilon_S'^{(0,0,0)}\,(i,z)\,\widetilde{\Psi}'^{(0,0,0)}(i,t,z,\zeta(z)) \\
&\times \frac{1}{L}\sum_{l=1}^{L}\left[\frac{\left(1-\widetilde{\mathcal{P}}_{(i,t,z)}(\Theta)\right)}{\widetilde{\mathcal{P}}_{(i,t,z)}(\Theta)}\exp(\gamma_{zl})\Big|\mathbf{y},\Theta^{(k)}\right] - \left(\Upsilon_S''^{(0,0,0)}\,(i,z)\right)\left[\widetilde{\Psi}'^{(0,0,0)}(i,t,z,\zeta(z))\right]^2 \\
&\times \frac{1}{L}\sum_{l=1}^{L}\left[\frac{\left(1-\widetilde{\mathcal{P}}_{(i,t,z)}(\Theta)\right)}{\left(\widetilde{\mathcal{P}}_{(i,t,z)}(\Theta)\right)^2}\exp(2\gamma_{zl})\Big|\mathbf{y},\Theta^{(k)}\right].
\end{aligned}$$

CM-Step 2: Update $\boldsymbol{\beta}_1$ using the following recursive relationship

$$\boldsymbol{\beta}_1^{(k+1)} = \boldsymbol{\beta}_1^{(k)} - \frac{\frac{\partial}{\partial \boldsymbol{\beta}_1}\widetilde{Q}(\Theta \mid \Theta^{(k)})}{\frac{\partial^2}{\partial \boldsymbol{\beta}_1 \partial \boldsymbol{\beta}_1^\top}\widetilde{Q}(\Theta \mid \Theta^{(k)})}, \tag{4.5.3}$$

where

$$\begin{aligned}\frac{\partial \widetilde{Q}(\Theta \mid \Theta^{(k)})}{\partial \boldsymbol{\beta}_1} &= -\sum_{t=1}^{T} \sum_{i \in S(t,z)} \sum_{z=1}^{Z} \Upsilon_S'^{(1,0,0)}(i,z)\, \widetilde{\Psi}'^{(0,0,0)}(i,t,z,\zeta(z)) \\ &\times \frac{1}{L}\sum_{l=1}^{L}\Big[\exp(\gamma_{zl})\Big|\mathbf{y}, \Theta^{(k)}\Big] + \sum_{t=1}^{T} \sum_{i \in E_s(t+1,z,\zeta(z)) \setminus E_s(t,z,\zeta(z))} \sum_{z=1}^{Z} \Upsilon_S'^{(1,0,0)}(i,z) \\ &\times \widetilde{\Psi}'^{(0,0,0)}(i,t,z,\zeta(z)) \frac{1}{L}\sum_{l=1}^{L}\left[\frac{\Big(1-\widetilde{\mathcal{P}}_{(i,t,z)}(\Theta)\Big)}{\widetilde{\mathcal{P}}_{(i,t,z)}(\Theta)}\exp(\gamma_{zl})\Bigg|\mathbf{y}, \Theta^{(k)}\right],\end{aligned}$$

and

$$\begin{aligned}\frac{\partial^2 \widetilde{Q}(\Theta \mid \Theta^{(k)})}{\partial \boldsymbol{\beta}_1 \partial \boldsymbol{\beta}_1^\top} &= -\sum_{t=1}^{T} \sum_{i \in S(t,z)} \sum_{z=1}^{Z} \Upsilon_S'^{(1,0,0)}(i,z)\, \mathbf{X}_i^\top \widetilde{\Psi}'^{(0,0,0)}(i,t,z,\zeta(z)) \\ \times \frac{1}{L}\sum_{l=1}^{L}\Big[\exp(\gamma_{zl})\Big|\mathbf{y}, \Theta^{(k)}\Big] &+ \sum_{t=1}^{T} \sum_{i \in E_s(t+1,z,\zeta(z)) \setminus E_s(t,z,\zeta(z))} \sum_{z=1}^{Z} \Upsilon_S'^{(1,0,0,0,0)}(i,z)\, \mathbf{X}_i^\top \widetilde{\Psi}'^{(0,0,0)}(i,t,z,\zeta(z)) \\ \times \frac{1}{L}\sum_{l=1}^{L}&\left[\frac{\Big(1-\widetilde{\mathcal{P}}_{(i,t,z)}(\Theta)\Big)}{\widetilde{\mathcal{P}}_{(i,t,z)}(\Theta)}\exp(\gamma_{zl})\Bigg|\mathbf{y}, \Theta^{(k)}\right] - \Big(\Upsilon_S''^{(1,0,0)}(i,z)\Big)\Big[\widetilde{\Psi}'^{(0,0,0)}(i,t,z,\zeta(z))\Big]^2 \\ \times \frac{1}{L}\sum_{l=1}^{L}&\left[\frac{\Big(1-\widetilde{\mathcal{P}}_{(i,t,z)}(\Theta)\Big)}{\Big(\widetilde{\mathcal{P}}_{(i,t,z)}(\Theta)\Big)^2}\exp(2\gamma_{zl})\Bigg|\mathbf{y}, \Theta^{(k)}\right].\end{aligned}$$

CM-Step 3: Update $\boldsymbol{\beta}_2$ using the following recursive relationship

$$\boldsymbol{\beta}_2^{(k+1)} = \boldsymbol{\beta}_2^{(k)} - \frac{\frac{\partial}{\partial \boldsymbol{\beta}_2}\widetilde{Q}(\Theta \mid \Theta^{(k)})}{\frac{\partial^2}{\partial \boldsymbol{\beta}_2 \partial \boldsymbol{\beta}_2^\top}\widetilde{Q}(\Theta \mid \Theta^{(k)})}, \tag{4.5.4}$$

where

$$\begin{aligned}\frac{\partial \widetilde{Q}(\Theta \mid \Theta^{(k)})}{\partial \boldsymbol{\beta}_2} &= -\sum_{t=1}^{T} \sum_{i \in S(t,z)} \sum_{z=1}^{Z} \Upsilon_S'^{(1,1,0)}(i,z)\, \widetilde{\Psi}'^{(0,0,0)}(i,t,z,\zeta(z)) \\ &\times \frac{1}{L}\sum_{l=1}^{L}\Big[\exp(\gamma_{zl})\Big|\mathbf{y}, \Theta^{(k)}\Big] + \sum_{t=1}^{T} \sum_{i \in E_s(t+1,z,\zeta(z)) \setminus E_s(t,z,\zeta(z))} \sum_{z=1}^{Z} \Upsilon_S'^{(1,1,0)}(i,z) \\ &\times \widetilde{\Psi}'^{(0,0,0)}(i,t,z,\zeta(z)) \frac{1}{L}\sum_{l=1}^{L}\left[\frac{\Big(1-\widetilde{\mathcal{P}}_{(i,t,z)}(\Theta)\Big)}{\widetilde{\mathcal{P}}_{(i,t,z)}(\Theta)}\exp(\gamma_{zl})\Bigg|\mathbf{y}, \Theta^{(k)}\right],\end{aligned}$$

and

$$\frac{\partial^2 \widetilde{Q}(\Theta \mid \Theta^{(k)})}{\partial \boldsymbol{\beta}_2 \partial \boldsymbol{\beta}_2^\top} = -\sum_{t=1}^{T} \sum_{i \in S(t,z)} \sum_{z=1}^{Z} \Upsilon_S'^{(1,1,0)}\,(i,z)\, \mathbf{X}_{zS}^\top \widetilde{\Psi}'^{(0,0,0)}(i,t,z,\zeta(z))$$

$$\times \frac{1}{L} \sum_{l=1}^{L} \Big[\exp(\gamma_{zl}) \Big| \mathbf{y}, \Theta^{(k)} \Big] + \sum_{t=1}^{T} \sum_{i \in E_s(t+1,z,\zeta(z)) \setminus E_s(t,z,\zeta(z))} \sum_{z=1}^{Z} \Upsilon_S'^{(1,1,0,0,0)}\,(i,z)\, \mathbf{X}_{zS}^\top \widetilde{\Psi}'^{(0,0,0)}(i,t,z,\zeta(z))$$

$$\times \frac{1}{L} \sum_{l=1}^{L} \left[\frac{\Big(1 - \widetilde{\mathcal{P}}_{(i,t,z)}(\Theta)\Big)}{\widetilde{\mathcal{P}}_{(i,t,z)}(\Theta)} \exp(\gamma_{zl}) \bigg| \mathbf{y}, \Theta^{(k)} \right] - \Big(\Upsilon_S''^{(1,1,0}\,(i,z) \Big) \Big[\widetilde{\Psi}'^{(0,0,0)}(i,t,z,\zeta(z)) \Big]^2$$

$$\times \frac{1}{L} \sum_{l=1}^{L} \left[\frac{\Big(1 - \widetilde{\mathcal{P}}_{(i,t,z)}(\Theta)\Big)}{\Big(\widetilde{\mathcal{P}}_{(i,t,z)}(\Theta)\Big)^2} \exp(2\gamma_{zl}) \bigg| \mathbf{y}, \Theta^{(k)} \right].$$

CM-Step 4: Update $\widetilde{\alpha}_T$ using the following recursive relationship

$$\widetilde{\alpha}_T^{(k+1)} = \widetilde{\alpha}_T^{(k)} - \frac{\frac{\partial}{\partial \widetilde{\alpha}_T} \widetilde{Q}(\Theta \mid \Theta^{(k)})}{\frac{\partial^2}{\partial^2 \widetilde{\alpha}_T} \widetilde{Q}(\Theta \mid \Theta^{(k)})}, \tag{4.5.5}$$

where

$$\frac{\partial \widetilde{Q}(\Theta \mid \Theta^{(k)})}{\partial \widetilde{\alpha}_T} = -\sum_{t=1}^{T} \sum_{i \in S(t,z)} \sum_{z=1}^{Z} \Upsilon_S'^{(1,1,1)}\,(i,z)\, \widetilde{\Psi}'^{(0,0,0)}(i,t,z,\zeta(z))$$

$$\times \frac{1}{L} \sum_{l=1}^{L} \Big[\exp(\gamma_{zl}) \Big| \mathbf{y}, \Theta^{(k)} \Big] + \sum_{t=1}^{T} \sum_{i \in E_s(t+1,z,\zeta(z)) \setminus E_s(t,z,\zeta(z))} \sum_{z=1}^{Z} \Upsilon_S'^{(1,1,1)}\,(i,z)$$

$$\times \widetilde{\Psi}'^{(0,0,0)}(i,t,z,\zeta(z)) \frac{1}{L} \sum_{l=1}^{L} \left[\frac{\Big(1 - \widetilde{\mathcal{P}}_{(i,t,z)}(\Theta)\Big)}{\widetilde{\mathcal{P}}_{(i,t,z)}(\Theta)} \exp(\gamma_{zl}) \bigg| \mathbf{y}, \Theta^{(k)} \right],$$

and

$$\begin{aligned}
\frac{\partial^2 \widetilde{Q}(\Theta \mid \Theta^{(k)})}{\partial^2 \widetilde{\alpha}_T} &= -\sum_{t=1}^{T} \sum_{i \in S(t,z)} \sum_{z=1}^{Z} \Upsilon_S'^{(1,1,1)}(i,z)\, \widetilde{\Psi}'^{(0,0,0)}(i,t,z,\zeta(z)) \\
&\times \frac{1}{L}\sum_{l=1}^{L} \Big[\exp(\gamma_{zl}) \Big| \mathbf{y}, \Theta^{(k)}\Big] + \sum_{t=1}^{T} \sum_{i \in E_s(t+1,z,\zeta(z)) \setminus E_s(t,z,\zeta(z))} \sum_{z=1}^{Z} \Upsilon_S'^{(1,1,1)}(i,z)\, \widetilde{\Psi}'^{(0,0,0)}(i,t,z,\zeta(z)) \\
&\times \frac{1}{L}\sum_{l=1}^{L} \left[\frac{\Big(1-\widetilde{\mathcal{P}}_{(i,t,z)}(\Theta)\Big)}{\widetilde{\mathcal{P}}_{(i,t,z)}(\Theta)} \exp(\gamma_{zl}) \Bigg| \mathbf{y}, \Theta^{(k)} \right] - \Big(\Upsilon_S''^{(1,1,1)}(i,z)\Big) \Big[\widetilde{\Psi}'^{(0,0,0)}(i,t,z,\zeta(z))\Big]^2 \\
&\times \frac{1}{L}\sum_{l=1}^{L} \left[\frac{\Big(1-\widetilde{\mathcal{P}}_{(i,t,z)}(\Theta)\Big)}{\Big(\widetilde{\mathcal{P}}_{(i,t,z)}(\Theta)\Big)^2} \exp(2\gamma_{zl}) \Bigg| \mathbf{y}, \Theta^{(k)} \right].
\end{aligned}$$

CM-Step 5: Update $\widetilde{\boldsymbol{\beta}}_3$ using the following recursive relationship

$$\widetilde{\boldsymbol{\beta}}_3^{(k+1)} = \widetilde{\boldsymbol{\beta}}_3^{(k)} - \frac{\frac{\partial}{\partial \widetilde{\boldsymbol{\beta}}_3} \widetilde{Q}(\Theta \mid \Theta^{(k)})}{\frac{\partial^2}{\partial \widetilde{\boldsymbol{\beta}}_3 \partial \widetilde{\boldsymbol{\beta}}_3^{\top}} \widetilde{Q}(\Theta \mid \Theta^{(k)})}, \tag{4.5.6}$$

where
$$\begin{aligned}
\frac{\partial \widetilde{Q}(\Theta \mid \Theta^{(k)})}{\partial \widetilde{\boldsymbol{\beta}}_3} &= -\sum_{t=1}^{T} \sum_{i \in S(t,z)} \sum_{z=1}^{Z} \Upsilon_S'^{(1,1,1)}(i,z)\, \widetilde{\Psi}'^{(1,0,0)}(i,t,z,\zeta(z)) \\
&\times \frac{1}{L}\sum_{l=1}^{L} \Big[\exp(\gamma_{zl}) \Big| \mathbf{y}, \Theta^{(k)}\Big] + \sum_{t=1}^{T} \sum_{i \in E_s(t+1,z,\zeta(z)) \setminus E_s(t,z,\zeta(z))} \sum_{z=1}^{Z} \Upsilon_S'^{(1,1,1)}(i,z) \\
&\times \widetilde{\Psi}'^{(1,0,0)}(i,t,z,\zeta(z)) \frac{1}{L}\sum_{l=1}^{L} \left[\frac{\Big(1-\widetilde{\mathcal{P}}_{(i,t,z)}(\Theta)\Big)}{\widetilde{\mathcal{P}}_{(i,t,z)}(\Theta)} \exp(\gamma_{zl}) \Bigg| \mathbf{y}, \Theta^{(k)} \right],
\end{aligned}$$

and

$$\begin{aligned}\frac{\partial^2 \widetilde{Q}(\Theta \mid \Theta^{(k)})}{\partial \widetilde{\boldsymbol{\beta}}_3 \partial \widetilde{\boldsymbol{\beta}}_3^\top} &= -\sum_{t=1}^{T}\sum_{i\in S(t,z)}\sum_{z=1}^{Z} \Upsilon'^{(1,1,1)}_S(i,z)\,\widetilde{\Psi}''^{(1,0,0)}(i,t,z,\zeta(z)) \\ &\times \frac{1}{L}\sum_{l=1}^{L}\left[\exp(\gamma_{zl})\Big|\mathbf{y},\Theta^{(k)}\right] + \sum_{t=1}^{T}\sum_{i\in E_s(t+1,z,\zeta(z))\setminus E_s(t,z,\zeta(z))}\sum_{z=1}^{Z}\Upsilon'^{(1,1,1)}_S(i,z)\,\widetilde{\Psi}''^{(1,0,0)}(i,t,z,\zeta(z)) \\ &\times \frac{1}{L}\sum_{l=1}^{L}\left[\frac{\left(1-\widetilde{\mathcal{P}}_{(i,t,z)}(\Theta)\right)}{\widetilde{\mathcal{P}}_{(i,t,z)}(\Theta)}\exp(\gamma_{zl})\Bigg|\mathbf{y},\Theta^{(k)}\right] - \left(\Upsilon''^{(1,1,1)}_S(i,z)\right)\left[\widetilde{\Psi}'^{(1,0,0)}(i,t,z,\zeta(z))\right] \\ &\times \left(\widetilde{\Psi}'^{(1,0,0)}(i,t,z,\zeta(z))\right)^\top \frac{1}{L}\sum_{l=1}^{L}\left[\frac{\left(1-\widetilde{\mathcal{P}}_{(i,t,z)}(\Theta)\right)}{\left(\widetilde{\mathcal{P}}_{(i,t,z)}(\Theta)\right)^2}\exp(2\gamma_{zl})\Bigg|\mathbf{y},\Theta^{(k)}\right].\end{aligned}$$

CM-Step 6: Update $\widetilde{\delta}$ using the following recursive relationship

$$\widetilde{\delta}^{(k+1)} = \widetilde{\delta}^{(k)} - \frac{\frac{\partial}{\partial\widetilde{\delta}}\widetilde{Q}(\Theta \mid \Theta^{(k)})}{\frac{\partial^2}{\partial^2\widetilde{\delta}}\widetilde{Q}(\Theta \mid \Theta^{(k)})}, \tag{4.5.7}$$

where

$$\begin{aligned}\frac{\partial \widetilde{Q}(\Theta \mid \Theta^{(k)})}{\partial \widetilde{\delta}} &= -\sum_{t=1}^{T}\sum_{i\in S(t,z)}\sum_{z=1}^{Z} \Upsilon'^{(1,1,1)}_S(i,z)\,\widetilde{\Psi}'^{(1,1,0)}(i,t,z,\zeta(z)) \\ &\times \frac{1}{L}\sum_{l=1}^{L}\left[\exp(\gamma_{zl})\Big|\mathbf{y},\Theta^{(k)}\right] + \sum_{t=1}^{T}\sum_{i\in E_s(t+1,z,\zeta(z))\setminus E_s(t,z,\zeta(z))}\sum_{z=1}^{Z}\Upsilon'^{(1,1,1)}_S(i,z) \\ &\times \widetilde{\Psi}'^{(1,1,0)}(i,t,z,\zeta(z))\frac{1}{L}\sum_{l=1}^{L}\left[\frac{\left(1-\widetilde{\mathcal{P}}_{(i,t,z)}(\Theta)\right)}{\widetilde{\mathcal{P}}_{(i,t,z)}(\Theta)}\exp(\gamma_{zl})\Bigg|\mathbf{y},\Theta^{(k)}\right],\end{aligned}$$

and

$$
\begin{aligned}
\frac{\partial^2 \widetilde{Q}(\Theta \mid \Theta^{(k)})}{\partial^2 \widetilde{\delta}} &= -\sum_{t=1}^{T} \sum_{i \in S(t,z)} \sum_{z=1}^{Z} \Upsilon_S'^{(1,1,1)}\,(i,z)\, \widetilde{\Psi}''^{(1,1,0)}(i,t,z,\zeta(z)) \\
&\times \frac{1}{L} \sum_{l=1}^{L} \left[\exp(\gamma_{zl}) \middle| \mathbf{y}, \Theta^{(k)} \right] + \sum_{t=1}^{T} \sum_{i \in E_s(t+1,z,\zeta(z)) \setminus E_s(t,z,\zeta(z))} \sum_{z=1}^{Z} \Upsilon_S'^{(1,1,1)}\,(i,z)\, \widetilde{\Psi}''^{(1,1,0)}(i,t,z,\zeta(z)) \\
&\times \frac{1}{L} \sum_{l=1}^{L} \left[\frac{\left(1 - \widetilde{\mathcal{P}}_{(i,t,z)}(\Theta)\right)}{\widetilde{\mathcal{P}}_{(i,t,z)}(\Theta)} \exp(\gamma_{zl}) \middle| \mathbf{y}, \Theta^{(k)} \right] - \left(\Upsilon_S''^{(1,1,1)}\,(i,z) \right) \left[\widetilde{\Psi}''^{(1,1,0)}(i,t,z,\zeta(z)) \right]^2 \\
&\times \frac{1}{L} \sum_{l=1}^{L} \left[\frac{\left(1 - \widetilde{\mathcal{P}}_{(i,t,z)}(\Theta)\right)}{\left(\widetilde{\mathcal{P}}_{(i,t,z)}(\Theta)\right)^2} \exp(2\gamma_{zl}) \middle| \mathbf{y}, \Theta^{(k)} \right].
\end{aligned}
$$

CM-Step 7: In the (k+1)th iteration, the score vector A and the expected information matrix B are used to estimate τ and λ, respectively. Given

$$
\mathbb{E}\left[\ln p(\mathbf{\Gamma}^{(k+1)}; \tau, \lambda)\right] = -\tfrac{Z}{2} \ln(2\pi) + \tfrac{Z}{2} \ln(\tau^2) + \tfrac{1}{2} \ln\left(|\lambda \mathcal{R} + (1-\lambda)\mathbf{I}|\right) - \tfrac{\tau^2}{2} \tfrac{1}{L} \textstyle\sum_{l=1}^{L} \left[(\mathbf{\Gamma}_l^{(k)})^\top (\lambda \mathcal{R} + (1-\lambda)\mathbf{I})\, (\mathbf{\Gamma}_l^{(k)}) \right],
$$

the elements of A and B can be defined as follows:

$$
A(\tau) = \frac{\partial \mathbb{E}\left[\ln p(\mathbf{\Gamma}^{(k+1)}; \tau, \lambda)\right]}{\partial \tau} = \frac{Z}{\tau} - \tau \frac{1}{L} \sum_{l=1}^{L} \left[(\mathbf{\Gamma}_l^{(k)})^\top (\lambda \mathcal{R} + (1-\lambda)\mathbf{I})\, (\mathbf{\Gamma}_l^{(k)}) \right], \tag{4.5.8}
$$

$$
A(\lambda) = \frac{\partial \mathbb{E}\left[\ln p(\mathbf{\Gamma}^{(k+1)}; \tau, \lambda)\right]}{\partial \lambda} = \frac{1}{2} \mathrm{tr}\left\{ (\lambda \mathcal{R} + [1-\lambda]\mathbf{I}]^{-1} (\mathcal{R} - \mathbf{I}) \right\} - \frac{\tau^2}{2} \frac{1}{L} \sum_{l=1}^{L} \left\{ (\mathbf{\Gamma}_l^{(k)})^\top [\lambda \mathcal{R} + (1-\lambda)\mathbf{I}]\, (\mathbf{\Gamma}_l^{(k)}) \right\}, \tag{4.5.9}
$$

$$
B(\tau, \tau) = \frac{\partial^2 \mathbb{E}\left[\ln p(\mathbf{\Gamma}^{(k+1)}; \tau, \lambda)\right]}{(\partial \tau)^2} = \frac{Z}{\tau^2} + \frac{1}{L} \sum_{l=1}^{L} \left\{ (\mathbf{\Gamma}_l^{(k)})^\top [\lambda \mathcal{R} + (1-\lambda)\mathbf{I}]\, (\mathbf{\Gamma}_l^{(k)}) \right\}, \tag{4.5.10}
$$

$$
B(\tau, \lambda) = \frac{\partial^2 \mathbb{E}\left[\ln p(\mathbf{\Gamma}^{(k+1)}; \tau, \lambda)\right]}{\partial \tau \partial \lambda} = \tau \frac{1}{L} \sum_{l=1}^{L} \left[(\mathbf{\Gamma}_l^{(k)})^\top (\mathcal{R} - \mathbf{I}) (\mathbf{\Gamma}_l^{(k)}) \right], \tag{4.5.11}
$$

$$
B(\lambda, \lambda) = \frac{\partial^2 \mathbb{E}\left[\ln p(\mathbf{\Gamma}^{(k+1)}; \tau, \lambda)\right]}{(\partial \lambda)^2} = \frac{1}{2} \mathrm{tr}\left\{ (\mathcal{R} - \mathbf{I})\, [\lambda \mathcal{R} + (1-\lambda)\mathbf{I}]^{-1} (\mathcal{R} - \mathbf{I})\, [\lambda \mathcal{R} + (1-\lambda)\mathbf{I}]^{-1} \right\}. \tag{4.5.12}
$$

Using the updated score and information matrix, the parameters (τ, λ) are updated via a Newton–Raphson step:

$$\begin{bmatrix} \tau^{(k+1)} \\ \lambda^{(k+1)} \end{bmatrix} = \begin{bmatrix} \tau^{(k)} \\ \lambda^{(k)} \end{bmatrix} - \begin{bmatrix} B(\tau,\tau)^{(k+1)} & B(\tau,\lambda)^{(k+1)} \\ B(\tau,\lambda)^{(k+1)} & B(\lambda,\lambda)^{(k+1)} \end{bmatrix}^{-1} \begin{bmatrix} A^{(k+1)}(\tau) \\ A^{(k+1)}(\lambda) \end{bmatrix}.$$

4.5.2 CM-Steps in SAECM Algorithm 5

The approximated expectation is given by

$$\widetilde{Q}^{(k+1)}(\Theta) = \widetilde{Q}^{(k)}(\Theta) + s^{(k)} \left[\ln \widetilde{\mathcal{L}}(\Theta; \mathbf{y}, \mathbf{\Gamma}^{(k+1)}) - \widetilde{Q}^{(k)}(\Theta) \right].$$

Therefore,

$$\begin{aligned} \widetilde{Q}^{(k+1)}(\Theta) = \widetilde{Q}^{(k)}(\Theta) + s^{(k)} \Bigg\{ & \sum_{t=1}^{T} \sum_{i \in S(t,z)} \sum_{z=1}^{Z} \left[-\exp(\alpha_S + \mathbf{X}_i^\top \boldsymbol{\beta}_2 + \mathbf{X}_{zS}^\top \boldsymbol{\beta}_2 + \gamma_z) \widetilde{\Psi}(i,t,z,\zeta(z)) \middle| \mathbf{y} \right] \\ & + \sum_{t=1}^{T} \sum_{i \in E_s(t+1,z,\zeta(z)) \setminus E_s(t,z,\zeta(z))} \sum_{z=1}^{Z} \left(\ln \left\{ 1 - \exp[\exp(\alpha_S + \mathbf{X}_i^\top \boldsymbol{\beta}_1 + \mathbf{X}_{zS}^\top \boldsymbol{\beta}_2 + \gamma_z) \widetilde{\Psi}(i,t,z,\zeta(z))] \right\} \middle| \mathbf{y} \right) \\ & - \frac{Z}{2} \ln(2\pi) + \frac{Z}{2} \ln(\tau^2) + \frac{1}{2} \ln\left(|\lambda \mathcal{R} + (1-\lambda)\mathbf{I}|\right) - \frac{\tau^2}{2} \left[(\mathbf{\Gamma}^{(k)})^\top (\lambda \mathcal{R} + (1-\lambda)\mathbf{I}) \, (\mathbf{\Gamma}^{(k)}) | \mathbf{y} \right] - \widetilde{Q}^{(k)}(\Theta) \Bigg\}. \end{aligned} \tag{4.5.13}$$

CM-Steps 1 to 6: The CM-Steps 1 to 6 in SAECM are the same as those in MCECM, with $\widetilde{Q}^{(k+1)}(\Theta)$ instead of $\widetilde{Q}(\Theta \mid \Theta^{(k)})$ and with $L = 1$.

CM-Step 7: At each iteration $k+1$, the expectation $\mathbb{E}\left[\ln g(\mathbf{\Gamma}) \mid \mathbf{y}, \Theta^{(k)}\right]$ is approximated recursively using a single sampled realization $\mathbf{\Gamma}^{(k+1)}$ drawn from the conditional distribution. Specifically, the recursive approximation is:

$$\widetilde{Q}^{(k+1)}(\tau,\lambda) = \widetilde{Q}^{(k)}(\tau,\lambda) + s^{(k)} \left[\ln p(\mathbf{\Gamma}^{(k+1)}; \tau, \lambda) - \widetilde{Q}^{(k)}(\tau,\lambda) \right],$$

where

$$\ln p(\mathbf{\Gamma}^{(k+1)}; \tau, \lambda) = -\frac{Z}{2} \ln(2\pi) + \frac{Z}{2} \ln(\tau^2) + \frac{1}{2} \ln |\lambda \mathcal{R} + (1-\lambda)\mathbf{I}| - \frac{\tau^2}{2} (\mathbf{\Gamma}^{(k+1)})^\top [\lambda \mathcal{R} + (1-\lambda)\mathbf{I}] \mathbf{\Gamma}^{(k+1)}.$$

To maximize this expectation with respect to the parameters (τ, λ), we take derivatives of $\ln p(\mathbf{\Gamma}^{(k+1)}; \tau, \lambda)$ with respect to each parameter to form the score vector A and the expected information matrix B. These derivatives are given in equations (4.5.8)-(4.5.12) of CM-Step 7 in MCECM. Then, the score vector and information matrix are updated recursively as:

$$A^{(k+1)}(\tau) = A^{(k)}(\tau) + s^{(k)} \left\{ \frac{Z}{\tau} - \tau(\mathbf{\Gamma}^{(k+1)})^\top [\lambda \mathcal{R} + (1-\lambda)\mathbf{I}]\mathbf{\Gamma}^{(k+1)} - A^{(k)}(\tau) \right\}, \tag{4.5.14}$$

$$A^{(k+1)}(\lambda) = A^{(k)}(\lambda) + s^{(k)} \left[\frac{1}{2}\mathrm{tr}\left\{ [\lambda \mathcal{R} + (1-\lambda)\mathbf{I}]^{-1}(\mathcal{R} - \mathbf{I}) \right\} - \frac{\tau^2}{2}(\mathbf{\Gamma}^{(k+1)})^\top (\mathcal{R} - \mathbf{I})\mathbf{\Gamma}^{(k+1)} - A^{(k)}(\lambda) \right], \tag{4.5.15}$$

$$B^{(k+1)}(\tau, \tau) = B^{(k)}(\tau, \tau) + s^{(k)} \left\{ \frac{Z}{\tau^2} + (\mathbf{\Gamma}^{(k+1)})^\top [\lambda \mathcal{R} + (1-\lambda)\mathbf{I}]\mathbf{\Gamma}^{(k+1)} - B^{(k)}(\tau, \tau) \right\}, \tag{4.5.16}$$

$$B^{(k+1)}(\tau, \lambda) = B^{(k)}(\tau, \lambda) + s^{(k)} \left[\tau(\mathbf{\Gamma}^{(k+1)})^\top (\mathcal{R} - \mathbf{I})\mathbf{\Gamma}^{(k+1)} - B^{(k)}(\tau, \lambda) \right], \tag{4.5.17}$$

$$B^{(k+1)}(\lambda, \lambda) = B^{(k)}(\lambda, \lambda) + s^{(k)} \left[\frac{1}{2}\mathrm{tr}\left\{ (\mathcal{R} - \mathbf{I})[\lambda \mathcal{R} + (1-\lambda)\mathbf{I}]^{-1}(\mathcal{R} - \mathbf{I})[\lambda \mathcal{R} + (1-\lambda)\mathbf{I}]^{-1} \right\} - B^{(k)}(\lambda, \lambda) \right]. \tag{4.5.18}$$

Finally, using the updated score and information matrix, the parameters (τ, λ) are updated via a Newton–Raphson step:

$$\begin{bmatrix} \tau^{(k+1)} \\ \lambda^{(k+1)} \end{bmatrix} = \begin{bmatrix} \tau^{(k)} \\ \lambda^{(k)} \end{bmatrix} - \begin{bmatrix} B^{(k+1)}(\tau, \tau) & B^{(k+1)}(\tau, \lambda) \\ B^{(k+1)}(\tau, \lambda) & B^{(k+1)}(\lambda, \lambda) \end{bmatrix}^{-1} \begin{bmatrix} A^{(k+1)}(\tau) \\ A^{(k+1)}(\lambda) \end{bmatrix}.$$

4.5.3 Variance Estimation of Model Parameters

A key aspect of statistical inference is quantifying the uncertainty of parameter estimates. In the context of MCECM and SAECM, standard errors can be obtained using the method introduced by [54], adapted to our setting. This method expresses the observed information matrix following [8, 7], which is essential for estimating the variance-covariance matrix of the maximum likelihood estimator as the difference between the complete-data and missing-data information matrices.

This section describes how Louis' method is employed within the MCECM and SAECM algorithms to compute standard errors for model parameters. We present separate treatments for each algorithm due to their differing structures and sampling strategies.

MCECM Algorithm

In the MCECM algorithm, the observed information matrix is defined as

$$\mathcal{I}_{\mathrm{o}}(\hat{\Theta};\mathbf{y}) = \mathcal{I}_{\mathrm{c}}(\hat{\Theta};\mathbf{y}) - \mathcal{I}_{\mathrm{m}}(\hat{\Theta};\mathbf{y}),$$

where $\hat{\Theta}$ is the maximum likelihood estimator, and $\mathcal{I}_{\mathrm{c}}$, $\mathcal{I}_{\mathrm{m}}$ are the complete-data and missing-data information matrices, respectively. These matrices are approximated as:

$$\mathcal{I}_{\mathrm{c}}(\Theta;\mathbf{y}) = -\mathbb{E}\left[\frac{\partial^2}{\partial\Theta\partial\Theta^\top}\ln\mathcal{L}(\Theta;\mathbf{y}_c)\middle|\mathbf{y},\Theta\right] = -\frac{1}{L}\sum_{l=1}^{L}\frac{\partial^2}{\partial\Theta\partial\Theta^\top}\ln\mathcal{L}(\Theta;\mathbf{y}_c^{(l)}),$$

and

$$\begin{aligned}\mathcal{I}_{\mathrm{m}}(\Theta;\mathbf{y}) &= \mathbb{E}\left[\left(\frac{\partial}{\partial\Theta}\ln\mathcal{L}(\Theta;\mathbf{y}_c)\right)\left(\frac{\partial}{\partial\Theta^\top}\ln\mathcal{L}(\Theta;\mathbf{y}_c)\right)\middle|\mathbf{y},\Theta\right]\\ &\quad - \mathbb{E}\left[\frac{\partial}{\partial\Theta}\ln\mathcal{L}(\Theta;\mathbf{y}_c)\middle|\mathbf{y},\Theta\right]\mathbb{E}\left[\frac{\partial}{\partial\Theta^\top}\ln\mathcal{L}(\Theta;\mathbf{y}_c)\middle|\mathbf{y},\Theta\right]\\ &= \frac{1}{L}\sum_{l=1}^{L}\frac{\partial}{\partial\Theta}\ln\mathcal{L}(\Theta;\mathbf{y}_c^{(l)})\frac{\partial}{\partial\Theta^\top}\ln\mathcal{L}(\Theta;\mathbf{y}_c^{(l)})\\ &\quad - \left(\frac{1}{L}\sum_{l=1}^{L}\frac{\partial}{\partial\Theta}\ln\mathcal{L}(\Theta;\mathbf{y}_c^{(l)})\right)\left(\frac{1}{L}\sum_{l=1}^{L}\frac{\partial}{\partial\Theta^\top}\ln\mathcal{L}(\Theta;\mathbf{y}_c^{(l)})\right),\end{aligned}$$

where each $\mathbf{y}_c^{(l)} = (\mathbf{y};\mathbf{z};\mathbf{\Gamma}_l)$, with $\mathbf{\Gamma}_l$ for $l = 1,\dots,L$, being drawn from the conditional distribution of missing data given the observed data and parameter Θ estimated via MCECM. At the maximum likelihood estimate $\hat{\Theta}$, the average score function over the Monte Carlo samples satisfies

$$\frac{1}{L}\sum_{l=1}^{L}\frac{\partial}{\partial\Theta}\ln\mathcal{L}(\Theta;\mathbf{y}_c^{(l)})\bigg|_{\Theta=\hat{\Theta}} = 0,$$

which simplifies the observed information matrix to

$$\mathcal{I}_{\mathrm{o}}(\hat{\Theta};\mathbf{y}) = -\frac{1}{L}\sum_{l=1}^{L}\frac{\partial^2}{\partial\Theta\partial\Theta^\top}\ln\mathcal{L}(\hat{\Theta};\mathbf{y}_c^{(l)}) - \frac{1}{L}\sum_{l=1}^{L}\left(\frac{\partial}{\partial\Theta}\ln\mathcal{L}(\hat{\Theta};\mathbf{y}_c^{(l)})\right)\left(\frac{\partial}{\partial\Theta^\top}\ln\mathcal{L}(\hat{\Theta};\mathbf{y}_c^{(l)})\right).$$

The variance-covariance matrix of $\hat{\Theta}$ is estimated as the inverse of the observed information matrix, and its diagonal entries provide the variances of the parameter estimates.

SAECM Algorithm

At each iteration k of the SAECM algorithm, the observed information matrix is updated using a weighted average of the current and previous estimates:

$$\mathcal{I}_{\mathrm{o}}^{(k)}(\Theta^{(k)};\mathbf{y}) \approx (1-s^{(k)})\mathcal{I}_{\mathrm{o}}^{(k-1)}(\Theta^{(k-1)};\mathbf{y}) + s^{(k)}\hat{\mathcal{I}}_{\mathrm{o}}^{(k)}(\Theta^{(k)};\mathbf{y}),$$

where $s^{(k)}$ is a step-size sequence that decreases over time, and $\hat{\mathcal{I}}_{\mathrm{o}}^{(k)}$ is the instantaneous Monte Carlo estimate at iteration k. This recursive formulation gradually refines the approximation of the observed information matrix as the algorithm progresses. Upon convergence, the inverted final estimate $\mathcal{I}_{\mathrm{o}}^{(k)}$ provides the variances of the parameter estimates.

4.6 Simulation Study

To assess both the computational efficiency and estimation performance of the proposed SAECM algorithm, along with the approximated likelihood based on the stratified temporally-weighted KDE-based PPS sampling method, we conducted a comprehensive simulation study at three spatial resolutions: 10×10, 20×20, and 30×30 grids. Each cell in these grids corresponds to a distinct geographic region, enabling us to evaluate how the algorithm scales and performs under varying spatial complexities and resolutions.

Spatial random effects were generated following the Leroux model [49], using fixed parameters $\tau = 0.4$ and $\lambda = 0.6$. We considered varying the number of PCRs within each grid cell to capture heterogeneity in population density. This configuration facilitated the evaluation of the proposed model's robustness and scalability across diverse demographic scenarios.

Table 4.2 presents the distributions employed to randomly generate PCR counts for each grid cell. It also details the grid-specific values for the incubation and infectious periods, as well as the sampling threshold $n_{\max}$ utilized in the approximation procedure.

Figure 4.3 provides a schematic illustration of the simulation, showing a 2×2 grid at time $t = 1$. Within each cell, PCRs were randomly drawn from a Uniform$(50, 100)$ distribution. The simulation began by randomly designating one PCR per grid cell as exposed at $t = 1$. Blue dots represent susceptible PCRs, while red dots denote infected PCRs.

To account for susceptibility and transmissibility dynamics, we included covariates at both the regional and individual levels. Regional covariates were sampled from a Laplace$(0, 1)$ distribution, which accommodates heavier tails and captures regions with extreme values, such as areas with high population density or limited healthcare access. Individual susceptibility covariates were drawn from a Uniform$(0, 1)$ distribution, representing a broad and non-preferential range of host susceptibility and reflecting heterogeneity in immunity, prior exposure, or vaccination coverage. Individual-level covariates related to transmissibility were generated from a standard normal distribution, $\mathcal{N}(0, 1)$, to model natural variation around a population mean and capture behavioral or social factors, such as contact rates, mobility, or adherence to preventive measures that can either increase or decrease the likelihood of infection. Collectively, these simulated covariates provide a realistic and robust framework for assessing the influence of regional and individual factors on disease transmission. The Euclidean distance, denoted d_{ij}, was employed to quantify the separation between PCRs. The spatial decay parameter was set to $\delta = 2.5$.

Using the GD-ILM framework, each simulation began by randomly designating one PCR per grid cell as exposed at time $t = 1$. The model subsequently simulates disease transmission and records the exposure times of PCRs over $T = 100$ discrete time units. For each grid configuration, 500 independent pandemic simulations were conducted, producing 500 datasets per grid size. Parameter estimation was then performed using the MCECM and SAECM algorithms (Algorithms 1 and 2), and their performance was assessed across varying sampling fractions ξ.

Table 4.2: Grid design for the simulation study

Grid Size	Number of PCRs per Cell	Incubation Period	Infectious Period	$n_{\max}$
10×10	Uniform$(50, 100)$	5	7	500
20×20	Uniform$(100, 200)$	4	6	700
30×30	Uniform$(200, 300)$	6	9	1000

The simulation study proceeded in two stages. In the first stage, the MCECM and SAECM

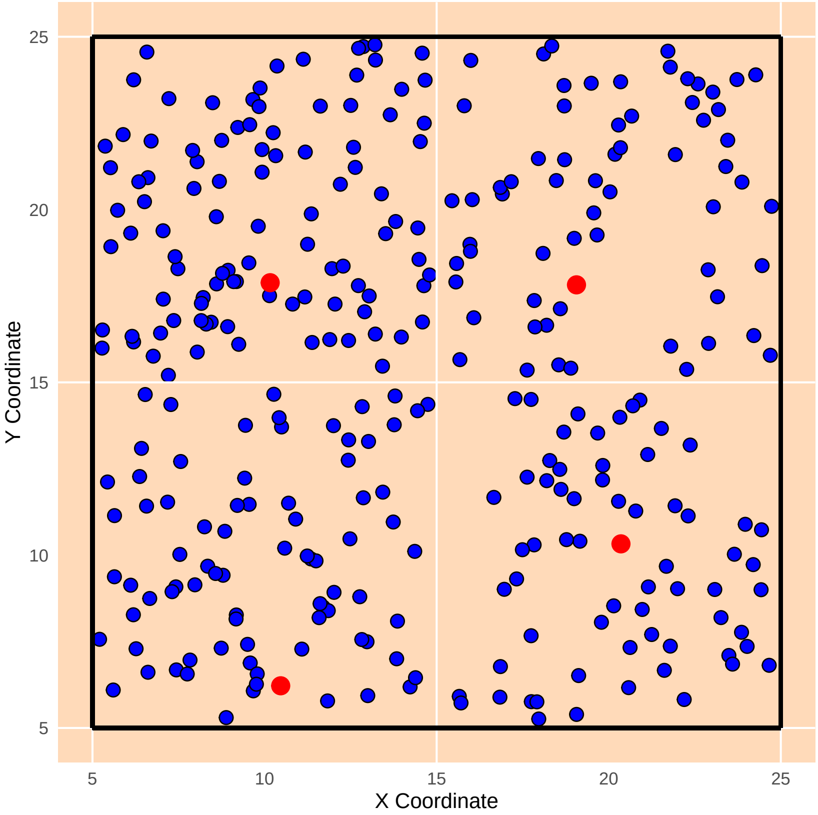

Figure 4.3: A schematic graphical representation of a 2×2 grid simulation at time $t = 1$, showing PCRs randomly generated within each grid cell from a Uniform$(50, 100)$ distribution. Blue dots indicate susceptible PCRs, while red dots represent infected PCRs.

algorithms were implemented using the full likelihood, wherein all infection data were incorporated without sampling ($\xi = 100\%$), to obtain parameter estimates for the GD-ILM model across each grid configuration. This stage established a baseline for assessing parameter estimation accuracy and computational efficiency by recording the time required for parameter estimation across different grid sizes.

Following established guidelines in the stochastic approximation literature, we set $\zeta_{\text{SA}} = 0.6$ for the simulation study. This choice provides a suitable balance, allowing the step size to decay slowly enough to ensure convergence to the true parameter values while keeping the variance of updates manageable. Consequently, $\zeta_{\text{SA}} = 0.6$ supports both the theoretical convergence guarantees and the practical stability of the SAECM procedure within the model fitting framework.

In the second stage, the MCECM and SAECM algorithms were applied using the approximate likelihood, incorporating the stratified temporally-weighted KDE-based PPS sampling method. Different sampling fractions were used for each grid configuration, and the time to convergence for parameter estimation was recorded. This comparison enables the evaluation of efficiency gains and the accuracy trade-offs between using the full dataset and the stratified temporally-weighted KDE-based PPS sampling method.

Through this simulation study, we aimed to assess the proposed model's computational efficiency and robustness across grids with varying sizes, incubation and infectious periods, and population distributions. The MCECM and SAECM algorithms were executed with a convergence threshold of $\epsilon_\Theta = 10^{-3}$, providing a balance between computational efficiency and the stability of parameter estimates.

Finally, we compared the ARBPs given by

$$\text{ARBP} = \left| \frac{\hat{\theta} - \theta}{\theta} \right| \times 100,$$

where $\hat{\theta}$ is the estimated parameter and θ is the true parameter.

Results

The simulation results, summarized in Table 4.3, offer critical insights into the estimation accuracy, robustness, and computational efficiency of the MCECM and SAECM algorithms across different spatial resolutions and sampling fractions.

Across all grid sizes and parameters, both MCECM and SAECM algorithms achieve high estimation accuracy when the full data are utilized ($\xi = 100\%$). The ARBP remains below 2% for nearly all parameters, indicating negligible bias under full likelihood estimation. Standard errors are also minimal, reflecting the stability and consistency of the estimators. Notably, the SAECM algorithm exhibits shorter convergence times compared to MCECM, highlighting its computational efficiency.

As the sampling fraction ξ decreases, ARBP increases across all parameters, reflecting the trade-off between computational efficiency and estimation precision when employing the KDE-based PPS approximation. However, when the sampling fraction is moderate to high (e.g., $\xi = 50\%$–80%), the resulting bias remains within an acceptable range, preserving estimation quality while benefiting from improved computational efficiency.

The increase in bias is especially pronounced at a low sampling fraction (e.g., $\xi = 30\%$), where ARBP exceeds 25% for several parameters, such as α_S, β_1, τ, and δ, particularly in the larger grid sizes. These results highlight that when the sampling fraction is low (e.g., $\xi = 30\%$), estimation accuracy may be substantially compromised, especially in complex or high-resolution spatial settings.

Among all parameters, the estimation of τ and λ appears to be more sensitive to low sampling fractions. For example, with $\xi = 30\%$ on the 30×30 grid, the ARBP for λ reaches over 50% for both algorithms. In contrast, parameters such as α_T and β_3 remain relatively robust, with moderate ARBP values even at lower sampling levels.

Interestingly, in some instances (e.g., β_2 at $\xi = 50\%$), the SAECM algorithm outperforms MCECM in terms of ARBP, suggesting that the stochastic approximation framework may offer greater robustness to data sparsity under certain conditions. However, when the sampling fraction drops further to 30%, both algorithms experience notable degradation in accuracy, with SAECM exhibiting slightly greater resilience.

Increasing the spatial resolution from 10×10 to 30×30 while sampling at a low fraction ($\xi =$

30%) leads to a noticeable increase in ARBP for most parameters. This trend underscores the challenges associated with scaling spatial models and highlights the increased difficulty in maintaining estimation precision under sparse data conditions in higher-resolution grids. For instance, the ARBP for β_1 at $\xi = 30\%$ rises from 24% in the 10×10 grid to 28% in the 20×20 grid, before slightly decreasing to 26% in the 30×30 grid. These findings emphasize the need for caution when applying aggressive subsampling strategies in complex spatial settings.

Similarly, the estimation of the spatial decay parameter δ is accurate when $\xi = 100\%$, with ARBP close to zero. However, at $\xi = 30\%$, ARBP exceeds 27% in all grid sizes. This reflects the critical role that dense infection data play in accurately capturing spatial transmission patterns. Figures 4.4, 4.5, and 4.6 illustrate the ARBP for each parameter across the various grid configurations and sampling fractions.

Table 4.4 presents the convergence time for both algorithms across grid sizes and sampling fractions. A substantial reduction in computational time is observed when switching from MCECM to SAECM, affirming the efficiency gains provided by the stochastic approximation approach. For instance, on the 30×30 grid using the full dataset, SAECM completes estimation in 124 hours compared to 213 hours for MCECM, yielding a 42% reduction in runtime. SAECM consistently outperforms MCECM in terms of speed across all scenarios. This advantage grows with larger grid sizes, reflecting the scalability of SAECM and its suitability for high-dimensional spatial models where the computational burden is a significant concern.

All simulations were executed on a virtual machine hosted within the Manitoba Centre for Health Policy (MCHP) secure environment. The system operated on an AMD EPYC 7H12 64-core processor, with 8 virtual CPUs allocated at 2.60 GHz, running Windows 10 Enterprise LTSC (Version 21H2). The machine was provisioned with an allocated 64 GB of RAM and accessed through the VMware Horizon Client.

Moreover, sampling fractions directly influence convergence time. Reducing ξ from 100% to 30% consistently decreases convergence time by more than 50% across all grid sizes and both algorithms. For example, on the 20×20 grid, SAECM's runtime decreases from 37 hours at full sampling to 13 hours at 30%, a 65% reduction. Figure 4.7 illustrates the convergence time for both algorithms across different grid sizes and sampling fractions.

The simulation study confirms that the proposed SAECM algorithm, when combined with the stratified temporally-weighted KDE-based PPS sampling method, offers a compelling balance between computational efficiency and estimation accuracy. However, when the sampling fraction is as low as 30%, the resulting bias becomes substantially high, particularly for certain spatial parameters and under high-resolution grids. In contrast, for moderate sampling fractions (e.g., ξ = 50%–80%), the bias remains within an acceptable range, making the trade-off justifiable given the substantial gains in computational speed. Notably, the proposed stratified temporally-weighted KDE-based PPS sampling method within the SAECM framework leads to a very time-efficient estimation process, significantly reducing runtime without severely compromising accuracy. For situations that demand real-time or near real-time analysis, the proposed SAECM approach, together with the proposed sampling method, offers a practical alternative to full-data likelihood techniques.

These results show that the proposed SAECM algorithm, paired with the proposed sampling method, offers a reliable and efficient alternative to MCECM, particularly for large-scale spatiotemporal epidemic modeling. Its flexibility and scalability make it a strong candidate for use in public health surveillance systems where rapid, reliable parameter estimation is essential.

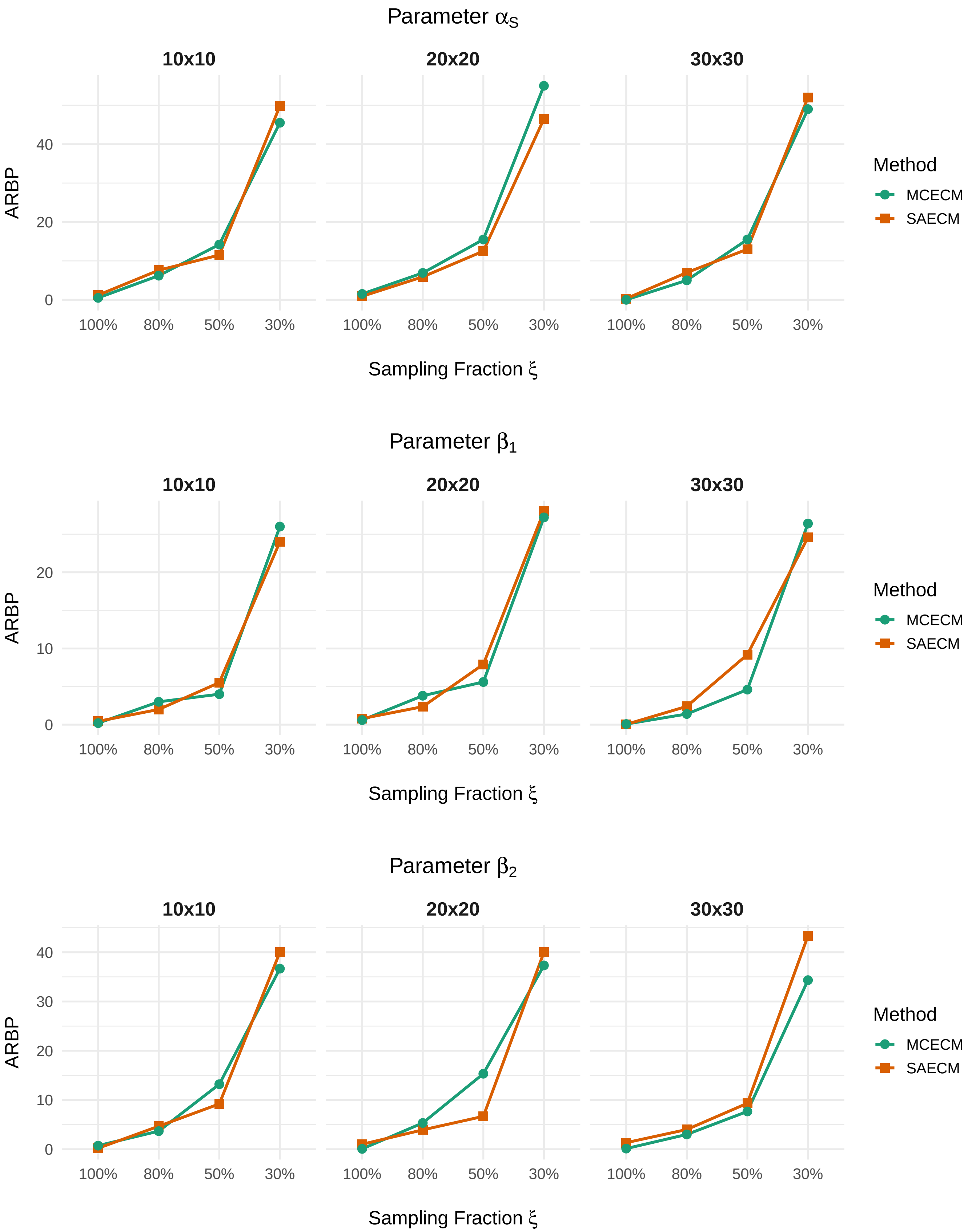

Figure 4.4: The ARBP for the estimated parameters α_S, β_1, and β_2.

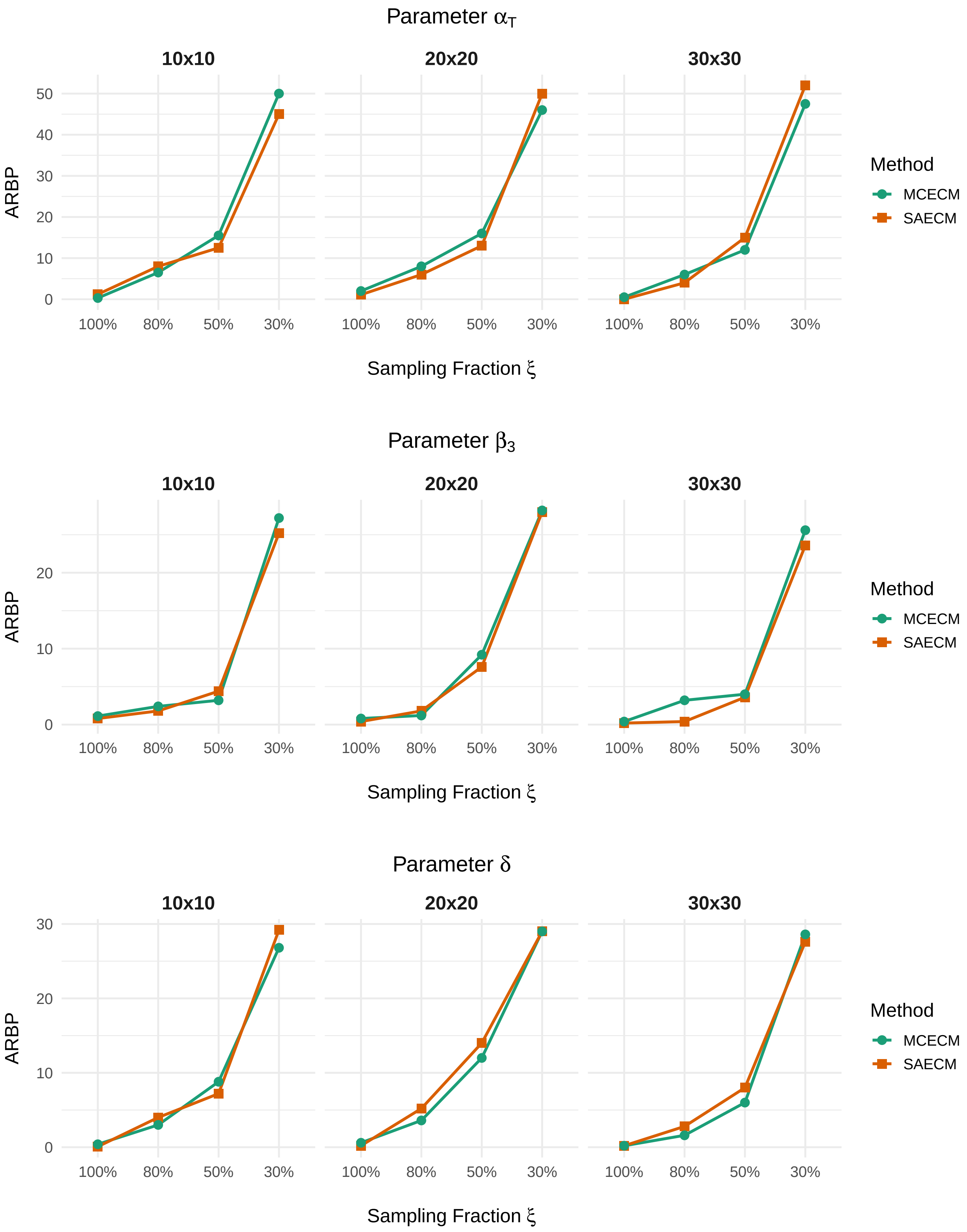

Figure 4.5: The ARBP for the estimated parameters α_T, β_3, and δ.

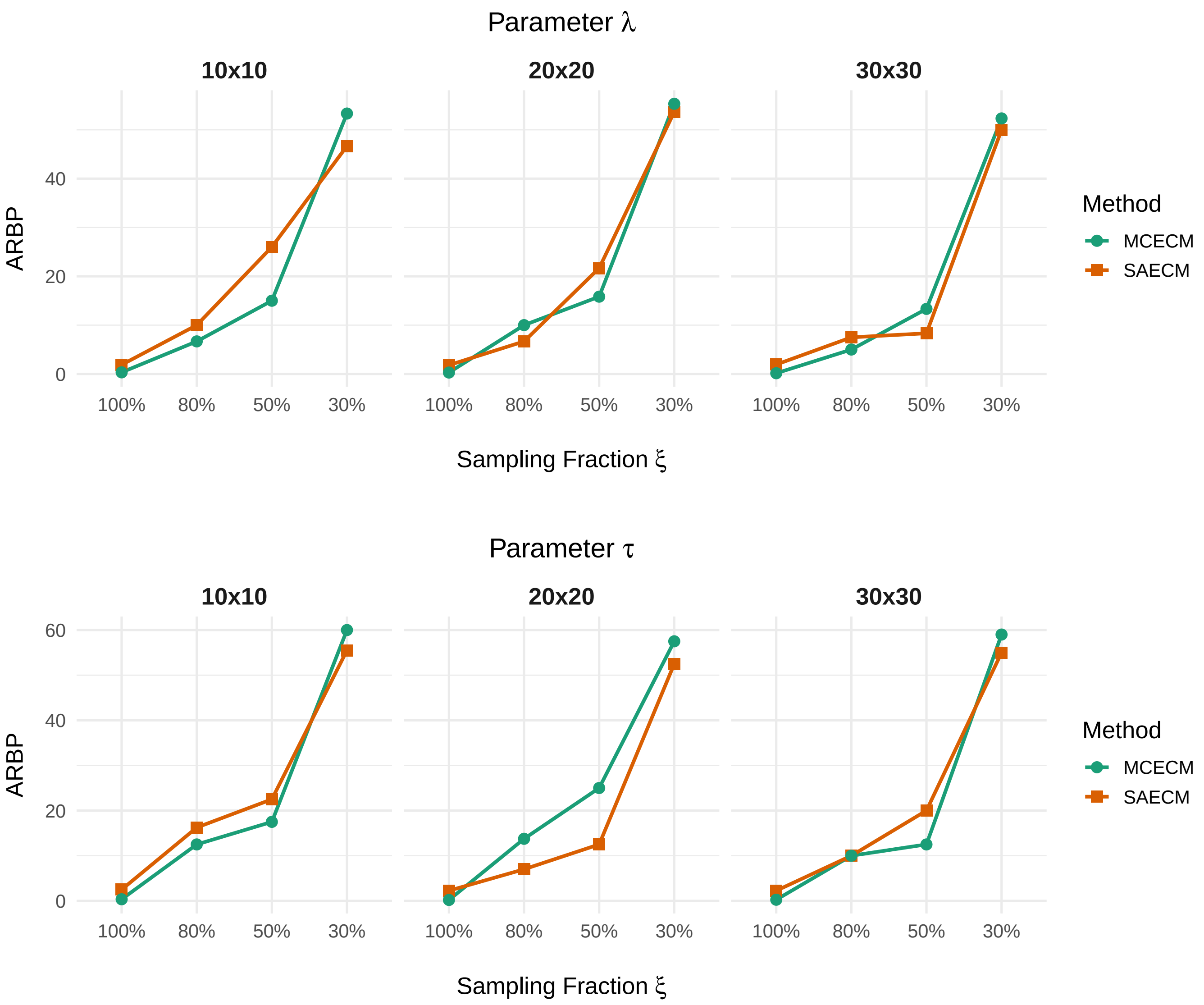

Figure 4.6: The ARBP for the estimated parameters λ and τ.

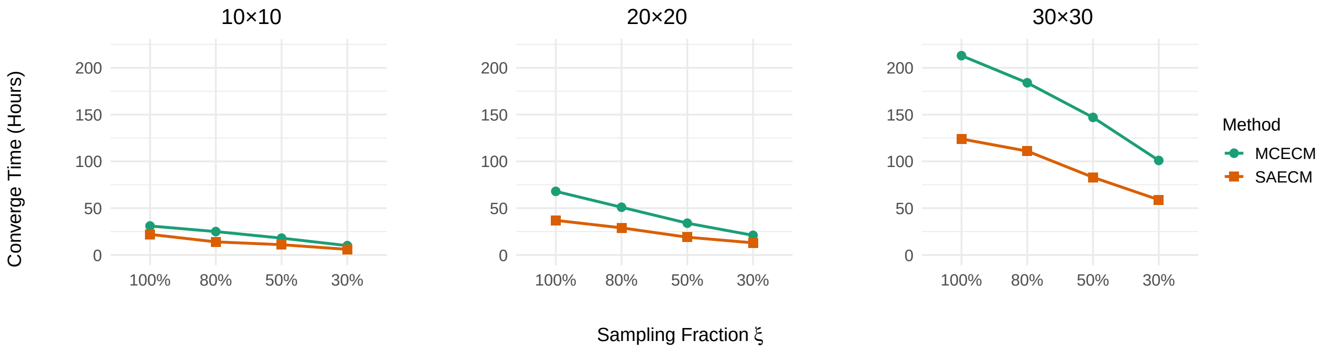

Figure 4.7: The convergence times of MCECM and SAECM.

Table 4.3: Results of the epidemic simulation study across various grid sizes and sampling fractions

True Parameter	ξ	10×10						20×20						30×30					
		SAECM			MCECM			SAECM			MCECM			SAECM			MCECM		
		Est	SE	ARBP	Est	SE	ARBP	Est	SE	ARBP	Est	SE	ARBP	Est	SE	ARBP	Est	SE	ARBP
$\alpha_S = 1$	100%	1.012	0.0003	1.20	1.005	0.0005	0.50	1.009	0.0004	0.90	1.015	0.0006	1.50	1.003	0.0002	0.30	1.000	0.0004	0.00
	80%	1.076	0.0006	7.60	1.062	0.0008	6.20	1.059	0.0005	5.90	1.069	0.0009	6.90	1.070	0.0004	7.00	1.050	0.0007	5.00
	50%	1.115	0.0009	11.50	1.142	0.0012	14.20	1.125	0.0008	12.50	1.155	0.0013	15.50	1.130	0.0007	13.00	1.155	0.0010	15.50
	30%	1.498	0.0014	49.80	1.455	0.0018	45.50	1.465	0.0010	46.50	1.550	0.0017	55.00	1.520	0.0016	52.00	1.490	0.0011	49.00
$\beta_1 = 2.5$	100%	2.5110	0.0004	0.44	2.5050	0.0005	0.20	2.4800	0.0003	0.80	2.4850	0.0006	0.60	2.4990	0.0002	0.04	2.5020	0.0004	0.08
	80%	2.5500	0.0007	2.00	2.5750	0.0008	3.00	2.5590	0.0005	2.36	2.5950	0.0009	3.80	2.5600	0.0006	2.40	2.5350	0.0008	1.40
	50%	2.6380	0.0010	5.52	2.6000	0.0012	4.00	2.6980	0.0009	7.92	2.6400	0.0012	5.60	2.7300	0.0008	9.20	2.6150	0.0011	4.60
	30%	3.1000	0.0016	24.00	3.1500	0.0017	26.00	3.2000	0.0013	28.00	3.1800	0.0016	27.20	3.1150	0.0015	24.60	3.1600	0.0012	26.40
$\beta_2 = 1.5$	100%	1.500	0.0004	0.20	1.500	0.0002	0.73	1.470	0.0003	1.00	1.500	0.0001	0.07	1.460	0.0006	1.33	1.496	0.0005	0.13
	80%	1.500	0.0007	4.67	1.500	0.0008	3.67	1.385	0.0005	3.93	1.348	0.0009	5.33	1.500	0.0004	4.00	1.500	0.0007	3.00
	50%	1.500	0.0011	9.20	1.150	0.0009	13.20	1.500	0.0013	6.67	1.100	0.0013	15.33	1.500	0.0008	9.33	1.500	0.0011	7.67
	30%	1.393	0.0017	40.00	1.388	0.0018	36.67	0.750	0.0012	40.00	1.388	0.0013	37.33	0.698	0.0016	43.33	1.388	0.0015	34.33
$\alpha_T = 1$	100%	1.000	0.0002	1.20	0.999	0.0003	0.30	0.978	0.0004	1.10	0.961	0.0006	2.00	1.000	0.0003	0.00	0.990	0.0005	0.50
	80%	1.000	0.0006	8.00	1.000	0.0009	6.50	0.887	0.0004	6.00	0.852	0.0008	8.00	1.000	0.0006	4.00	1.000	0.0007	6.00
	50%	1.000	0.0013	12.50	1.000	0.0010	15.50	0.769	0.0007	13.00	0.724	0.0012	16.00	1.000	0.0009	15.00	1.000	0.0010	12.00
	30%	0.931	0.0017	45.00	0.933	0.0016	50.00	0.400	0.0015	50.00	0.438	0.0011	46.00	0.934	0.0012	52.00	0.932	0.0014	47.50
$\beta_3 = 2.5$	100%	2.477	0.0001	0.80	2.444	0.0004	1.12	2.500	0.0006	0.40	2.500	0.0005	0.80	2.490	0.0002	0.20	2.480	0.0004	0.40
	80%	2.500	0.0007	1.80	2.498	0.0006	2.40	2.411	0.0005	1.80	2.500	0.0004	1.20	2.500	0.0006	0.40	2.344	0.0008	3.20
	50%	2.496	0.0008	4.40	2.502	0.0012	3.20	2.147	0.0009	7.60	2.293	0.0011	9.20	2.503	0.0010	3.60	2.308	0.0013	4.00
	30%	2.299	0.0018	25.20	2.304	0.0016	27.20	1.602	0.0012	28.00	2.305	0.0016	28.20	2.298	0.0017	23.60	2.301	0.0013	25.60
$\tau = 0.4$	100%	0.398	0.0005	2.50	0.403	0.0003	0.35	0.405	0.0002	2.25	0.400	0.0004	0.20	0.395	0.0006	2.25	0.399	0.0002	0.25
	80%	0.466	0.0008	16.25	0.448	0.0009	12.50	0.428	0.0006	7.00	0.455	0.0005	13.75	0.440	0.0007	10.00	0.440	0.0008	10.00
	50%	0.490	0.0012	22.50	0.470	0.0007	17.50	0.450	0.0013	12.50	0.500	0.0011	25.00	0.480	0.0009	20.00	0.450	0.0010	12.50
	30%	0.622	0.0017	55.50	0.640	0.0013	60.00	0.610	0.0018	52.50	0.630	0.0011	57.50	0.620	0.0016	55.00	0.636	0.0015	59.00
$\lambda = 0.6$	100%	0.587	0.0005	1.88	0.600	0.0003	0.33	0.585	0.0002	1.81	0.603	0.0003	0.29	0.600	0.0004	1.93	0.599	0.0006	0.15
	80%	0.600	0.0007	10.00	0.600	0.0008	6.67	0.525	0.0004	6.67	0.490	0.0007	10.00	0.600	0.0006	7.50	0.600	0.0009	5.00
	50%	0.758	0.0013	0.26	0.600	0.0011	15.00	0.386	0.0011	21.67	0.437	0.0009	15.83	0.600	0.0012	8.33	0.600	0.0010	13.33
	30%	0.559	0.0018	46.67	0.560	0.0016	53.33	0.208	0.0012	53.67	0.180	0.0014	55.33	0.560	0.0011	50.00	0.526	0.0016	52.33
$\delta = 2.5$	100%	2.498	0.0004	0.08	2.480	0.0005	0.40	2.500	0.0003	0.20	2.470	0.0004	0.60	2.490	0.0006	0.20	2.490	0.0002	0.20
	80%	2.500	0.0007	4.00	2.500	0.0008	3.00	2.250	0.0009	5.20	2.325	0.0006	3.60	2.500	0.0005	2.80	2.460	0.0008	1.60
	50%	2.500	0.0013	7.20	2.500	0.0011	8.80	1.880	0.0012	14.00	1.960	0.0010	12.00	2.500	0.0010	8.00	2.500	0.0013	6.00
	30%	2.300	0.0017	29.20	2.300	0.0018	26.80	1.960	0.0016	29.00	1.950	0.0013	29.00	2.280	0.0015	27.60	2.290	0.0014	28.60

Table 4.4: Convergence time (rounded to hours) for MCECM and SAECM across various grid sizes and sampling fractions

ξ	10×10		20×20		30×30	
	MCECM	SAECM	MCECM	SAECM	MCECM	SAECM
100%	31	22	68	37	213	124
80%	25	14	51	29	184	111
50%	18	11	34	19	147	83
30%	10	6	21	13	101	59

4.7 Real Data Analysis

This study utilized administrative daily health records of COVID-19 in Manitoba, Canada, from September 1, 2020, to March 1, 2021, provided by Manitoba Health. The individual-level dataset includes information such as birth date, gender, date of diagnosis, and 6-digit residential postal codes, with scrambled personal health identification numbers for confirmed COVID-19 cases.

We consider the geographical classification of Manitoba defined by MCHP and Manitoba Health for the allocation of health districts and neighborhood clusters based on municipality and postal codes [3].

The COVID-19 disease pattern was analyzed using the SEIR model applied to the entire province. Model parameters were estimated via maximum likelihood using the Nelder–Mead algorithm. Based on the fitted SEIR model, the incubation and infectious periods of COVID-19 in Manitoba were estimated to be 7 and 9 days, respectively. To evaluate the robustness and stability of the estimates, we fitted 500 SEIR models to the COVID-19 data using a range of initial values. This analysis confirmed that the SEIR model's parameter estimates were reliable and not affected by the choice of initialization.

In this study, we considered the entire province of Manitoba as the study area, treating 96 RHADs as regional units and 28,897 PCRs as individual units, which allowed for a high-resolution analysis. Each COVID-19 case was assigned to one of Manitoba's RHADs based on the 6-digit residential postal code, using the PCCF provided by Manitoba Health.

We included the proportion of individuals aged over 60 years within each PCR as an individual-level covariate associated with infectivity.

We examined how SES and its geographical variation related to susceptibility risk factors and patterns of COVID-19 transmission.

Parameter estimation was performed using the SAECM algorithm, with ζ_{SA} set to 0.6, following the rationale outlined in the simulation study. Moreover, a convergence threshold of $\epsilon_\Theta = 10^{-3}$ was applied to maintain a balance between computational efficiency and estimation accuracy. The sampling method was triggered once the number of daily COVID-19 cases exceeded the threshold $n_{\max} = 400$.

To effectively represent the estimated $\widetilde{\mathcal{P}}_{(i,t,z)}(\Theta)$, it is essential to aggregate this probability over all individuals for each HAD. We define the average infectivity rate for region z at time t as

$$\widetilde{\mathcal{P}}_{(t,z)}(\Theta) = \frac{1}{N_z} \sum_{i=1}^{N_z} \widetilde{\mathcal{P}}_{(i,t,z)}(\Theta), \tag{4.7.1}$$

where N_z denotes the population size of region z. Here, N_z is the number of PCRs in region z, as each PCR is treated as an individual.

Results

Table 4.5 presents the maximum likelihood estimates of the GD-ILM parameters obtained using the SAECM algorithm combined with the stratified temporally-weighted KDE-based PPS sampling from individual-level COVID-19 data from Manitoba. The fitted model incorporates covariates related to SES and age distribution and accounts for spatial transmission dynamics through parameters such as δ, τ, and λ. All estimates are accompanied by remarkably small standard errors, indicating high numerical precision and convergence stability.

The estimated baseline susceptibility, $\alpha_S = -2.000$, reflects a relatively low intrinsic susceptibility in the absence of covariate effects. Notably, the SES variable has a strong positive association with susceptibility (Estimate = 1.153), indicating that individuals residing in areas with higher SES (defined by lower income, reduced educational attainment, higher unemployment, and a greater prevalence of single-parent households) experience a significantly higher risk of becoming susceptible to infection. This is consistent with findings from other studies showing that socioeconomically disadvantaged populations face increased vulnerability to infectious diseases due to factors such as crowded living conditions, limited access to healthcare, and greater occupational exposure.

The baseline infectivity parameter, $\alpha_T = -1.000$, similarly suggests a relatively low baseline transmission potential. However, the proportion of individuals aged 60 years and older within a PCR is positively associated with infectivity (Estimate = 1.208), implying that areas with a higher proportion of older individuals are associated with increased transmission potential. This aligns with established knowledge that older adults are both more susceptible to infection and more likely to exhibit symptomatic disease, potentially increasing onward transmission.

The estimated spatial decay parameter, $\delta = 2.543$, indicates that inter-PCR transmission is highly localized, with the transmission probability declining rapidly with distance. The parameter $\tau = 0.607$ corresponds to the residual spatial precision τ^2, quantifying unobserved intra-RHAD heterogeneity that is not explained by SES. The parameter $\lambda = 0.551$ captures spatial autocorrelation between neighboring RHADs, accounting for cross-RHAD dependence.

The small standard errors (all less than 0.0002) demonstrate that the SAECM algorithm yields highly stable parameter estimates, even in a high-resolution spatial setting with nearly 28,000 PCRs. This degree of precision reflects both the robustness of the algorithm and the richness of the underlying data, which include detailed individual-level attributes and comprehensive spatial information.

These results carry meaningful public health implications. The pronounced role of SES in increasing susceptibility underscores the need for targeted interventions in socioeconomically disadvantaged regions. Furthermore, the association between areas with higher proportions of older individuals and increased infectivity suggests the necessity of maintaining vaccination and mitigation efforts directed toward older populations, not only to prevent adverse clinical outcomes but also to reduce transmission at the population level.

Figures 4.8 to 4.12 illustrate the average infectivity rates by RHADs within each HAD for all five HADs in Manitoba.

The GD-ILM combined with the proposed SAECM algorithm for parameter estimation and the proposed sampling method to approximate the likelihood, when applied to real-world data, is highly effective in capturing both individual-level and spatial determinants of disease spread. The use of high-resolution PCR-level data enables the detection of fine-grained transmission patterns, allowing for granular epidemiological insights that can inform precision public health strategies. By analyzing the probability of infection for each PCR within each RHAD at any given time point, or by considering the average infectivity rates of each RHAD over time, policymakers can monitor transmission risk trajectories and implement evidence-based strategies for targeted and adaptive resource allocation.

Table 4.5: Estimated model parameters with standard errors

Parameter	Est.	S.E.
α_S	-2.000	0.00005
SES	1.153	0.00004
α_T	-1.000	0.00002
Age 60+	1.208	0.00003
δ	2.543	0.00008
τ	0.607	0.00015
λ	0.551	0.00011

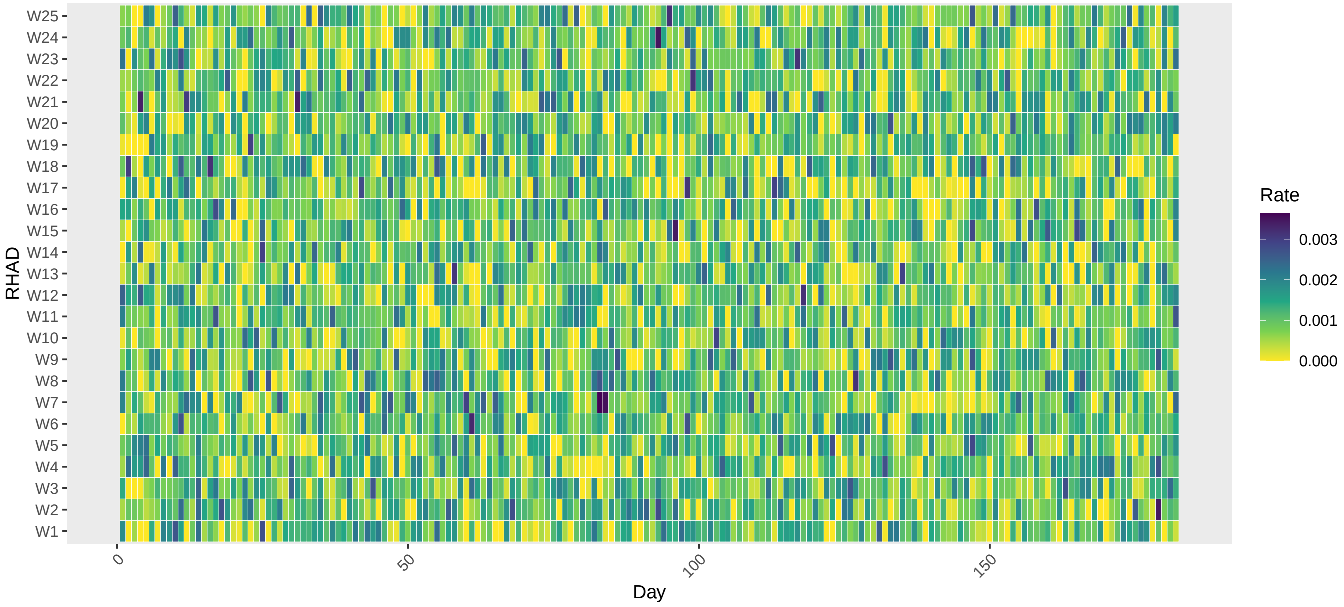

Figure 4.8: Average infectivity rates across RHADs in Winnipeg HAD

We initially aimed to fit the GD-ILM to the full COVID-19 dataset from Manitoba and estimate its parameters using the SAECM algorithm with the complete sample ($\xi = 100\%$), in order to

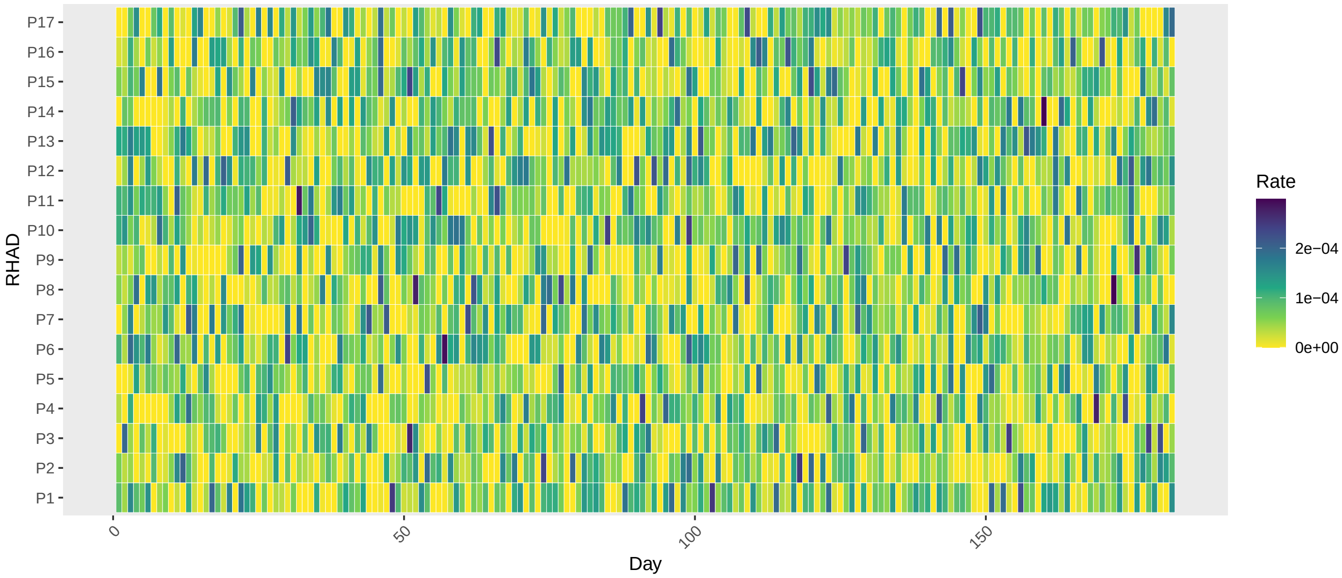

Figure 4.9: Average infectivity rates across RHADs in Prairie HAD

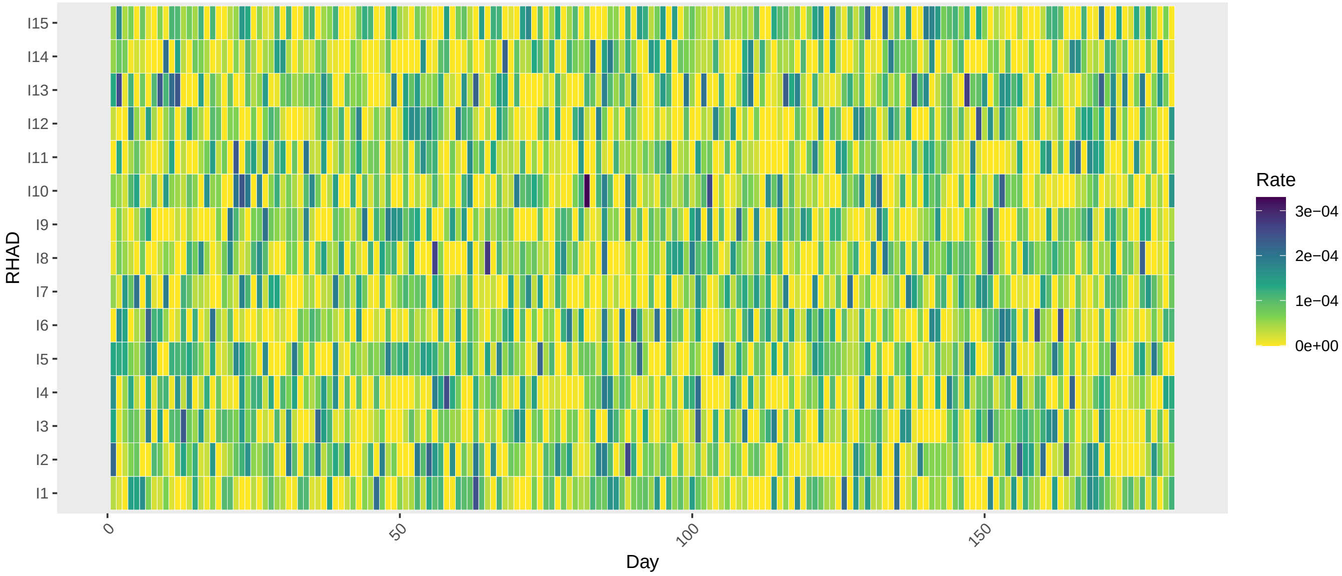

Figure 4.10: Average infectivity rates across RHADs in Interlake HAD

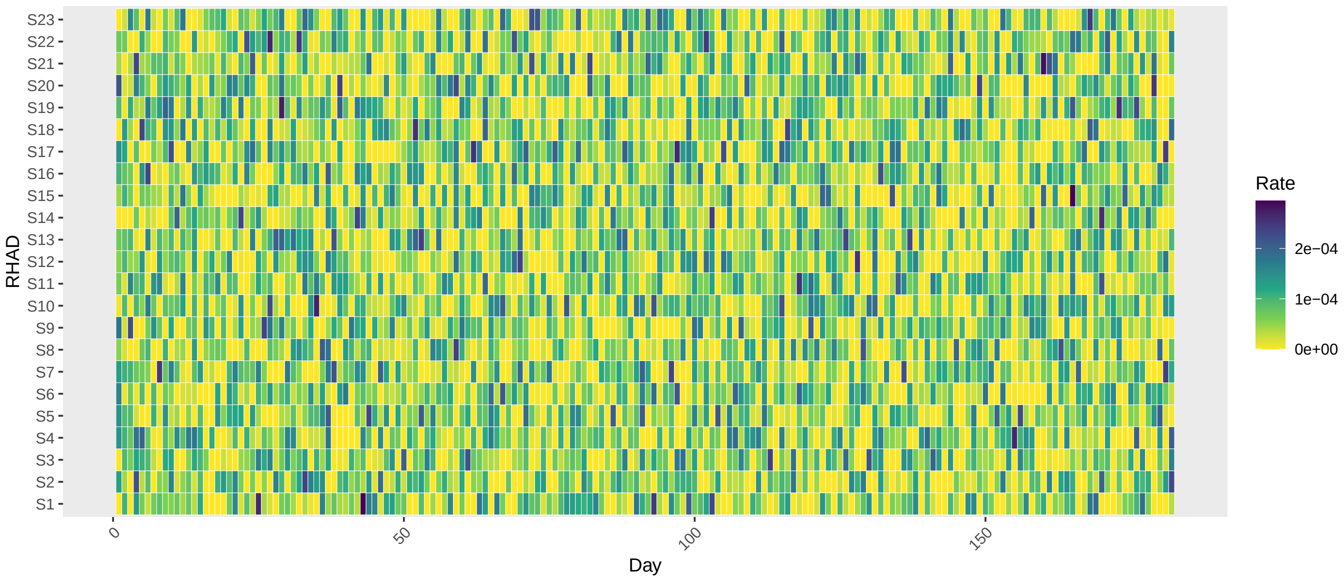

Figure 4.11: Average infectivity rates across RHADs in Southern HAD

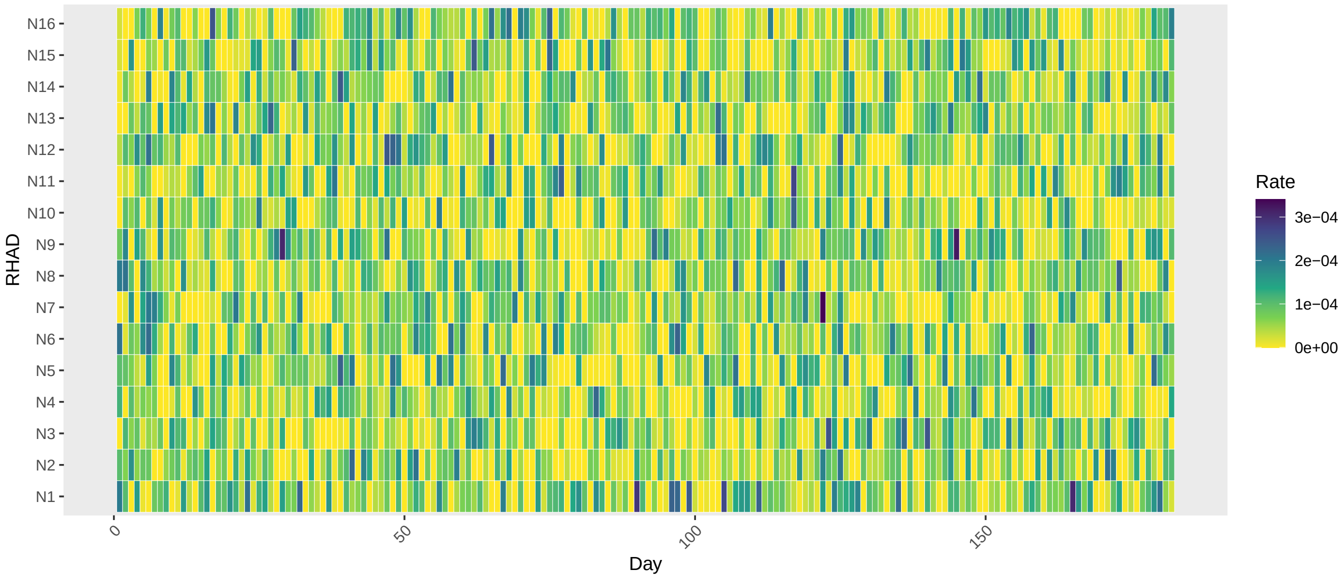

Figure 4.12: Average infectivity rates across RHADs in Northern HAD

compare these results with those obtained under the proposed sampling method ($\xi = 50\%$). However, the province-wide dataset comprises 96 RHADs, 27,897 PCRs, and a substantially large number of COVID-19 cases over the study period. Due to this scale, running the SAECM method on the full dataset became computationally prohibitive, with preliminary runs indicating that convergence could require more than a month.

Given these limitations, we restricted the comparison to the Winnipeg HAD, which contains 25 RHADs, 19,896 PCRs, and a comparatively smaller number of COVID-19 cases. This subset allowed the SAECM algorithm to converge in a reasonable timeframe while still providing a meaningful comparison. We considered the same time period and fitted an SEIR model to the COVID-19 data from Winnipeg, estimating the incubation and infectious periods to be 5 days and 7 days, respectively. We implemented the proposed sampling method with a sampling fraction of $\xi = 50\%$ once the daily number of COVID-19 cases surpassed the threshold $n_{\max} = 500$. Table 4.6 presents the GD-ILM parameter estimates obtained via the SAECM approach using the complete dataset ($\xi = 100\%$) as well as those estimated under the proposed sampling method with a sampling fraction of $\xi = 50\%$. As shown in Table 4.6, the parameter estimates obtained from the sampled dataset are reasonably close to those estimated from the full dataset. It is important to note that, in the real-data analysis of COVID-19 in Winnipeg, both the number of PCRs and the number of time points were considerably larger than those considered in the simulation study. These differences in data scale may contribute to the differing magnitudes of variability observed in the estimates.

Table 4.6: Estimated model parameters with standard errors for the COVID-19 data from Winnipeg

	Full dataset ($\xi = 100\%$)		Sampled ($\xi = 50\%$)	
Parameter	Est.	S.E.	Est.	S.E.
α_S	-1.083	0.00012	-1.221	0.00020
SES	2.656	0.00011	2.255	0.00015
α_T	-1.164	0.00012	-1.430	0.00021
Age 60+	1.320	0.00019	1.651	0.00024
δ	1.567	0.00017	1.247	0.00012
τ	0.611	0.00025	0.723	0.00031
λ	0.781	0.00014	0.623	0.00021

4.8 Discussion

This study presents a comprehensive and efficient framework for accelerating parameter estimation in GD-ILMs, which are essential for understanding and predicting epidemic dynamics in large populations with complex spatial structures. By combining the SAECM algorithm with a stratified temporally-weighted KDE-based PPS sampling method to approximate the likelihood, we significantly improve computational efficiency while maintaining reliable estimation accuracy across a variety of settings.

The extensive simulation study conducted across different spatial grid resolutions (10×10, 20×20, and 30×30) and sampling fractions demonstrates the robustness and scalability of the proposed method. Under full data usage ($\xi = 100\%$), both SAECM and the traditional MCECM algorithms yield highly accurate parameter estimates with minimal bias, confirming the validity of the modeling and estimation approaches. Importantly, the simulation results reveal that the SAECM algorithm, coupled with the proposed sampling method, achieves notable computational speed-ups without compromising estimation quality when moderate sampling fractions ($\xi = 50\%$ to 80%) are employed. However, low sampling fractions (e.g., $\xi = 30\%$) introduce pronounced bias, especially for key spatial parameters and in high-resolution grids, highlighting the necessity of balancing computational gains with precision requirements. The simulation further shows that increasing spatial resolution exacerbates bias when sampling fractions are excessively low; nevertheless, this limitation can be mitigated through the judicious selection of sampling fractions. The R codes used for the simulation study are available at: `https://github.com/Amin-Abed/R-Codes/tree/main`.

Complementing the simulation results, the real data analysis of COVID-19 transmission in Manitoba, Canada, provides a practical demonstration of the framework's applicability to large-scale, real-world epidemic data. Utilizing detailed administrative health records, the model incorporates fine-scale geographic units (RHADs and PCRs) and relevant covariates, such as SES and age structure, enabling nuanced insights into transmission dynamics. Parameter estimation via SAECM with the stratified temporally-weighted KDE-based PPS sampling method is both computationally feasible and statistically sound, effectively capturing spatial heterogeneity and temporal patterns of COVID-19 spread. The analysis not only produces incubation and infectious period estimates consistent with established epidemiological knowledge but also illustrates how demographic and SES factors influence disease transmission risk. This real-world application affirms the method's utility for timely epidemic monitoring and public health decision-making in complex, data-rich environments.

From a public health perspective, this methodological advancement offers significant potential to enhance epidemic surveillance and response strategies. The ability to efficiently estimate model parameters at high spatial and temporal resolutions allows public health officials to identify transmission hotspots, monitor the impact of interventions, and allocate resources more effectively. By reducing computational time without sacrificing accuracy, the SAECM combined with the proposed sampling method supports near-real-time analysis, which is critical for rapidly evolving outbreaks. This capability facilitates more responsive and targeted public health actions, ultimately helping to mitigate disease spread and improve population health outcomes. Moreover, the flexibility of this approach in incorporating diverse covariates and spatial structures makes it adaptable to various infectious diseases and geographic contexts, broadening its relevance for public health practitioners worldwide.

In conclusion, the integration of SAECM and the stratified temporally-weighted KDE-based PPS sampling method provides a promising and scalable approach to parameter estimation in GD-ILMs, balancing computational tractability with accuracy in both simulated and empirical contexts. This method is well-positioned to support rapid, high-resolution epidemic modeling and surveillance, offering public health practitioners a practical tool for effective outbreak response. This study highlights several potential future directions, including the exploration of alternative spatial kernels, the extension of the framework to other compartmental models, such as the SEIRS compartmental model, and the examination of the proposed approach in the presence of covariates subject to measurement error.

5

Gonorrhea cluster detection in Manitoba, Canada: Spatial, temporal, and spatiotemporal analysis

This chapter includes an open access article published in *Infectious Disease Modelling* [3]. It is reproduced here in its original form, with only minor formatting adjustments for consistency within the thesis. Reproduction is permitted under the terms of the Creative Commons Attribution-NonCommercial-NoDerivatives 4.0 International License (CC BY-NC-ND 4.0).

5.1 Introduction

Gonorrhea, caused by Neisseria gonorrhoeae (specifically, the gonococcus), is an STI [104] and continues to be a significant global public health issue [94]. In Canada, Gonorrhea is the second most frequent STI, following Chlamydia [19, 55]. Gonorrhea is usually spread through unprotected vaginal, anal, or oral sexual interactions and results in cervicitis in women and urethritis in both men and women [86, 37, 106]. Moreover, transmission rates are higher from men to women compared to the reverse direction through vaginal intercourse [98]. Most of the infected men with gonococcal urethritis exhibit symptoms. However, fewer women with urogenital Gonorrhea manifest symptoms, and when they do, the symptoms lack specificity. Rectal and pharyngeal Gonorrhea are primarily detected in men who have sex with men [11]. It is also common among women and often does not show any noticeable symptoms.

Microbiological diagnosis of Gonorrhea encompasses the culture of Gonorrhea, and/or the utilization of Nucleic Acid Amplification Tests (NAATs) [56]. NAATs provide increased sensitivity while upholding a strong degree of specificity. However, the sensitivity can differ among various NAATs and depending on the specific anatomical site being examined [93, 56, 19]. Gonorrhea also plays a role in enhancing the transmission of the Human Immunodeficiency Virus (HIV) [37, 19, 94] and facilitating the propagation of other sexually transmitted infections [94]. Transmission of Gonorrhea infection can occur from infected mothers to their newborns during the birthing process (intrapartum). This is due to the vulnerability of the neonate's conjunctiva as it traverses the birth canal, potentially resulting in ophthalmia neonatorum if the conjunctiva becomes infected with Gonorrhea [94]. Additionally, infection during pregnancy is linked to outcomes like low birth weight and neonatal conjunctivitis, which can escalate and lead to vision impairment [108, 94, 95].

In women, since Gonorrhea frequently persists without symptoms, it complicates the prompt identification and treatment of the infection [22]. Failure to detect and adequately treat infections can lead to ascending complications like epididymitis and salpingitis. This situation raises the likelihood of women developing cervicitis, pelvic inflammatory disease, ectopic pregnancy, and infertility [90, 37, 48, 108, 19]. In men, asymptomatic Gonorrhea increases the probability of contracting epididymitis, epididymal-orchitis, chronic prostatitis, and infertility [69, 92, 99, 70]. Increased vulnerability is attributed to various sexual practices, including irregular condom usage, engagement with multiple partners, and instances where a partner or partners maintain concurrent relationships [37, 108, 19]. Certain populations are especially susceptible to infection. These include adolescents and young adults, specific ethnic and racial communities, socioeconomically disadvantaged groups, community of men who have sex with men, and sex workers [47]. Gonorrhea has significantly been underestimated and not fully reported on a global scale even in high-income countries with established STI surveillance systems [108]. Annually reported Gonorrhea infections are estimated to represent only a fraction of the actual rates, with at least 70 percent going undetected or unreported [96, 19], primarily because these infections are often asymptomatic [19]. While the asymptomatic nature of the infection partly explains this, underreporting is also due to delayed healthcare seeking and limited availability or inadequacy of Gonorrhea testing and treatment options [47, 104]. Curable STIs including Gonorrhea do not establish robust and long-lasting protective immunity. After treating Gonorrhea, recurrent infection rates usually range from 10% to 20% [38, 11].

Researchers identified a connection between areas with lower socioeconomic status and higher rates of Gonorrhea and Chlamydia infections in the health regions of Calgary, Canada [17]. These areas were concentrated primarily in downtown and the northeastern part of the city. A study conducted in Manitoba, Canada, revealed that among cases of Gonorrhea and their associated contacts, the top 10% of relationships spanned distances of 237 km or more [36]. Furthermore, this study found a higher proportion of long-distance partnerships among Gonorrhea cases compared to Chlamydia cases. Another study examined and compared the transmission patterns of Chlamydia and Gonorrhea in Winnipeg, Manitoba, Canada [13]. Based on these results, the infections in both cases displayed high incidence rates that were concentrated in particular geographic areas characterized by lower socioeconomic status.

In 2017, the recorded annual incidence rate of Gonorrhea in Canada was 95.8 infections per 100,000 population. In 2018, Manitoba reported a significantly higher incidence of Gonorrhea, with a rate of 265 infections per 100,000 individuals. This sharp increase in rates exceeding the national average highlights the significant importance of Gonorrhea as a relevant and essential topic in the field of public health in Manitoba.

Our research aims to investigate the spatial, temporal, and spatiotemporal patterns of Gonorrhea infection in Manitoba. We utilize administrative data from 2000 to 2016 to identify RHADs and time periods with higher Gonorrhea incidence than what would be expected by chance. Therefore, the results of this study provide public health officials and decision-makers with a more comprehensive understanding of infection clusters and dynamics. The generated risk maps visually illustrate the geographical concentration of high-risk RHADs at different time periods, offering valuable insights for the implementation of targeted surveillance and more effective preventative strategies and control measures.

5.2 Materials and Methods

5.2.1 Data Sources

The Cadham Provincial Laboratory (CPL), operated by Manitoba Health, serves as the only public health laboratory in the province of Manitoba over three centuries and provides a diverse set of public health laboratory services. These services encompass areas such as the storage of testing data related to notifiable diseases, early detection of health risks, monitoring of outbreak investigations, and the identification of disease causes. CPL is organized into different sections, comprising media/quality assurance, microbiology, perinatal chemistry, serology/parasitology, and virus detection. One of the responsibilities of the clinical microbiology section is to conduct investigations into STIs, including Gonorrhea. Gonorrhea infection is confirmed through laboratory tests like culture or NAAT. CPL is required to report all confirmed infections of Gonorrhea to the Epidemiology and Surveillance Unit, which operates within the Public Health Branch of the Manitoba Health [52]. The unit's responsibility is to assist the public health system by actively monitoring, analyzing, and reporting on the occurrence, dissemination, and severity of both communicable and non-communicable diseases and their conditions in Manitoba.

In this study, we consider administrative health records of diagnosed infections of Gonorrhea in the province of Manitoba, Canada, from 2000 to 2016 provided by Manitoba Health. The individual-level data consists of sex, date of birth, date of diagnosis, 6-digit postal code of residence, and scrambled personal health identification numbers of confirmed Gonorrhea infections. The ICD-9-CM codes 098, V02, and V02.7 were utilized to identify Gonorrhea infections in the dataset.

5.2.2 Study Area

We consider the geographical classification defined by MCHP and Manitoba Health for the allocation of health districts and neighbourhood clusters based on municipality and postal codes [3]. Using the geographic classification algorithm, we aggregate diagnosed Gonorrhea infections into 96 RHADs, which are then linked to 2016 Statistics Canada census data to obtain information on the sex, age, and population of residents in those RHADs.

5.2.3 Time Series Analysis

Time Series Decomposition

A fundamental goal in the analysis of time series data involves breaking down a sequence into a collection of hidden components that are not directly observable. These components are linked to diverse forms of temporal changes. Time series data can encompass four primary kinds of fluctuations including trend or long-term tendency T_t, cyclical movements C_t, seasonal variations S_t, and irregular component, noise, or residual variations I_t. Therefore, considering an additive model, the time series x_t can be conceptualized as $x_t = T_t + C_t + S_t + I_t$ while multiplicative model would be as $x_t = T_t \times C_t \times S_t \times I_t$. The seasonal index is computed by dividing the average number of infections for a specific month by the average monthly case count observed throughout the entire study period [103]. This index approaching a value of 1.0 indicates that there are no clear and distinct seasonal patterns present in the data.

Seasonal Auto-Regressive Integrated Moving Average Model

A time series comprises a sequence of numerical information collected at consistent time intervals over a specific duration. The Auto-Regressive Integrated Moving Average (ARIMA) model consists of three hyperparameters that specify the autoregressive (AR), integrated (I), and moving average (MA) components used to model the non-seasonal part of a time series. The ARIMA model is represented by ARIMA(p, d, q), where p is the order of the non-seasonal AR component, d indicates the degree of differencing applied to the non-seasonal part by subtracting past values a certain number of times, and q specifies the order of the non-seasonal MA component.

The Seasonal ARIMA (SARIMA) model is a broader version of the ARIMA model designed to explicitly accommodate univariate time series data featuring both a seasonal component and non-seasonal trends using a multiplicative approach [20, 15, 29]. Seasonality involves a regular and repeating pattern within a dataset, usually following a specific time interval. The SARIMA model extends this concept, incorporating the three hyperparameters from the non-seasonal ARIMA(p, d, q) model, along with additional hyperparameters that define the seasonal period (S). The model is denoted as SARIMA(p, d, q)(P, D, Q)m, where the initial three parameters (p, d, q) pertain to the non-seasonal aspect (the ARIMA model), while the latter parameters (P, D, Q)m are associated with the seasonal aspect. More precisely, P signifies the order of the seasonal AR component, D indicates the level of differencing for the seasonal part, Q denotes the order of the seasonal MA component, and m represents the number of periods within each season. To predict the value of x_t at time t within a time series dataset $x_i, i = 0, \ldots, t-1$, the SARIMA model is employed and formulated as follows:

$$\left(1 - \sum_{i=1}^{p} \phi_i L^i\right) \left(1 - \sum_{i=1}^{P} \Phi_i L^{im}\right) (1-L)^d \left(1 - L^m\right)^D x_t = \left(1 + \sum_{i=1}^{q} \theta_i L^i\right) \left(1 + \sum_{i=1}^{Q} \Theta_i L^{im}\right) \epsilon_t,$$

where $Lx_t = x_{t-1}$ and $L^i x_t = x_{t-i}$ represent the lag operators, ϵ_t denotes the error terms, ϕ_i and Φ_i represent the parameters of the non-seasonal and seasonal AR components, respectively, and θ_i and Θ_i denote the parameters of the non-seasonal and seasonal MA components, respectively.

5.2.4 Spatial and Spatiotemporal Clustering

Spatial Autocorrelation

Spatial autocorrelation, as measured by Global Moran's I [65], serves as an indicator for analyzing spatial autocorrelation. The Global Moran's I statistic falls within a range between -1 and 1. A Global Moran's I statistic equal to 0 shows the absence of spatial autocorrelation, indicating a random distribution and no clustered districts across the entire study area. A value greater than 0 indicates the presence of positive spatial correlation, and when it approaches 1, it signifies strong positive autocorrelation, indicating that districts are clustered. The significance of the Global Moran's I statistic is assessed through the Monte Carlo test. This test helps determine whether the observed spatial autocorrelation is statistically significant or could have occurred by random chance. The interpretation of Global Moran's I should be considered in the context of its null hypothesis. The null hypothesis specifies that the features are randomly distributed among the districts within the area under study. A p-value resulting from this test below the 5% significance level shows the existence of spatial autocorrelation among districts across the entire area under study. The Global

Moran's I statistic is given by:

$$I = \frac{N \sum_{i=1}^{z} \sum_{j=1}^{z} w_{ij} \left(x_i - \bar{x}\right) \left(x_j - \bar{x}\right)}{\left(\sum_{i=1}^{z} \sum_{j=1}^{z} w_{ij}\right) \sum_{i=1}^{z} (x_i - \bar{x})},$$

where N represents the total number of features, z is the number of districts, x_i and x_j denote the number of features in district i and j respectively, $\bar{x}$ represents the mean value across the entire districts, and w_{ij} represents the spatial weight between districts i and j.

Spatial and Spatiotemporal Scan Statistics

Kulldorff's space–time scan statistic [45] has been applied in diverse contexts within the field of epidemiology [31]. Assume that the geographical area under study is divided into z districts. The districts can be counties, enumeration districts, or health authorities. For each district i, consider N_i as the number of infections with observed value $n_i,\ i = 1, \ldots, z$, and the total number of observed infections $n = \sum_{i=1}^{z} n_i$. The number of infections within each district follows a Poisson distribution with a parameter $\psi_i \zeta_i$ (i.e., $N_i \sim \text{Poisson}(\psi_i \zeta_i), \quad i = 1, \ldots, z$), where ψ_i and ζ_i denote the expected number of infections and the relative risk in district i, respectively. Consider the following hypothesis test

$$\begin{aligned} H_0 &: \mathbb{E}(N_i) = \psi_i, && \forall i \in \{1, \ldots, z\}, \\ H_1 &: \mathbb{E}(N_i) > \psi_i, && \exists i \in \{1, \ldots, z\}, \end{aligned} \tag{5.2.1}$$

where the null hypothesis states there is no clustering. The circular spatial scan statistic is a circular scanning window represented as ω and is applied to each centroid of z districts shifted across the area under study. As a result, as the circular scanning window moves to different positions within the district, distinct sets of districts are included. For any given centroid, the radius of the circular scanning window changes smoothly, ranging from zero to a predetermined maximum distance or up to a predetermined maximum count of K districts that should be included within the cluster. Typically, the value of K is selected to encompass a maximum of 50% of the population at risk. Hence, the circular scanning window is flexible both in distance and in the number of districts. If the circular scanning window contains the centroid of a district, then that whole district is included in the circular window. In total, a considerable quantity of distinct yet overlapping circular windows is generated. Each circular scanning window possesses a unique position and size, representing a potential cluster candidate. Let ω_{ik} denote the circular window composed by the $(k-1)$-nearest neighbours to district i, for $k = 1, \ldots, K$ and $i = 1, \ldots, z$. Then, all the circular windows to be scanned by the spatial scan statistic are included in the set which is $\Omega = \{\omega_{ik} | 1 \leqslant i \leqslant z, 1 \leqslant k \leqslant K\}$. Therefore, the null and alternative hypotheses in (5.2.1) are expressed as

$$\begin{aligned} &H_0 : \mathbb{E}(N(\omega)) = \psi(\omega), \qquad \forall \omega \in \Omega, \\ &H_1 : \mathbb{E}(N(\omega)) > \psi(\omega), \qquad \exists \omega \in \Omega, \end{aligned}$$

where $N(\cdot)$ and $\psi(\cdot)$ denote the random variable for the number of infections and the null expected number of infections within the specified circular window, respectively. The alternative hypothesis H_1 states there is at least one window $\omega \in \Omega$ for which the underlying risk is higher inside the circular window when compared with outside. A likelihood of the observed count of infections both inside and outside the circular window can be calculated for every circular window $\omega \in \Omega$. Considering the Poisson assumption, the likelihood ratio for the specific circular window $\omega \in \Omega$ is given by:

$$\underset{\omega \in \Omega}{\mathcal{L}(\omega)} = \begin{cases} \left(\frac{n(\omega)}{\psi(\omega)}\right)^{n(\omega)} \left(\frac{n-n(\omega)}{n-\psi(\omega)}\right)^{n-n(\omega)}, & n(\omega) > \psi(\omega), \\ 1, & n(\omega) \leqslant \psi(\omega), \end{cases}$$

where $n(\omega)$ is the observed number of infections in the circular window $\omega \in \Omega$. The circular window $\omega^* \in \Omega$ that achieves the highest likelihood ratio is defined as the most likely cluster and is given by $\omega^* = \arg\max_{\omega \in \Omega} \; \mathcal{L}(\omega)$.

The scanning window takes on different shapes depending on the context. In spatial scanning, it typically manifests as a circular or elliptical shape. In temporal scanning, the scanning window represents a specific time span. However, in space-time scanning, the window adopts a cylindrical shape. Here, the cylinder's base symbolizes the spatial dimension, while its height corresponds to the temporal dimension.

As our study uses aggregated data based on RHADs, if the centroid of a RHAD falls within the radius of the circle associated with a specific RHAD, then that particular RHAD should be included as part of the window. Spatial and spatiotemporal clustering analysis of Gonorrhea infections are performed using the SaTScan™ software developed by Kulldorff [44]. *R* software version 4.3.1 is used for time series analysis, decomposition, and estimating the seasonal occurrences of monthly infections.

5.3 Results

5.3.1 Age and Sex Patterns

Figure 5.1a presents the total and sex-specific annual incidence rates of reported infections per 100,000 population. It is evident that there is a significant increase in the annual rate of infections for both sexes in 2016 when compared to preceding years. The data highlight a significant change in the sex distribution during the study period. From mid-2005 onward, there is a shift in the sex distribution, as the rate of infections in females started to exceed that of males by an average of around 10 more infections per 100,000 population annually. This shift could be influenced by a combination of factors, such as sexual behavior factors, underreporting in males, asymptomatic infections, sexual network dynamics, and demographic changes. This trend in sex continues until the end of the study period in 2016, when a near balance occurred, with nearly equal numbers of reported infections in both sexes. Figure 5.1b also illustrates that the mean age of infected individuals is approximately 25 years. Moreover, there exists a notable sex-age disparity within the dataset. Specifically, the mean age for female cases hovered around 23 years, whereas for male cases, it was observed to be around 28 years. This divergence underscores a distinctive age-related pattern, with male cases presenting as roughly 5 years older than their female counterparts, thereby suggesting a propensity for Gonorrhea to manifest at younger ages among females. Furthermore, the analysis of the mean age among both male and female cases, as well as the overall mean age across the entire study period, exhibits a consistent and stable pattern. No specific trend or significant deviation in mean age is observed over the duration of the study. This finding suggests that the infection's prevalence among different age groups remained relatively constant during the years under study.

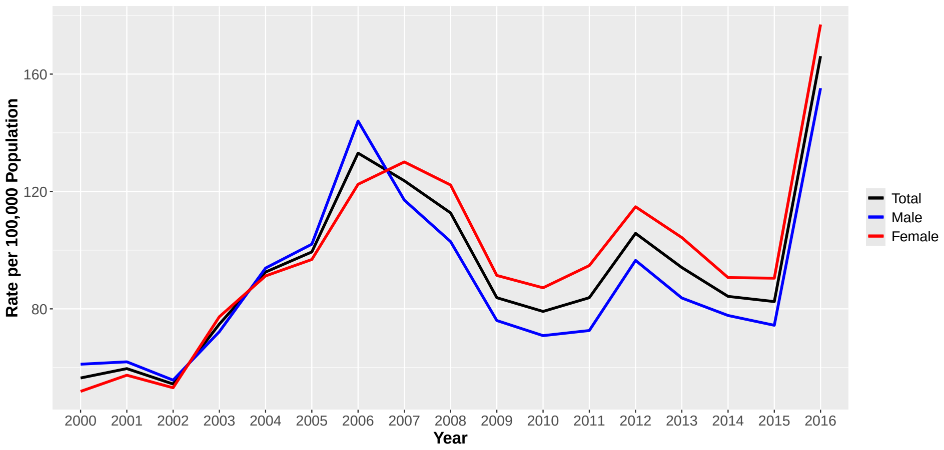

(a) Annual incidence rates

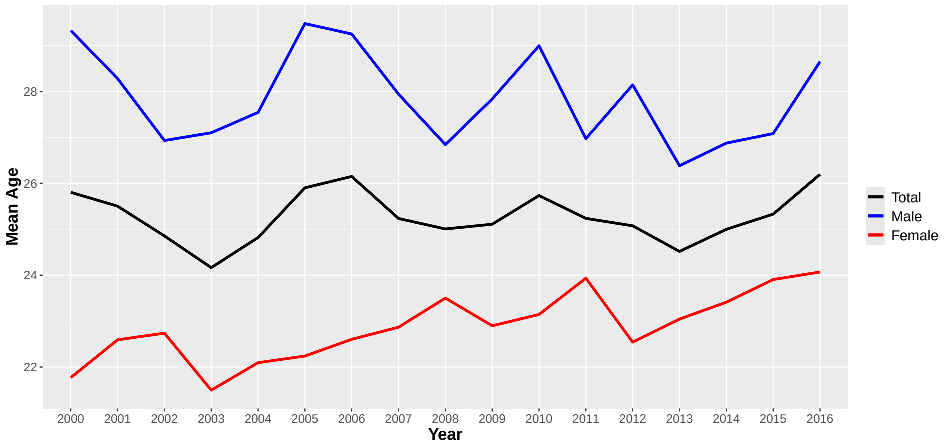

(b) Annual mean age distribution

Figure 5.1: Annual incidence rates (a) and age-sex distribution (b) of Gonorrhea infections in Manitoba, 2000-2016.

Figure 5.2 illustrates the annual rates of age and sex-specific age groups of reported Gonorrhea infections per 100,000 population, categorized into distinct age groups (0–14, 15-19, 20–24, 25–29, 30 and older). This graphical representation offers valuable insights into the prevalence and distribution of infections among various age groups. It enables a better understanding of how the infection affects different ages and highlights potential sex disparities in its impact. This classification corresponds to the stages of development and milestones associated with sexual behavior. Adolescents usually start exploring their sexuality in their mid-teens (ages 15–19), and this trend of increased sexual activity and engagement in risky behaviors continues into early adulthood (ages 20–24 and 25-29) [76, 94]. This breakdown highlights important phases of sexual development and the potential risk of Gonorrhea exposure. Moreover, research consistently indicates that Gonorrhea infections typically peak during late adolescence and young adulthood, emphasizing the significance of these age groups for monitoring and intervention efforts [94, 18]. By focusing on these peak transmission periods, public health authorities can allocate resources efficiently and implement targeted prevention strategies where they are most needed. In Figure 5.2b, for instance, it is readily observable that a notable portion of annual rates of females occurs within the age group of 15-19, whereas annual rates of males are primarily concentrated within the age group of 20-24.

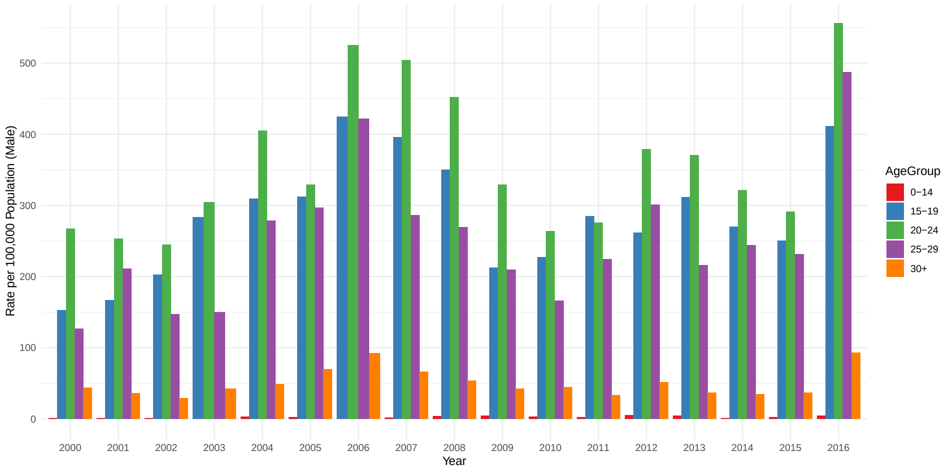

(a) Males

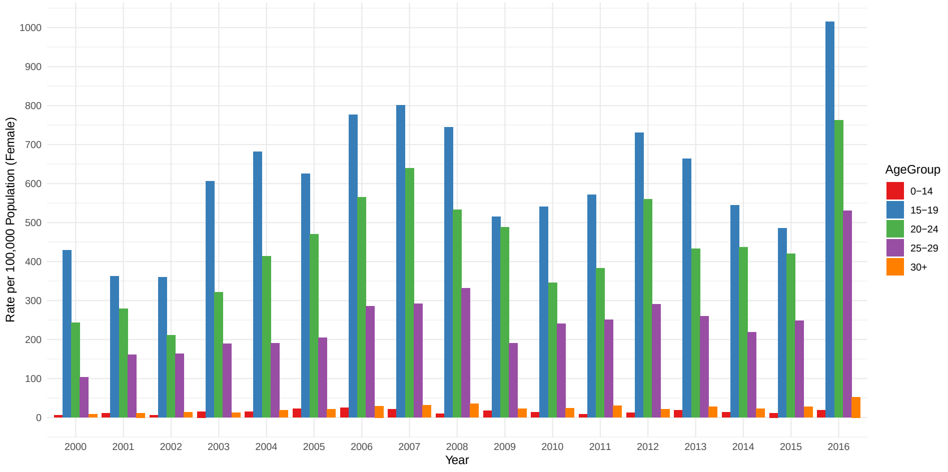

(b) Females

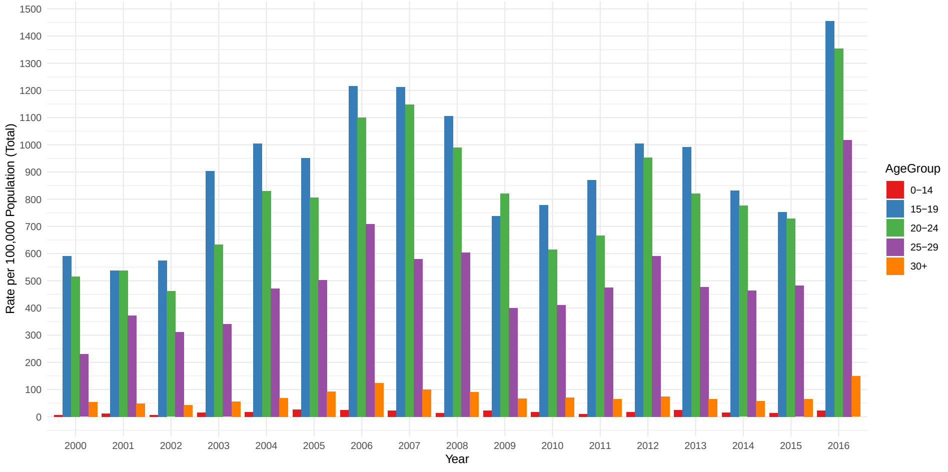

(c) Total

Figure 5.2: Annual rates of reported Gonorrhea infections per 100,000 population by age group in Manitoba, 2000-2016, for males (a), females (b), and total (c).

Given access to the personal health identification numbers of infections, we were able to identify instances of repeat infections, denoting infections where individuals contracted the same infection more than once within a single year. To quantify the prevalence of repeated infections for each year, we computed the percentage by dividing the number of repeat infections by the total number of infections for that respective year. Figure 5.3 presents a visual representation of the percentage of repeated infections in Manitoba from 2000 to 2016. This figure illustrates a significant rise in the percentage of reported infections in 2016, with approximately 16% of infections being linked to individuals who had multiple infections within the same year. This marks a substantial increase compared to previous years. Additionally, from the second half of 2007 onward, there is a higher occurrence of recurrent infections among females compared to males.

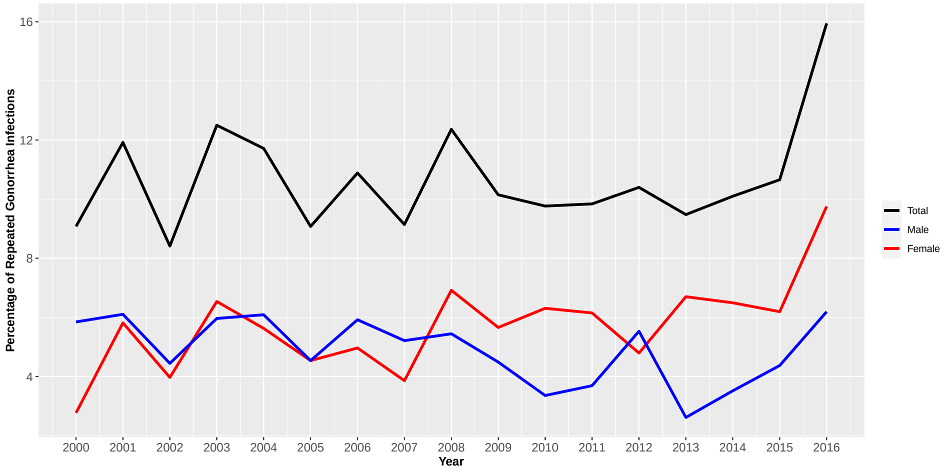

Figure 5.3: Percentage of annually repeated Gonorrhea infections in Manitoba, 2000-2016.

5.3.2 Spatial Patterns

The Global Moran's I value of 0.48 (p-value< 0.05) suggests a statistically significant positive spatial autocorrelation of infections among the RHADs in Manitoba from 2000 to 2016. This indicates a non-random spatially clustered distribution of Gonorrhea infections.

We aggregate the data of Gonorrhea infections for each RHAD ignoring temporal information. We adjust the expected number of cases for age groups (0–14, 15-19, 20–24, 25–29, 30 and older) and sex (male and female) using 2016 Statistics Canada census data of residence and population residing in the 96 RHADs for purely spatial analysis. We also consider a circular window scanning for a maximum of 50% of the total at-risk population. Kulldorff's space-time scan statistic, implemented using a discrete Poisson model within a purely spatial framework, results in the detection of 26 RHADs, as illustrated in Figures 5.4. This indicates that the northern districts of Manitoba, with 20 RHADs, and the central districts of Winnipeg, with 6 RHADs, are significant clusters for the incidence of the infection.

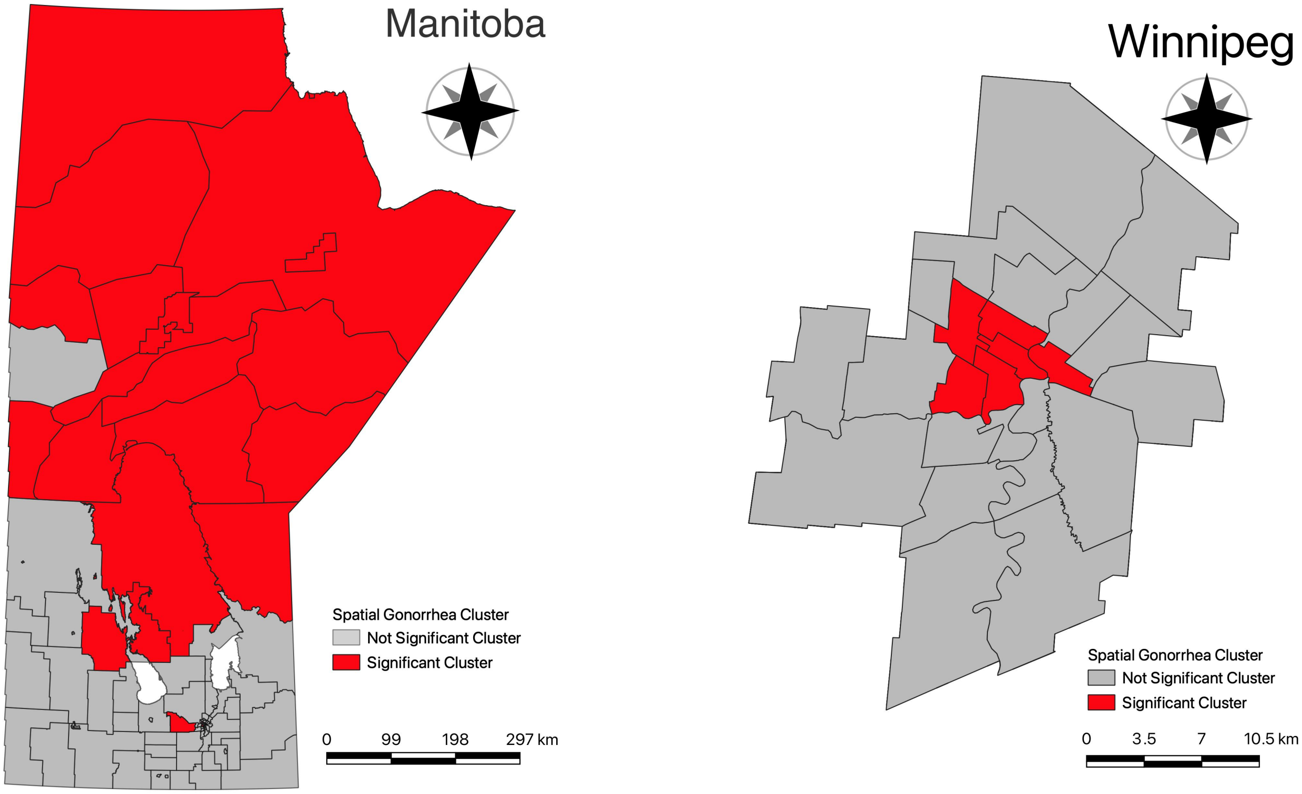

(a) Manitoba

(b) Winnipeg

Figure 5.4: Spatial clusters of Gonorrhea infections in Manitoba, 2000-2016.

5.3.3 Temporal Patterns

As temporal information is not incorporated in our purely spatial analysis presented in Section 3.2, we intend to explore the temporal patterns of Gonorrhea in Manitoba. The annual incidence rates of infections exhibit cyclical fluctuations throughout the study period (Figure 5.1a). These fluctuations suggest the presence of temporal patterns influencing the infection's transmission dynamics. Figure

5.5 illustrates the additive time series decomposition of monthly infections. Gonorrhea infections experience a rise from August 2005 to October 2008, reaching a historical peak of 158 infections in September 2007, and a mild increase occurs from August 2011 to November 2013, with a peak of 145 infections in August 2012. Additionally, there is a significant increase in the number of infections from 2015 until the end of the study period in 2016, with a peak of 274 infections in September 2016.

The time series decomposition reveals that Gonorrhea occurrence has seasonal and recurring patterns over the late summer and fall (Figure 5.5), with higher numbers of infections occurring from August through November each year. The Friedman test [72] for seasonality is utilized to assess the statistical significance of the existence of the seasonal trend within the dataset. Furthermore, a SARIMA$(2,0,0)(1,0,0)12$ model with $\phi_1 = 0.47$, $\phi_2 = 0.45$, and $\Phi_1 = 0.17$ is effectively applied (Figure 5.6), confirming the presence of a strong temporal trend in infections. We apply a Box-Cox transformation [14] with the parameter estimated at 0.01 before fitting the SARIMA model to achieve model variance stationarity. The residuals from the fitted SARIMA model demonstrate that they are uncorrelated and normally distributed, with a mean of zero and a constant variance. The Ljung-Box test [53] is employed to investigate the existence of residual autocorrelation subsequent to model fitting. The outcomes of the test reveal that no residual autocorrelation persisted within the fitted model.

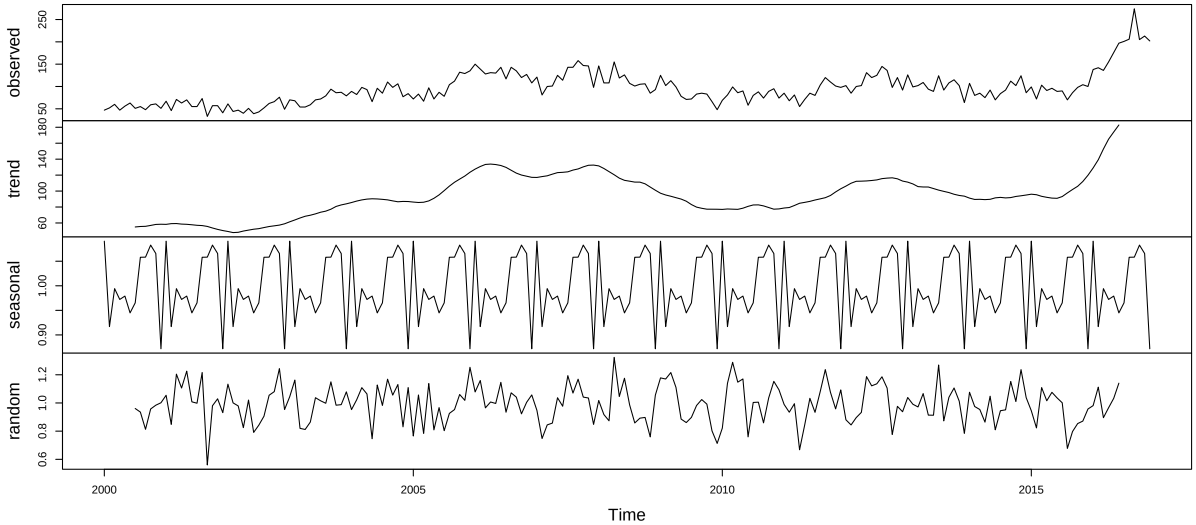

Figure 5.5: Monthly time series data decomposition.

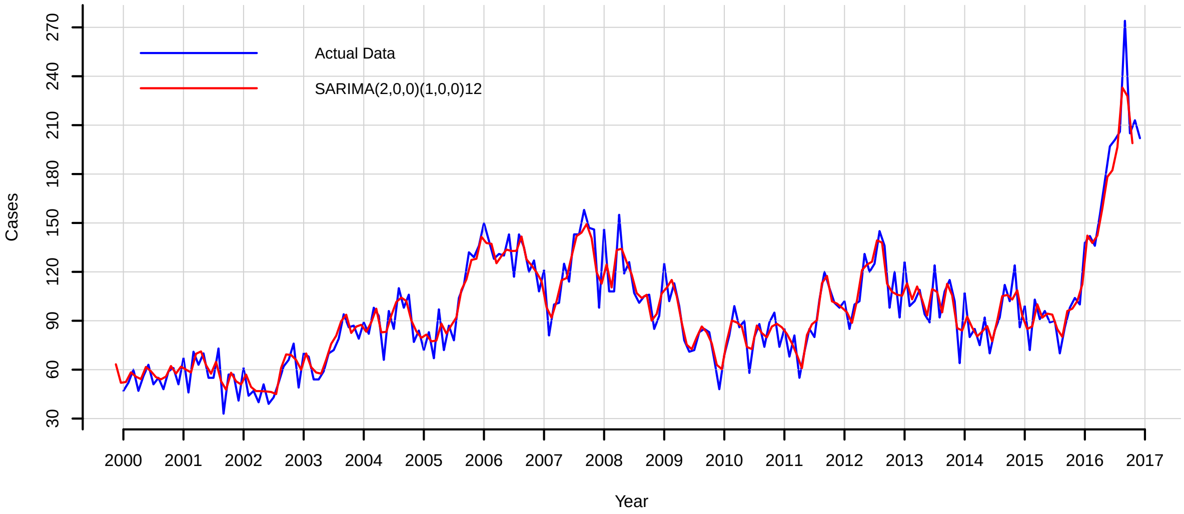

Figure 5.6: Monthly time series data and SARIMA model fitting.

5.3.4 Spatiotemporal Patterns

We employ a spatial and temporal scanning window size of 50% of the total population at risk and the entire study duration to detect significant space-time clusters. Additionally, we consider aggregated monthly data of infections across all RHADs from 2000 to 2016 in our spatiotemporal analysis. Kulldorff's space-time scan statistic, applied through a discrete Poisson model within a spatiotemporal framework, reveals space-time heterogeneity in the spread of infections in Manitoba from 2000 to 2016 and identifies the most likely and the secondary statistically significant high-risk clusters illustrated in Figure 5.7. The most likely space-time cluster is located in the northern districts of Manitoba, including 16 RHADs. This most likely space-time cluster occurs during the high-risk period from January 2006 to June 2014, with 3617 reported infections and a relative risk of 5.3. In addition, the secondary cluster is identified in the central districts of Winnipeg, covering 2 RHADs. This secondary space-time cluster is associated with a high-risk period from June 2004 to November 2012, including a total of 1896 reported infections and a relative risk of 2.91.

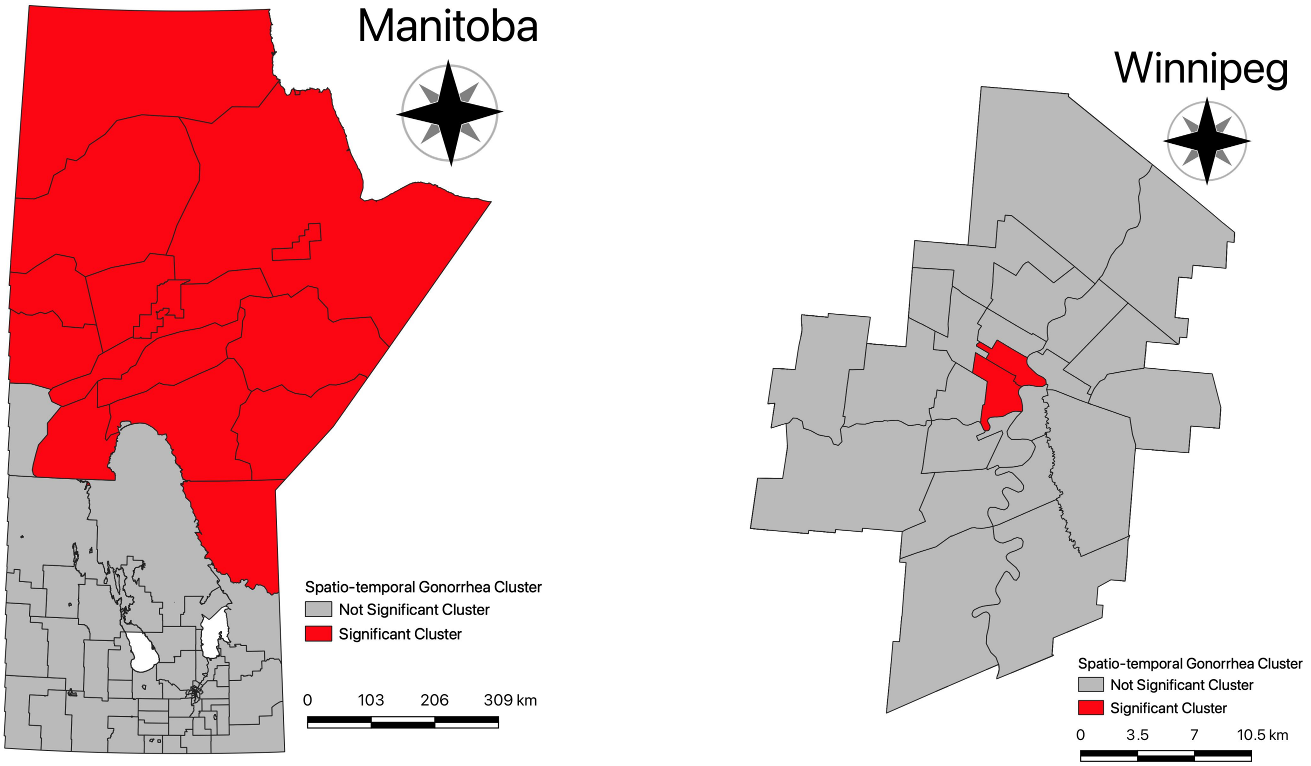

(a) Manitoba

(b) Winnipeg

Figure 5.7: Spatiotemporal clusters of Gonorrhea infections in Manitoba, 2000-2016.

5.4 Discussion

The findings of this study enhance our knowledge of Gonorrhea transmission dynamics, the epidemic, and its spread through space and time in Manitoba. This research investigates the temporal, spatial, and spatiotemporal clusters of the infection at the RHAD level within the Canadian province of Manitoba, from 2000 to 2016. Purely spatial analysis of the infections reveals that there are significant clusters of Gonorrhea in Manitoba, particularly in the northern district of the province with 20 RHADs and the central districts of Winnipeg with 6 RHADs. The temporal analysis of the infections uncovers a seasonal and recurrent pattern, with Gonorrhea infections consistently peaking during the late summer and fall months each year. The spatiotemporal cluster analysis offers additional evidence of RHADs experiencing a higher number of infections than what would be expected within a specified geographic area and time frame. The spatiotemporal analysis shows that the distribution of the infections in Manitoba from 2000 to 2016 exhibits significant spatial and temporal variations. Specifically, high-risk clusters are identified in two distinct periods and geographical locations: the identified high-risk clusters are located in the northern parts of Manitoba from 2006 to 2014 and the central districts of Winnipeg from 2004 to 2012. The high-risk cluster located in the northern parts of Manitoba is the larger cluster covering a total of 16 RHADs. Furthermore, there are disparities in reported infections based on sex and age, with a higher incidence among females and a lower mean age compared to males. The higher rates of female cases may be attributed to the fact that Gonorrhea tends to be more asymptomatic in males. Moreover, nearly 16% of the 2016 reported infections are associated with individuals who experienced multiple infections within a single year. Those individuals can significantly contribute to the spread of the infection. Therefore, it is essential to identify and address this specific group to minimize the overall transmission of the infection in the community.

This study has some limitations. First, while our administrative data includes all laboratory-confirmed infections in the province, these data are potentially underreported due to the asymptomatic nature of the disease and the healthcare-seeking behaviors of individuals. Second, individual-level data on laboratory-confirmed Gonorrhea infections after 2016 were not accessible during the time of conducting this study. Additionally, due to the lack of data on the sexual behaviors of the infected individuals, we are unable to identify high-risk sexual behaviors that could be informative for public health officials regarding further interventions and prevention strategies.

5.5 Conclusion

To the best of our knowledge, this study is the first investigation into the spatial, temporal, and spatiotemporal clustering of Gonorrhea infection in Manitoba between 2000 and 2016 at the RHAD level, using individual-level, laboratory-confirmed administrative data. This study detects the existence of the temporal, spatial, and spatiotemporal clusters of the infection at the RHAD level. This study also evaluates the variations in the spread of Gonorrhea across different age groups and sexes within the province. Emphasizing the frequency of repeat Gonorrhea infections can play a crucial role in increasing public awareness about the importance of practicing safe sexual behaviors, getting regular testing, and adhering to prescribed treatments. This heightened awareness has the potential to stimulate behavioral changes that effectively lower the risk of infection.

The outcomes of this study provide valuable insights for public health and Manitoba Health as they reveal the existence of high-risk clusters of Gonorrhea infections. These high-risk clusters determine where prevention strategies, control measures, and allocation of resources should be focused and strengthened to reduce the burden of the infection. Furthermore, policymakers should prioritize age and sex groups that are at higher risk of both contracting and spreading the infection. This emphasis is essential for the development of targeted and localized prevention strategies and control programs. Given that Gonorrhea is more prevalent among younger age groups, particularly among females, there is a clear need for comprehensive health education programs in schools, colleges, universities, and the general public. These programs should aim to educate individuals about the risks associated with the infection, modes of transmission, available treatments, common symptoms, and the importance of utilizing screening programs and accessing clinical services. This proactive approach is vital in raising awareness and promoting responsible sexual health practices to reduce the spread of Gonorrhea.

6

Conclusion

This thesis advanced spatiotemporal individual-level modeling of infectious disease transmission dynamics by developing, extending, and implementing the GD-ILM framework. It addressed major epidemiological challenges, including reinfection and seasonality, introduced computational innovations to improve efficiency, and demonstrated the practical relevance of the models through applications to multiple infectious diseases in Manitoba, Canada.

Chapter 2 introduced a novel and extensible modeling framework that advances the GD-ILM framework by explicitly accounting for reinfection dynamics within spatially structured populations. The proposed GD-ILM SEIRS model moves beyond classical compartmental formulations by stratifying the susceptible population according to infection history, thereby distinguishing individuals at risk of initial infection from those vulnerable to reinfection following waning immunity. This distinction is particularly important for diseases such as TB, where recurrent disease plays a substantial role in long-term transmission dynamics and where failure to account for reinfection can lead to biased inference and suboptimal public health decision-making. This chapter provides a more realistic representation of how immunity, exposure, and spatial proximity interact to shape disease spread over time.

Through extensive simulation studies conducted on both regular and irregular spatial grids, Chapter 2 demonstrated the robustness, identifiability, and stability of the GD-ILM SEIRS model across a wide range of epidemiological and spatial scenarios. These simulations highlighted the importance of spatial granularity, showing that transmission dynamics, latent periods, infectious durations, and waning immunity periods can vary substantially across sub-regions, even within the same broader geographic unit. The consistency of parameter recovery across simulation settings provided strong evidence that the model can reliably capture key features of real-world epidemics, despite the absence of closed-form likelihoods and standard inferential tools. The use of the MCECM algorithm enabled efficient likelihood-based estimation in this complex setting, further reinforcing the feasibility of applying the model to large-scale, individual-level surveillance data.

The empirical application of TB data from Manitoba illustrated the practical value of the proposed framework for public health research and policy. The analysis revealed distinct SES, demographic, and spatial risk factors associated with both initial TB infection and reinfection, underscoring the heterogeneous nature of disease risk across the province. By explicitly modeling spatial dependence between neighboring RHADs, the chapter highlighted the role of localized transmission processes and demonstrated how geographically targeted interventions may be more effective than uniform, province-wide strategies. The findings emphasize the importance of integrating fine-scale spatial information into infectious disease surveillance systems, particularly for addressing health inequities in underserved and high-risk communities.

Chapter 3 introduced a substantial methodological extension of the GD-ILM framework by incorporating seasonally driven transmission dynamics, thereby addressing a critical temporal feature of many infectious diseases that is often simplified or ignored in spatial epidemic models. By embedding a seasonally forced infection kernel within the GD-ILM framework structure, this chapter provided a principled and flexible approach for capturing periodic fluctuations in infection risk while preserving fine-scale spatial heterogeneity. The resulting seasonal GD-ILM framework enables simultaneous inference on spatial clustering, temporal seasonality, and individual-level heterogeneity, offering a more realistic representation of disease spread in settings characterized by strong cyclical patterns, such as Influenza and other respiratory infections.

Through a combination of high-resolution simulation studies and an empirical application to individual-level Influenza data from Manitoba, Chapter 3 demonstrated the practical and inferential advantages of explicitly modeling seasonality. The results showed that incorporating seasonal effects substantially improves model fit, interpretability, and parameter recovery while reducing bias in spatial dependence estimates that can arise when temporal dynamics are misspecified. The simulation experiments clearly illustrated that omitting seasonality distorts the inferred spatial structure of transmission, reinforcing the methodological necessity of jointly modeling spatial and temporal processes in spatiotemporal infectious disease analysis. These findings emphasize that accurate epidemic modeling requires careful consideration of both where and when infections occur, particularly in diseases with strong seasonal drivers.

The real-data application further highlighted the model's ability to uncover meaningful epidemiological insights with direct public health relevance. The seasonal parameters captured well-established cyclical patterns in Influenza transmission, while the spatial components revealed localized clusters of elevated infection risk across Manitoba's HAD. The analysis also identified pronounced urban–rural disparities and heterogeneous SES effects on susceptibility, underscoring the role of social determinants in shaping both temporal and spatial patterns of disease transmission. By integrating these dimensions within a unified framework, Chapter 3 provided a granular understanding of how biological seasonality, geographic context, and SES conditions jointly influence epidemic dynamics.

From a policy and intervention standpoint, Chapter 3 demonstrated how seasonally informed spatial models can support more timely and efficient public health responses. The ability to anticipate seasonal transmission peaks allows health authorities to strategically plan vaccination campaigns, allocate healthcare resources, and implement preventive measures ahead of periods of heightened risk. At the same time, the identification of persistent spatial hotspots enables geographically targeted interventions, ensuring that limited public health resources are directed toward districts and communities most vulnerable to infection. The explicit incorporation of SES effects further highlights the need for equity-oriented public health strategies that address structural factors contributing to increased disease risk.

Overall, Chapter 3 extended the GD-ILM framework into the temporal domain by formally integrating seasonality with spatial heterogeneity at the individual level. By demonstrating the consequences of temporal misspecification and the benefits of seasonally informed modeling, this chapter reinforces the importance of jointly modeling space, time, and social context in infectious disease epidemiology. The methodological advances and empirical insights developed in this chapter contribute to a comprehensive, data-driven framework for understanding, predicting, and controlling infectious diseases in complex, heterogeneous populations.

Chapter 4 introduced a comprehensive and computationally efficient framework for parameter estimation in GD-ILMs, addressing a critical challenge in scaling individual-level epidemic models to large populations with complex spatial structures. By combining the SAECM algorithm with a stratified temporally-weighted KDE-based PPS sampling method, this chapter demonstrated how approximate likelihood estimation can dramatically reduce computational burden while maintaining reliable parameter inference. The integration of temporally and spatially informed sampling ensures that the approximation captures the most informative observations, preserving estimation accuracy even in high-dimensional settings and enabling the practical application of GD-ILMs to real-world epidemic data.

Extensive simulation studies conducted across multiple spatial grid resolutions (10×10, 20×20, and 30×30) and varying sampling fractions highlighted the robustness, scalability, and limitations of the proposed method. When using full data, SAECM and traditional MCECM yielded highly accurate parameter estimates, confirming the validity of both the modeling and estimation procedures. More importantly, the stratified temporally-weighted KDE-based PPS sampling method achieved substantial computational speed-ups with moderate sampling fractions (50%–80%) without sacrificing accuracy. These results emphasize the method's capacity to handle large-scale spatiotemporal epidemic data efficiently. However, the simulations also revealed that extremely low sampling fractions introduce bias, particularly in high-resolution grids, underscoring the importance of balancing computational efficiency with statistical precision when designing practical implementations.

The real-data application to COVID-19 transmission in Manitoba further demonstrated the utility and applicability of this framework in a complex, data-rich setting. By leveraging detailed administrative health records, fine-scale spatial units, and key covariates such as SES and age structure, the chapter illustrated how the SAECM and stratified temporally-weighted PPS sampling method can provide nuanced insights into disease transmission dynamics. The estimated incubation and infectious periods were consistent with established epidemiological knowledge, and the analysis highlighted spatial heterogeneity and temporal trends in disease spread. Furthermore, the framework revealed how demographic and SES factors shape transmission risk across communities, offering actionable information for public health decision-making.

From a practical and policy-oriented perspective, Chapter 4 demonstrated that this computational innovation enables high-resolution epidemic modeling and near-real-time surveillance, which is particularly valuable for rapidly evolving outbreaks. The ability to identify transmission hotspots, evaluate intervention effects, and efficiently allocate resources enhances the capacity of public health authorities to respond in a timely and targeted manner. Moreover, the flexibility of the framework to incorporate diverse spatial structures, covariates, and compartmental models ensures broad applicability across different infectious diseases and epidemiological contexts, extending the relevance of GD-ILMs for both research and operational public health.

Overall, Chapter 4 provides a critical advancement in the practical implementation of GD-ILMs, demonstrating that accurate, high-resolution parameter estimation is achievable even in large and complex datasets. By balancing computational efficiency with inferential reliability, the SAECM and stratified temporally-weighted KDE-based PPS sampling method equip epidemiologists and public health practitioners with a robust tool for monitoring, predicting, and mitigating disease spread.

Chapter 5 introduced a detailed investigation into the spatial, temporal, and spatiotemporal dynamics of Gonorrhea transmission across Manitoba from 2000 to 2016, leveraging individual-level, laboratory-confirmed administrative data at the RHAD level. By integrating purely spatial, purely temporal, and combined spatiotemporal analyses, this chapter provided a comprehensive characterization of the geographic and temporal patterns of infection, offering critical insights into the epidemiology of Gonorrhea in both urban and rural settings. The study revealed significant spatial clustering in northern Manitoba, encompassing 20 RHADs, as well as concentrated clusters in central Winnipeg, illustrating the heterogeneous distribution of risk across the province. Temporal analysis identified a clear recurrent and seasonal pattern, with infections peaking consistently during late summer and fall months, emphasizing the role of temporal periodicity in shaping transmission dynamics.

The spatiotemporal analysis further refined these findings, highlighting high-risk clusters that combined both geographic location and temporal windows of heightened transmission. Notably, a large cluster covering 16 RHADs in northern Manitoba was identified between 2006 and 2014, while central Winnipeg exhibited a high-risk cluster from 2004 to 2012. These results demonstrate how the integration of spatial and temporal dimensions provides a more precise understanding of disease propagation than either dimension alone. Additionally, analysis of demographic factors revealed disparities in infection incidence by sex and age, with higher infection rates among females and a lower mean age compared to males. The identification of individuals experiencing multiple infections within a single year underscores the role of repeat infections in sustaining transmission chains, suggesting that targeted interventions for this subgroup could have a disproportionate impact on reducing overall incidence.

From a public health perspective, the findings of Chapter 5 have important implications for prevention, control, and resource allocation. The identification of high-risk clusters enables public health authorities to prioritize geographic areas and demographic groups for targeted interventions, including enhanced screening, contact tracing, education campaigns, and treatment programs. Given the higher prevalence among younger age groups, particularly females, the results support the development of comprehensive sexual health education programs in schools, universities, and community settings. These programs can promote awareness about safe sexual practices, the importance of regular testing, timely treatment, and adherence to prescribed regimens, thereby contributing to behavioral changes that mitigate infection risk. Moreover, understanding the seasonal patterns of Gonorrhea transmission allows public health practitioners to strategically time interventions to anticipate periods of heightened risk, enhancing the efficiency and impact of public health measures.

Overall, Chapter 5 advances knowledge of Gonorrhea transmission in Manitoba by integrating spatial, temporal, and demographic dimensions, identifying critical high-risk clusters, and emphasizing the role of repeat infections in driving disease spread. By providing a data-driven foundation for targeted, timely, and equitable public health interventions, this chapter contributes to more effective epidemic management and supports evidence-based strategies to reduce the burden of Gonorrhea across the province.

The development and dissemination of the `GDILM.SEIRS` and `SeasEpi` R packages were documented in the Appendix. These packages, publicly available on CRAN, operationalized the reinfection-extended and seasonal GD-ILM frameworks, respectively. They provided tools for model fitting, simulation, and evaluation using example epidemiological data, promoting reproducibility and facilitating the practical adoption of spatiotemporal infectious disease modeling in research and public health contexts.

Taken together, these studies represent a comprehensive advancement in spatiotemporal infectious disease modeling, combining theoretical developments, epidemiological realism, computational innovation, and applied public health relevance.

While this thesis laid a robust foundation, several avenues remained for further exploration. Enhancing the GD-ILMs to incorporate additional sources of heterogeneity, such as age-structured contact patterns or social network data, could improve predictive performance. Incorporating variable infectious and incubation periods, rather than assuming fixed durations, would better capture the natural variability in disease progression across individuals and pathogens. Making the seasonality coefficients region-specific could further refine the models' ability to capture local transmission dynamics. Further extensions include exploring alternative spatial kernels and extending the GD-ILM framework to other compartmental structures, all of which would further enhance the flexibility, robustness, and overall impact of the proposed methodology.

In summary, this thesis bridged the gap between advanced spatiotemporal statistical modeling of infectious disease transmission and practical disease control, providing both methodological innovations and actionable insights for public health. Collectively, the thesis demonstrates that integrating individual-level, spatially explicit, and temporally informed models with efficient computational approaches can substantially enhance our understanding of infectious disease transmission. By combining rigorous methodology with empirical applications and reproducible software tools, this work equips researchers and public health practitioners with robust frameworks for predicting disease spread, identifying high-risk populations, and designing timely, equitable, and effective interventions. Beyond its methodological contributions, the thesis emphasizes the importance of linking statistical innovation with actionable insights, highlighting how advanced modeling can directly inform public health policy, resource allocation, and intervention strategies in diverse epidemiological contexts.

Overall, this research offers a comprehensive methodological framework for understanding, monitoring, and mitigating infectious disease dynamics, advancing both the theoretical foundations and practical applications of biostatistics and spatiotemporal epidemiology.

The results and conclusions are those of the authors, and no official endorsement by the MCHP, Manitoba Health, or other data providers is intended or should be inferred. Data used in this study are from the Population Health Research Data Repository, housed at the MCHP, University of Manitoba, and were derived from data provided by Manitoba Health.

Appendices

This appendix introduces two R packages, available and published on CRAN, developed as part of this thesis to support the implementation, estimation, and application of the proposed models: the GD-ILM with Reinfection (GD-ILM SEIRS) and Seasonal GD-ILM. Both packages are designed to enhance reproducibility, provide accessible computational tools, and facilitate the application of the proposed models in biostatistical research. They provide a comprehensive framework for investigating the spread of infectious diseases, allowing researchers to better understand patterns in transmission and to inform the design and timing of targeted public health interventions and control strategies.

The first package, `GDILM.SEIRS`, implements the GD-ILM with reinfection within the SEIRS framework. It employs the MCECM algorithm for parameter estimation, providing tools for model fitting, parameter inference, and evaluation through AIC. In addition, the package supports simulation studies under user-defined configurations, enabling exploration of reinfection dynamics and spatial heterogeneity in disease spread.

The second package, `SeasEpi`, implements the seasonal GD-ILM for modeling periodic patterns of infectious disease transmission. Similar to `GDILM.SEIRS`, it applies the MCECM algorithm for parameter estimation and offers tools for model fitting and simulation experiments.

Together, these packages provide a computational foundation for the methodological contributions of this thesis, bridging theoretical development with practical applications in spatiotemporal modeling of infectious disease transmission dynamics.

Package ‘GDILM.SEIRS’

November 3, 2025

Title Spatial Modeling of Infectious Disease with Reinfection

Version 0.0.5

Description Geographically Dependent Individual Level Models (GDILMs) within the Susceptible-Exposed-Infectious-Recovered-Susceptible (SEIRS) framework are applied to model infectious disease transmission, incorporating reinfection dynamics. This package employs a likelihood based Monte Carlo Expectation Conditional Maximization (MCECM) algorithm for estimating model parameters. It also provides tools for GDILM fitting, parameter estimation, AIC calculation on real pandemic data, and simulation studies customized to user-defined model settings.

License MIT + file LICENSE

Encoding UTF-8

LazyData true

Imports MASS, mvtnorm, ngspatial, stats

RoxygenNote 7.3.2

Suggests testthat (>= 3.0.0)

Config/testthat/edition 3

NeedsCompilation no

Author Amin Abed [aut, cre, cph] (ORCID:
<https://orcid.org/0000-0002-7381-4721>),
Mahmoud Torabi [ths],
Zeinab Mashreghi [ths]

Maintainer Amin Abed <abeda@myumanitoba.ca>

Depends R (>= 3.5.0)

Repository CRAN

Date/Publication 2025-11-02 23:10:02 UTC

Contents

`Datasets` *Hypothetical Datasets*

Description

The primary function, `GDILM_SEIRS_Par_Est`, fits the Geographically Dependent Individual Level Model (GDILM) for infectious disease transmission incorporating reinfection dynamics within the SEIRS framework, using real-world data. It can be applied to any dataset with the appropriate structure, requiring two dataframes: `data` and `adjacency_matrix`, along with the necessary parameters. For illustration purposes, we provide two hypothetical examples of `data` and `adjacency_matrix` to demonstrate the structure of the inputs. These examples will also be used to illustrate how the function works in practice.

`data`

A data frame with 100 rows and 12 columns.

This hypothetical dataset demonstrates the structure required for the dataframe used in this package. The dataset for use with the package should adhere to the same column format and order but can include any number of rows, with each row representing an infected individual. The example dataset includes individual-level characteristics (e.g., age, infection status) and area-level characteristics (e.g., socioeconomic status, STI rate) for 100 individuals, each associated with a postal code. This dataset will be used as input in the example for the `GDILM_SEIRS_Par_Est` function.

Ave_Postal_Pop Average population of each postal code

AverageAge Average age of individuals within each postal code (individual-level data)

InfectedTime Time of infection for each individual, represented as a numerical value from 1 to the end of the pandemic period

LAT Latitude of the postal code

LONG Longitude of the postal code

Label_NC_shape The region number that the postal code belongs to, here assuming the study area is divided into five subregions

MaleRate Rate of males in the population of the postal code (individual-level data)

NInfected Number of infected individuals in the postal code

SES Socioeconomic status indicator of the region to which the postal code belongs (area-level data)

STI Sexually transmitted infection rate of the region that the postal code belongs to (area-level data)

SymptomRate Rate of disease symptoms in the postal code (individual-level data), indicating whether individuals are symptomatic or asymptomatic

status 1 if the postal code is infected for the first time, and 0 if the postal code is reinfected `adjacency_matrix`

A 5x5 matrix.

This hypothetical adjacency matrix is provided to illustrate the structure required for use with this package. The matrix used with the package should follow a similar format, maintaining the same layout but allowing for any number of regions. The adjacency matrix defines the neighborhood relationships between subregions in a hypothetical study area. In this example, it represents a spatial structure with five subregions, where each cell indicates the presence or absence of a connection between the corresponding subregions. The example for the `GDILM_SEIRS_Par_Est` function will use this matrix as input.

V1 Subregion 1: Represents the first subregion in the region under study

V2 Subregion 2: Represents the second subregion in the region under study

V3 Subregion 3: Represents the third subregion in the region under study

V4 Subregion 4: Represents the fourth subregion in the region under study

V5 Subregion 5: Represents the fifth subregion in the region under study

Value Each cell in the matrix (e.g., between subregion 1 and subregion 2) represents the connection (typically 0 or 1) between the two subregions, where 1 indicates they are neighbors and 0 indicates they are not.

`GDILM_SEIRS_Par_Est` *GDILM SEIRS for Real Data*

Description

This function applies the Geographically Dependent Individual Level Model (GDILM) for infectious disease transmission, incorporating reinfection dynamics within the Susceptible-Exposed-Infectious-Recovered-Susceptible (SEIRS) framework, to real data. It employs a likelihood based Monte Carlo Expectation Conditional Maximization (MCECM) algorithm for parameter estimation and AIC calculation. This function requires two dataframes, named `data` and `adjacency_matrix`, along with the necessary parameters. Detailed information on the structure of these two datasets is provided in the package.

Usage

```
GDILM_SEIRS_Par_Est(
  data,
  adjacency_matrix,
  DimCovInf,
  DimCovSus,
  DimCovSusReInf,
  tau0,
  lambda0,
  alphaS0,
  delta0,
  alphaT0,
```

```
  InfPrd,
  IncPrd,
  NIterMC,
  NIterMCECM
)
```

Arguments

`data`	Dataset. The dataset should exactly match the `data` file in the data folder, including all the columns with the same names.
`adjacency_matrix`	Adjacency matrix representing the regions in the study area (0 if no connection between regions)
`DimCovInf`	Dimensions of the individual infectivity covariate
`DimCovSus`	Dimensions of the area-level susceptibility to initial infection covariate
`DimCovSusReInf`	Dimensions of the area-level susceptibility to reinfection covariate
`tau0`	Initial value for spatial precision
`lambda0`	Initial value for spatial dependence
`alphaS0`	Initial value for the susceptibility intercept
`delta0`	Initial value for the spatial decay parameter
`alphaT0`	Initial value for the infectivity intercept
`InfPrd`	Infectious period that can be obtained either from the literature or by fitting an SEIRS model to the data
`IncPrd`	Incubation period that can be obtained either from the literature or by fitting an SEIRS model to the data
`NIterMC`	Number of MCMC iterations
`NIterMCECM`	Number of MCECM iterations

Value

`alphaS` Estimate of alpha S

`BetaCovInf` Estimate of beta vector for the individual level infection covariate

`BetaCovSus` Estimate of beta vector for the areal susceptibility to first infection covariate

`BetaCovSusReInf` Estimate of beta vector for the areal susceptibility to reinfection covariate

`alphaT` Estimate of alpha T

`delta` Estimate of delta

`tau1` Estimate of tau

`lambda1` Estimate of lambda

`AIC` AIC of the fitted GDILM SEIRS

Examples

```
data(data)
data(adjacency_matrix)
GDILM_SEIRS_Par_Est(data,adjacency_matrix,2,2,2,0.5, 0.5, 1, 2, 1, 1, 1, 20, 2)
```

`GDILM_SEIRS_Sim_Par_Est`
GDILM SEIRS for a Simulation Study

Description

This function conducts a simulation study for the Geographically Dependent Individual Level Model (GDILM) of infectious disease transmission, incorporating reinfection dynamics within the Susceptible-Exposed-Infectious-Recovered-Susceptible (SEIRS) framework, using a user-defined grid size. It applies a likelihood based Monte Carlo Expectation Conditional Maximization (MCECM) algorithm to estimate model parameters and compute the AIC.

Usage

```
GDILM_SEIRS_Sim_Par_Est(
  GridDim1,
  GridDim2,
  NPostPerGrid,
  MaxTimePand,
  tau0,
  lambda0,
  alphaS0,
  delta0,
  alphaT0,
  PopMin,
  PopMax,
  InfFraction,
  ReInfFraction,
  InfPrd,
  IncPrd,
  NIterMC,
  NIterMCECM
)
```

Arguments

`GridDim1`	First dimension of the grid
`GridDim2`	Second dimension of the grid
`NPostPerGrid`	Number of postal codes per grid cell

`MaxTimePand`	Last time point of the pandemic
`tau0`	Initial value for spatial precision
`lambda0`	Initial value for spatial dependence
`alphaS0`	Initial value for the susceptibility intercept
`delta0`	Initial value for the spatial decay parameter
`alphaT0`	Initial value for the infectivity intercept
`PopMin`	Minimum population per postal code
`PopMax`	Maximum population per postal code
`InfFraction`	Fraction of each grid cell's population to be infected
`ReInfFraction`	Fraction of each grid cell's population to be reinfected
`InfPrd`	Infectious period that can be obtained either from the literature or by fitting an SEIRS model to the data
`IncPrd`	Incubation period that can be obtained either from the literature or by fitting an SEIRS model to the data
`NIterMC`	Number of MCMC iterations
`NIterMCECM`	Number of MCECM iterations

Value

`alphaS` Estimate of alpha S

`BetaCovInf` Estimate of beta vector for the individual level infection covariate

`BetaCovSus` Estimate of beta vector for the areal susceptibility to first infection covariate

`BetaCovSusReInf` Estimate of beta vector for the areal susceptibility to reinfection covariate

`alphaT` Estimate of alpha T

`delta` Estimate of delta

`tau1` Estimate of tau

`lambda1` Estimate of lambda

`AIC` AIC of the fitted GDILM SEIRS

Examples

```
GDILM_SEIRS_Sim_Par_Est(5,5,10,30,0.7, 0.5, 1, 2.5, 0,40, 50,0.3,0.6, 5, 5, 10, 3)
```

Index

Package ‘SeasEpi’

November 3, 2025

Title Spatiotemporal Modeling of Seasonal Infectious Disease

Version 0.0.3

Description Spatiotemporal individual-level model of seasonal infectious disease transmission within the Susceptible-Exposed-Infectious-Recovered-Susceptible (SEIRS) framework are applied to model seasonal infectious disease transmission. This package employs a likelihood based Monte Carlo Expectation Conditional Maximization (MCECM) algorithm for estimating model parameters. In addition to model fitting and parameter estimation, the package offers functions for calculating AIC using real pandemic data and conducting simulation studies customized to user-specified model configurations.

Encoding UTF-8

LazyData true

Imports MASS, mvtnorm, ngspatial, stats

RoxygenNote 7.3.2

Suggests testthat (>= 3.0.0)

Config/testthat/edition 3

NeedsCompilation no

Author Amin Abed [aut, cre, cph] (ORCID:
<`https://orcid.org/0000-0002-7381-4721`>),
Mahmoud Torabi [ths],
Zeinab Mashreghi [ths]

Maintainer Amin Abed <`abeda@myumanitoba.ca`>

Depends R (>= 3.5.0)

Repository CRAN

Date/Publication 2025-11-02 23:00:02 UTC

Contents

`Datasets` *Hypothetical Datasets*

Description

The main function, `SeasEpi_Par_Est`, applies the spatiotemporal individual-level model of seasonal infectious disease transmission within the SEIRS framework to a hypothetical dataset. It is compatible with any dataset that follows the required format, which includes two dataframes: `data` and `adjacency_matrix`, along with relevant parameter inputs. To demonstrate the expected input structure and the function's practical use, we provide two hypothetical examples of `data` and `adjacency_matrix`.

`data`

A data frame with 100 rows and 11 columns.

This sample dataset illustrates the required structure for the dataframe used with this package. While the number of rows can vary, each row must represent a single infected individual, and the column names and order must follow the specified format. The example includes individual-level attributes (e.g., age, infection status) as well as area-level information (e.g., socioeconomic status) for 100 individuals, each linked to a postal code. This dataset will serve as input in the example demonstrating the `SeasEpi_Par_Est` function.

Ave_Postal_Pop	Average population of each postal code
AverageAge	Average age of individuals within each postal code (individual-level data)
InfectedTime	Time of infection for each individual, represented as a numerical value from 1 to the end of the pandemic period
LAT	Latitude of the postal code
LONG	Longitude of the postal code
Label_NC_shape	The region number that the postal code belongs to, here assuming the study area is divided into five subregions
MaleRate	Rate of males in the population of the postal code (individual-level data)
NInfected	Number of infected individuals in the postal code
SES	Socioeconomic status indicator of the region to which the postal code belongs (area-level data)
STI	Sexually transmitted infection rate of the region that the postal code belongs to (area-level data)
SymptomRate	Rate of disease symptoms in the postal code (individual-level data), indicating whether individuals are symptomatic or asymptomatic

`adjacency_matrix`

A 5x5 matrix.

This hypothetical adjacency matrix is provided to illustrate the structure required for use with this package. The matrix used with the package should follow a similar format, maintaining the same layout but allowing for any number of regions. The adjacency matrix defines the neighborhood relationships between subregions in a hypothetical study area. In this example, it represents a spatial structure with five subregions, where each cell indicates the presence or absence of a connection between the corresponding subregions. The example for the `SeasEpi_Par_Est` function will use this matrix as input.

V1	Subregion 1: Represents the first subregion in the region under study
V2	Subregion 2: Represents the second subregion in the region under study
V3	Subregion 3: Represents the third subregion in the region under study
V4	Subregion 4: Represents the fourth subregion in the region under study
V5	Subregion 5: Represents the fifth subregion in the region under study
Value	Each cell in the matrix (e.g., between subregion 1 and subregion 2) represents the connection (typically 0 or 1) between the two subregions, where 1 indicates they are neighbors and 0 indicates they are not.

`SeasEpi_Par_Est` *SeasEpi for Real Data*

Description

This function applies the spatiotemporal individual-level model of seasonal infectious disease transmission within the Susceptible-Exposed-Infectious-Recovered-Susceptible (SEIRS) framework, to real data. It employs a likelihood based Monte Carlo Expectation Conditional Maximization (MCECM) algorithm for parameter estimation and AIC calculation. This function requires two dataframes, named `data` and `adjacency_matrix`, along with the necessary parameters. Detailed information on the structure of these two datasets is provided in the package.

Usage

```
SeasEpi_Par_Est(
  data,
  adjacency_matrix,
  DimCovInf,
  DimCovSus,
  tau0,
  lambda0,
  alphaS0,
  delta0,
  alphaT0,
  InfPrd,
  IncPrd,
```

```
  NIterMC,
  NIterMCECM,
  zeta10,
  zeta20,
  T_cycle
)
```

Arguments

`data`	Dataset. The dataset should exactly match the `data` file in the data folder, including all the columns with the same names.
`adjacency_matrix`	Adjacency matrix representing the regions in the study area (0 if no connection between regions)
`DimCovInf`	Dimensions of the individual infectivity covariate
`DimCovSus`	Dimensions of the area-level susceptibility to initial infection covariate
`tau0`	Initial value for spatial precision
`lambda0`	Initial value for spatial dependence
`alphaS0`	Initial value for the susceptibility intercept
`delta0`	Initial value for the spatial decay parameter
`alphaT0`	Initial value for the infectivity intercept
`InfPrd`	Infectious period that can be obtained either from the literature or by fitting an SEIRS model to the data
`IncPrd`	Incubation period that can be obtained either from the literature or by fitting an SEIRS model to the data
`NIterMC`	Number of MCMC iterations
`NIterMCECM`	Number of MCECM iterations
`zeta10`	Initial value for the amplitude of the seasonal oscillation parameter (sin part)
`zeta20`	Initial value for the phase of the seasonal oscillation parameter (cos part)
`T_cycle`	The duration of a complete seasonal cycle (e.g., 12 months for an annual cycle)

Value

`alphaS` Estimate of alpha S

`BetaCovInf` Estimate of beta vector for the individual level infection covariate

`BetaCovSus` Estimate of beta vector for the areal susceptibility to first infection covariate

`alphaT` Estimate of alpha T

`delta` Estimate of delta

`zeta1` Estimate of zeta1

`zeta2` Estimate of zeta2

`tau1` Estimate of tau

`lambda1` Estimate of lambda

`AIC` AIC of the fitted GDILM SEIRS

Examples

```
data(data)
data(adjacency_matrix)
SeasEpi_Par_Est(data,adjacency_matrix,2,2,0.5, 0.5, 1, 0.1, 1, 1, 1, 20, 2,0.2,0.2,5)
```

`SeasEpi_Sim_Par_Est` *SeasEpi for a Simulation Study*

Description

This function conducts a simulation study for spatiotemporal individual-level model of seasonal infectious disease transmission within the Susceptible-Exposed-Infectious-Recovered-Susceptible (SEIRS) framework, using a user-defined grid size. It applies a likelihood based Monte Carlo Expectation Conditional Maximization (MCECM) algorithm to estimate model parameters and compute the AIC.

Usage

```
SeasEpi_Sim_Par_Est(
  GridDim1,
  GridDim2,
  NPostPerGrid,
  MaxTimePand,
  tau0,
  lambda0,
  alphaS0,
  delta0,
  alphaT0,
  PopMin,
  PopMax,
  InfFraction,
  InfPrd,
  IncPrd,
  NIterMC,
  NIterMCECM,
  zeta10,
  zeta20,
  T_cycle
)
```

Arguments

`GridDim1`	First dimension of the grid
`GridDim2`	Second dimension of the grid

`NPostPerGrid`	Number of postal codes per grid cell
`MaxTimePand`	Last time point of the pandemic
`tau0`	Initial value for spatial precision
`lambda0`	Initial value for spatial dependence
`alphaS0`	Initial value for the susceptibility intercept
`delta0`	Initial value for the spatial decay parameter
`alphaT0`	Initial value for the infectivity intercept
`PopMin`	Minimum population per postal code
`PopMax`	Maximum population per postal code
`InfFraction`	Fraction of each grid cell's population to be infected
`InfPrd`	Infectious period that can be obtained either from the literature or by fitting an SEIRS model to the data
`IncPrd`	Incubation period that can be obtained either from the literature or by fitting an SEIRS model to the data
`NIterMC`	Number of MCMC iterations
`NIterMCECM`	Number of MCECM iterations
`zeta10`	Initial value for the amplitude of the seasonal oscillation parameter (sin part)
`zeta20`	Initial value for the phase of the seasonal oscillation parameter (cos part)
`T_cycle`	The duration of a complete seasonal cycle (e.g., 12 months for an annual cycle)

Value

`alphaS` Estimate of alpha S

`BetaCovInf` Estimate of beta vector for the individual level infection covariate

`BetaCovSus` Estimate of beta vector for the areal susceptibility to first infection covariate

`alphaT` Estimate of alpha T

`delta` Estimate of delta

`zeta1` Estimate of zeta1

`zeta2` Estimate of zeta2

`tau1` Estimate of tau

`lambda1` Estimate of lambda

`AIC` AIC of the fitted GDILM SEIRS

Examples

```
SeasEpi_Sim_Par_Est(5,5,10,30,0.7, 0.7, -1, 0.1, 0,40, 50,0.6, 5, 5, 10, 3,0.2,0.2,5)
```

Index

References

[1] Amin Abed. *GDILM.SEIRS: Spatial Modeling of Infectious Disease with Reinfection.* R package version 0.0.3, The Comprehensive R Archive Network (CRAN), 2025.

[2] Amin Abed. *SeasEpi: Spatiotemporal Modeling of Seasonal Infectious Disease.* R package version 0.0.1, The Comprehensive R Archive Network (CRAN), 2025.

[3] Amin Abed, Mahmoud Torabi, and Zeinab Mashreghi. Gonorrhea Cluster Detection in Manitoba, Canada: Spatial, Temporal, and Spatio-Temporal Analysis. *Infectious Disease Modelling*, 9(4):1045–1056, 2024.

[4] Amin Abed, Mahmoud Torabi, and Zeinab Mashreghi. Individual-Level Modeling of Infectious Disease Transmission with Reinfection Dynamics: Application to Tuberculosis in Manitoba, Canada. *Spatial and Spatio-Temporal Epidemiology*, page 100780, 2025.

[5] Waleed Almutiry and Rob Deardon. Incorporating Contact Network Uncertainty in Individual-Level Models of Infectious Disease Using Approximate Bayesian Computation. *The International Journal of Biostatistics*, 16(1), 12 2019.

[6] Waleed Almutiry, Vineetha Warriyar KV, and Rob Deardon. Continuous Time Individual-Level Models of Infectious Disease: Package EpiILMCT. *Journal of Statistical Software*, 98:1–44, 2021.

[7] Leila Amiri, Mahmoud Torabi, and Rob Deardon. Analyzing COVID-19 Data in the Canadian Province of Manitoba: A New Approach. *Spatial Statistics*, 55:100729, 2023.

[8] Leila Amiri, Mahmoud Torabi, Rob Deardon, and Michael Pickles. Spatial Modeling of Individual-Level Infectious Disease Transmission: Tuberculosis Data in Manitoba, Canada. *Statistics in Medicine*, 40(7):1678–1704, 2021.

[9] Emmanuelle Augeraud-Véron and Nadir Sari. Seasonal Dynamics in an SIR Epidemic System. *Journal of Mathematical Biology*, 68(3):701–725, 2014.

[10] Trevor C Bailey, Anthony C Gatrell, et al. *Interactive Spatial Data Analysis*, volume 413. Longman Scientific & Technical Essex, 1995.

[11] Kyle T Bernstein, Julia L Marcus, Giuliano Nieri, Susan S Philip, and Jeffrey D Klausner. Rectal Gonorrhea and Chlamydia Reinfection Is Associated with Increased Risk of HIV Seroconversion. *JAIDS Journal of Acquired Immune Deficiency Syndromes*, 53(4):537–543, 2010.

[12] Julian Besag. Spatial Interaction and the Statistical Analysis of Lattice Systems. *Journal of the Royal Statistical Society Series B (Statistical Methodology)*, 36(2):192–225, 1974.

[13] James F Blanchard, Stephen Moses, Christina Greenaway, Pamela Orr, GW Hammond, and RC Brunham. The Evolving Epidemiology of Chlamydial and Gonococcal Infections in Response to Control Programs in Winnipeg, Canada. *American Journal of Public Health*, 88(10):1496–1502, 1998.

[14] George EP Box and David R Cox. An Analysis of Transformations. *Journal of the Royal Statistical Society Series B: Statistical Methodology*, 26(2):211–243, 1964.

[15] George EP Box, Gwilym M Jenkins, Gregory C Reinsel, and Greta M Ljung. *Time Series Analysis: Forecasting and Control*. John Wiley & Sons, 2015.

[16] Bruno Buonomo, Nakul Chitnis, and Alberto d'Onofrio. Seasonality in Epidemic Models: A Literature Review. *Ricerche di Matematica*, 67:7–25, 2018.

[17] Kathryn R Bush, Elizabeth A Henderson, James Dunn, Ron R Read, and Ami Singh. Mapping the core: chlamydia and gonorrhea infections in Calgary, Alberta. *Sexually Transmitted Diseases*, 35(3):291–297, 2008.

[18] Valeria D Cantos and Carlos del Rio. Gonorrhea in Adolescents and Young Adults. *Sexually Transmitted Infections in Adolescence and Young Adulthood: A Practical Guide for Clinicians*, pages 169–182, 2020.

[19] Y Choudhri, J Miller, J Sandhu, A Leon, and J Aho. Sexually Transmitted Infections: Gonorrhea in Canada, 2010–2015. *Canada Communicable Disease Report*, 44(2):37, 2018.

[20] Jonathan D Cryer and Kung-Sik Chan. *Time Series Analysis with Applications in R*. Springer, 2008.

[21] Ralph B D'Agostino. *Goodness-of-Fit-Techniques*. Routledge, 2017.

[22] Karina W Davidson, Michael J Barry, Carol M Mangione, Michael Cabana, Aaron B Caughey, Esa M Davis, Katrina E Donahue, Chyke A Doubeni, Alex H Krist, Martha Kubik, et al. Screening for Chlamydia and Gonorrhea: US Preventive Services Task Force Recommendation Statement. *Journal of the American Medical Association*, 326(10):949–956, 2021.

[23] Rob Deardon, Stephen P Brooks, Bryan T Grenfell, Matthew J Keeling, Michael J Tildesley, Nicholas J Savill, Darren J Shaw, and Mark EJ Woolhouse. Inference for Individual-Level Models of Infectious Diseases in Large Populations. *Statistica Sinica*, 20(1):239, 2010.

[24] Elizabeth Cahill Delmelle and Jean-Claude Thill. Urban Bicyclists: Spatial Analysis of Adult and Youth Traffic Hazard Intensity. *Transportation Research Record*, 2074(1):31–39, 2008.

[25] Bernard Delyon, Marc Lavielle, and Eric Moulines. Convergence of a Stochastic Approximation Version of the EM Algorithm. *Annals of Statistics*, 27(1):94–128, 1999.

[26] Arthur P Dempster, Nan M Laird, and Donald B Rubin. Maximum Likelihood from Incomplete Data via the EM Algorithm. *Journal of the Royal Statistical Society: Series B (Methodological)*, 39(1):1–22, 1977.

[27] Scott F Dowell. Seasonal Variation in Host Susceptibility and Cycles of Certain Infectious Diseases. *Emerging Infectious Diseases*, 7(3):369–374, 2001.

[28] Saffet Erdogan, Ibrahim Yilmaz, Tamer Baybura, and Mevlut Gullu. Geographical Information Systems Aided Traffic Accident Analysis System Case Study: City of Afyonkarahisar. *Accident Analysis & Prevention*, 40(1):174–181, 2008.

[29] Céline Faverjon and John Berezowski. Choosing the Best Algorithm for Event Detection Based on the Intended Application: A Conceptual Framework for Syndromic Surveillance. *Journal of Biomedical Informatics*, 85:126–135, 2018.

[30] JoAnne L Flynn and John Chan. Immunology of Tuberculosis. *Annual Review of Immunology*, 19(1):93–129, 2001.

[31] Yoshiharu Fukuda, Masahiro Umezaki, Keiko Nakamura, and Takehito Takano. Variations in Societal Characteristics of Spatial Disease Clusters: Examples of Colon, Lung, and Breast Cancer in Japan. *International Journal of Health Geographics*, 4:1–13, 2005.

[32] Nicholas C Grassly and Christophe Fraser. Seasonal Infectious Disease Epidemiology. *Proceedings of the Royal Society B Biological Sciences*, 273(1600):2541–2550, 2006.

[33] Seran Hakki, Jie Zhou, Jakob Jonnerby, Anika Singanayagam, Jack L Barnett, Kieran J Madon, Aleksandra Koycheva, Christine Kelly, Hamish Houston, Sean Nevin, et al. Onset and Window of SARS-CoV-2 Infectiousness and Temporal Correlation with Symptom Onset: A Prospective, Longitudinal, Community Cohort Study. *The Lancet Respiratory Medicine*, 10(11):1061–1073, 2022.

[34] W. K. Hastings. Monte Carlo Sampling Methods Using Markov Chains and Their Applications. *Biometrika*, 57(1):97–109, 1970.

[35] Hans Heesterbeek, Roy M Anderson, Viggo Andreasen, Shweta Bansal, Daniela De Angelis, Chris Dye, Ken TD Eames, W John Edmunds, Simon DW Frost, Sebastian Funk, et al. Modeling infectious disease dynamics in the complex landscape of global health. *Science*, 347(6227):aaa4339, 2015.

[36] Janelle Hippe and Ann M Jolly. STI Phase and the Geography of Sexual Partnerships: Prevalence of Long-Distance Sexual Contacts Among Chlamydia, Gonorrhea, and Coinfected STI Cases in Manitoba, Canada. *Spatial and Spatio-Temporal Epidemiology*, 3(3):255–263, 2012.

[37] King K Holmes, P Frederick Sparling, Walter E Stamm, Peter Piot, Judith N Wasserheit, Lawrence Corey, Myron Cohen, D Heather Watts, and Ronald A Nelson. *Sexually Transmitted Diseases*. McGraw-Hill, 2007.

[38] Christina B Hosenfeld, Kimberly A Workowski, Stuart Berman, Akbar Zaidi, Jeri Dyson, Debra Mosure, Gail Bolan, and Heidi M Bauer. Repeat infection with Chlamydia and gonorrhea among females: a systematic review of the literature. *Sexually Transmitted Diseases*, 36(8):478–489, 2009.

[39] Yujie Hu, Fahui Wang, Cecile Guin, and Haojie Zhu. A Spatio-Temporal Kernel Density Estimation Framework for Predictive Crime Hotspot Mapping and Evaluation. *Applied Geography*, 99:89–97, 2018.

[40] Behnaz Jafari and Robert Deardon. Bias and Bias-Correction for Individual-Level Models of Infectious Disease. *Spatial and Spatio-Temporal Epidemiology*, 43:100524, 2022.

[41] Matt J Keeling and Pejman Rohani. *Modeling Infectious Diseases in Humans and Animals*. Princeton University Press, 2008.

[42] Matt J Keeling, Mark EJ Woolhouse, Darren J Shaw, Louise Matthews, Margo Chase-Topping, Dan T Haydon, Stephen J Cornell, Jens Kappey, John Wilesmith, and Bryan T Grenfell. Dynamics of the 2001 UK Foot and Mouth Epidemic: Stochastic Dispersal in a Heterogeneous Landscape. *Science*, 294(5543):813–817, 2001.

[43] Jukka Matthias Krisp and Sara Durot. Segmentation of Lines Based on Point Densities—An Optimisation of Wildlife Warning Sign Placement in Southern Finland. *Accident Analysis & Prevention*, 39(1):38–46, 2007.

[44] M Kulldorff, K Rand, G Gherman, G Williams, D DeFrancesco, and V2 1 SaTScan. Software for The Spatial and Space-Time Scan Statistics. *SaTScan & M. Version*, 2, 1998.

[45] Martin Kulldorff. A Spatial Scan Statistic. *Communications in Statistics-Theory and Methods*, 26(6):1481–1496, 1997.

[46] Grace PS Kwong and Rob Deardon. Linearized Forms of Individual-Level Models for Large-Scale Spatial Infectious Disease Systems. *Bulletin of Mathematical Biology*, 74(8):1912–1937, 2012.

[47] Jami S Leichliter, Patricia J Dittus, Casey E Copen, and Sevgi O Aral. Trends in Factors Indicating Increased Risk for STI Among Key Subpopulations in the United States, 2002–2015. *Sexually Transmitted Infections*, 96(2):121–123, 2020.

[48] Jonathan D Lenz and Joseph P Dillard. Pathogenesis of Neisseria Gonorrhoeae and the Host Defense in Ascending Infections of the Human Fallopian Tube. *Frontiers in Immunology*, 9:2710, 2018.

[49] Brian G Leroux, Xingye Lei, and Norman Breslow. Estimation of Disease Rates in Small Areas: A New Mixed Model for Spatial Dependence. In *Statistical Models in Epidemiology, The Environment, and Clinical Trials*, pages 179–191. Springer, 2000.

[50] Ned Levine et al. CrimeStat III: A Spatial Statistics Program for the Analysis of Crime Incident Locations (Version 3.0). *Houston (TX): Ned Levine & Associates/Washington, DC: National Institute of Justice*, 2004.

[51] Zeyi Liu, Rob Deardon, Yanghui Fu, Tahsin Ferdous, Tony Ware, and Qing Cheng. Estimating Parameters of Two-Level Individual-Level Models of the COVID-19 Epidemic Using Ensemble Learning Classifiers. *Frontiers in Physics*, 8:602722, 2021.

[52] Lisa M Lix, Mark Smith, Mahmoud Azimaee, M Dahl, P Nicol, C Burchill, E Burland, and A Bailly. A Systematic Investigation of Manitoba's Provincial Laboratory Data. *Winnipeg, MB: Manitoba Centre for Health Policy*, 2012.

[53] Greta M Ljung and George EP Box. On a Measure of Lack of Fit in Time Series Models. *Biometrika*, 65(2):297–303, 1978.

[54] Thomas A Louis. Finding the Observed Information Matrix When Using the EM Algorithm. *Journal of the Royal Statistical Society Series B: Statistical Methodology*, 44(2):226–233, 1982.

[55] Diane Lu, Barbara Strauss, Kristen Simkus, Martin Tepper, François Gagnon, Noémie Johnson, Eric Girard, and Kirsten Barnes. Adverse Events Following Mass Antibiotic Prophylaxis During a Group A Streptococcus Outbreak in the Canadian Forces Leadership and Recruit School. *Canada Communicable Disease Report= Releve des Maladies Transmissibles au Canada*, 46(9):264–271, 2020.

[56] Carole Lunny, Darlene Taylor, Linda Hoang, Tom Wong, Mark Gilbert, Richard Lester, Mel Krajden, and Gina Ogilvie. Self-Collected Versus Clinician-Collected Sampling for Chlamydia and Gonorrhea Screening: A Systematic Review and Meta-Analysis. *PLOS One*, 10(7):e0132776, 2015.

[57] MD Mahsin, Rob Deardon, and Patrick Brown. Geographically Dependent Individual-Level Models for Infectious Disease Transmission. *Biostatistics*, 23(1):1–17, 2022.

[58] Rajat Malik, Rob Deardon, and Grace PS Kwong. Parameterizing Spatial Models of Infectious Disease Transmission That Incorporate Infection Time Uncertainty Using Sampling-Based Likelihood Approximations. *PLOS One*, 11(1):e0146253, 2016.

[59] Geoffrey J McLachlan and Thriyambakam Krishnan. *The EM Algorithm and Extensions.* John Wiley & Sons, 2008.

[60] Xiao-Li Meng and Donald B Rubin. Maximum Likelihood Estimation via the ECM Algorithm: A General Framework. *Biometrika*, 80(2):267–278, 1993.

[61] Xiao-Li Meng and David Van Dyk. The EM Algorithm—An Old Folk-Song Sung to a Fast New Tune. *Journal of the Royal Statistical Society Series B: Statistical Methodology*, 59(3):511–567, 1997.

[62] Nicholas Metropolis, Arianna W Rosenbluth, Marshall N Rosenbluth, Augusta H Teller, and Edward Teller. Equation of State Calculations by Fast Computing Machines. *The Journal of Chemical Physics*, 21(6):1087–1092, 1953.

[63] Paige B Miller, Eamon B O'Dea, Pejman Rohani, and John M Drake. Forecasting Infectious Disease Emergence Subject to Seasonal Forcing. *Theoretical Biology and Medical Modelling*, 14(1):17, 2017.

[64] Todd K Moon. The Expectation-Maximization Algorithm. *IEEE Signal Processing Magazine*, 13(6):47–60, 1996.

[65] Patrick AP Moran. Notes on Continuous Stochastic Phenomena. *Biometrika*, 37(1/2):17–23, 1950.

[66] G Nakamura, B Grammaticos, and M Badoual. Vaccination Strategies for a Seasonal Epidemic: A Simple SIR Model. *Open Communications in Nonlinear Mathematical Physics*, 1, 2021.

[67] Elena N Naumova. Mystery of Seasonality: Getting the Rhythm of Nature. *Journal of Public Health Policy*, 27(1):2–12, 2006.

[68] John A Nelder and Roger Mead. A Simplex Method for Function Minimization. *The Computer Journal*, 7(4):308–313, 1965.

[69] FR Ochsendorf. Sexually Transmitted Infections: Impact on Male Fertility. *Andrologia*, 40(2):72–75, 2008.

[70] Friday Ebhodaghe Okonofua, Lorretta Favour Chizomam Ntoimo, Akhere Omonkhua, Oladiran Ayodeji, Celestina Olafusi, Emmanuel Unuabonah, and Victor Ohenhen. Causes and Risk Factors for Male Infertility: A Scoping Review of Published Studies. *International Journal of General Medicine*, pages 5985–5997, 2022.

[71] Ronen Olinky, Amit Huppert, and Lewi Stone. Seasonal Dynamics and Thresholds Governing Recurrent Epidemics. *Journal of Mathematical Biology*, 56(6):827–839, 2008.

[72] Daniel Ollech and Karsten Webel. A Random Forest-Based Approach to Identifying the Most Informative Seasonality Tests. Technical report, Deutsche Bundesbank, Discussion Paper No. 55/2020, 2020.

[73] Philip D O'Neill. Introduction and Snapshot Review: Relating Infectious Disease Transmission Models to Data. *Statistics in Medicine*, 29(20):2069–2077, 2010.

[74] Karl Pearson. On the Criterion that a Given System of Deviations from the Probable in the Case of a Correlated System of Variables is Such that it Can be Reasonably Supposed to have Arisen from Random Sampling. *The London, Edinburgh, and Dublin Philosophical Magazine and Journal of Science*, 50(302):157–175, 1900.

[75] Jeffrey Peitsch, Gyanendra Pokharel, and Shakhawat Hossain. Ensemble Learning Methods of Inference for Spatially Stratified Infectious Disease Systems. *The International Journal of Biostatistics*, 20(2):507–529, 2024.

[76] Casey N Pinto, Lorah D Dorn, Vernon M Chinchilli, and Ping Du. Chlamydia and Gonorrhea Acquisition Among Adolescents and Young Adults in Pennsylvania: A Rural and Urban Comparison. *Sexually Transmitted Diseases*, 45(2):99–102, 2018.

[77] Gyanendra Pokharel and Rob Deardon. Supervised Learning and Prediction of Spatial Epidemics. *Spatial and Spatio-Temporal Epidemiology*, 11:59–77, 2014.

[78] Gyanendra Pokharel and Rob Deardon. Gaussian Process Emulators for Spatial Individual-Level Models of Infectious Disease. *Canadian Journal of Statistics*, 44(4):480–501, 2016.

[79] José M Ponciano and Marcos A Capistrán. First-Principles Modeling of Nonlinear Incidence Rates in Seasonal Epidemics. *PLOS Computational Biology*, 7(2):e1001079, 2011.

[80] Public Health Agency of Canada. Tuberculosis in Canada: 2012 to 2021 expanded report, 2024. Accessed: April 17, 2024.

[81] Srinivas S Pulugurtha, Vanjeeswaran K Krishnakumar, and Shashi S Nambisan. New Methods to Identify and Rank High Pedestrian Crash Zones: An Illustration. *Accident Analysis & Prevention*, 39(4):800–811, 2007.

[82] Chinmoy Roy Rahul and Rob Deardon. Individual-Level Models of Disease Transmission Incorporating Piecewise Spatial Risk Functions. *Spatial and Spatio-Temporal Epidemiology*, 50:100664, 2024.

[83] Steven Riley. Large-Scale Spatial-Transmission Models of Infectious Disease. *Science*, 316(5829):1298–1301, 2007.

[84] Herbert Robbins and Sutton Monro. A Stochastic Approximation Method. *The Annals of Mathematical Statistics*, pages 400–407, 1951.

[85] Mick Roberts, Viggo Andreasen, Alun Lloyd, and Lorenzo Pellis. Nine Challenges for Deterministic Epidemic Models. *Epidemics*, 10:49–53, 2015.

[86] John D Schmale, John E Martin, and Gerald Domescik. Observations on the Culture Diagnosis of Gonorrhea in Women. *Journal of the American Medical Association*, 210(2):312–314, 1969.

[87] Shashi Shekhar, Michael R Evans, James M Kang, and Pradeep Mohan. Identifying Patterns in Spatial Information: A Survey of Methods. *Wiley Interdisciplinary Reviews Data Mining and Knowledge Discovery*, 1(3):193–214, 2011.

[88] Constantinos I Siettos and Lucia Russo. Mathematical Modeling of Infectious Disease Dynamics. *Virulence*, 4(4):295–306, 2013.

[89] Bernard W Silverman. *Density Estimation for Statistics and Data Analysis.* Routledge, 2018.

[90] Ian Simms and Judith Stephenson. Pelvic Inflammatory Disease Epidemiology: What Do We Know and What Do We Need to Know? *Sexually Transmitted Infections*, 76(2):80–87, 2000.

[91] George R Terrell and David W Scott. Variable Kernel Density Estimation. *The Annals of Statistics*, 20(3):1236–1265, 1992.

[92] Thomas H Trojian, Timothy S Lishnak, and Diana Heiman. Epididymitis and Orchitis: An Overview. *American Family Physician*, 79(7):583–587, 2009.

[93] Magnus Unemo, Ronald Ballard, Catherine Ison, David Lewis, Francis Ndowa, and Rosanna Peeling, editors. *Laboratory Diagnosis of Sexually Transmitted Infections, Including Human Immunodeficiency Virus*. World Health Organization, Geneva, Switzerland, 2013.

[94] Magnus Unemo, H Steven Seifert, Edward W Hook III, Sarah Hawkes, Francis Ndowa, and Jo-Anne R Dillon. Gonorrhoea. *Nature Reviews Disease Primers*, 5(1):79, 2019.

[95] Lisa M Vallely, Dianne Egli-Gany, Handan Wand, William S Pomat, Caroline SE Homer, Rebecca Guy, Bronwyn Silver, Alice R Rumbold, John M Kaldor, Andrew J Vallely, et al. Adverse Pregnancy and Neonatal Outcomes Associated with Neisseria Gonorrhoeae: Systematic Review and Meta-Analysis. *Sexually Transmitted Infections*, 97(2):104–111, 2021.

[96] Alies van Lier, Scott A McDonald, Martijn Bouwknegt, EPI group, Mirjam E Kretzschmar, Arie H Havelaar, Marie-Josée J Mangen, Jacco Wallinga, and Hester E de Melker. Disease Burden of 32 Infectious Diseases in the Netherlands, 2007–2011. *PLOS One*, 11(4):e0153106, 2016.

[97] Irene Vrbik, Rob Deardon, Zeny Feng, Abbie Gardner, and John Braun. Using Individual-Level Models for Infectious Disease Spread to Model Spatio-Temporal Combustion Dynamics. *Bayesian Analysis*, 7(3), 2012.

[98] Cheryl K Walker and Richard L Sweet. Gonorrhea Infection in Women: Prevalence, Effects, Screening, and Management. *International Journal of Women's Health*, pages 197–206, 2011.

[99] Y-C Wang, C-H Chung, J-H Chen, M-H Chiang, C-H Tsao, F-H Lin, W-C Chien, S-T Shang, and F-Y Chang. Gonorrhea Infection Increases the Risk of Prostate Cancer in Asian Population: A Nationwide Population-Based Cohort Study. *European Journal of Clinical Microbiology & Infectious Diseases*, 36(5):813–821, 2017.

[100] Caitlin Ward, Grant D Brown, and Jacob J Oleson. An Individual-Level Infectious Disease Model in the Presence of Uncertainty from Multiple, Imperfect Diagnostic Tests. *Biometrics*, 79(1):426–436, 2023.

[101] Caitlin Ward, Rob Deardon, and Alexandra M Schmidt. Bayesian Modeling of Dynamic Behavioral Change During an Epidemic. *Infectious Disease Modelling*, 8(4):947–963, 2023.

[102] Greg CG Wei and Martin A Tanner. A Monte Carlo Implementation of the EM Algorithm and the Poor Man's Data Augmentation Algorithms. *Journal of The American Statistical Association*, 85(411):699–704, 1990.

[103] Mike West. Time Series Decomposition. *Biometrika*, 84(2):489–494, 1997.

[104] Jane Whelan, Victoria Abbing-Karahagopian, Laura Serino, and Magnus Unemo. Gonorrhoea: A Systematic Review of Prevalence Reporting Globally. *BMC Infectious Diseases*, 21(1):1–23, 2021.

[105] Winnipeg Regional Health Authority. Epidemiology of Tuberculosis, 2016.

[106] Kimberly Workowski. Chlamydia and Gonorrhea. *Annals of Internal Medicine*, 158(3):ITC2–1, 2013.

[107] World Health Organization. Treatment of Tuberculosis: Guidelines, 2010.

[108] World Health Organization. Report on Global Sexually Transmitted Infection Surveillance 2018, 2018.

[109] World Health Organization. News Room, Tuberculosis, 2023. Accessed: November 7, 2023.